NOVEL/GREEN SYNTHESIS AND CHARACTERIZATION OF HYBRID TITANIUM DIOXIDE PHOTOCATALYSTS FOR VISIBLE LIGHT PHOTODEGRADATION OF POLLUTANTS AND THE REACTIVE OXYGEN SPECIES INVOLVED

A Thesis submitted
in partial fulfillment for the Degree of

Doctor of Philosophy

by

S.M.Y. MOHAMED MUKTHAR ALI

Department of Chemistry
INDIAN INSTITUTE OF SPACE SCIENCE AND TECHNOLOGY
THIRUVANANTHAPURAM

December, 2016

CERTIFICATE

This is to certify that the thesis entitled **Novel/Green synthesis and characterization of hybrid titanium dioxide photocatalysts for visible light photodegradation of pollutants and the reactive oxygen species involved** submitted by **S.M.Y. Mohamed Mukthar Ali** to the Indian Institute of Space Science and Technology, Thiruvananthapuram, in partial fulfillment for the award of the degree of **Doctor of Philosophy** is a *bonafide* record of research work carried out by him under my supervision. The contents of this thesis, in full or in parts, have not been submitted to any other Institution or University for the award of any degree or diploma.

Dr. K.Y. Sandhya
Supervisor
Department of Chemistry
IIST

Thiruvananthapuram
September, 2016

Counter signature of HOD with seal

DECLARATION

I declare that this thesis entitled **Novel/Green synthesis and characterization of hybrid titanium dioxide photocatalysts for visible light photodegradation of pollutants and the reactive oxygen species involved** submitted in partial fulfillment of the degree of **Doctor of Philosophy** is a record of original work carried out by me under the supervision of Dr. K.Y. Sandhya and has not formed the basis for the award of any other degree or diploma, in this or any other Institution or University. In keeping with the ethical practice in reporting scientific information, due acknowledgements have been made wherever the findings of others have been cited.

S.M.Y. Mohamed Mukthar Ali
SC11D028

Thiruvananthapuram – 695547
December, 2016

ACKNOWLEDGEMENTS

This thesis is the summary of the past five years of my work at IIST, which is a journey consisting of patience and joy, passion and exciting achievements. The good fortune of working in a field of significance to future and my interest and the knowledge I acquired throughout these years gives me a great sense of satisfaction and happiness, for which I am fully indebted and grateful to my thesis supervisor, Dr. K.Y. Sandhya, who inspires me. Her scientific intuitions, never dying interest and firm belief in students and hard work, influenced and helped me to grow us an independent researcher and good person at the end of this journey. She was always there when I needed support in all matters relating to professional and personal life. I express my heartfelt gratitude for her guidance and encouragement, which lead me to the successful completion of this thesis.

I thank Dr. K.S. Dasgupta, Former Director IIST and Dr. V.K. Dhadhwal, Director IIST for providing me opportunity to work in the excellent ambience of IIST. My special thanks to Dr. Adimurthy, former Dean R & D, for his inspirational words when I first stepped to IIST as a student. I express my sincere gratitude to Prof. Kuruvilla Joseph, Former HOD of Chemistry and Prof. Nirmala Rachael James, HOD, Chemistry for their readiness in finding solution for all our problems in the lab. I am very much indebted to my doctoral committee members for their critical and valuable suggestions. I render my thanks to the faculty members of Department of Chemistry and my fellow research students for their support. I express my thanks to all staff members of Chemistry department, especially K. G. Dileepkumar for his supports. .

I am extremely thankful to SAIF, IIT Chennai for extending their facility for SEM analysis, Department of Aerospace, IIST and VSSC for Raman measurements, PSG College of Engineering, Coimbatore and NIIST, Thiruvananthapuram for TEM and SEM, IISc and AIMS for XPS analyses.

I remember with pleasure the time I spent with my fellow researchers Raneesh, Narasimman, Aswathi, Reshma, Jalaja, Sarah, Rakesh, Meegle, Devi Renuka, Haritha, Anurudha Shukla, Neema, Sarika, Kavitha, Raja, Arun, Rohith, Bharath,

Praveen Wilson, Sujith Vijayan, Muthukumaran, Mathiyazhagan, Remyamol and Yogesh, they made my life at IIST pleasant and memorable. Special thanks to Manjunath for the fruitful discussions and healthy arguments. I thank all my friends who have been a part of my life. At this time, I remember all my teachers with gratitude, their blessings made me what I am.

In no words I can express my gratitude for the love and care of my parents. I wish to thank them for their loving and patient support for all the endeavors in my life. I will never forget the pillars of my growth, my sisters (Majitha, Sulaiha & Bathula) and brothers Aslif, especially my elder brother Abu. Special thanks to my wife Najeeba who has been a pillar of support in all my joys and hardships. Apart from them, I must acknowledge my main driving forces my nieces, nephews and also my daughter for making my life more meaningful. Without their prayers, this thesis would have never become a reality. Finally, I acknowledge the supreme power for all the blessings. Finally, I acknowledge the Almighty for all the blessings.

S.M.Y. Mohamed Mukthar Ali

ABSTRACT

TiO_2 based visible light photodegradation is one of the amenable solution to the environmental problems especially the water pollution. However, various surface modifications has to done to make them visible light responsive. The reaction course and reactivity of these modified surfaces differ significantly from unmodified TiO_2. Deep insights and the photodegradation mechanistic views of these new systems are highly essential in designing an efficient visible light photocatalytic materials.

This thesis mainly focuses on the preparation methods of various TiO_2 modified composites, its characterization, to study its photodegradation properties and also to examine the reactive oxygen species (ROS) involvement in the photodegradation of rhodamine B (RhB) under visible light. In the (001) exposed facet TiO_2-graphene composite, the composite is prepared using photochemical reduction method using UV light. The composite is showing excellent selectivity towards the photodegradation of positive dyes and •OH and $^1O_2$ are the dominant ROS species (This work was published in Solar Energy Materials and Solar Cells, 2016).

Nitrogen doped TiO_2 (N-TiO_2) and TiO_2-MoS_2 (TMS) photocatalysts are prepared using one step solvothermal method lead and exhibit excellent visible light photodegradation properties. ROS O_2•− plays dominant role in the visible light photodegradation of RhB by N-TiO_2 and TMS photocatalysts (N-TiO_2 work was published in RSC Advances, 2016 and TMS photocatalyst work was published in New Journal of Chemistry, 2016). In N-TiO_2 photocatalyst, intra-band gap states is for visible light enhancement while in TMS composites few layered MoS_2 sensitized TiO_2 mechanism is the reason.

Modification of commercial P25 with carbon dot (C-dot) lead to the improved visible light absorption and the photodegradation properties. Here the composite is prepared from the physical mixing of P25 and C-dot. Up-converted photoluminescence is responsible for the dominant •OH ROS production. Scavenging studies reveal how ROS contributions alters the reaction pathway of the resulting intermediate especially the importance of •OH ROS in the mineralization of RhB dye.

Similarly the photochemical reduction is employed in the preparation of TiO_2-C_{60} (This work was published in Carbon, 2014) or TiO_2-reduced graphene oxide (rGO) (This work was published in Environmental Progress and Sustainable Energy, 2016) composites using cyclcodextrin as a linker molecule. Visible light absorption is achieved by ligand to metal charge transfer (LMCT) mechanism. ROS O_2•− and $^1O_2$ are dominant with TiO_2-CD-C_{60} and TiO_2-CD-rGO composites respectively.

In conclusion, this thesis presents an understanding of, how the various surface modifications of TiO_2 and the resulting photodegradation mechanism affects the contribution of ROS in the visible light photodegradation.

TABLE OF CONTENTS

DESCRIPTION **PAGE NUMBER**

LIST OF FIGURES

LIST OF TABLES

ABBREVIATIONS

°C	Degree Celsius
µm	micrometer
µM	micromolar
4CP	4-Chlorophenol
AM	Air mass
AMS	Ammonium molybdenum sulfide
aN-TiO_2	Annealed nitrogen doped TiO_2
BET	Brunauer-Emmet-Teller
BQ	1,4 – benzoquinone
C	Carbon
CB	Conduction Band
CD	Cyclodextrin
C-dots	Carbon dots
CNT	Carbon nanotube
DSSC	Dye-sensitized solar cell
DSPD	Dye-sensitized photodegradation
DMPO	5, 5-dimethyl-1-pyrolline-N-oxide
DOS	Density of states
DRS	Diffuse Reflectance Spectra
e-h	electron-hole
eV	electron volt
EDAX	Energy Dispersive X-ray spectroscopy

EIS	Electrochemical Impedance Spectroscopy
EPR	Electron Paramagnetic Resonance
ESR	Electron Spin Resonance
FESEM	Field emission scanning electron microscopy
FTIR	Fourier Transfer Infra-Red
FLAPW	Full potential linearized augmented plane-wave
F-TO_2	Fluorine doped TiO_2
Gr	Graphene
GO	Graphene oxide
HOMO	Highest Occupied Molecular Orbital
HRTEM	High Resolution Transmission Electron Microscope
$HRTiO_2$	Highly reactive facet (001) exposed TiO_2
hr	Hour
ISC	Intersystem Crossing
LDA	Local density approximation
LMCT	Ligand to Metal Charge Transfer
LUMO	Lowest Unoccupied Molecular Orbital
MB	Methylene Blue
MO	Methyl Orange
mg	milligram
min	minutes
ml	milliliter

mM	millimolar
mV	millivolt
NHE	Normal Hydrogen Electrode
N	Nitrogen
nm	nanometer
N-TiO_2	Nitrogen doped TiO_2
NMP	N-methyl-1-pyrrolidone
PC	Photocatalytic
PD	Photodegradation
PEC	Photoelectrochemical
PL	Photoluminescence
PLQY	Photoluminescence Quantum Yield
QY	Quantum Yield
ROD	Reactive Oxygen Species
rGO	Reduced graphene oxide
RhB	Rhodamine B
SA	Surface area
SACS	Solvent-based ambient condition sol
SAED	Small Area Electron Diffraction
SEM	Scanning electron microscope
SMPC	Semiconductor Photocatalysis
SMH	Semiconductor mediated hydrogen generation
SMPD	Semiconductor mediated photodegradation

SOD	Superoxide Dismutase
SPR	Surface Plasmon Resonance
t-BuOH	tertiary butyl alcohol
Ti	Titanium
TMS	TiO_2-MoS_2
TIOP	Titanium isopropoxide
TTBT	Titanium butoxide
TEA	Triethylamine
TGA	Thermogravimetric Analysis
TW	Terawatts
UV	Ultra-Violet
VB	Valence Band
VL	Visible light
W	Watt
WACS	Water-based ambient condition sol
wt%	Weight %
XPS	X-ray Photoelectron Spectroscopy
XRD	X-ray Diffraction
ZP	Zeta potential

NOTATIONS

T_1 & T_2	Transitional intermediates
S_1	Stationary intermediates
$^1\Delta_g$	Low energy state of singlet oxygen
$^1\sum_g^+$	High energy state of singlet oxygen
P25	TiO_2 with anatase and rutile phase
•OH	Hydroxyl radical
O_2•−	Superoxide anion
$^1O_2$	Singlet Oxygen
ϖ	QY of standard sample
V_o	Oxygen vacancies

NOMENCLATURE

TiO_2	Titanium dioxide
NH_4OH	Ammonium Hydroxide
NH_4Cl	Ammonium Chloride
MoS_2	Molybdenum disulfide
O_2	Oxygen
H_2	Hydrogen
C_{60}	Fullerene C_{60}
Fe_2O_3	Iron oxide
WO_3	Tungsten oxide
ZnO	Zinc oxide
CeO_2	Cerium oxide
CdS	Cadmium sulfide
MoO_3	Molybdenum oxide
ZrO_2	Zirconium oxide
SnO_2	Tin oxide
KMnO4	Potassium permanganate
H_2O_2	Hydrogen Peroxide
HCl	Hydrochloric acid
HF	Hydrofluoric acid
$K_4Fe(CN)_6$	Potassium ferrocyanide
$(K_3Fe(CN)_6)$	Potassium ferricyanide
IPA	Isopropanol

Na_2CO_3	Sodium carbonate
Na_2SO_4	Sodium sulfate
H_2SO_4	Sulfuric acid
NaF	Sodium fluoride
TiN	Titanium nitride
Na_2MoO_4	Sodium molybdate
$[(NH_4)_6\ Mo_7S_{24}.4H_2O]$	Ammonium heptamolybdate
NaN_3	Sodium azide
-COOH	Carboxylic acid group
-C-O-C-	Ether group
-OH	Hydroxyl group
-C=O	Carbonyl group

CHAPTER 1

INTRODUCTION

This chapter comprises the state-of-the-art literature survey on the strategies adopted for extending the absorption of TiO_2 to the visible light (VL) region of the solar spectra and to improve its photocatalytic (PC) properties under VL. Further this chapter explores the role of reactive oxygen species (ROS) formed during photodegradation (PD) reactions and the influences of the modifications in the formation of ROS. Finally, the chapter briefs about the motivation of our research work, research problem and the expected outcomes of the proposed work. In addition, the outline of the thesis and a brief introduction of each chapter is provided at the end of the chapter,

1.1. Background

In average, the energy consumption by humans on earth in 2004 was ~15 terawatts (TW) and by 2050, the demand and consumption is expected to reach ~35 TW. Presently, more than 85% of these energy needs are met from fossil-fuel sources. Fossil-fuel sources are the dominant players in the causes of environmental issues and climate changes such as production of greenhouse gases, ozone depletion, global warming etc. Though the current technology and the available coal reserves may provide the energy needed for centuries, due to its calamitous effects on environment and society, which are creating harmful effects to earth, and due to their non-renewable nature this approach cannot sustain for long. For the progressive and benign development of humanity, a green technologies to extract or convert energy from renewable and sustainable energy resources are imminent. The major renewable energy sources are hydropower, biomass energy, wind energy, solar energy, geothermal energy and tidal energy. Even though there are numerous renewable sources available, abundance of the solar energy and its omnipresence makes it the most popular source.

According to International Energy Agency data, the solar energy that reaches annually on the earth surface on an average is 1.2×10^5 TW, which is about

10,000 times more than the power consumption in 2004. Solar spectral irradiance is given in Figure 1.1. Solar spectra predominantly contains infrared (IR) irradiation (~50%) and VL irradiation (~46%) and very minimal ultraviolet (UV) light irradiation (~4%). Conversion and consumption of solar energy, if done efficiently, is the most viable solution that can address all the energy and environmental concerns. The energy source, in addition to be being abundant and renewable, should couple with a green and economically viable conversion technology for a sustainable approach.

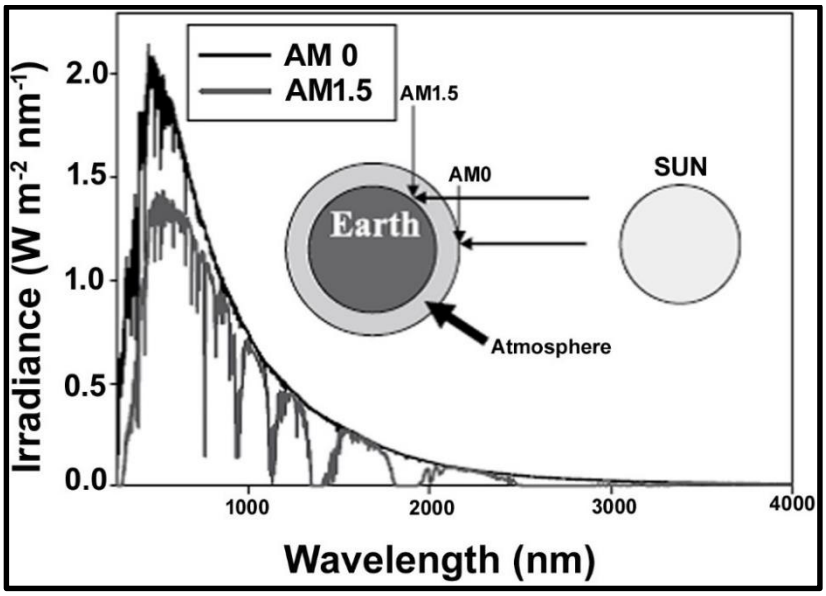

Figure 1.1. An illustration of the solar spectrum in space just outside the atmosphere (air mass is negligible; AM 0) and the solar spectrum at the surface of the earth at the northern latitudes of Europe (AM 1.5). The distances in the drawing of the sun, earth, and atmosphere is not to scale.

1.2. Semiconductor Photocatalysis

Semiconductor photocatalysis (SMPC) is one of the effective way to tap the solar energy. SMPC has been around for long, such as fading of paints on the walls, bleaching of paper, though it was not recognized for what it was. Even though the experimental observation of the PC activity of semiconductor oxides date back to

early twentieth century, the question of where it first originated may continue to be question difficult to answer. The first photodegradation (PD) of organic molecule was observed in 1921 by Renz et al. (Renz, 1921) which lead to the reduced products of the organic compounds. The utilization of TiO_2 for the photo-decolouration of dye was studied way back in 1938 by Goodeeve and Kitchener (Goodeve & Kitchener, 1938), and the oxidation of organic solvents in 1950s, by Kato and Mashio and later in 1967 Morrison and Freund (Morrison, 1967) studied the photocatalyzed oxidation of aqueous phase formic acid in the presence of ZnO to CO_2 and H_2O_2 and thus the study perhaps places ZnO the first semiconductor to be used in PC mineralization. It was not until 1972, when Fujishima and Honda (Fujishima & Honda, 1972) made the ground breaking discovery of the photoelectrolysis of water molecule using an n-type rutile TiO_2 anode against platinum cathode that photocatalysis came into much limelight and prompted the beginning of keen research in the field of photon energy conversion as an alternative energy source, through 1970s to early 1980s (Gaya, 2014).

SMPC is a process which utilizes a semiconductor as photocatalyst for harvesting the solar energy to effect the reactions on the surface of the semiconductor. Using this method, the clean solar energy can be harnessed. It is the basic principle of many applications like semiconductor mediated hydrogen (H_2) generation (SMH) (Xia & Zhang et al., 2013; Xing & Tian et al., 2011; Zuo & Wang et al., 2010) and semiconductor mediated PD (SMPD) (Chowdhury, Moreira, Gomaa, & Ray, 2012; Qin et al., 2011; Sakthivel et al., 2004; Yamashita et al., 2002), dye sensitized solar cells (DSSC) etc. The mentioned technologies have common mechanism in harvesting the light energy and they differ in the conversion of light energy. The common mechanism is mainly comprised of two steps as given in Figure 1.2,

(i) Absorption of light energy and generation of electrons and holes by a semiconductor;
(ii) Separation of the electrons and holes to the surface of the semiconductor.

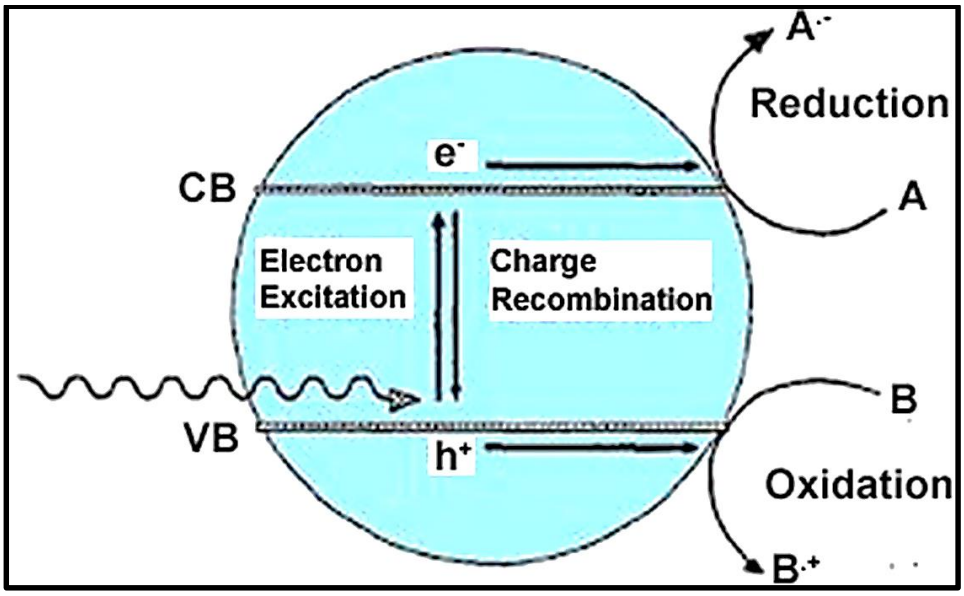

Figure 1.2. Schematic representation of semiconductor photocatalysis mechanism.

When a semiconductor is irradiated with light energy equal to or higher than the energy of its band gap, it absorbs the light energy and produces holes in the valence band (VB) and electrons in the conduction band (CB) of the semiconductor. The extent of electron-hole (e-h) generation depends on the light absorbing ability of the semiconductor. Separation of these electrons and holes depends on the exciton binding energy, charge carrier mobility, crystallinity and defect nature etc. of the semiconductor. SMH process leads to the splitting of water into oxygen (O_2) and H_2 either solely using light energy (photochemical water splitting) or partially in combination with electrical energy (photoelectrochemcial (PEC) water splitting). Apart from these applications, SMPC can be focused on destruction of bacteria, viruses, fixation of nitrogen and clean-up of oil spills (Blake et al., 1999; Gerrity, Ryu, Crittenden, & Abbaszadegan, 2008; Hsu et al., 2008; M. Khan, 1988; Ziolli & Jardim, 2001). Among the various photocatalysts, based on their band structure the following are some of the widely investigated photocatalysts: TiO_2, Fe_2O_3, WO_3, ZnO, CeO_2, CdS, Fe_2O_3, ZnS, MoO_3, ZrO_2 and SnO_2 due to their properties or combination of properties such as stability or narrow band gap or distinct electronic structure or their easy recycling properties (unoccupied CB and occupied

VB) (Etacheri, Seery, & Michlits, 2013; Fujishima & Honda, 1972; P. V. Kamat, 2007; L. Li et al., 2010; Yu Liu et al., 2012; Vayssieres, 2003).

1.2.1. Semiconductor mediated photodegradation

The degradation of the organic pollutants into CO_2 and water or other less harmful organic intermediates using light energy and a semiconductor photocatalysts is called SMPD. For this process, activation of either O_2 or organic pollutant has to happen. Even though organic pollutants degradation by O_2 is thermodynamically favorable (C. Chen, Ma, & Zhao, 2010), i.e., the degradation reaction has negative free energy change, the kinetics of the reaction is rather slow under room temperature (Pathway A in Figure. 1.3). The slowness of the (uncatalyzed) reaction is attributed to the difference in spin multiplicity (ground state O_2 is triplet while organic pollutant is in singlet state) and lower one-electron reduction potential of ground state O_2 (-0.16 eV) (Sawyer & Valentine, 1981). So there is a necessity to catalyze the degradation reactions either by thermally or by photo catalytically to make it faster.

Of the two strategies, thermal catalysis reactions are shown in pathway B in Figure 1.3. In this pathway, either O_2 or organic pollutants or both activated thermally to form the transitional (T_1 and T_2) and the stationary intermediates (S_1) and followed by the degradation. In this strategy, free radicals are rarely involved. Catalytic aerobic oxidation of organic compounds or the noble-metal catalyzed activation of O_2 for oxidation of organic compounds are typical examples of thermal catalysis. Photocatalysis is another mechanism to improve the degradation of pollutants. In this process, O_2 and organic pollutant is activated high energy light to overcome the barrier (pathway C, in Figure 1.3). Still the reaction kinetics is lower. Incorporation of semiconductor photocatalyst can speed up the rate of reaction further. This is called as SMPD. Under SMPD, activation of either photocatalyst or the pollutant or both will lead to the PD of pollutant. Based on the mechanism of PD, it can be classified mainly as organic or dye-sensitized PD (DSPD) and photocatalyst activated PD (PCPD).

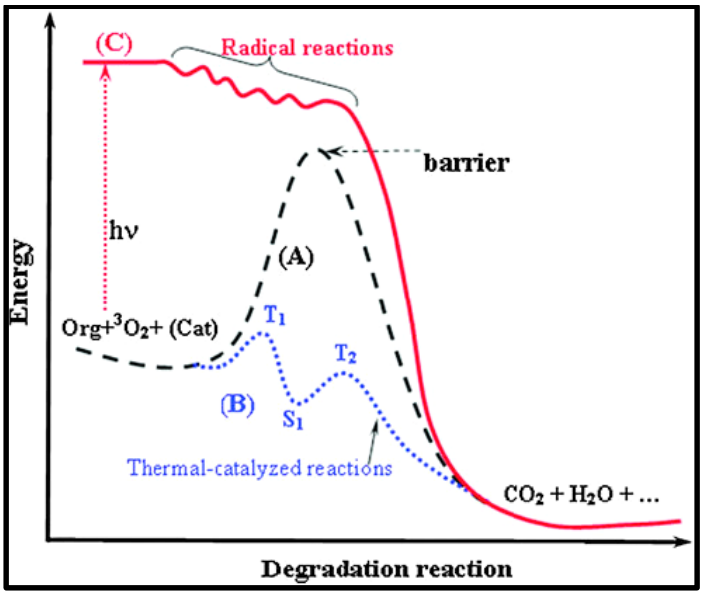

Figure 1.3. Different paths for the reaction between organic pollutants (Org) and triplet ground state of molecular oxygen ($^3O_2$). (A) Direct thermal reaction process with a high barrier; (B) thermal-catalyzed degradation with lowered barrier via stationary and transitional intermediates; (C) photochemical or PC degradation.

In addition to these mechanisms, other mechanism such as Ligand to Metal Charge Transfer (LMCT) can also be operated depending on the photocatalyst and pollutants. Electrons and holes are the primary species formed during photocatalysis. These species can directly attack the organic pollutants to initiate the PD or can react with water to produce various ROS. Hydroxyl radicals (•OH), superoxide anion (O_2•−), hydrogen peroxide (H_2O_2), singlet oxygen ($^1O_2$) and hydroperoxide (•OOH) are some of the ROS produced during PD and causes the destruction of pollutants. Of these ROS, •OH, O_2•− and $^1O_2$ are the primary ROS. The mechanism of formation of ROS based on TiO_2 photocatalyst are given in Figure 1.4. (C. Chen et al., 2010; F. Chen, Zou, Qu, & Zhang, 2009; Schneider et al., 2014),

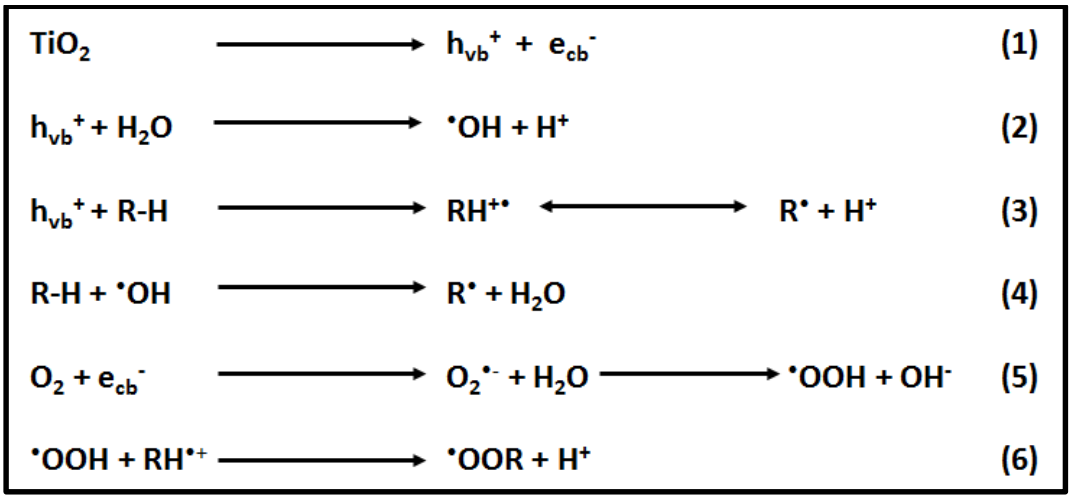

Figure 1.4. Mechanisms of formation of ROS during PD.

1.2.2. Reactive oxygen species (ROS) in photodegradation

In SMPD, electrons from the VB of a semiconductor are excited to the CB by light of equal or higher energy than the respective band gap, resulting in the formation of e-h) pairs. CB electrons are good reducing agents (+0.5 to −1.5 V vs NHE) whereas the VB holes are strong oxidizing agents (+1.0 to +3.5 V vs. NHE). The lack of a continuum of inter-band states in semiconductors assures an adequately extended lifetime for photogenerated e-h pairs to initiate redox reactionson the catalyst surface. Electrons in the CB can reduce O_2 to form O_2•−. Secondary reactions of O_2•− with holes in the VB produce $^1O_2$ (Daimon & Nosaka, 2007; A. U. Khan, 1970). Subsequent reactions of VB holes with surface adsorbed H_2O result in the formation of •OH, H_2O_2 and •OOH. H_2O_2 results from the coupling of two HOO• species. These activated oxygen species are collectively called as ROS. The ROS formation is influenced by the type of mechanism, energy level position of semiconductors and the redox potential of ROS formation reactions. Of these various ROS involved in PD reactions of organic molecules/ dyes/ pollutants, •OH, O_2•− and $^1O_2$ are the focus of interest of our work due to their primary involvement in the PD.

1.2.2.1. Hydroxyl radicals (•OH)

The •OH is the one of the strongest oxidant with an oxidation potential of E° = 2.80 eV produced in the PC reactions. In addition to that the typical rate constants (10^6-10^{11} mol dm^{-3} s^{-1}) (Schipper, 2012) of •OH with organic molecules are diffusion-limited i.e. it immediately reacts with the surrounding organic species. There are few proposed ways by which •OH may react with organic pollutant and oxidize them (Draper & Fox, 1990; Turchi & Ollis, 1990) (i) Adsorbed •OH oxidizes nearby pollutant molecules; (ii) Conversely, free •OH oxidizes adsorbed organic molecule, both of these processes are classified under the Langmuir-Rideal bimolecular mechanism. (iii) Thirdly, oxidation can take place while both the •OH and the pollutant are in the adsorbed phase in accordance with the Langmuir-Hinshelwood mechanism and finally, (iv) free •OH may react with pollutant molecules in solution (Sclafani & Herrmann, 1998). It is important to note that, the last process usually does not occur in PC systems as most works have given substantial evidence towards the occurrence of PC reactions solely at the adsorbed phase. The three probable mechanisms are pictorially represented in Figure 1.5.

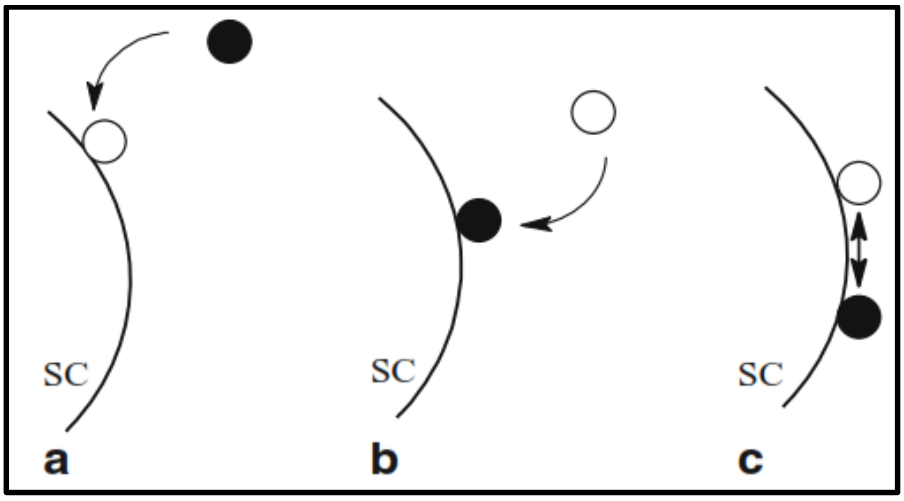

Figure 1.5. Bimolecular schemes for the reaction of pollutant molecule with •OH in the presence of semiconductor particle. (a) pollutant in the vicinity of semiconductor surface attacked by adsorbed •OH (b) oxidation of pollutant while at the surface of semiconductor photocatalyst and the •OH in solution (c) oxidation reaction while both •OH and pollutant are in the adsorbed phase.

1.2.2.2. Superoxide anion ($O_2^{\bullet-}$)

The $O_2^{\bullet-}$ is formed by a one-electron reduction of oxygen and it is the most common ROS in both the semiconductor photocatalysis and dye-sensitized mechanisms. It is easily protonated to form •OOH. $O_2^{\bullet-}$ are suggested to play dominant role in the VL PD (Jin Wang et al., 2009). Its oxidation potential E° is 0.94 eV. It is formed by the reduction of O_2 by the photo generated electron during photocatalysis. Despite its moderately high reduction potential (0.94 eV), its reactivity with non-radical targets is limited. Besides the direct involvement of $O_2^{\bullet-}$in photo oxidation, the efficient formation of $O_2^{\bullet-}$ means a reduced recombination rate in the photocatalyst as this oxidizing species is formed via electron transfer to O_2 molecule. The experimental evidence for the formation of $O_2^{\bullet-}$ has been obtained in many degradation systems by the spin-trapping ESR technique (Hongbo Fu, Zhang, Zhang, Zhu, & Zhao, 2006). In ESR technique, $O_2^{\bullet-}$ can be trapped by spin-trapping reagent 5, 5-dimethyl-1-pyrolline-N-oxide (DMPO) leading to the trapped DMPO radical which can be identified by ESR method. Addition of superoxide scavengers such as Superoxide Dismutase (SOD) or 1,4-benzoquinone (BQ) into the degradation systems markedly suppresses the degradation of the dyes. Presence of metal ions such as Cu^{2+} or Fe^{3+} can hinder the degradation of dyes as they can react with the photo generated electrons preferentially than that of O_2.

1.2.2.3. Singlet Oxygen ($^1O_2$)

The $^1O_2$ refers to the excited states of O_2; the $^1\Delta_g$ and $^1\sum_g^+$ state. They have energies of around 94.3 kJ/mol and 156.9 kJ/mol above the triplet ground state, respectively. Singlet state has an extremely short lifetime (~10^{-11} s) in H_2O, decaying rapidly to the $^1\sum_g^+$ state, which is considered the biologically relevant form of $^1O_2$. The lifetime of $^1O_2$ is greatly influenced by the solvent type, being in the range of 1 x 10^{-6} to 5 x 10^{-6} s in H_2O and about ten times higher in deuterium oxide (D_2O). Photo sensitization is the most conventional source of $^1O_2$ in PC process. Hence for an efficient $^1O_2$ formation, intersystem crossing (ISC) of the dye has to be higher. When the dye is excited to singlet excited state followed by ISC,

it can attain the excited triplet state. At this state, it can react with triplet state O_2 to form $^1O_2$. Apart from this process, photo produced $O_2^{\bullet-}$ is likely to be converted to lowest excited state of singlet oxygen $^1O_2$ ($^1\Delta_g$) (Daimon & Nosaka, 2007; A. U. Khan, 1970). Consequently, the formed $^1O_2$ lends support in the PC oxidation of pollutants on semiconductor photocatalysts. $^1O_2$ is a powerful oxidant that can even mediate the photo-oxidation of alkenes. However, there has been only a few reports indicating experimentally, the formation of $^1O_2$ on TiO_2 photocatalyst. Khan et al. (A. U. Khan, 1970) , attempted the elucidation of the nature of TiO_2 photo excitation and observed singlet oxygen signals at 355 nm. Recently, Daimon and Nosaka (Daimon & Nosaka, 2007) detected singlet molecular oxygen from a TiO_2 photocatalyst irradiated with a 355 nm laser pulse by monitoring its near-infrared phosphorescence at 1270 nm. The quantum yield was significant (0.12–0.38 in air) while the lifetimes ranged from 2.0 to 2.5 μs which suggests that $^1O_2$ contribute in the photo-oxidation of organic molecules. An examination of eighteen TiO_2 samples revealed an increase in the formation of $^1O_2$ with decrease in the size of TiO_2 particles, indicating that a large specific surface area causes a higher possibility of reduction producing $O_2^{\bullet-}$ which further forms a large amount of the $^1O_2$ (Jańczyk, Krakowska, Stochel, & Macyk, 2006; Mukthar Ali & Sandhya, 2014, 2016c). Janczyk et al. (Jańczyk et al., 2006) reported the strong evidence for the degradation of cyanuric acid on F-TiO_2 by $^1O_2$, which opens new discussion on the role of oxidizing species in PC oxidation.

1.3. TiO_2 as a Photocatalyst

Studies on harvesting the solar spectrum using semiconductor gained attention after the PEC water splitting experiment using TiO_2 semiconductor by Fujishima and Honda in 1972 (Fujishima & Honda, 1972). For a semiconductor to be a good photocatalyst, the following criteria is required,

i. Good spectral coverage;
ii. Large number of surface active sites;
iii. High photo corrosion stability and

iv. Low toxicity.

TiO_2 materials in different types and forms have shown great potential as ideal and powerful photocatalysts for various significant reactions due to its properties such as chemical and photo stability, nontoxicity, and high thermal stability. Investigations of well-defined PC reaction systems and of their detailed reaction mechanisms and kinetics using various molecular spectroscopic techniques have led to the development of various TiO_2-based PC materials. Photocatalysts have been employed for various significant applications such as the purification of polluted water and air, self-cleaning glasses, tiles, TiO_2 materials with unique photo induced super hydrophilicity for mirrors, glasses, tents etc. and advanced applications such as photo chemical water splitting, DSSC etc. TiO_2 is an unassailable photocatalyst in UV light however its VL PC activity has to be improved a lot due to its wider band gap.

1.3.1. Crystalline and Electronic Structure of TiO_2

TiO_2 is found in nature in three crystalline polymorphs namely anatase, rutile and brookite. All the polymorphs are primarily made up of TiO_6 octahedra, each of the Ti^{4+} ion is surrounded by O^{2-} ions, only variation between them is in their mode of connection either via edges or corners or both. The differences will result in different optical and electronic properties of the polymorphs. Unit cell structures of the polymorphs are given in Figure 1.6. In the case of rutile and brookite, TiO_6 octahedron is connected through their edges and corners while for the anatase, they are connected via edges only, but they differ in their orientation. TiO_6 octahedron has a slight orthorhombic distortion in rutile, while it is distorted significantly in anatase and hence the symmetry of anatase is lower than that of orthorhombic. The Ti-Ti distance in anatase is larger and the Ti-O distance is shorter than that of in rutile. Anatase has four edge shared each TiO_6 octahedron while rutile has two edge shared each TiO_6 octahedron. This causes the lowering of the density of anatase (3.89) than that of the rutile (4.27). In rutile, each octahedron shares corners with eight neighbors, and shares edges with two other neighbors, forming a linear chain. In contrast, in anatase, each octahedron shares corners with four neighbors, and shares edges with four other neighbors, forming a zigzag chain

with a screw axis (Banerjee et al., 2014; Etacheri, Di Valentin, Schneider, Bahnemann, & Pillai, 2015; Schneider et al., 2014). Also, anatase has a large metal−metal distance of 5.35 Å. These differences in lattice structures cause different mass densities and electronic band structures between the two forms of TiO_2.

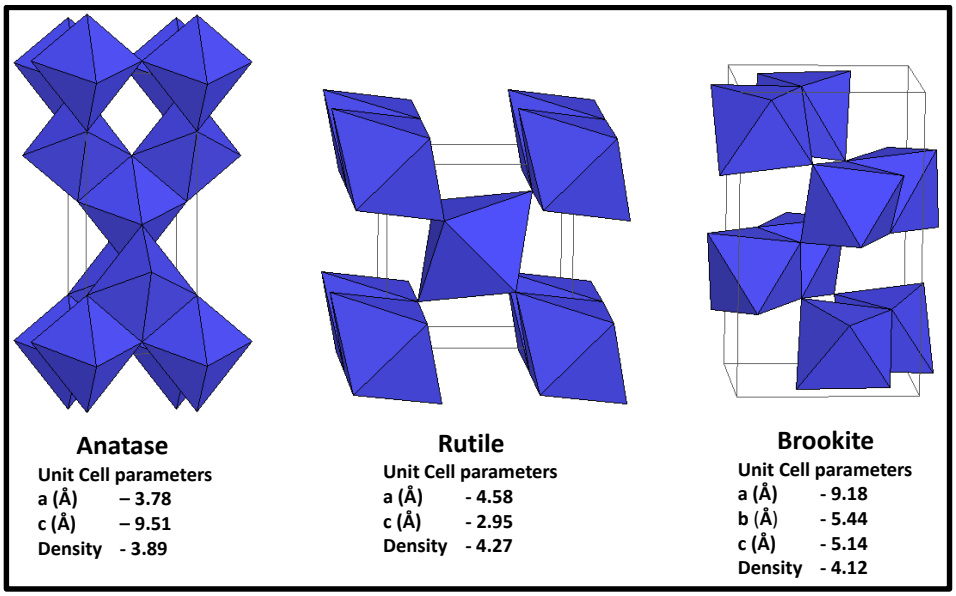

Figure 1.6. Crystalline structure of polymorphs of TiO_2.

Most of the investigations of semiconductor-based photocatalysis have focused on anatase TiO_2 because of its relatively high reactivity and chemical stability. The electronic structure of TiO_2 has been studied by several ab-initio calculations. A fundamental feature of the molecular orbital bonding diagram of anatase TiO_2 is shown in a Figure 1.7. The non-bonding 2pπ orbital of O atom (out of the Ti_3O cluster plane) is at the top of the VB and the non-bonding d_{xy} states at the bottom of the CB, the feature though seen in rutile, is of less significant than in anatase. As a consequence, the Ti d_{xy} orbitals at CB are relatively isolated, while the t_{2g} orbitals at CB in rutile provide the metal−metal interaction with a smaller distance of 2.96 Å. The band gap of anatase is thus smaller than that of rutile, resulting in a slightly wide bandgap of 3.2 eV as compared to 3.0 eV for rutile. Compared to anatase and rutile phases, brookite form of TiO_2 was least studied

because of its difficulty in preparation which requires higher temperature and less reactivity.

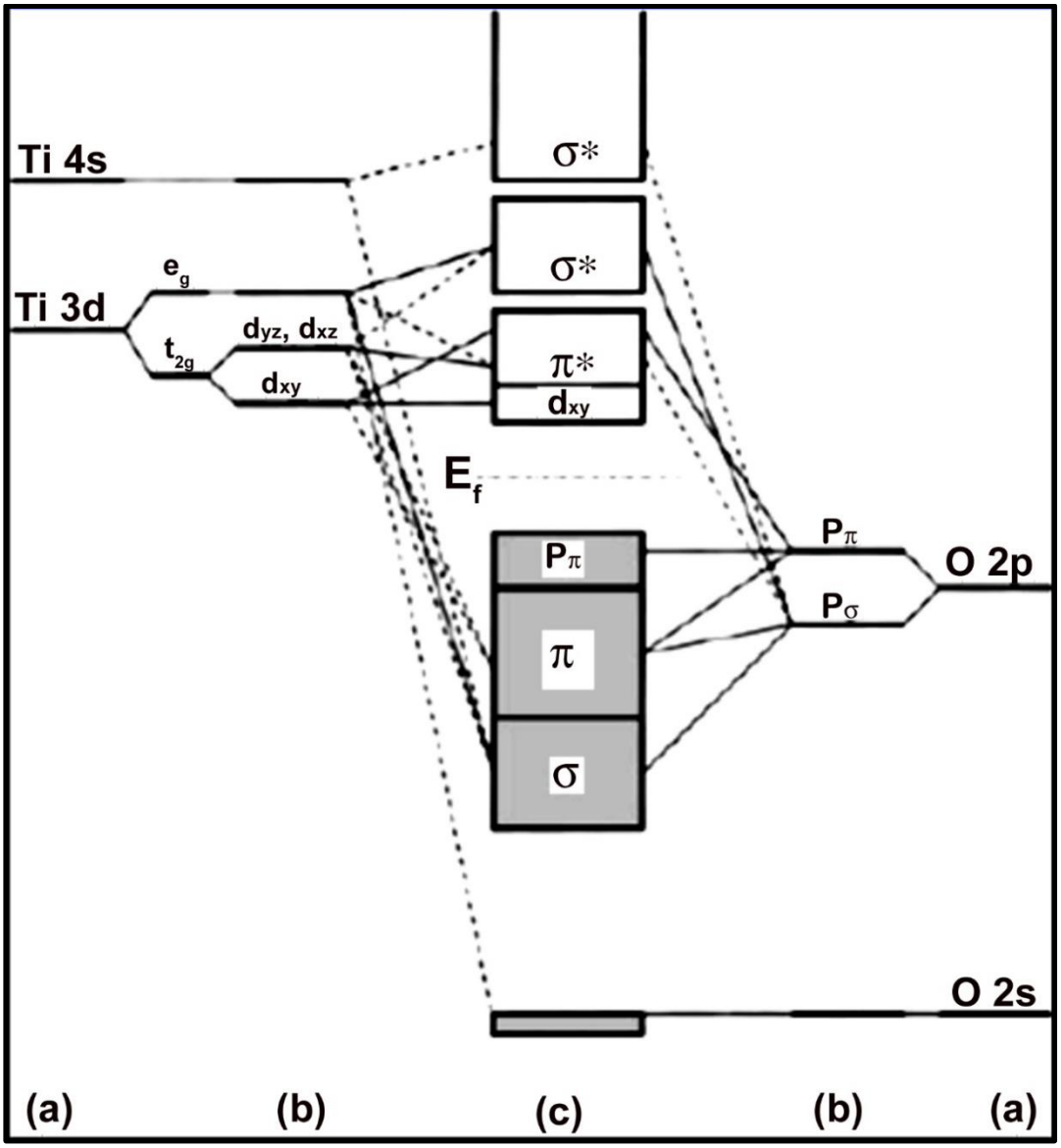

Figure 1.7. Molecular-orbital bonding structure for anatase TiO_2: (a) atomic levels, (b) crystal-field split levels, and (c) final interaction states. The thin-solid and dashed lines represent large and small contributions, respectively.

1.4. Strategies for visible light active TiO_2

The potential application of TiO_2 as a photocatalyst is limited in the solar spectra due to its wide band gap which limits its absorption only to the UV region of the solar spectra. Only ~5% of the energy of the solar spectra UV light, hence it is inevitable to enhance the light response of TiO_2 to the visible region in order to achieve better PC activity. Thus employing suitable strategies to enhance VL responsiveness of TiO_2 in order to improve its PC properties is necessary. Investigations have been carried out to the development of VL responsive TiO_2 photocatalysts using various strategies such as metal doping (Choi, Termin, & Hoffmann, 1994; Yanqin Wang, Hao, Cheng, Ma, & Xu, 1999), non-metal doping (R Asahi, Morikawa, Ohwaki, Aoki, & Taga, 2001; Ryoji Asahi, Morikawa, Irie, & Ohwaki, 2014; Lin et al., 2013; Mukthar Ali & Sandhya, 2016c), reduced TiO_2 (X. Chen, Liu, Yu, & Mao, 2011), defect engineering (Wendt et al., 2008) by electron beam modification (Etacheri, Seery, Hinder, & Pillai, 2011; Kalathil, Khan, Ansari, Lee, & Cho, 2013; M. M. Khan et al., 2014) and by physical ion-implantation methods such as anion and transition metal ion implantations (Anpo & Takeuchi, 2003; Ghicov, Macak, Tsuchiya, & Kunze, 2006) to operate effectively under natural sunlight irradiation. Different strategy exerts different mechanism of photo generation of e-h pair or combination of mechanisms and this considerably influences the formation of ROS during PD process. ROS are the driving force for PD of dyes, determining the ROS involvement is essential in designing a good photocatalyst. ROS formation is influenced by the dye/ pollutants itself and hence can vary depending on the pollutant for the same photocatalyst. So it is essential to keep a common pollutant to see the effect of photocatalyst while investigating the role of ROS. In this section, we are discussing different strategies adopted for making VL responsive TiO_2 and how the changes affect the formation/contribution of ROS.

1.4.1. Non-metal doping

Doping of TiO_2 with non-metals such as carbon (C) (Jong Hyeok, Sungwook, & Allen, 2006; Kiran & Sampath, 2013; Park, Kim, et al., 2009), nitrogen (N) (Z. Jiang et al., 2014; Junwei, Wei, Yinqing, & Shuangxi, 2007;

Mukthar Ali & Sandhya, 2016c; Sato, Aita, Komatsu, & Yin, 2006; Torres, Lindgren, Lu, Granqvist, & Lindquist, 2004; Wawrzyniak, Morawski, & Tryba, 2006), fluorine (M. V. Dozzi, D'Andrea, Ohtani, Valentini, & Selli, 2013; Huang et al., 2007), boron (N. Lu, Zhao, Li, Quan, & Chen, 2008) and sulphur (Devi & Kavitha, 2014; Rockafellow, Stewart, & Jenks, 2009; Szatmary et al., 2011) are promising strategies to prepare VL responsive TiO_2. Studies on non-metal doping of TiO_2 was triggered by Asahi et al. (R Asahi et al., 2001) and it was observed that N-doping serves well for an efficient VL absorption. Doping of TiO_2 with N has been predominantly studied since its easier introduction into the TiO_2 lattice due to its comparable size with O_2 atomic radii. Asahi et al. (R Asahi et al., 2001) first simulated and prepared the $TiO_{2-x}N_x$ film by sputtering a TiO_2 target in N_2 atmosphere. The yellowish $TiO_{2-x}N_x$ films was able to absorb light up to 500 nm.

Various methods have been adopted for the N-doping of TiO_2. Under dry process, N doped TiO_2 (N-TiO_2) can be prepared by the oxidation of titanium nitride (TiN) powder by passing O_2 gas (Balcerski, Ryu, & Hoffmann, 2007; T Morikawa, Asahi, Ohwaki, Aoki, & Taga, 2001) and nitrification of TiO_2 powder by passing NH_3 gas at high temperature (R Asahi et al., 2001; Balcerski et al., 2007). The conversion of TiN to N-TiO_2 occurs above 400°C in O_2 flow. A homogeneous rutile phase is obtained in samples annealed at 550 °C, while a small amount of TiN still remains among the rutile phase of TiO_2 in samples annealed at 400 °C. N-TiO_2 prepared from nitrification of TiO_2 lead to the anatase phase at 600°C in NH_3/Ar gas flow. The decomposition of NH_3 above 550°C lead to N_2 and H_2 and hence the resulting N-TiO_2 become N-doped as well, reduced. Similarly plasma treated TiO_2 with either N_2 or N_2-H_2 mixture also lead to the formation of N-doped TiO_2 with various shades of yellow depending on the % of N-doping (Lee et al., 2014; Matsubara, Danno, Inoue, Honda, & Abe, 2012). In mechanochemical method (Yin, Zhang, Saito, & Sato, 2003), TiO_2 is mixed with hexamethylene tetramine and urea and the mixture is ball milled at high speed leading to N-TiO_2 with the phase change i.e. anatase TiO_2 is converted to rutile N-TiO_2. This is because, the high mechanical energy favors the formation of anatase to rutile phase as rutile is the more stable phase. The residual organic chemicals are removed during the calcination at 400°C. Hydrothermal, solvothermal and sol−gel methods are some

of the widely preferred methods using different precursors of TiO_2 and N. The precursors of TiO_2 include titanium isopropxide (TiOP), titanium butoxide (TTBT), titanium sulfate and $TiCl_3$ while the N-precursors include ammonium hydroxide (NH_4OH), ammonium chloride (NH_4Cl), hydrazine hydrate and triethylamine (TEA) etc. Controlled hydrolysis of TIOP to TiO_2 nanocrystal followed by the addition of TEA gave N-TiO_2. Upon vacuum drying, the treated nanoparticle solution forms deep-yellow crystallites (Gole, Stout, Burda, Lou, & Chen, 2004). In a hydrothermal synthesis of N-TiO_2, TTBT is dissolved in nitric acid with various nitrogen sources TEA or urea or hydrazine hydrate. This mixture is transferred into a Teflon-lined autoclave and heated to 120 to 200°C for several hours. In place of TTBT, TIOP can also be used. In some reports (Kaewgun et al., 2009; Kaewgun, Nolph, & Lee, 2008; Park, Kim, et al., 2009) solvents itself act as dopant materials for preparing N-TiO_2. Kaewgun et al (Kaewgun et al., 2009) utilized the N-methyl-1-pyrrolidone (NMP) as a N source for doping TiO_2 by solvothermal method. Similarly, molecular level doping was achieved using NMP as a solvent cum dopant for N-doping and TIOP as TiO_2 precursor (Mukthar Ali & Sandhya, 2016b, 2016c).

Even though there are discrepancies over the mechanism of VL activity by N-TiO_2, there is no issue with the VL responsiveness as well as its activity. Electronic structure and type of dopant species of N-TiO_2 highly depends on the synthetic method. Several researchers proposed that lattice nitrogen causes the VL absorption, while other studies attributed NO_x and NH_x adsorbed on the surface to band gap narrowing (R Asahi et al., 2001; T Morikawa et al., 2001). Thus, a controversy still remains regarding the dopants nature and electronic structure of anion doped TiO_2. Based on the density of states (DOS) calculations by the full potential linearized augmented plane-wave (FLAPW) formalism in the framework of the local density approximation (LDA) led Asahi et al. (R Asahi et al., 2001) to choose N since the 2p states apparently contribute to band gap narrowing through mixing with O 2p states in the VB. This finding was also supported by the observations of Irie et al (Irie, Watanabe, & Hashimoto, 2003). However, a negative contribution of Ti-N bonding towards to band gap narrowing was identified by Diwald et al. (Diwald, Thompson, Goralski, Walck, & Yates, 2004). Further

detailed investigations of the electronic structure modification mechanism of N–TiO_2 have subsequently been conducted by a number of researchers (Emeline, Kuznetsov, Rybchuk, & Serpone, 2008; Ihara, Miyoshi, Iriyama, Matsumoto, & Sugihara, 2003; Irie et al., 2003; Martyanov, Uma, Rodrigues, & Klabunde, 2004; Nakamura, Tanaka, & Nakato, 2004; Spadavecchia, Cappelletti, Ardizzone, Ceotto, & Falciola, 2011). Di Valentin et al. performed a DFT study of N-doped TiO_2 with the hybrid functional B3LYP (Di Valentin, Pacchioni, Selloni, Livraghi, & Giamello, 2005; Torres et al., 2004). Their results showed that substitutional N-doping introduces localized impurity states just above the VB level, and negligible mixing occurs between N2p and O2p states. In the same study it was also shown that N could occupy the interstitial positions of the TiO_2 lattice (NO species). It is evident that both conduction and VB edges are unaffected by the dopants, and visible-absorption is resulted by localized energy levels generated by the NO bond (Irie et al., 2003). Two binding energy-levels are positioned below the VB level and anti-bonding orbitals lie 0.73 eV above the VB. It is also proposed that anti-bonding NO orbitals act as stepping stone between CB and VB of TiO_2 (Figure 1.8) (Kongkanand, Tvrdy, Takechi, Kuno, & Kamat, 2008) and facilitate VL absorption (Barolo et al., 2012; Livraghi et al., 2006; Segall et al., 2002). Ilhara and co-workers (Ihara et al., 2003) have indicated that nitrogen doping could stabilize oxygen vacancies, which induce VL absorption.

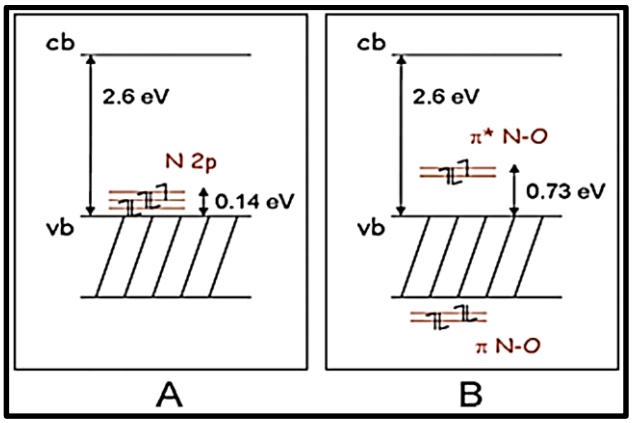

Figure 1.8. Electronic band structure of (A) substitutional and (B) interstitial N-doped anatase TiO_2.

It is widely accepted (Banerjee et al., 2014; Mrowetz, Balcerski, Colussi, & Hoffmann, 2004; Torres et al., 2004) that oxidative power of N-TiO_2 is greatly reduced under the VL irradiation, since the intra-band state of N-TiO_2 is lying well above the VB of TiO_2. The oxidation potential of pure TiO_2 is 2.8 eV while for the intra-band state of N-TiO_2 is ~2 eV (Banerjee et al., 2014; C. Chen et al., 2010). Hence this will influence the contribution of ROS formation in the VL PD of pollutants. Oxidation of water is essential for the formation of •OH and the redox potential for that reaction (E° = 2.33 eV) to happen, the reduction potential has to be more positive than 2.33 eV (Etacheri et al., 2015; Mrowetz et al., 2004; Nakamura et al., 2004; Souza, Pinheiro, Krambrock, & Alves, 2016). Since the oxidation potential of intra-band state in N-TiO_2 is lesser than the redox potential of the reaction, this will result in no formation of •OH. Apart from doping of TiO_2 with N, other non-metals doped and co-doped TiO_2 were also be reported with enhanced VL response (Dai, Liu, Liang, Liu, & Zhong, 2013; He et al., 2012; Z. Jiang et al., 2014; Pang & Abdullah, 2013; Szatmary et al., 2011).

1.4.2. Metal ion doping

Metal ion doping is another approach which will enhance the absorption of the solar light and generate the e-h pair efficiently. Based on the type of metal ion doping, it can be mainly classified into three: namely transition metal ion, rare earth metal based and noble metal based doping (Akpan & Hameed, 2010). Zhu and Yuan (Yuan, Zhang, Anpo, & He, 2010; J. Zhu, Chen, Zhang, Chen, & Anpo, 2006) have studied the physical and PC properties of Fe^{3+} doped TiO_2. Introduction of Fe^{3+} lead to increased O_2 vacancies which favors the formation -OH groups on the surface of TiO_2. Fe^{3+} can easily separate the e-h pair formed during the PD by acting as hole trapping site and further the redox reaction between Fe^{3+}/ Fe^{4+} lead to better PC activity. Early on Choi et al. (Choi et al., 1994) studied the PC activity of TiO_2 doped with 21 transition metal ions by using PC oxidation of chloroform and the PC reduction of carbon tetrachloride as model reactions (Schneider et al., 2014). The researchers discovered that the doping with Fe^{3+}, Mo^{5+}, Ru^{3+}, Os^{3+}, Re^{5+}, V^{4+} and Rn^{3+} cations are beneficial as evidenced by the enhancement of the PD of

chloroform. Borgarello et al (Borgarello, Kiwi, Graetzel, Pelizzetti, & Visca, 1982) reported the PC H_2O splitting reaction on Cr^{3+}-doped TiO_2 nanoparticles in the VL region (400−550 nm). The photo excitation of 3d electrons of Cr^{3+} into the CB of TiO_2 was responsible for the VL absorption. Zn^{2+}-TiO_2 and La^{3+}-TiO_2 composites (Quan, Tan, Zhao, & Sang, 2007) showed improved PD properties towards rhodamine B (RhB) (Guoguang Liu et al., 2005). Rare earth metal doped TiO_2 are known to improve the VL absorption intensity and improve the interfacial electron transfer rate (Choi et al., 1994; Quan et al., 2007). Even though there is a discrepancy over whether the adsorbed La (Liming Sun et al., 2012) or doped La (Anandan, Ikuma, & Murugesan, 2012) responsible for the improved VL absorption of TiO_2, it is clear that La-TiO_2 showed improved VL PD activity. Noble metals like Pt, Ag and Au improved the VL activity by surface plasmon resonance (SPR) and by improved separation of the e-h pair. Pt , Fe or Cu loading enhanced the PD rate of acetaldehyde oxidation while more addition of Cu lead to faster toluene and acetic acid oxidation (Takeshi Morikawa, Ohwaki, Suzuki, Moribe, & Tero-Kubota, 2008). Extremely high rate enhancement of formic acid oxidation was attributed to the combined effect of photocatalysis and thermal catalysis.

In all metal ion or metal doped TiO_2 system, the metal does the job of enhancing the VL absorption either by SPR or by introducing intra-band states. Apart from this, the metal ions acted as hole trapping sites i.e. increased the e-h pair separation. They are regenerated back by interfacial electron transfer reaction followed by the generation of •OH, O_2•−, $^1O_2$ and other ROS species (Choi et al., 1994; Ni, Leung, Leung, & Sumathy, 2007).

1.4.3. Surface-sensitized complexes of TiO_2

This is an interesting and novel approach for making the VL sensitive TiO_2. This method facilitates the TiO_2 to VL active by sensitizing the TiO_2 surface which is slightly different from well-known dye-sensitized mechanism. This type of sensitization based on the ligand-to-metal charge transfer (LMCT) between surface adsorbates and TiO_2 nanoparticles under VL irradiation has been proposed but far less studied compared to the popular dye sensitization process (Alvaro, Carbonell, Fornés, & García, 2006; C. Chen et al., 2010; Kaniyankandy, Rawalekar, Sen,

Ganguly, & Ghosh, 2014; Lana-Villarreal, Rodes, Perez, & Gomez, 2005; Mukthar Ali & Sandhya, 2014; Varaganti & Ramakrishna, 2010; G. Wang, Wu, Zhang, Luo, & Deng, 2006; G. Zhang, Kim, & Choi, 2014). However, the uncommon LMCT sensitization has many advantages in that a wide variety of organic or inorganic compounds (that do not absorb VL) can form surface complexes with TiO_2 and introduce new absorbance bands in the VL region unlike the case of dye sensitization where the sensitizer itself should absorb the VL. The LMCT-mediated activation of TiO_2 and other wide band gap semiconductors has significant potential to be developed as a more general method of solar energy utilization in PC systems.

In the case of LMCT sensitization, the mechanism involves with the photo excitation of electrons directly from the ground state highest occupied molecular orbital (HOMO) of the adsorbate to CB of TiO_2 semiconductor of the complex. The oxidized adsorbate (with the hole left) might get degraded into its intermediate molecules or it would get regenerated by the recombination with the photo excited electron (back electron transfer) or by reacting with suitable electron donors available in the medium (Figure 1.9).

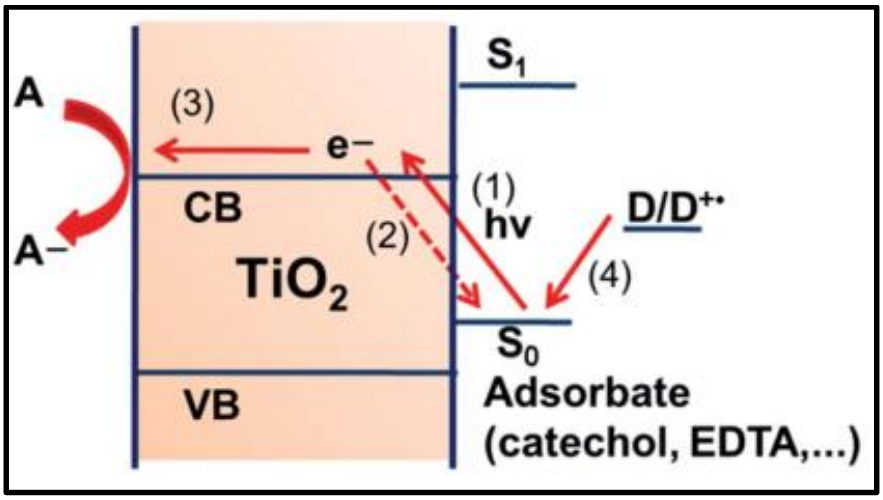

Figure 1.9. The schematic illustration of LMCT sensitization: (1) VL-induced LMCT transfer, (2) recombination, (3) electron transfer to the acceptor, and (4) regeneration of adsorbates by an electron donor. S, D, and A represent the sensitizer (or adsorbate), electron donor, and electron acceptor, respectively. (S_0: ground state, S* and S_1: excited state of the sensitizer/ adsorbate).

LMCT complexes on TiO_2 is usually accompanied by the appearance of a VL absorption band, which is absent with either the adsorbate or TiO_2 alone. VL absorption range of LMCT process is determined the difference in level between HOMO of adsorbate and TiO_2 CB. Further proper LMCT transition to occur, there must be a close association between adsorbent and adsorbate. Therefore a variety of organic or inorganic compounds (that do not absorb VL) with suitable HOMO levels can be potential LMCT sensitizers. LMCT sensitization gives a great deal of flexibility in its design and application of the photocatalyst.

Variety of molecules can form surface sensitized complex with TiO_2 notably phenols (Anik Sen , Bishwajit Ganguly, 2012; Yuhuang Wang, Hang, Anderson, & Lian, 2003), carboxylic acids (Xagas et al., 2000), polyhydroxyls (P. Lu, Wu, & Deng, 2004; Mukthar Ali & Sandhya, 2014; G. Wang et al., 2006; X. Zhang, Wu, & Deng, 2010), peroxides (Xiangzhong Li, Chen, & Zhao, 2001; Rao & Chu, 2009), cyanides (Vrachnou, Gratzel, & McEvoy, 1989; Weng, Wang, Asbury, Ghosh, & Lian, 1999), isocyanates (F. Chen et al., 2009; D. Jiang, Xu, Wu, & Sun, 2009) and polyaromatic compounds (Seo, Lee, Lee, & Yoon, 2005). The schematic representation of various adsorbates binding on TiO_2 is given in Figure 1.10. The surface-sensitized complex formation can be explained using TiO_2-fullerol composite (Park, Singh, et al., 2009). The composite was prepared by physical adsorption method and the composite showed strong CT absorption in the visible range (400-550 nm). Observation of fullerol$^{\bullet+}$ in transient spectroscopic measurements arise from the LMCT process. The polyhydroxyl groups of fullerol attached to the surface of TiO_2 lead to the formation LMCT transition. TiO_2-cyclodextrin (TiO_2-CD) based surface-sensitized complexes (G. Wang et al., 2006) are prepared and utilized in the VL PD of bisphenol A. It was found that chemically bonded TiO_2-CD composite showed much improved PD than the physically adsorbed (J. Kim & Nichols, 2012; G. Wang et al., 2006).

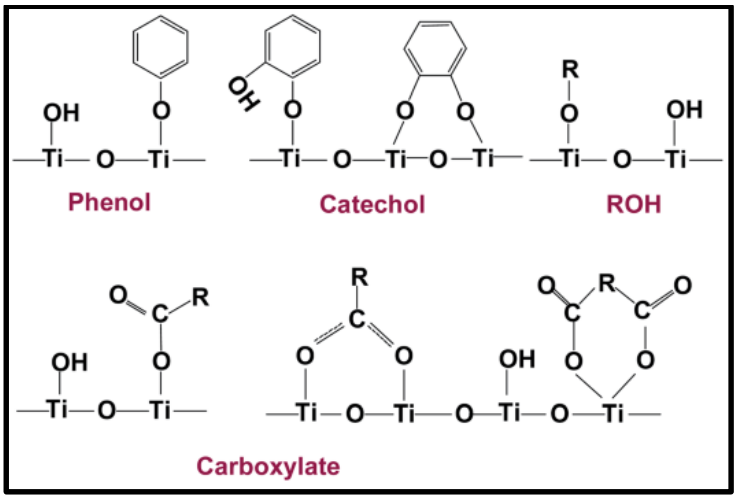

Figure 1.10. Possible binding modes of representative complexes on TiO_2 surface.

Since the VL induced mechanism follows LMCT transition, it is obvious that oxidation potential of HOMO of adsorbate could not oxidize the water to form •OH. The photo excited electrons in the CB of TiO_2 lead to the formation of O_2•−. This fact is supported by Zhang et al (X. Zhang, Wu, & Deng, 2011) in the VL PD of MO and it was observed that O_2•− is the dominant ROS species in the PD. Again the incorporation of CD increase redox ability of the composite and becomes more photo stable (P. Lu et al., 2004).

1.4.4. Heterostructures with TiO_2

Enhanced VL absorption and suppressed charge recombination can be achieved by modifying TiO_2 with suitable conducting or semiconducting materials with appropriate energy levels. Hierarchical structure of two or more materials that forms heterostructures were often used to exploit the strengths of individual materials and compensate the respective shortcomings for improved PC properties. The construction of well-defined heterostructures by appropriate coupling of foreign components to host TiO_2 matrix is capable of improving PC activity. Heterostructure of TiO_2 with suitable semiconductors can effectively enhance photocatalysis through (i) extension of light absorption spectral range, (ii) suppression of charge recombination and (iii) facile transfer of charges across the interface. Of the many heterostructures formation, coupling TiO_2 with other small

or wide band gap semiconductor (D. Li et al., 2013; Yu Liu et al., 2012; Xiao, 2012; J. Yu, Wang, & Cheng, 2010; Z. Zhang et al., 2012), carbonaceous materials (Katsumata, Matsushita, & Okada, 2012; S. Liu, Liu, Wang, Cheng, & Yu, 2012; M. Mukthar (Mukthar Ali & Sandhya, 2016a) Ali & Sandhya, 2014, 2016; Pan et al., 2014; Reddy, Hassan, & Gomes, 2015; Xiang, Yu, & Jaroniec, 2011; X. Yu, Liu, Yu, Zuo, & Li, 2014; X. Zhou, Shi, Wu, & Zhou, 2013) and p-type semiconductors (Mukthar Ali & Sandhya, 2016b; X. Shao, Tian, Xue, & Ma, 2003; M. Shen et al., 2014) are some of the desirable approaches.

MoS_2 is a p-type and small band gap semiconductor and incorporation of MoS_2 in TiO_2 can lead to heterojunction formation and thus can improve the PC activity, provided the MoS_2 is single or few layered. Hydrothermally prepared n-type TiO_2 was coupled with p-type MoS_2 nanobelt to produce TiO_2-MoS_2 composite (W. Zhou et al., 2013) which acted as an efficient photocatalyst for H_2 evolution as well VL PD of RhB. Similarly TiO_2 heterostructures with MoO_3, NiO, Fe_2O_3, ZnO, SnS_2 and various other are proved to be efficient as VL responsive photocatalyst (Banerjee et al., 2014; Reddy et al., 2015; Schneider et al., 2014).

Apart from these heterostructures, nowadays carbonaceous nanomaterials can make an efficient photocatalyst with extended VL activity and improved charge transfer and transport. Carbon nanotube (CNT) (Woan, Pyrgiotakis, & Sigmund, 2009), fullerene (Katsumata et al., 2012; Z.-D. Meng, Zhu, Choi, Chen, & Oh, 2011; Mukthar Ali & Sandhya, 2014), graphene (Gr) (How, Pandikumar, Ming, & Ngee, 2014; Mukthar Ali & Sandhya, 2016a; L. Zhu, Jo, Ye, Ullah, & Oh, 2014) and recently invented carbon dots (C-dots) (Mo, Lei, Sun, & Rooney, 2013; Youfu Wang & Hu, 2014) are the new generation carbonaceous materials possessing overall outstanding and unique properties. Each of these material differing greatly in their morphology which lead to greater change in the composite properties. Especially, Gr possesses an excellent mobility of charge carriers at room temperature (200 000 cm^2 V^{-1} s^{-1}) and exhibits an extremely high theoretical specific surface area (~2600 m^2g^{-1}) are expected to improve the PC property. (Allen, 2009; Geim & Novoselov, 2007). Kamat et al (P. V. Kamat, 2007; Williams, Seger, & Kamat, 2008) reported a novel method of preparing Gr sheets by the reduction of graphene oxide using TiO_2 photo irradiation method which can be extended to

prepare TiO_2-Gr composites. Zhang et al (H. Zhang, Lv, Li, Wang, & Li, 2010) reported P25-Gr composite synthesized under hydrothermal conditions that exhibited an enhanced PC activity for the degradation of methylene blue (MB) in aqueous solutions. Similarly highly reactive facet (001) exposed TiO_2-Gr (HRTiO_2-Gr) composites have been explored to improve the properties (T. Lu et al., 2013; Mukthar Ali & Sandhya, 2016d).

Since the landmark paper by Iijima (Iijima, 1991), CNTs have attracted significant attention in a variety of scientific fields because of their unique properties; structural, chemical, thermal, electrical and more. TiO_2-CNT composites (Linsebigler et al., 1995; K. Liu et al., 2008) known to enhance the VL PD of pollutants due to the faster electron transfer across the interface and there is slight C-doping proposed (Woan et al., 2009) to support the VL enhancement (Figure 1.11). TiO_2-CNT synergistically enhances the VL absorption and suppresses charge carrier recombination.

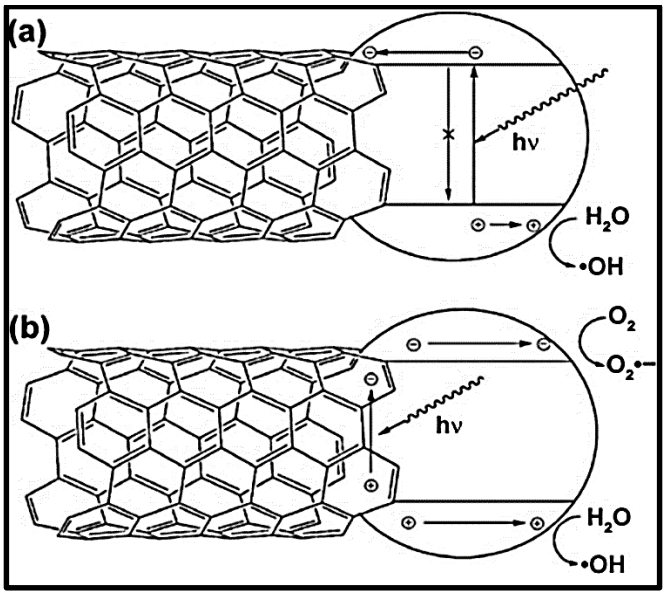

Figure 1.11. Proposed mechanisms of synergistic enhancement in TiO_2–CNT composites. (a) CNTs inhibit recombination by acting as sinks for photogenerated electrons in TiO_2. (b) Photosensitizing mechanism based on e–h pair generation in the CNT.

Similarly, fullerenes and C-dots are also known to improve the VL response of TiO_2 as well enhance the charge separation with their own mechanisms. Fullerenes (C_{60}) are widely known for their unique electronic properties such as low lying electronic energy levels which are able to accept up to 6 electrons and quantum yield close to unity for the formation of $^1O_2$ (Arbogast, Foote, & Kao, 1992; Imahori & Sakata, 1997; T. Liu & Troisi, 2013) etc and hence in combination with TiO_2, their PC activity can be improved (Katsumata et al., 2012; Mukthar Ali & Sandhya, 2014). C-dots improve the PC activity of TiO_2 by its unique up-conversion photo luminescence as well as VL absorbing ability (J. Q. Pan et al., 2014; J. Shen, Zhu, Yang, & Li, 2012; Youfu Wang & Hu, 2014).

1.5. Objective and scope of the thesis

The focus of our research work is to improve the PD performance of TiO_2 under VL. In order to realize the better PC activity of TiO_2, the main modification that needs to be done is to extend its absorption to the visible region of the solar spectrum. We have applied various approaches to improve the VL absorption of TiO_2 such as: (i) Doping of TiO_2 with N using a single step solvothermal using solvent NMP as the doping agent. In addition to restricting the number of steps required to produce N-TiO_2 to one, it helps to preserve the antase nature of TiO_2, and in addition, produces ultra-fine sized (4-6 nm) TiO_2 particles with high crystallinity and surface area. (ii) Using CD to disperse carbon nanomaterials such as C_{60} and Gr to produce TiO_2-CD-C_{60} and TiO_2-CD-Gr by linking CD to TiO_2. In this CD will surface sensitize TiO_2 and thus enhance the VL absorption by LMCT, and disperse C_{60} or rGO in water and thus create a compatible environment for TiO_2 and the hydrophobic C nano materials. Gr or C_{60} improves the charge separation of the composite. Moreover the method is environmental friendly and is green in nature as it utilizes water as solvent and the solar energy for formation of TiO_2-CD linkages. (iii) Coupling of TiO_2 with single / few layered MoS_2 to improve the VL absorption by sensitizing the TiO_2. This has been achieved using a single step solvothermal method using a novel molybdenum-sulphur cluster as the precursor to MoS_2. (iv) incorporation of high photoluminescence quantum yield (PLQY) C-

dot with TiO_2 to enhance the VL absorption PD through its up-conversion properties. Apart from this, lowering the recombination of the photogenerated electron-holes was expected when TiO_2 was coupled with Gr, C_{60}, MoS_2 or C-dots due to the heterojunction formation and improved VL absorption. Furthermore, $HRTiO_2$ (Lazzeri et al, 2001 & Yang et al, 2008) was prepared and coupled with Gr sheet to enhance the PD efficiency and found that the composite exhibits selective PD properties. Moreover, the involvement of the ROS were investigated with focus to ROS such as •OH, O_2•−, $^1O_2$ and their contribution towards the PD reaction of RhB was estimated using scavenger studies. Based on the results and the theoretically available energy levels of the components of the composite, illustrative mechanisms were proposed, as an attempt, to explain the formation of the ROS. Thus, this study demonstrates novel and green synthesis / preparation methods to modify TiO_2 for better PD efficiency and throw some insight into the ROS species involved and their formation pathways. Our findings may find potential use in the design of PD reactor for improving the PD efficiency.

The specific objectives of this research work are summarized below:

- A green method of preparation of $HRTiO_2$-Gr composites and its VL PD properties.
- Single step N-doping of TiO_2 using NMP solvent and its VL PD activity.
- In-situ preparation of TiO_2-MoS_2 composites using a novel molybdenum-sulphur cluster as precursor for MoS_2 and its PC studies.
- A method for the synthesis C-dot and its P25/C-dot composite and VL PD performance.
- A green method for preparing P25-CD-Gr composite and their PD property studies.
- New green method for preparing P25-CD-C_{60} composite without altering the C_{60} structure and their VL PD studies.
- Investigation of ROS involvement using the VL PD reaction of RhB for all the above mentioned composites.

1.6. Organization of Thesis

This thesis describes the research work on the preparation and characterization of TiO_2 based composites using various strategies in an attempt to improve the VL PD of TiO_2. The research focuses on the strategies involved in making VL responsive TiO_2, the differences in their PD mechanism based on the ROS contribution and finally proposes illustrative mechanism or the ROS formation based on the structure of the composites. The thesis is organized in eight chapters as given below.

Chapter 1 provides a detailed introduction, basics and fundamentals of photocatalysis, PD and TiO_2 as photocatalysts, its structure, properties etc and a state-of-the-art literature survey on visible semiconductor photocatalysis, strategies adopted, and our research problem & objectives.

In **Chapter 2** is the experimental section and describes the synthesis or preparation procedures of different TiO_2 based photocatalyst, their characterization and other general experimental procedures for PD studies, scavenging studies and recycling studies etc.

The preparation, characterization and PC studies of $HRTiO_2$-Gr using a green approach along with its selectivity is described in **Chapter 3**.

Chapter 4 describes a single-step synthesis and characterization of N-TiO_2 and its VL PC activity under. In addition to that, in-situ preparation of TiO_2-MoS_2 composites from a novel molybdenum-sulphur cluster precursors and its PC studies has been reported.

In **Chapter 5,** a novel method for the preparation of C-dot is reported and further has been utilized for making P25/C-dot composite and the VL PD performance of the composite and the involvement of ROS has been discussed.

Chapter 6 describes the composites prepared from commercial P25 TiO_2 using C_{60} or rGO in a benign and green approach. Here P25 is attached with CD-C_{60} or CD-rGO using solar light irradiation and their PC properties are discussed.

The highlights of the results in the research work are summarized and suggestions for future work in this subject are given in **Chapter 7**.

CHAPTER 2
MATERIALS AND METHODS

This chapter describes the materials and methods used for the synthesis of various TiO_2 modified hybrid composites. Various characterization techniques, PLQY calculations, PD procedure, recycling studies and scavenger studies are also discussed.

2.1. Materials

P25 nanopowder (21 nm), Anatase TiO_2 (25 nm), graphite (21 µm particle size), RhB, beta cyclodextrins (CD), and TiOP were purchased from Sigma Aldrich India Co. Ltd. Methlyene blue (MB) was purchased from Alfa Aesar Co. India Ltd. Methyl Orange (MO), Potassium permanganate ($KMnO_4$), hydrogen peroxide (H_2O_2), hydrochloric acid (HCl), hydrofluoric acid (HF), isopropanol (IPA), ammonium thiomolybdate, sodium sulphate (Na_2SO_4), sodium carbonate (Na_2CO_3), phosphorous pentoxide (P_2O_5), acetyl acetone and sulphuric acid (H_2SO_4) were purchased from Merck, India Ltd. 4-Chlorophenol (4CP) and NMP were obtained from Spectrochem India Ltd. Distilled water was used for all studies. All the solvents and reagents used in this study were of analytical grade.

2.2. Methods

2.2.1. Electrode preparations

Titanium (Ti) electrodes of 0.25 mm thickness were cleaned by ultrasonicating in water and isopropanol sequentially. A 5% suspension of the photocatalyst in IPA and acetylacetone (4:1) was spin coated onto the cleaned Ti electrodes. The active electrode area was limited to 1 cm^2. The prepared electrodes were annealed at 400°C for 1 hr. Electrochemical characterizations were carried out using a conventional three electrode configuration. Ag/AgCl, platinum and the coated Ti electrodes were used as reference, counter and working electrodes respectively. Aqueous Fe^{2+}/Fe^{3+} solution (0.1 M) was used as the electrolyte.

2.2.2. Photoluminescence Quantum Yield (PLQY) Calculation

PLQY of C-dots was calculated at the excitation of 345 nm. Excitation and emission are set as 1 and 2 nm respectively. Quinine sulfate in 0.1 M H_2SO_4 (literature quantum yield 0.54 at 345 nm) was chosen as a standard. The PLQY of C-dot in water was calculated according to:

$$\varphi_x = \varphi_x \left(\frac{F_x}{F_{std}}\right)\left(\frac{A_{std}}{A_x}\right)\left(\frac{n_x}{n_{std}}\right)^2$$

Where, φ, F, A, and n are QY of the standard sample, integrated photoluminescence (PL) intensity, absorbance, and refractive index, respectively. The subscript "std" refers to known quantum yield of the standard. To minimize self-quenching effects, the absorbance of C-dot and quinine sulfate solution in the 10 mm fluorescence cuvette were adjusted never exceed 0.1 at the excitation wavelength. We choose 345 nm as moderate excitation wavelength. As the quantum yield of quinine bisulfate is almost independent (within 5%) on the wavelength excitation for 200~400 nm, we still take 0.54 as the φ_{std}.

2.2.3. Visible light photodegradation studies of RhB, MB, MO and 4CP

Stock solutions of dyes MB (72 μM), RhB (30 μM), MO (60 μM) and 4CP (77 μM) were prepared. Typically, 17 mg of the photocatalyst was dispersed in 25 ml of the dye's stock solution in the case of MB, RhB and MO while for 4CP PD, 10 mg photocatalyst was taken. The suspension was stirred for 60 or 120 min under dark conditions for attaining adsorption equilibrium. Under ambient conditions, the suspensions were irradiated with UV light (<365 nm) or visible light (> 420 nm) using 84 W light sources. Photocatalyst was removed by centrifugation prior to recording UV-Vis spectra and concentration of MB, RhB, MO and 4CP were determined using the absorbance values at 660, 554, 460 and 224 nm, respectively. The digital images of the photoreactor used for the studies are given in Figure 2.1.

Figure 2.1. Photoreactor setup used in the PD studies.

2.2.4. Scavenger Studies

VL PD of RhB was chosen for scavenger studies because it was found to be the most suitable for all the composites, as it has fairly good amount of PD with all the composites, adsorption was minimal etc. Other dyes such as MB had adsorption issues (95 % adsorption with N-TiO_2), 4CP did not undergo degradation in the presence of TiO_2-MoS_2 composites, etc. Further, in the PD process, dyes also to some extent influence the mechanism of formation of ROS. Therefore, PD of RhB was used for finding the contribution of ROS. The procedure for performing the scavenger studies was as follows. 50 mM aqueous of t-BuOH, NaN_3 and BQ were prepared and used as stock solutions for the scavenging studies. To the 17 mg of the photocatalyst, 25 ml of the stock solution of RhB was added followed by the addition of 2.7 ml of the corresponding scavenger stock solution. Rest of the procedure was similar to that of described in VL PD studies.

2.2.5. Recycling Studies

PC recycling studies were carried out using RhB dye. Solar simulator with 150 W Xenon lamp was used as the light source. Typically 4.5 mg of the catalyst was added to 20 ml of 1.5 μM RhB solution. The suspension was sonicated for 10 min in a bath sonicator and then irradiated with Xenon lamp for the PD reaction. Complete decolouration of RhB was taken as the end point of each cycle. No washing of the photocatalyst was performed between the cycles.

2.3. Characterization Techniques

Several techniques such as spectroscopic, microscopic and thermal are performed for the characterizations of synthesized composite materials. Fourier transform Infra-red (FTIR) spectra were recorded in a Perkin Elmer spectrum100 FTIR spectrophotometer. The range of FTIR spectra is 4500- 400 cm^{-1} with an optical resolution of 0.5 cm^{-1}. The sample was diluted with KBr pellet before doing the analyses.

PL spectra were recorded in Horiba FluoroMax-4 with the excitation and emission slits of 1 and 5 nm respectively for solid state PL measurements. For liquid state PL and PLQY calculations, excitation and emission slits are set as 1 and 2 nm respectively.

Absorption spectra in the solutions were recorded using CARY 100 Bio UV-Visible spectrophotometer. Solid state diffuse reflectance spectra (DRS) were recorded out in Shimadzu 2600 instrument. The spectral range and the optical resolution are 200-800 nm and 1 nm respectively. The DRS spectra of various composites were transformed to Kubelka-Munk function using the measured reflectance:

$$K = \frac{(1-R)^2}{2R} = F(R) \qquad (2.1)$$

Where K is the transformed reflectance, R is the reflectance (%) and F(R) is the Kubelka-Munk function. From this band gap (Eg) can be related to absorption coefficient (α) were related by:

$$\alpha h\nu = A\,(h\nu - E_g)^{0.5} \tag{2.2}$$

Raman spectroscopic measurements were carried out in Renishaw inVia Raman microscope with the excitation laser wavelength of 532 nm. Thermogravimmetric Analysis (TGA) were done using TA Q50 instrument with the rate of 10°C/min either in the presence of air or nitrogen. X-ray diffraction (XRD) analyses were carried out on a Bruker D8 discover small angle X-ray diffractometer. The Cu Kα radiation (λ = 1.54 Å) was used as an excitation source. XRD pattern also allows estimating crystal size by Debye-Scherrer equation as given in equation 2.3. This equation gives the relationship between diffraction peak broadening (β) and crystallite size (D),

$$D = \frac{0.94\,\lambda}{\beta cos\theta} \tag{2.3}$$

Scanning electron microscope (SEM) images were taken using Hitachi SU6600 variable pressure field emission SEM. High resolution transmission electron microscopy (HRTEM) analyses were done using JOEL JEM 2100 electron microscope with an accelerating voltage of 200 kV. Brunauer-Emmett-Teller (BET) SA analyses were made in Tristar II micromeritics. X-ray photoelectron spectroscopy (XPS) analyses were carried out using Kratos analytical axis ultra X-ray photoelectron spectrometer with the excitation source of Al Kα. Electrochemical characterizations were carried out using Autolab PGstat320N from Metrohm. Aqueous 0.2M Na_2SO_4 used as electrolyte. Coiled Pt wire and Ag/AgCl were as auxiliary and reference electrodes. Composite coated over Ti foil act as working electrode.

CHAPTER 3

PHOTOIRRADIATION METHOD OF (001) FACET EXPOSED TiO_2 – GRAPHENE PREPARATION AND ITS VISIBLE LIGHT PHOTOCATALYTIC PROPERTIES

This chapter discusses about the synthesis and characterization of highly exposed (001) facet TiO_2-graphene ($HRTiO_2$-Gr) composite using a green (photo irradiation) method. The VL PD property of the composite was tested using various dyes/pollutants and found to have improved and in addition composite exhibited selective PD properties. The ROS involved in the VL PD of RhB was studied and a mechanism has been elucidated to explain the formation of ROS.

3.1. Introduction

Use of TiO_2 in PC applications is advantageous because of highly photo stable, cost effective and good charge carrier mobility. Despite these desirable properties, it has two major drawbacks. The large band gap (3.2 eV) and photo generated charge carrier recombination. The decrease in the charge-carrier recombination of TiO_2 is essential otherwise the rate of forward reactions are limited and thus the efficiency (Gu et al., 2013; Han, Wei, Pan, Li, & Chen, 2015; How et al., 2014; Xin Li, Wen, Low, Fang, & Yu, 2014; Linsebigler et al., 1995; Q Xiang, Yu, & Jaroniec, 2012; Quanjun Xiang & Yu, 2013) are dented.

Facet engineering is an emerging concept to improve the charge separation and faster electron transport in semiconductors. AnataseTiO_2 is the widely explored polymorph of TiO_2 over other polymorphs. Typical anatase TiO_2 consists of more than 90% of (101) facets and ~4-5% of (001) facets. The surface reactivity (Lazzeri, Vittadini, & Selloni, 2001) of these facets play a dominant role in the photo induced charge separation and hence the PC properties. Theoretical observations suggest (Gong & Selloni, 2005; H. G. Yang et al., 2008) that TiO_2 anatase with exposed

(001) facets exhibits higher reactivity because of its higher surface energy, the surface energy of the (001) facet is 0.90 J m^{-2}whereas for the stable facet (101) it is 0.44 J m^{-2} (M. Dozzi & Selli, 2013). Intense efforts were carried out for exploiting the facet controlled PC properties of TiO_2, as a result Yang and co-workers (H. G. Yang et al., 2008) reported the preparation of a TiO_2 anatase with highly exposed percentage of (001) facet using hydrofluoric acid (HF) as the morphology controlling agent. Even though further research resulted in improving the percentage of (001) facet in TiO_2 to ~100% (J. S. Chen et al., 2010), improvements in the charge separation were limited. To further improve the charge recombination is to attach the TiO_2 with good electron accepting and transporting materials like graphene, fullerene and carbon nanotubes.

Gr with its excellent conductivity (Novoselov et al., 2005) and minimum light blocking (Nair et al., 2008) ability prompts its usage in optoelectronic devices. Recently, research interest has been directed towards high reactive facet (001) exposed TiO_2 anatase ($HRTiO_2$) and Gr based composites to exploit the combination of the high reactivity of the (001) facets and the exceptional electron mobility properties of Gr. The Gr loading onto the semiconductor modifies properties like specific surface area (SA), porosity, pore volume, charge recombination, charge transfer, etc. Many reports of hydro/solvothermally prepared TiO_2/$HRTiO_2$–Gr composites with improved PC activity (Gu et al., 2013; B. Jiang et al., 2011; B. Liu et al., 2012; T. Lu et al., 2013; Lei Sun, Zhao, Zhou, & Liu, 2012; X. Zhou et al., 2013) and an increase in the photo conversion efficiency of DSSCs (Fan, Liu, & Yu, 2012) and H_2 evolution (Quanjun Xiang et al., 2011) has been reported. Pioneering works on TiO_2–Gr composite by Kamat et al.(Williams et al., 2008) using the photo irradiation method, report that the TiO_2–Gr made by the photochemical reduction (PCR) method is mostly advantageous in terms of charge transfer and transport (Morales-Torres, Pastrana-Martinez, Figueiredo, Faria, & Silva, 2012). However, so far, the PCR approach for preparing $HRTiO_2$–Gr with exposed (001) facets was not explored. Moreover, it is a green approach and therefore the method was chosen for the preparation of $HRTiO_2$–Gr with exposed (001) facets for to its room temperature conditions and utilization of the solar energy.

Typical semiconductor PD of dyes/ pollutants can lead to the mineralization of dyes/ pollutants or end up in the formation of certain intermediate products. This depends on the nature of the ROS involved as its oxidation ability is a crucial factor. Among the various ROS's, •OH is the strongest oxidizing species followed by $^1O_2$ while O_2•− is a strong reducing species. Further the formation and the extent of formation of each ROS depends on the semiconductor, dye/ pollutant, energy of incident light and the conditions of reactions.

In this chapter, we report the preparation of HRTiO_2–Gr by the PCR method and its structural characterization and PC properties. The composite exhibits higher PC activity for the PD of MB, RhB and MO than that of the P25. Our study reveals that the HRTiO_2–Gr10 (composite with 10 wt% Gr has exhibited highest activity amongst the composites) has selective adsorption and PD properties towards the positive dyes such as MB and RhB. The synergistic effect of higher adsorption and PD of the composite for positive dyes may provide a method to efficiently and selectively remove pollutants from waste water.

3.2. Experimental

3.2.1. Preparation of TiO_2 and HRTiO_2

In a typical procedure, TiOP (3.125 ml) was added to isopropanol (10 ml) taken in a 100 ml Teflon lined autoclave. To the mixture 40% HF (0.75 ml) was added slowly and the mixture was heated to 180 °C for 24 hr in a furnace. After the solvothermal treatment, the resulting mixture was cooled to room temperature and then HF was quenched by adding 10% aqueous Na_2CO_3 solution, followed by filtering and washing to remove NaF, IPA and any other organic as well as inorganic impurities. The product formed was dried at 70 °C for overnight. The same method without HF was followed for preparing control TiO_2.

3.2.2. Preparation of GO

Modified Hummer's method was adopted or the synthesis of GO (Hummers Jr & Offeman, 1958; Venugopal, Krishnamoorthy, Mohan, & Kim, 2012). Commercial graphite powder was oxidized with H_2SO_4 and $KMnO_4$ at 90

°C followed by the addition of H_2O_2 under cooling. The solid brown product of the GO was filtered and washed repeatedly with1 M HCl followed by distilled water and dried under vacuum at room temperature.

3.2.3. Preparation of TiO_2–Gr and $HRTiO_2$–Gr composite by PCR method

In a typical procedure, the GO (8 mg) was sonicated in distilled water (15 ml) to form a homogeneous suspension. The particle free GO suspension was mixed with the $HRTiO_2$ suspension (72 mg in 65 ml of distilled water) in a quartz beaker, followed by sonication for 30 min and stirring under N_2 atmosphere for 1 h in an air-tight quartz vessel. The resulting suspension was irradiated with UV light/ solar light (365 nm) for 15 h. The gray color solid product formed was centrifuged and dried at 70 °C for overnight. Composites with varying wt% of Gr (1–25 wt%) were prepared. Similarly, TiO_2–Gr10 composite was prepared using control TiO_2 (instead of $HRTiO_2$) and GO for comparative study.

3.3. Results and Discussions

3.3.1. Characterization of the $HRTiO_2$ and $HRTiO_2$-Gr

The FTIR spectra of $HRTiO_2$, $HRTiO_2$–Gr and GO are provided in Figure 3.1A. The spectrum of GO displays peak at 3400 cm^{-1} corresponding to –OH functional group and peaks at 1719 and 1626 cm^{-1} are assigned to the acidic/ keto –C=O and -C=C– stretching vibrations, respectively. A shift was observed in the –C=O stretching frequency of $HRTiO_2$–Gr10 from that of the $HRTiO_2$, suggests the formation of the ester linkage between $HRTiO_2$ and Gr. The appearance of a new peak at 1623 cm^{-1} in the composite corresponds to the –C=C– stretching and the change in color of the reaction mixture ($HRTiO_2$ and GO) (Figure 3.1B) on photoirradiation showcase a change from brownish yellow to black which indicates the formation of Gr from GO. The photogenerated electrons from $HRTiO_2$ is accepted by GO and thus reduces to Gr, thus forming the composite $HRTiO_2$–Gr with linkages between $HRTiO_2$ and Gr nanosheets (Williams et al., 2008). The SEM images presented in Figure 3.2 (A & B) illustrate the trapezoidal shaped TiO_2 nanocrystals which indicate the formation of exposed (001) facets of $HRTiO_2$ The

percentage of exposed (001) facets in $HRTiO_2$ is calculated from SEM image (H. G. Yang et al., 2008) and found to be ~26%.

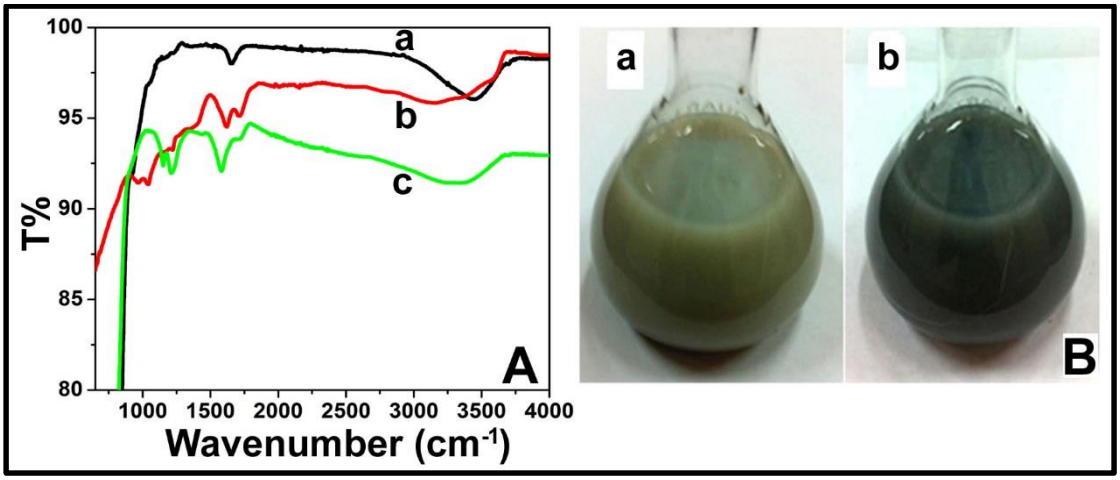

Figure 3.1. (A): FTIR spectra of (a): $HRTiO_2$; (b): GO and (c): $HRTiO_2$-Gr and (B): Photoimages of $HRTiO_2$-GO mixture (a) and $HRTiO_2$-Gr formed (b), before and after irradiation respectively.

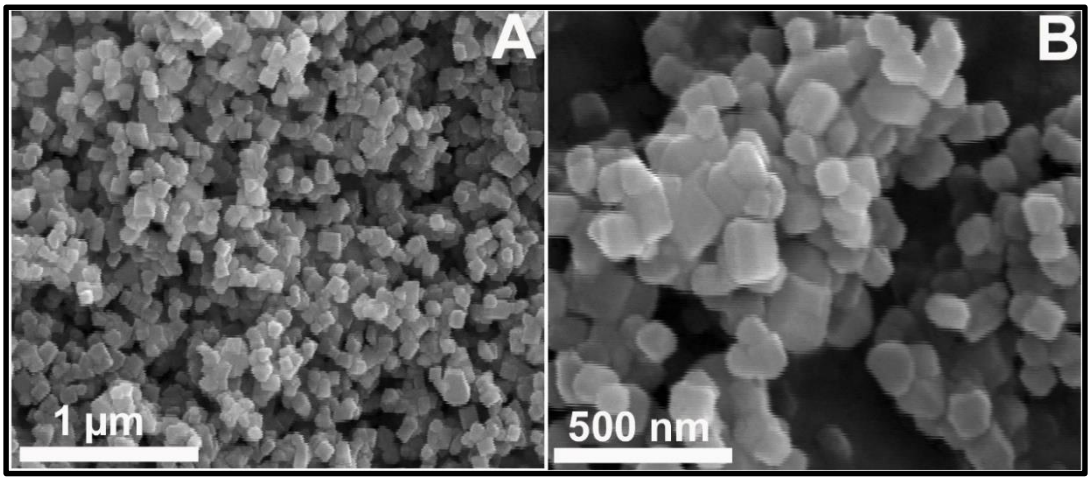

Figure 3.2. (A and B): SEM images of trapezoidal shaped $HRTiO_2$ particles.

HRTEM was used to analyze the morphology and structure of $HRTiO_2$–Gr composites and the images (Figure 3.3A) displayed a thin sheet of Gr decorated with $HRTiO_2$ nanoparticles. During the synthesis procedure, GO was dispersed in water before reduction by $(HR)TiO_2$, therefore, the prospect of formation of single layer Gr nanosheets decorated with $HRTiO_2$ is highly possible. The HRTEM

images reveal square, rectangular and rhombohedral shaped $HRTiO_2$ nanoparticles of 30–50 nm sizes (Figure 3.3B) on the surface of thin Gr nanosheets (H. G. Yang et al., 2008). The higher magnification (Figure 3.3C) images show the flat top surface of TiO_2 with a spacing of 0.33 nm, which corresponds to the (101) facet of anatase TiO_2. Figure 3.3D shows the SAED diffraction pattern with 0.235 nm spacing corresponding to the (001) facets. Figure 3.4A shows the representative structure of TiO_2 anatase with exposed (001) facets.

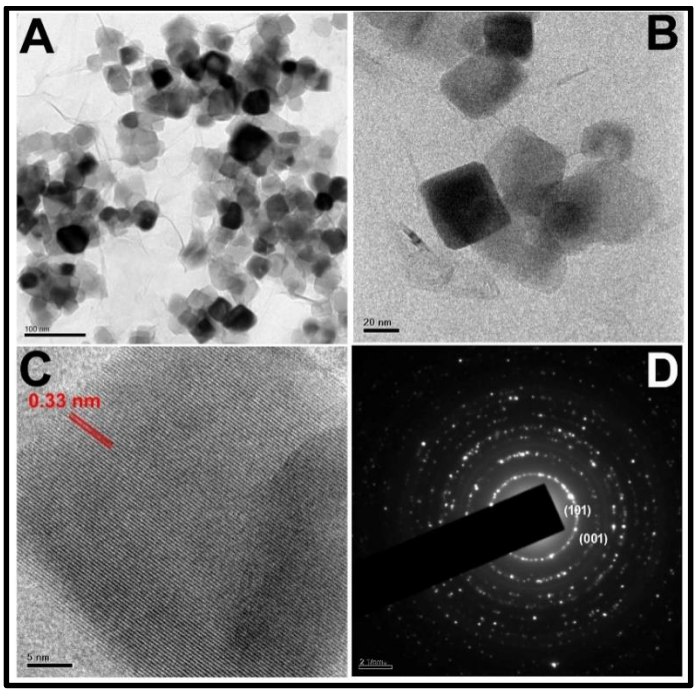

Figure 3.3. (A & B): TEM images of $HRTiO_2$-Gr composite; (C): HRTEM of (001) facet of a single nanocrystal displaying the d-spacing of the (101) facet in the edges and (D): SAED pattern of the composite exhibiting diffraction of exposed (001) facets.

According to the symmetries of anatase $HRTiO_2$, both top and bottom flat and square surfaces of the octahedral (bi-pyramidal) structure are (001) facets and the eight trapezoidal surfaces are (101) facets. The structure of anatase combined with the spacing and the morphology of the $HRTiO_2$, the flat and square surfaces is assigned to (001) facets (B. Liu et al., 2012; H. G. Yang et al., 2008). The SEM and TEM images agrees to the structure of TiO_2 represented in Figure 3.4A and the thus confirms the formation of $HRTiO_2$ and $HRTiO_2$–Gr composites with exposed (001) facets. The images suggest that the chances of (001) facets coming in contact with

the Gr sheets are relatively high. The XRD patterns (Figure 3.4B) of (HR)TiO_2 show well defined crystalline peaks and the absence of rutile peaks confirm the pure anatase nature of the (HR)TiO_2 and the composites (X. Zhou et al., 2013).The higher intensity of 48° (200) suggest the higher length of (001) direction while broader peak at 37.8° (004) indicates the larger area of (001) facets in $HRTiO_2$ and in the composite (F. Tian, Zhang, Zhang, & Pan, 2012). The absence of the characteristic (002) peak of Gr (~26°) suggests the absence of aggregation of Gr sheets in the composites.

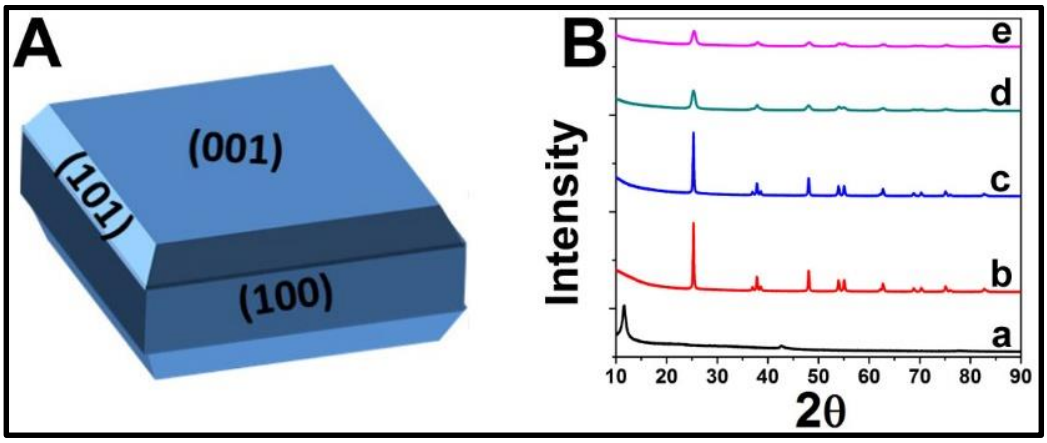

Figure 3.4. (A): Illustrative crystal structure of TiO_2 with exposed (001) facets. (B) XRD pattern of (a): GO; (b): $HRTiO_2$; (c): $HRTiO_2$- Gr10; (d): TiO_2 and (e): TiO_2-Gr10.

Figure 3.5 gives the Raman spectra of GO, $HRTiO_2$ and $HRTiO_2$–Gr10. The E_g (~142 and 631 cm^{-1}), B_{1g} (393 cm^{-1}) and A_{1g} (513 cm^{-1}) correspond to the typical TiO_2 anatase in $HRTiO_2$ and $HRTiO_2$–Gr10. A shift in the E_g peak corresponding to the symmetric stretching vibration of O–Ti–O was observed in $HRTiO_2$–Gr10 compared to that of $HRTiO_2$ indicating the presence of interaction between O–Ti–O and Gr. The D, G and 2D peaks of Gr are present in the spectrum of $HRTiO_2$–Gr10. The I_D/I_G ratio of the composite increased from GO (0.76) to 1.05 suggesting a decrease in the average size of the in-plane graphitic domains, thus suggesting the reduction of GO to Gr (Mukthar Ali & Sandhya, 2014; Quanjun Xiang et al., 2011). The shifts in the D and G peaks of $HRTiO_2$–Gr10 compared to that of in GO suggest the presence of interaction of Gr with TiO_2 (C. Hu et al., 2014; T. Lu et al., 2013).

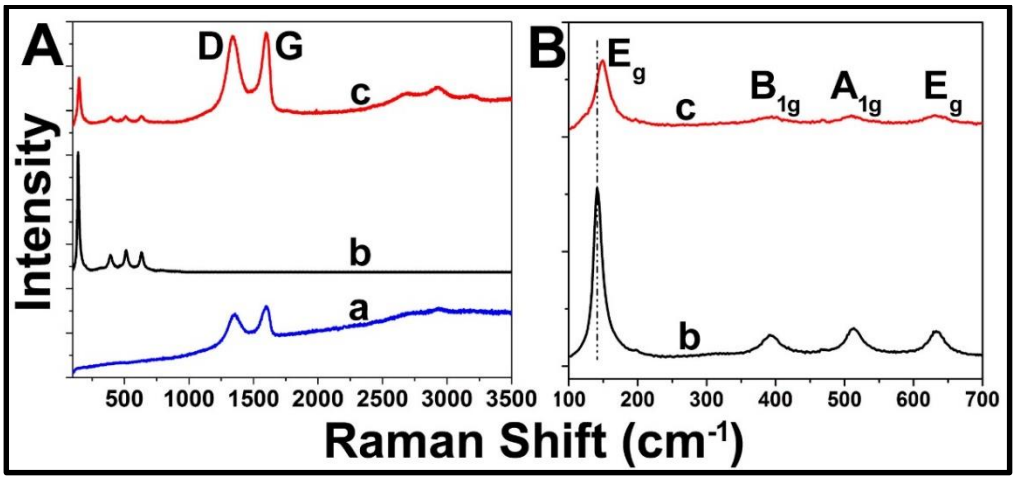

Figure 3.5. (A): Raman spectra of (a): GO; (b): $HRTiO_2$ and (c) $HRTiO_2$-Gr10. (B): Expanded view of (b): $HRTiO_2$ and (c) $HRTiO_2$-Gr10.

The XPS analyses data show typical deconvoluted peaks of C 1 s, (Figure 3.6 A &B) at 285.8 and 284.6 eV for $HRTiO_2$-Gr andTiO_2–Gr, respectively, due to the sp^2 C from Gr (B. Jiang et al., 2011). Deconvoluted binding energy (BE) peaks corresponding to the C1s of oxygen functionalized C atoms with different environments such as C–OH, COOH and C–O–Ti are observed at 286.5, 288.5 and 283.5 eV for TiO_2–Gr, while that of the $HRTiO_2$–Gr occurs at 287.3, 289.5 and 284.6 eV (B. Jiang et al., 2011). A shift is observed in the peaks of the $HRTiO_2$–Gr from that of the TiO_2–Gr. The peak area corresponding to the O functional groups is lesser for $HRTiO_2$–Gr10 to that of the TiO_2–Gr10, suggesting that the amount of O functional groups is comparatively lesser in case of $HRTiO_2$–Gr. The peak of the O1s BE of Ti–O–Ti bonding is observed at 530.6 eV while it is at 528 eV in TiO_2–Gr10. Higher energy peaks at 533 and 534 eV in $HRTiO_2$–Gr10 and at 530 and 532.5 eV in TiO_2–Gr10 composite are assigned to the O1s in Ti–O–C bonding as well as in –C–O groups of Gr. For comparison, full scale XPS results and Ti2p deconvolution spectra are given in Figure 3.7. The peaks at ~458 and ~464 eV in $HRTiO_2$ are assigned to the Ti($2p_{3/2}$) and Ti($2p_{1/2}$), respectively (Gu et al., 2013; B. Jiang et al., 2011). Thus, the XPS data clearly indicates the presence of Gr, TiO_2 and interaction between them in the composites.

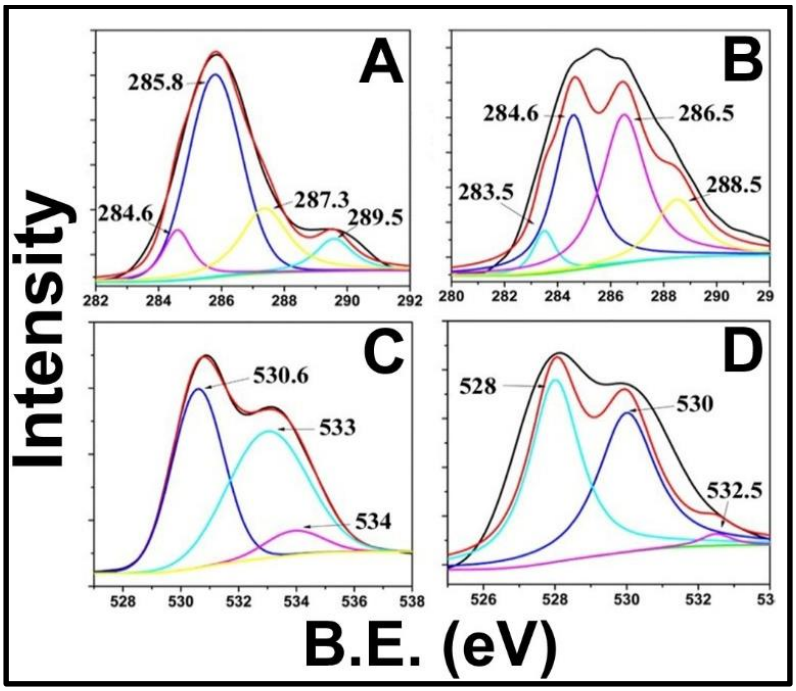

Figure 3.6. XPS analyses of the composites: C1s deconvolution spectra (A and B) and O1s deconvolution spectra (C and D) of HRTiO_2-Gr10 and TiO_2-Gr10 respectively.

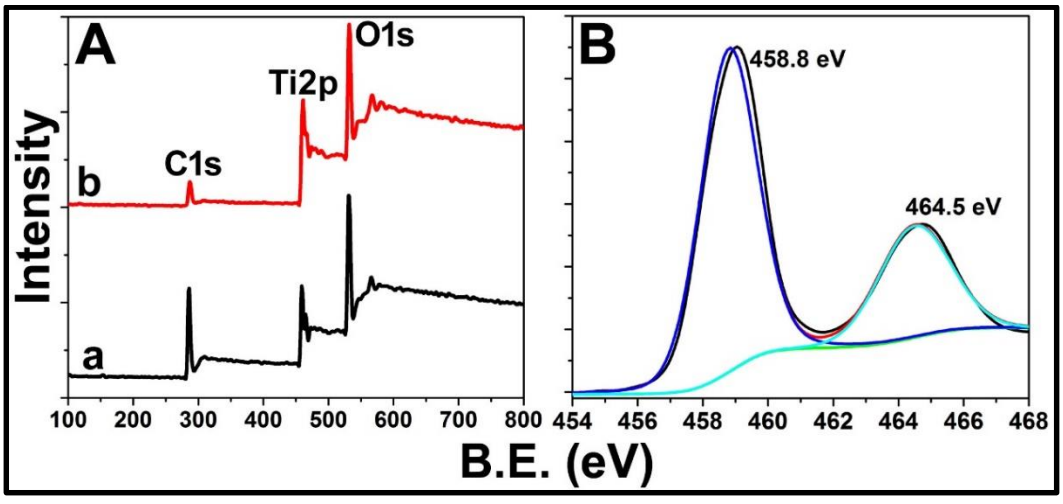

Figure 3.7. Full scale XPS results of (A): (a) HRTiO_2-Gr10; (b): TiO_2-Gr10 and (B): Ti 2p deconvolution spectra.

The BET SA analyses (Table 3.1) reveal that the composites possess higher specific SA than that of the corresponding (HR)TiO_2. The specific SA of HRTiO_2–Gr increases with Gr content up to 10 wt% and then decreases and is assigned to the commencement of aggregation of Gr sheets with amount higher than 10 wt%.

The specific SA and pore volume of $HRTiO_2$–Gr10 are 2–2.5 times higher than that of $HRTiO_2$.

Table 3.1. BET SA analysis results of $HRTiO_2$ and $HRTiO_2$-Gr composites

Sample	BET SA (m^2/g)	Pore volume (cm^3/g)	Pore size (nm)
$HRTiO_2$	20.7	0.11	20.4
$HRTiO_2$-Gr0.1	22.2	0.22	40.0
$HRTiO_2$-Gr5	28.1	0.26	36.7
$HRTiO_2$-Gr10	37.9	0.24	30.7
$HRTiO_2$-Gr20	37.8	0.3	32.2
$HRTiO_2$-Gr25	33.4	0.24	34.4
TiO_2	100.6	0.29	9.6
TiO_2-Gr10	102.8	0.27	9.3

The percentage of Gr loading in $HRTiO_2$–Gr10 was confirmed by TGA under air (Figure 3.8) and found to be ~10 wt% agreeing to our added %. The thermogram showed a gradual decrease in wt% from room temperature to 200°C attributed to the surface adsorbed water and hydroxyl group removal. The sharp decrease in wt% around 450°C is due to the removal of Gr present in the composite. The shape of nitrogen (N_2) adsorption-desorption isotherms (Figure 3.9 A) can give valuable information about the shapes and sizes of pores. According to the De-boer classification of mesoporous materials (Alothman, 2012), $HRTiO_2$ and $HRTiO_2$-Gr10 can be classified as type H3 while TiO_2-Gr10 as type H2. Type H3 refers to the slit-like pores and type H2 refers to the distribution of pore shapes which are not well defined (Alothman, 2012). Inset of Figure 3.9 A and Figure 3.9 B show the pore size distribution of $HRTiO_2$ and its composites and that of $HRTiO_2$-Gr10 and TiO_2-Gr10, respectively.

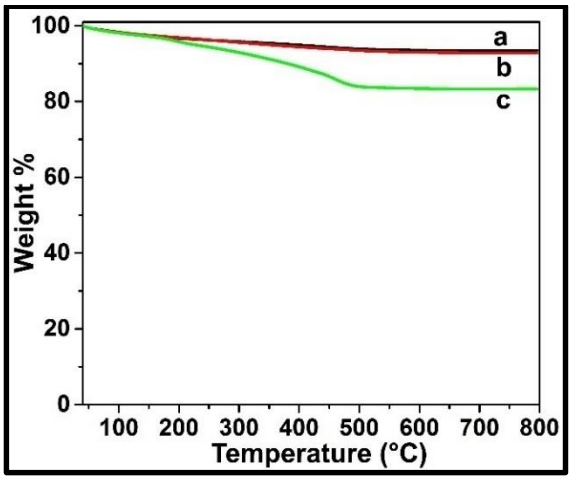

Figure 3.8. TGA of (a): $HRTiO_2$; (b): $HRTiO_2$-Gr1 and (c): $HRTiO_2$-Gr10.

$HRTiO_2$-Gr10 has both mesopores (2–50 nm) and macropores (>50 nm) while the TiO_2-Gr10 has only mesopores. The difference may be due to the different shape of the $HRTiO_2$ from that of TiO_2 which influences the pore size and morphology of the composite. The increased pore area exhibited by $HRTiO_2$-Gr10 shall be assigned to the narrow gaps and holes between the $HRTiO_2$ nanoparticles bonded to the Gr sheets. The slit-like pores (Figure 3.10) are expected to enhance the PC activity by internally scattering light (J. Yu, Fan, & Lv, 2010) and thus enhancing the PC activity.

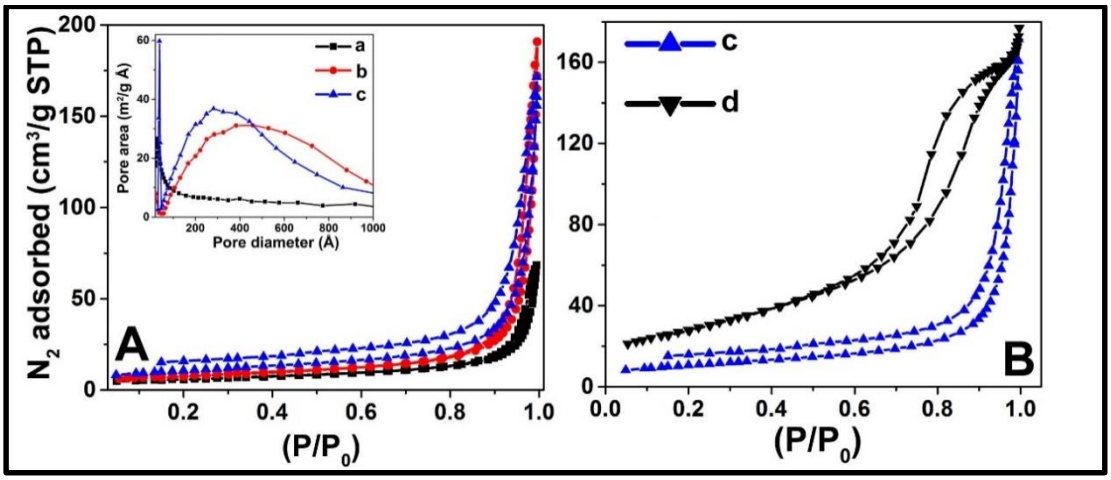

Figure 3.9. (A and B): N_2 adsorption-desorption isotherms of (a): $HRTiO_2$; (b): $HRTiO_2$-Gr5; (c): $HRTiO_2$-Gr10 and (d): TiO_2-Gr10 composites (Inset image of Figure 3.9 A shows the pore size distribution curves).

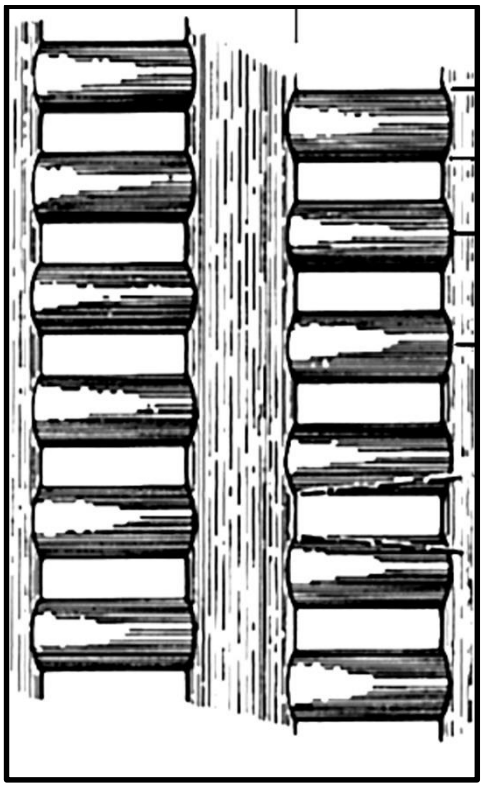

Figure 3.10. Schematic representation of slit-like pores

In order to study the charge separation/recombination properties, solid state PL measurements of $HRTiO_2$ and the composites are done and the results are given in Figure 3.11. It is interesting to note that while the $HRTiO_2$ shows a strong PL emission with a peak around 430 nm, that of the composites are almost completely quenched. PLQY of $HRTiO_2$, $HRTiO_2$-Gr10 and TiO_2-Gr10 excited at 300 nm are 2.36, 1.54 and 1.66% respectively. The decrease in PLQY of $HRTiO_2$-Gr10 is possibly due to the efficient transfer of e-ns from TiO_2 to Gr sheet which is having a lower work function (4.7 eV) than CB of TiO_2 as shown in Figure 3.12. The efficient e-n transfer may be due to the excellent charge separation and transporting ability of thin Gr nanosheets formed by the PCR method and due to the linkages between Gr and TiO_2.

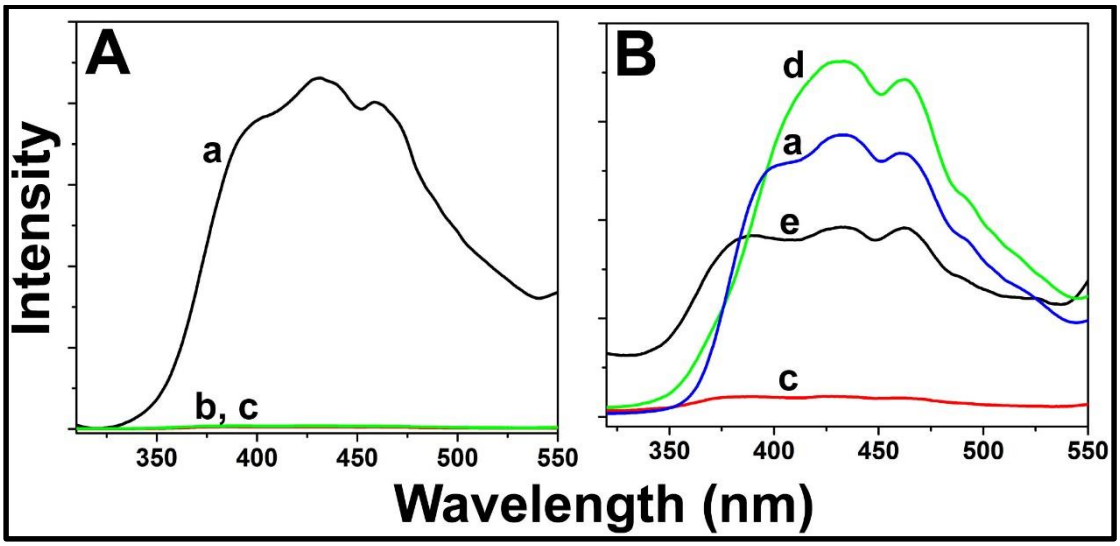

Figure 3.11. (A and B): Solid state PL spectra of (a): $HRTiO_2$; (b): $HRTiO_2$-Gr5; (c): $HRTiO_2$-Gr10; (d): P25 and (e): TiO_2-Gr10 excited at 290 nm

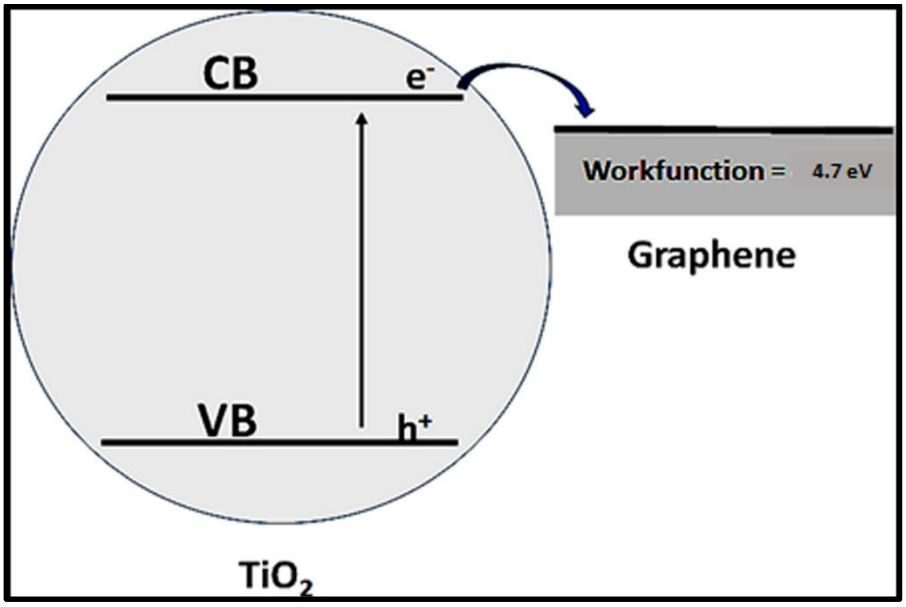

Figure 3.12. Photo induced electron transfer from $HRTiO_2$ to Gr in $HRTiO_2$-Gr composites.

3.3.2. Adsorption of dyes by the composites

The adsorption efficiency of the composites on MB was studied and it increased up to 10 wt% Gr loading and thereafter it decreased which followed the SA trend. $HRTiO_2$-Gr10 exhibited the highest adsorption for MB with a remarkable ~84 % (Table 3.2). Adsorption is an important property which influences the PC activity. The higher adsorption shall be attributed to the π-π interactions between

the benzene rings and the cation-π interactions between the positive MB and the electron rich Gr sheets. However, the adsorption of MB by the physical mixture (PM) of $HRTiO_2$ (90 wt%) and the rGO (10 wt%) made by hydrazine hydrate reduction ($PMHRTiO_2$+Gr10), was only 13.7 % and for TiO_2-Gr10 it was 55%. Adsorption efficiencies of both control $HRTiO_2$ and TiO_2 were only 6.3 and 0.4% while for its corresponding 10 wt% Gr loaded composites were 84 and 55%, respectively. This drastic increase can be attributed to the synergistic effect of Gr and the unique surface properties and pore morphology of the composite.

Table 3.2. Percentage adsorption of MB dye by the $HRTiO_2$-Gr composites

S.No.	Semiconductor	% Ads
1	$HRTiO_2$	6.3
2	$HRTiO_2$-Gr5	22.9
3	$HRTiO_2$-Gr10	84.0
4	$HRTiO_2$-Gr25	30.6
5	P25 TiO_2	6.5
6	TiO_2	0.4
7	TiO_2-Gr10	55
9	$HRTiO_2$+Gr10	13.7

3.3.3. Photodegradation studies

3.3.3.1. Photocatalytic activity versus Gr loading

To find out the optimum Gr loading, the VL PD reaction of MB was used. The UV and VL PD of MB by the photocatalysts are given in Figure 3.13. In the VL PD, the PC efficiency follows the order of $HRTiO_2$-Gr10 > $PMHRTiO_2$+Gr10 > $HRTiO_2$-Gr5 > $HRTiO_2$ > $HRTiO_2$-Gr20 > $HRTiO_2$-Gr1. Under UV and VL, the optimum Gr for higher PC efficiency was found to be 10 wt%. The higher activity

of the $HRTiO_2$-Gr10 compared to that of the physical mixture ($PMHRTiO_2$+Gr10) was possibly due to the lower aggregation of Gr which gave superior properties to the composite. Kamat et al. (Ng, Lightcap, Goodwin, Matsumura, & Kamat, 2010) reported that TiO_2-Gr made by the PCR method yielded better incident photon to charge carrier efficiency (IPCE) values than that of the (hydrazine hydrate reduced) Gr-TiO_2 PM. The control experiment (Figure 3.14) clearly shows that adsorption is not contributing during the PD reaction.

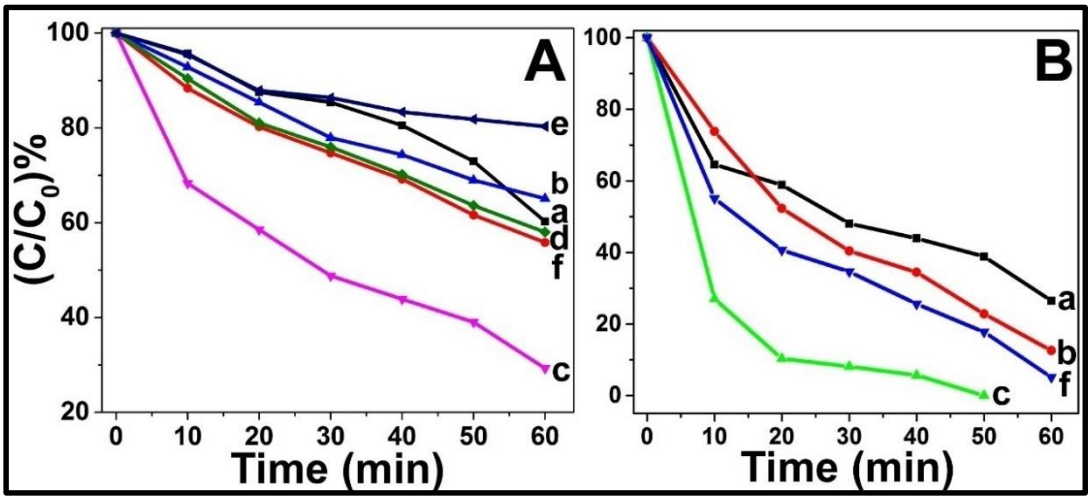

Figure 3.13. PD of MB in (A) visible and (B) UV light respectively by (a): $HRTiO_2$; (b): $HRTiO_2$-Gr5; (c): $HRTiO_2$-Gr10; (d): $HRTiO_2$-Gr15; (e): $HRTiO_2$-Gr20 and (f): $HRTiO_2$+Gr10.

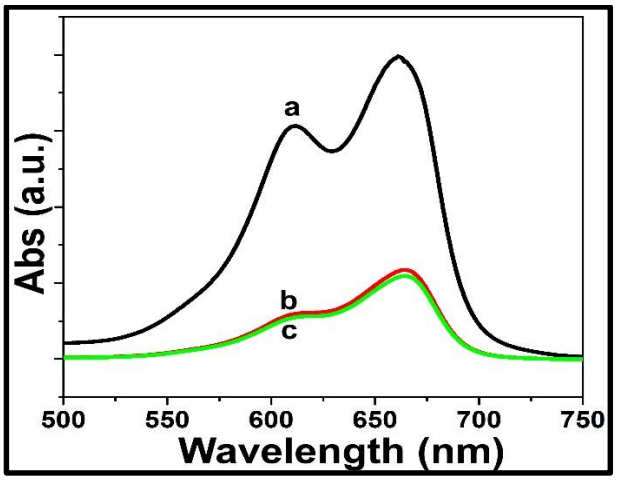

Figure 3.14. UV-Vis absorption spectra of MB in presence of $HRTiO_2$-Gr10 in dark condition (a): 0 min; (b): 60 min and (c): 120 min

The PD reaction results (Figure 3.15) show that the PC activity of $HRTiO_2$-Gr10 was greater than that of TiO_2-Gr10 in the UV and VL. The result clearly indicated that TiO_2 (001) facets play a role in the enhancement of the PC activity (S. Liu, Yu, & Jaroniec, 2010; H. G. Yang et al., 2008). VL PD of MB by P25 is 26 % at 60 min, whereas that of the TiO_2-Gr10 and $HRTiO_2$-Gr10 is 38 and 71 %, respectively. The rate constant values (Table 3.3) of TiO_2-Gr10 and $HRTiO_2$-Gr10 are 2.25 and 5 times that of the P25.

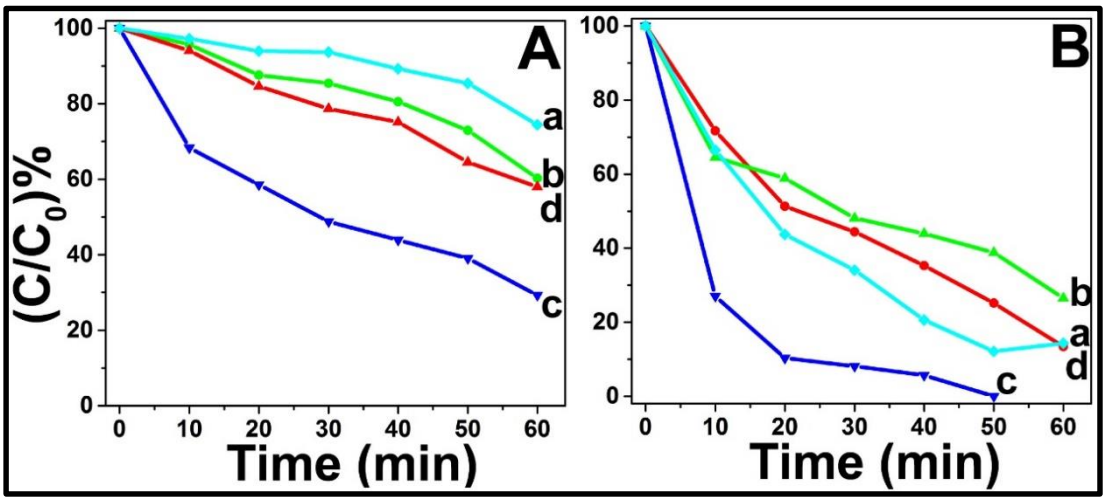

Figure 3.15. PD of MB in (A) visible and (B) UV light respectively by (a): P25; (b): $HRTiO_2$; (c): $HRTiO_2$-Gr10 and (d): TiO_2-Gr10.

Table 3.3. Rate constants for the PD of MB under UV and VL of $HRTiO_2$-Gr composites

Photocatalyst	Rate constant (min^{-1})	
	UV light irradiation	VL irradiation
$HRTiO_2$	0.02 ± 0.0012	0.007 ± 0.0005
TiO_2	0.01 ± 0.001	0.002 ± 0.0001
$HRTiO_2$-Gr10	0.08 ± 0.0082	0.02 ± 0.001
TiO_2-Gr10	0.03 ± 0.0013	0.009 ± 0.0003
$HRTiO_2$+Gr10	0.055 ± 0.009	0.01 ± 0.0001
P25	0.04 ± 0.0017	0.004 ± 0.0004

3.3.3.2. Versatility of $HRTiO_2$-Gr10

In order to study the versatility of the catalyst $HRTiO_2$-Gr10, the VL PD studies were extended to other organic pollutants/dyes such as RhB, MO and 4CP and the results are given in Figure 3.16. The $HRTiO_2$-Gr10 exhibited higher adsorption for MB and RhB compared to that of for MO and 4CP. Analysis of the structure of the dyes (Figure 3.17) reveal that the positive dyes are adsorbed more compared to the neutral or negative dyes. This suggests that the interaction is mainly between the negative Gr and the dye, which promotes the adsorption of positive dyes.

The result indicates that the Gr and the pore morphology of the composite play a major role in determining the adsorption and in turn the PC activity of the composite, thus leading to selective and higher degradation of the positive dyes. To further confirm the results, we have conducted PD experiments using the mixtures of the dyes.

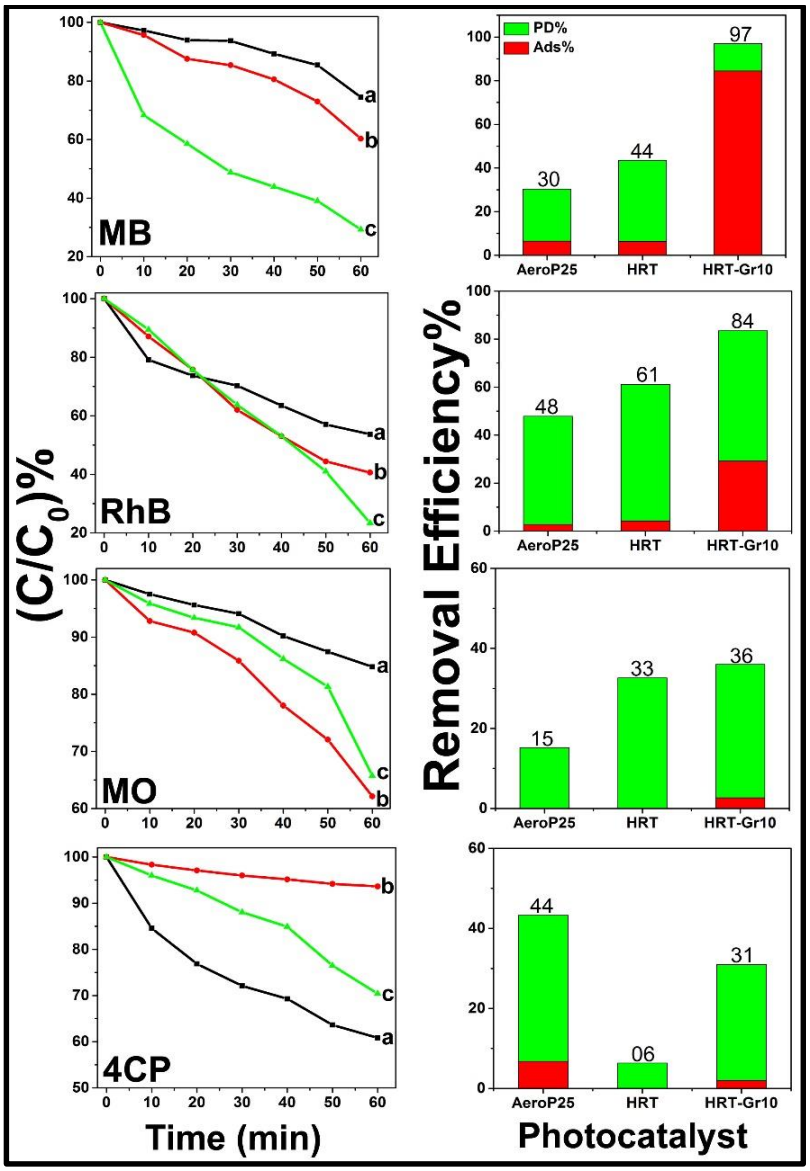

Figure 3.16. VL PD of MB; RhB; MO and 4CP by (a) P25; (b) HRTiO$_2$ and (c) HRTiO$_2$-Gr10. Bar chart depicting the removal efficiency of each composite by the combined effect of adsorption and PD.

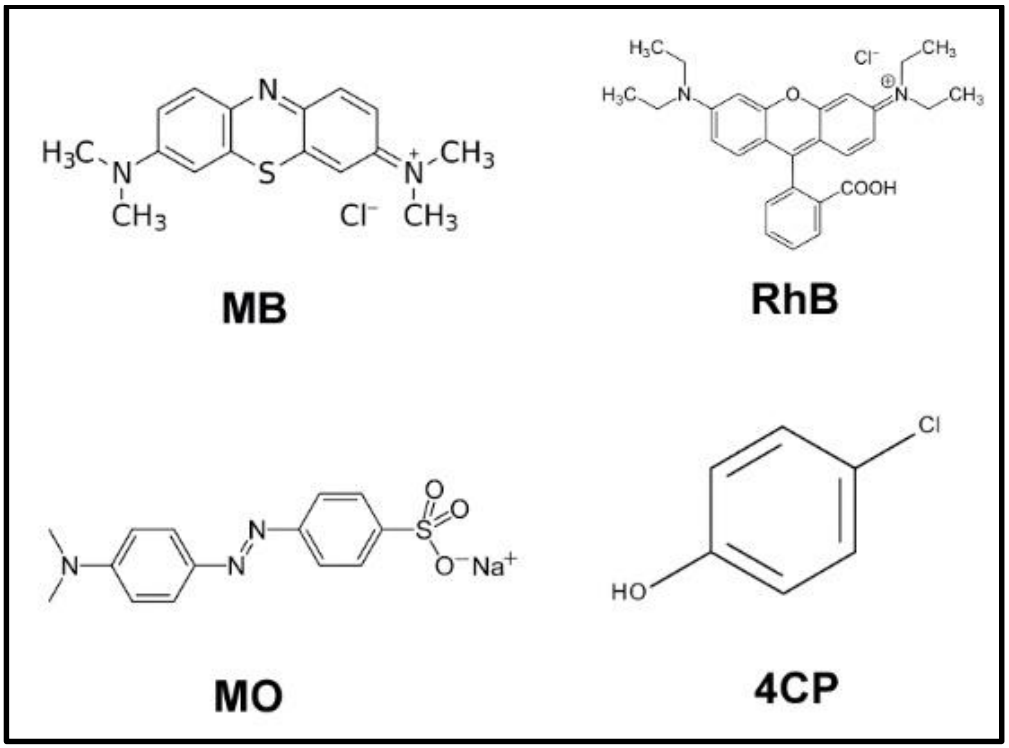

Figure 3.17. Molecular Structures of MB, RhB, MO and 4CP.

3.3.3.3. Selectivity of HRTiO$_2$-Gr10 towards dye removal

The digital images of the dye mixtures before and after PD by HRTiO$_2$-Gr10r are given in Figure 3.18; the mixture of a positive and a negative dye (MB & MO) given in Figure 3.18A and the mixture of both positive dyes (MB & RhB) in Figure 3.18B, The pictures clearly demonstrated the selectivity of HRTiO$_2$-Gr10 towards positive dyes. Selective removal of MB happens in the mixture of MB & MO and did not happen in the mixture of MB & RhB. In the case of MB & MO mixture, the total removal of MB and MO were ~96 and ~11%, respectively while the removal of MB and MO from their individual solutions (the ratio between the total dye and photocatayst remain same in both conditions) were ~97 and 36 %, respectively. In the meantime, in the MB & RhB mixture, the removal percentage of MB & RhB were ~61 & 47 % respectively, and that of from their individual solutions were ~97 and 83 %, respectively. While a proportionate decrease in the PD of MB & RhB was observed in their mixture, the PD of MO was selectively decreased in the mixture of MB and MO, showing selectivity towards the positive dye MB. To further confirm the selectivity of HRTiO$_2$-Gr towards positive dyes, the VL PD of another combination of a positive and a negative dyes: RhB & MO,

respectively, was conducted and the enhancement in the removal of RhB (Figure 3.18C) clearly indicated that the composite exhibits selective PD towards the positive dyes. Li et al (C. J. Li, Xu, Zhang, & Gong, 2012) reported the selective PC oxidation of benzyl alcohol into benzaldehyde of by TiO_2 nanorods and attributed to its slit-like mesoporous structure. Thus we attribute the selective removal of positive dyes to the surface properties and slit-like pores dominated by negative Gr, possibly due to the high quality thin Gr sheets and with higher loading % and dispersion.

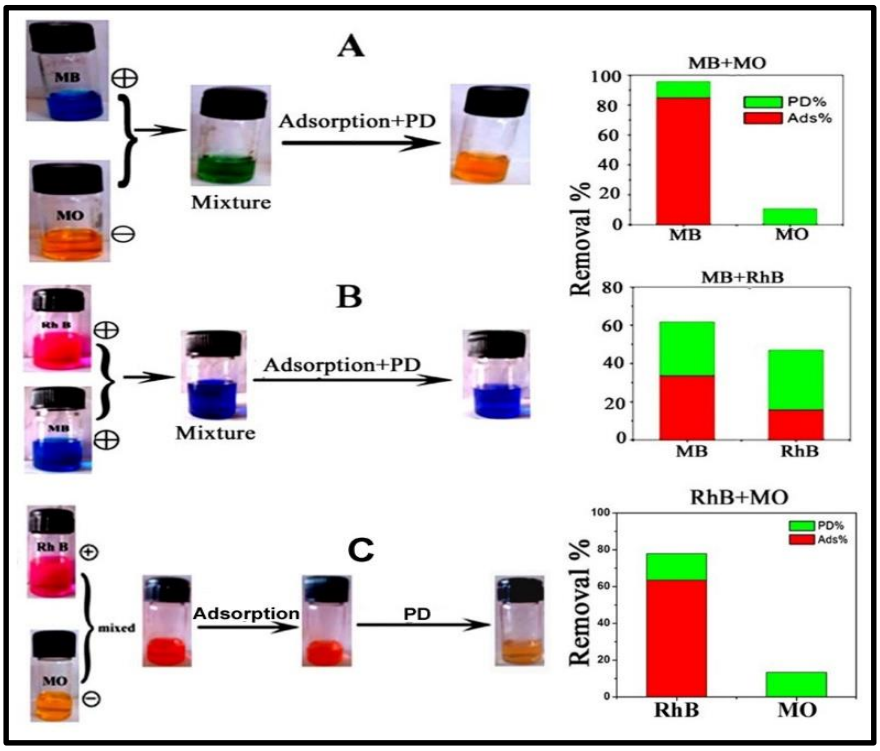

Figure 3.18. Digital images and bar charts demonstrating the selective removal of the (A): positive dye MB from a mixture of positive and negative dyes MB & MO; (B): positive dyes RhB & MO show that both the dyes undergo PD by $HRTiO_2$-Gr10, no selective removal of MB is observed and (C): positive dye RhB from a mixture of positive and negative dyes RhB & MO.

Nyquist plots of the $HRTiO_2$ and $HRTiO_2$-Gr10 are given in Figure 3.19. The diameter of the semi-circle of $HRTiO_2$-Gr10, at high frequencies, was remarkably lower compared to that of $HRTiO_2$ (Figure 3.19) indicating a decrease in the charge-transfer resistance at the electrode/electrolyte interfaces and is

attributed to the presence of Gr. Decrease in the charge transfer resistance of the composite proved that the GO was reduced to Gr which in turn decrease the solid state interface layer resistance and charge transfer at the interfaces (Bell et al., 2011).

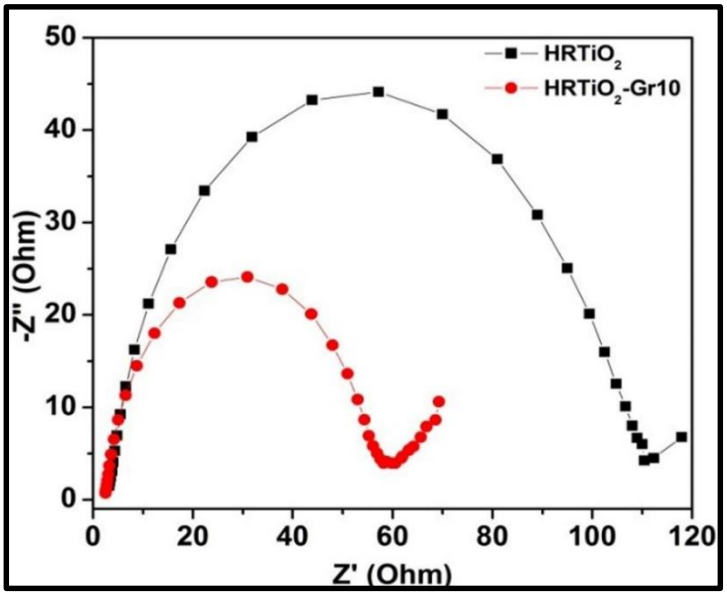

Figure 3.19. EIS of (A) $HRTiO_2$ and (B) $HRTiO_2$-G10

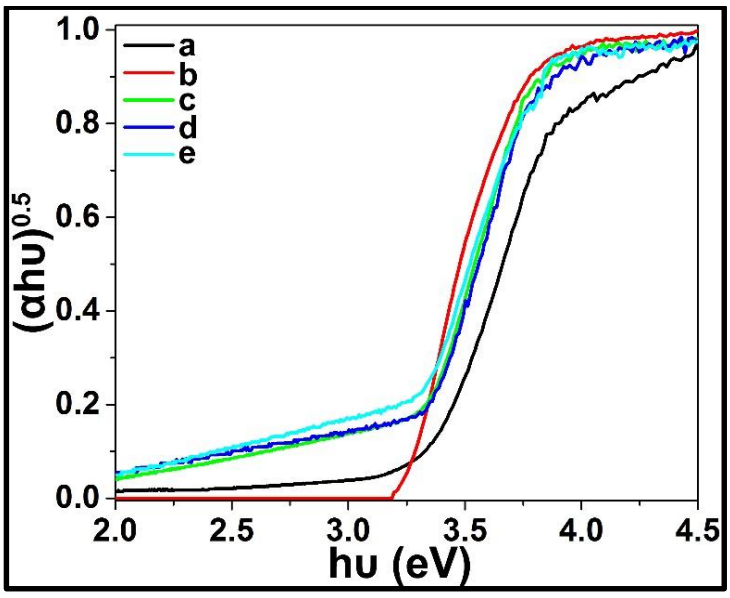

Figure 3.20. Tauc plot of (a): P25; (b): $HRTiO_2$; (c): $HRTiO_2$-Gr5; (d): $HRTiO_2$-Gr10 and (e): $HRTiO_2$-Gr25

The DRS spectra of the $HRTiO_2$ and the composites in Figure 3.20 showed that the $HRTiO_2$-Gr composites exhibited extended absorption in the VL region compared to that of the $HRTiO_2$. It has been reported that the formation of the Ti-O-C bond between TiO_2 and Gr sheet (J. Yu, Fan, et al., 2010; H. Zhang et al., 2010) leads to VL absorption. This may contribute to the enhancement in the PC efficiency of $HRTiO_2$-Gr compared to that of the $HRTiO_2$.

3.3.3.4. Estimation of ROS in the photodegradation of RhB by $HRTiO_2$-Gr

The ROS reactivity can be quenched by certain chemical scavengers (Mukthar Ali & Sandhya, 2014; X. Zhang et al., 2011) prior to its reaction with dyes/ pollutant molecules, these reactions in the presence of different scavengers (Mukthar Ali & Sandhya, 2014) are used to estimate the contribution of each ROS in the PD reaction. For example, •OH can be quenched by t-BuOH, O_2•− can be quenched by BQ and the combination of $^1O_2$ and •OH can be suppressed by NaN_3. Apart from these ROS, there are other ROS such as hydrogen peroxide (H_2O_2), hydroxyl ion ($^-$OH) and carbonate (CO_3^-) can contribute towards the PD of dyes/pollutants but their contribution is greatly limited because of two reasons (i) they are the secondary ROS products from the primary ROS (•OH, $^1O_2$ and O_2•−); (ii) their oxidation potential neither low or high (Schipper, 2012). In addition to these, another highly oxidative species is the valence band holes which can also partially contribute for the PD of dyes/ pollutants but it is believed that most of the holes are converted to •OH rather than directly participating in the PD.

The results of scavenger studies are given in Figure 3.21. The actual PD% at 60 min with no scavenger is 84% which is considered 100% for calculation purpose. In the presence of scavengers t-BuOH, NaN_3 and BQ the PD% were 68, 36 and 100% respectively. This suggested that there was no suppression of PD with BQ i.e. nil or negligible contribution from O_2•− while the contributions from •OH and $^1O_2$ were almost equal (~32%). UV-Vis absorption spectra of RhB during VL PD in the presence of $HRTiO_2$-Gr10 was given in Figure 3.22 and suggested that the PD pathway lead to mineralization, since the production of powerful oxidizing agent •OH.

Based on the results of scavenger studies, the following reaction mechanism

was proposed (Figure 3.23). Upon irradiation with VL, the electrons were excited to the intra-band states formed due to C-doping. Incorporation of Gr can enhance the VL absorption either by doping the TiO_2 (Chao et al., 2010; Quanjun Xiang & Yu, 2013) or can act as a macromolecular photosensitizer of TiO_2 (Photosensitizer, Zhang, Zhang, Tang, & Xu, 2012). In addition to this transition, RhB can also sensitize the TiO_2. The electrons in the CB and intra-band states of TiO_2 can partially or fully be transferred to the electron accepting Gr sheets which has a work function of 4.7 eV. The electrons in Gr can be converted to $^1O_2$ while the holes in the VB level oxidize water to form •OH (E° =2.80 eV). The $^1O_2$ formation is facilitated by the energy transfer between excited triplet state of MB and the ground $^3O_2$. It has been reported that presence of Gr enhances the extent of $^1O_2$ formation (Wojtoniszak, Roginiska, Machalinski, Drozdzik, & Mijowskaa, 2013) in the photosensitization of dyes. Typically longer lifetime of triplet states favour the formation of $^1O_2$ and Gr is one of such nanomaterial with longer triplet state (Mueller, Yan, Mcguire, & Li, 2010) lifetimes (3.97 µs). Even though $^1O_2$ forming efficiency of RhB dyes, they can contribute to the $^1O_2$ formation. The lack of $O_2^{\bullet-}$ formation is explained by the faster electron from CB of TiO_2 due to exposed (001) facets as well as lower redox potential of superoxide ($E^\circ_{O2/\,O2^{\bullet-}}$ = -0.33 eV). The schematic representation of ROS formation under VL is given in Figure 3.22.

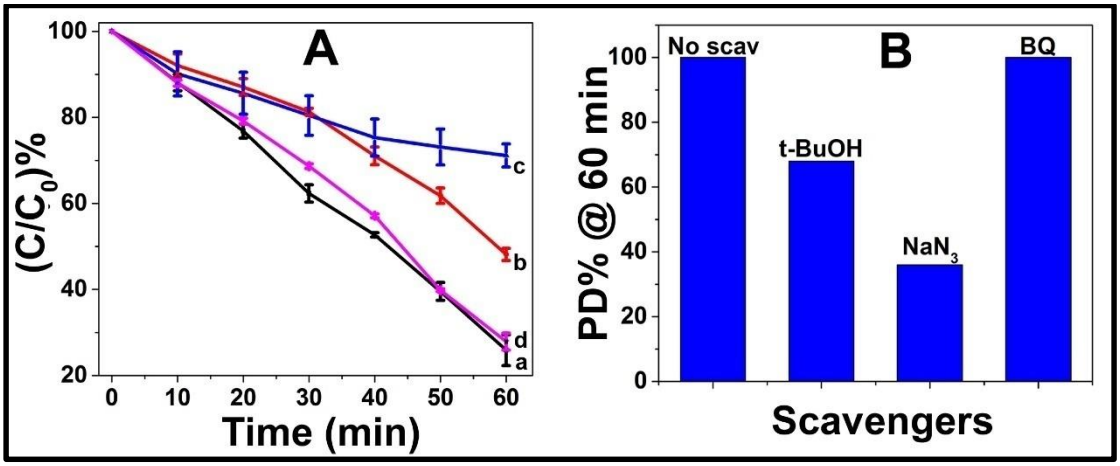

Figure 3.21. (A) VL PD of RhB by $HRTiO_2$-Gr in the presence of (a): no scavengers; (b): t-BuOH; (c): NaN_3 and (d): BQ. (B): Bar graph representation for the PD% @ 60 min in the presence of scavengers (PD% is normalized to 100% for no scavenger studies).

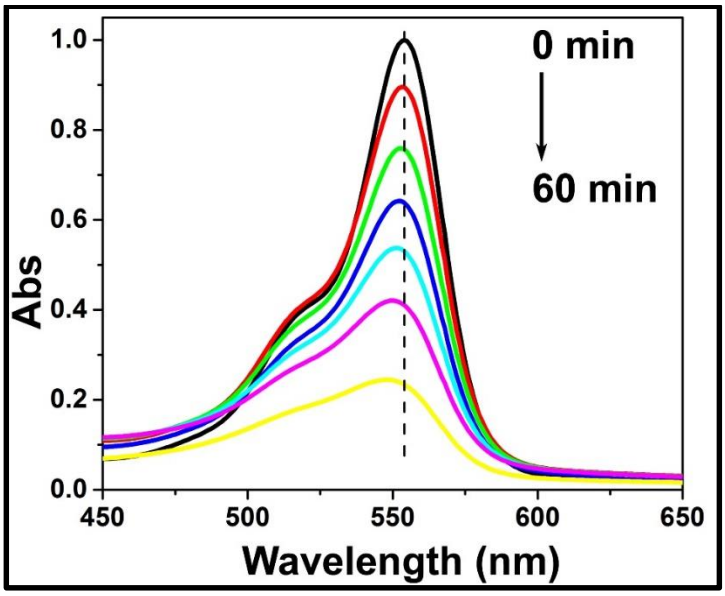

Figure 3.22. UV-Vis absorption spectra of RhB during VL PD in the presence of $HRTiO_2$-Gr10 with no scavenger.

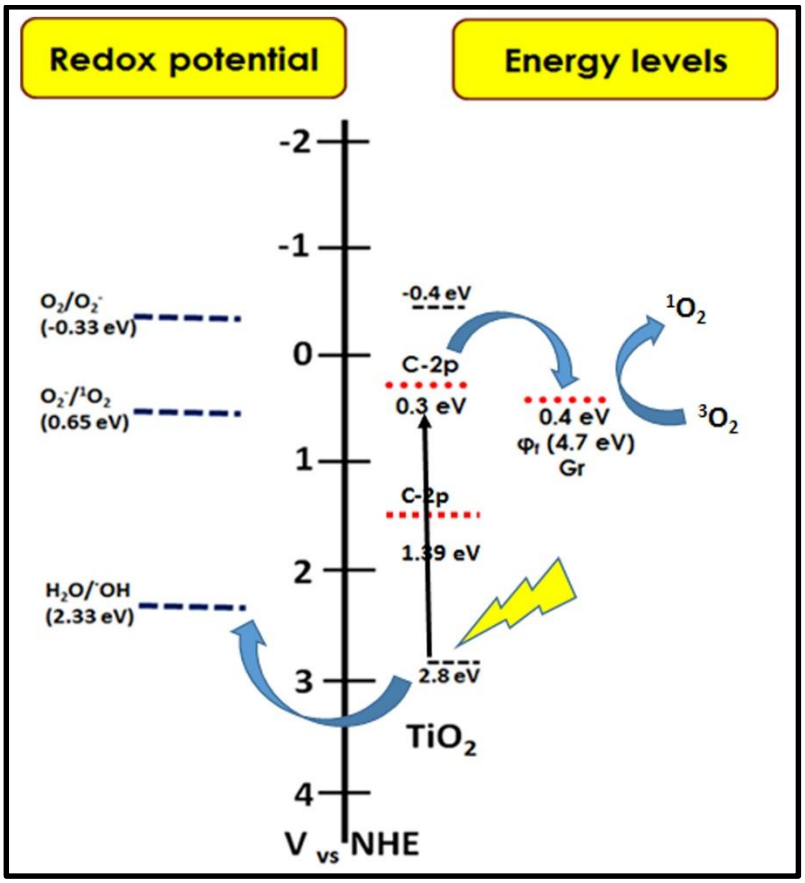

Figure 3.23. Schematic of the proposed mechanism for the ROS formation in the VL PD of RhB in the presence of $HRTiO_2$-Gr10.

3.4. Conclusions

In conclusion, we report for the first time the green preparation of HRTiO_2-Gr composites with exposed (001) facets by PCR method and its selective PD properties. BET SA analysis suggested a slit-like pore morphology to the composite. The PC efficiency of the composite was higher than that of the P25 for various dyes/ pollutants such as RhB, MB, MO and 4CP. The composite exhibits selective PD towards positive dyes and the effect was observed in the mixture of positive and negative dyes, due to the selective adsorption of the positive dyes to the active sites. Composite exhibits superior charge transfer properties compared to that of the bare HRTiO_2 and P25. Our results showed that the PCR method of preparation of HRTiO_2-Gr facilitates quality thin Gr sheets with good dispersion which in turn combined with the unique pore morphology imparts enhanced and selective PC activity to the composite. Scavenging studies suggested that •OH and $^1O_2$ are the predominant ROS involved in the VL PD of RhB.

CHAPTER 4

ONE-STEP SOLVOTHERMAL SYNTHESIS OF N-TiO_2 AND TiO_2-MoS_2 PHOTOCATALYSTS FOR ENHANCED VISIBLE LIGHT CATALYTIC PROPERTIES

This chapter discusses about a one-step solvothermal synthesis and characterization of two type of TiO_2 based photocatalysts composed of ultra-fine nanoparticles (4-8 nm) with high SA and crystalline nature: (i) nitrogen doped TiO_2 (N-TiO_2) and (ii) TiO_2-MoS_2 (TMS) composite with VL activity. N-doping of TiO_2 was done using solvent NMP whereas the same procedure and a novel MoS_2 precursor which is a molybdenum-sulphur cluster compound, was utilized for the synthesis of TMS. The PC activities of both the composites were studied using the UV and VL PD reactions of RhB. It was demonstrated that VL activity has been enhanced due to the extended absorption of TiO_2 due to N-doping and MoS_2, respectively for N-TiO_2 and TMS. Further the ROS involved in the VL PD of RhB in the presence of the photocatalysts were studied and mechanisms were proposed for the formation of the ROS based on the energy level of the photocatalysts.

4.1. INTRODUCTION

Of the many strategies (R Asahi et al., 2001; Ryoji Asahi et al., 2014; X. Chen et al., 2011; Kalathil et al., 2013; M. M. Khan et al., 2014; Lin et al., 2013; S. U. M & Jr, 2002; Wendt et al., 2008) adopted to broaden the VL photo response of TiO_2, non-metal doping of TiO_2 attracts lots of interests owing to its much simpler approach. Asahi et al. (R Asahi et al., 2001) showed that the doping of non-metal such as N, S, P and C into TiO_2 extends the VL activity by decreasing the band gap. Among these, N and C doping has been widely investigated due to their compatible ionic sizes to oxygen as compared to that of S and P (Ryoji Asahi et al., 2014). Typical N-doping of TiO_2 has been achieved by utilizing ammonia, urea,

triethylamine, NH_4OH and hexamethylene tetramine, guanidine hydrochloride etc (Emeline et al., 2008; Kaewgun et al., 2008; Pang & Abdullah, 2013; Xu et al., 2014; G. Yang, Jiang, Shi, Xiao, & Yan, 2010) as external dopants, mechanochemical method (Yin et al., 2003), sol-gel and hydrothermal/solvothermal methods, plasma treatment using N_2 or N_2-H_2 gas mixtures (Matsubara et al., 2012) etc. Two step hydrothermal synthesis (Gang Liu, Wang, et al., 2009) of N-TiO_2 was achieved by TEA as a dopant from TIOP. N-doping of TiO_2 can also be achieved without any specialized doping agent. Hydrolysis of TiN (Gang Liu, Yang, et al., 2009) under highly acidic condition in a hydrothermal can lead to the formation of facet controlled N-TiO_2 with significant VL activity. In some cases, solvents such as IPA (Park, Kim, et al., 2009) and NMP (Kaewgun et al., 2008) are used as doping agent for C and N-doping, respectively by subjecting already prepared TiO_2 to water based ambient condition sol (WACS) method (Kaewgun et al., 2008). Kaewgun et al (Kaewgun et al., 2008) reported a N-doped P25 using NMP by solvent-based ambient condition sol method (SACS). The method utilized the P25 as a starting material which leads to the formation of N-doped polymorphic titania.

In addition to VL responsiveness, charge separation can be achieved by forming a heterojunction with an ideal candidate like MoS_2 due to its ability to absorb VL and conducting properties. The combination of p-type MoS_2 and n-type TiO_2 lead to p-n heterojunction (Hao Fu et al., 2015). This lead to band bending followed by the development of built-in potential. Based on this potential, electrons generated at the p-type MoS_2 move to the conduction band of n-type TiO_2, and holes generated at TiO_2 diffuse to the valence band of p-type MoS_2 in the PC process. Therefore, the built-in electric field can significantly reduce the e-h pair recombination (Hao Fu et al., 2015).

MoS_2 is a two dimensional layered material, similar to that of Gr, and one of the promising candidate for forming heterojunction with TiO_2. If incorporated as few layered sheets, it can act as VL sensitizer to TiO_2 since the CB level of bulk MoS_2 is higher than that of TiO_2. Moreover, single or few-layer nanosheets of MoS_2 (direct band gap of 1.8-1.9 eV) incorporation can make the composite VL responsive (C. H. Meng, Liu, Zhang, & Zhai, 2015; Quanjun Xiang, Yu, &

Jaroniec, 2012; Zong et al., 2008), and thus can enhance the PD. Single/ few layered MoS_2 nanocrystals serve as a sensitizer to TiO_2 and thus enhance the activity of the composite to hydrogen production (G. Yang, Yan, & Xiao, 2012) and PD of organic molecules (C. H. Meng et al., 2015; Quanjun Xiang et al., 2012).

Despite the promising PC and PEC properties, scalability remains a common challenge as few layered MoS_2 sheets production and incorporation is not easy, growth of MoS_2 single crystals is slow and not economically viable. Mixing of chemically exfoliated bulk MoS_2 and TiO_2, may not produce a composite with homogenous structure and the interaction may also be minimal. In-situ synthesis of few layered MoS_2 sheets can possibly create better interaction between TiO_2 and MoS_2, however, not many reports of TMS are available due to the difficulty involved in the synthesis of MoS_2 restricted to few layers and with good uniformity throughout the composite which depends on many factors such as the structure of precursor, solubility of the precursor in the solvent used etc. Typically single/ few layered MoS_2 sheets are made from delamination of bulk MoS_2 which was originally established in 1986 (Joensen, Frindt, & Morrison, 1986). Even though this method leads to single layer MoS_2, it involves organo-lithium compounds and economically not viable. Later there are various attempts to prepare either single/ few layered MoS_2 nanosheets by surfactant assisted or ultrasound assisted exfoliation of MoS_2 (Afanasiev, Xia, Berhault, Jouguet, & Lacroix, 1999). These prepared MoS_2 nanosheets can be mixed with TiO_2 powders or its precursors to produce TMS composites. Apart from the exfoliation of bulk MoS_2, precursors of MoS_2 were used in the literature for preparing composites. TMS composite was made using ammonium molybdenum sulphide (AMS) as precursor (C. H. Meng et al., 2015). In this AMS was mixed with pre-prepared TiO_2 nanotube and on sunlight irradiation it produces MoS_2 to form TMS. Similarly TMS composite nanobelts were prepared using TiO_2 nanotube, sodium molybdate (Na_2MoO_4) and thioacetamide (W. Zhou et al., 2013). Fu et al. described how the change in reaction conditions can bring about changes in the resulting morphology of TMS composites (Hao Fu et al., 2015). Likewise there are various MoS_2 precursors such as thiomolybdates, molybdenum-sulphur clusters etc. which are not explored greatly for composite synthesis.

Here in this chapter, we report a single step procedure to the synthesis of N-TiO_2 from its precursor by solvothermal method using NMP as solvent and dopant and further attempted to combine N-doping and TMS heterostructure in an attempt to can enhance the VL response of TiO_2 and thus the PC activitiy. Since NMP was acting as solvent cum dopant, the same method in the presence of MoS_2 precursor was used synthesize TMS composites by conducting the reactions in the presence of a novel molybdenum-sulphur cluster compound [$(NH_4)_2$ $Mo_3S_{13}.2H_2O$] as the precursor for MoS_2. While previous reports (Kaewgun et al., 2008) have obtained polymorphic titania as it involves two steps, our method yielded ultra-fine sized (~4 nm) highly crystalline N-TiO_2 with pure anatase phase and very high SA (191 m^2/g). N-TiO_2 was annealed at 400°C under inert atmosphere to remove any surface adsorbed N-species and thus to ensure that the N-doping was not a mere surface functionalized one and the annealed product was referred to as aN-TiO_2. It was interesting to note that the aN-TiO_2 showed a narrowed band gap of 3.10 eV as compared to the 3.15 and 3.3 eV of N-TiO_2 and P25, respectively. The N-TiO_2 and aN-TiO_2 exhibited enhanced VL PD for RhB and was attributed to the N-doping which induces intra-band electronic states and thus enables the TiO_2 to absorb in the VL region.

The TMS composites obtained were of higher BET SA (274 m^2/g for TMS0.7), had C-doping and few layered MoS_2 and exhibited higher VL PC activity, than that of N-TiO_2. However no N-doping was observed in TMS and may possibly due to the interference from the MoS_2 precursor. The high SA was owed to the nano dimensions and uniform distribution of TiO_2 and MoS_2 and is one of the highest SA so far reported for TMS composites. The composite exhibited improved VL PC activity and was assigned to the VL responsiveness of the composite due to C-doping and the few layered MoS_2 sheets and to the heterostructure formation between TiO_2 and MoS_2 which facilitates effective charge separation.

4.2. Experimental

4.2.1. Preparation of aN-TiO_2

Typical synthesis involved with the addition of 3 ml TIOP with 25 ml of NMP-IPA (4:1) mixture in an autoclave under stirring. Then the autoclave was heated to 180°C for 20 hr. After the reaction, the reaction mixture was allowed to cool to room temperature. Then 50 ml of water was added to it and then stirred for 1 hr. The yellowish white precipitate was centrifuged and washed plenty of time with water and finally washed with IPA and dried at 75°C overnight. To study the effect of doping, temperature and time varied and the photocatalysts were labelled as N-TiO_2 (T-t), where T referred to temperature while t refers to duration of reaction in hours. Initially the PC activities were tested and the N-TiO_2 (180-20) was found to be a best photo catalyst and it was called as N-TiO_2 for further discussion. This N-TiO_2 was annealed to 400°C for 2 hr under inert atmosphere and it was named as aN-TiO_2.

4.2.2. Preparation of the TMS

TiOP and $(NH_4)_2$ $Mo_3S_{13}.2H_2O$ were used as precursors to prepare TiO_2 and MoS_2 respectively. The preparation of $(NH_4)_2$ $Mo_3S_{13}.2H_2O$ was mentioned elsewhere. For the loading of 0.7 % MoS_2, 3.5 mg of $(NH_4)_2$ $Mo_3S_{13}.2H_2O$ was added to a 25 ml of NMP-IPA (4:1) mixture and probe sonicated for 30 min. To this 3 ml of TiOP was added under stirring in an autoclave. The autoclave was sealed and heated to 180°C for 20 hrs in an electric oven. The reaction mixture was cooled to room temperature and then 50 ml of distilled water was added and stirred followed by centrifugation. The precipitate was again centrifuged and washed with CS_2 and with plenty of water and finally washed with IPA and dried at 75°C overnight. Washing with CS_2 will remove the by-product sulphur. It was labelled as TMS0.7 corresponding to 0.7 wt% of MoS_2. Similarly TMS with different percentages of MoS_2 (0.24%, 1.5% and 2.2%) was prepared. For comparison studies, control TiO_2 was prepared with the same procedure, without the addition of MoS_2 precursor.

4.3. Results and discussions

4.3.1. Characterization of the N-TiO_2 and TMS

The SEM image of the prepared N-TiO_2 and TMS0.7 were given in Figure 4.1. No distinct changes were observed in the particle size, nature and morphology between the N-TiO_2 and the composite in the SEM images due to the ultra-fine size of TiO_2 particles. The precursor for MoS_2, a molybdenum-sulphur cluster compound $(NH_4)_2Mo_3S_{13}.2H_2O$ (structure of the precursor is given in Figure 4.2), was made by a reaction between ammonium heptamolybdate $[(NH_4)_6 Mo_7S_{24}.4H_2O]$ and ammonium polysulfide (Xiv, Wold, & Ruff, n.d.) and was used for the first time for making TMS composite. The formation of 2H type MoS_2 is known to improve the VL PD in association with TiO_2 and its formation is favored from this precursor (Hibble & Feaviour, 2001). Since 2H type MoS_2 behaves more like a semiconductor in nature while the 1T type is more of metallic in nature.

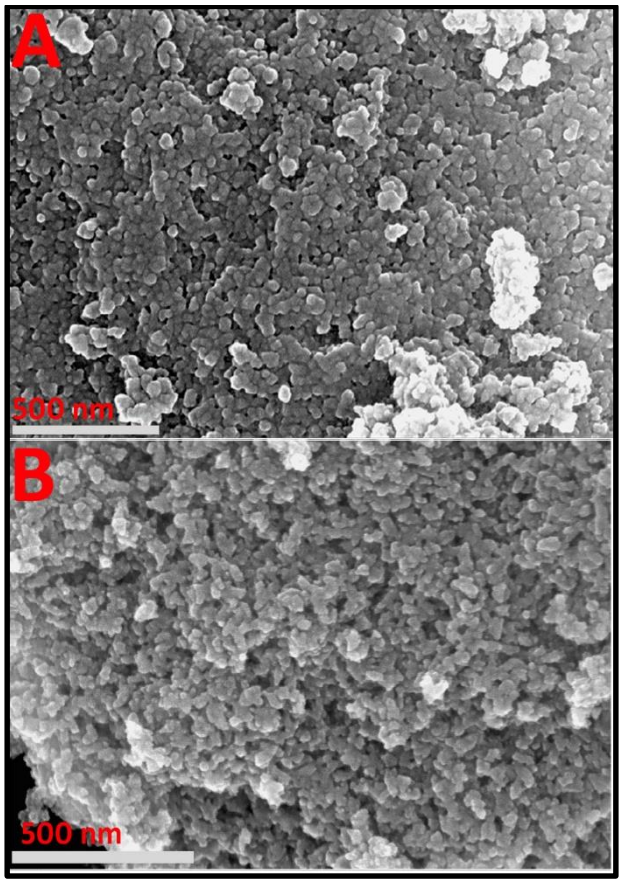

Figure 4.1. SEM image of (A): TMS0.7 and (B): N-TiO_2 (Each scale bar is 500 nm)

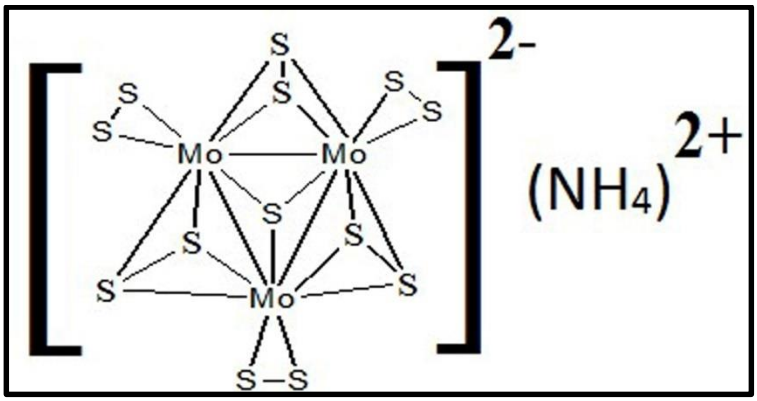

Figure 4.2. Structure of the precursor molybdenum-sulphur cluster.

The XRD patterns of N-TiO_2 and the composites (TMS with different percentage of MoS_2) were given Figure 4.3. The peaks at 25.8°, 38.5°, 48.1°, 54.8° and 63.2° correspond to the anatase phase (JCPDS no. 71-1168) of TiO_2 and the absence of peaks of rutile nature indicates that the TiO_2 was purely anatase in nature. The crystallite sizes of the TiO_2 particles were calculated using Debye-Scherrer equation and found to be ~5 nm, in case of both N-TiO_2 and TMS. The ultra-fine size is ascribed to the solvothermal method which utilizes an organic solvent only. The previous reports (Kaewgun et al., 2009, 2008) of N-TiO_2 from NMP based SACS method yielded polymorphic N-doped titania and this was due to the difference in the synthetic procedure followed, the reports use WACS treated P25 for SACS treatment while in our case N-TiO_2 was prepared from TIOP and NMP: IPA mixture. The MoS_2 peaks were not present in the XRD patterns and were possibly due to the lower loading % of MoS_2 (Q. Liu et al., 2013) and due to the exfoliated nature of MoS_2 in the composite.

The FTIR and Raman spectra of N-TiO_2, aN-TiO_2 and TMS0.7 are given in Figure 4.4. The peaks at 3400 and 1633 cm^{-1} were assigned to the stretching and bending of surface –OH groups of TiO_2, respectively. The difference in N functional group intensity between N-TiO_2 and aN-TiO_2 can be distinguished from the spectra. The nitrogen incorporation was evident from the peaks at 1060 and 1398 cm^{-1} which correspond to the Ti–N bond vibration and the surface adsorbed NO_3^- which were

present in both N-TiO_2 groups respectively, and aN-TiO_2. The intensity of the peak at 1398 cm^{-1} in aN-TiO_2 was decreased and attributed to the partial removal of surface adsorbed NO_3^- groups during annealing. Stretching vibration of Mo-S bond was at 472 cm^{-1} (Ghosh, Srivastava, Nath, & Celis, 2013) cannot be seen in TMS0.7 composite due to the dominant nature of TiO_2 broad peak (400-1080 cm^{-1}) corresponding to the stretching and bending of Ti-O and Ti-O-Ti respectively.

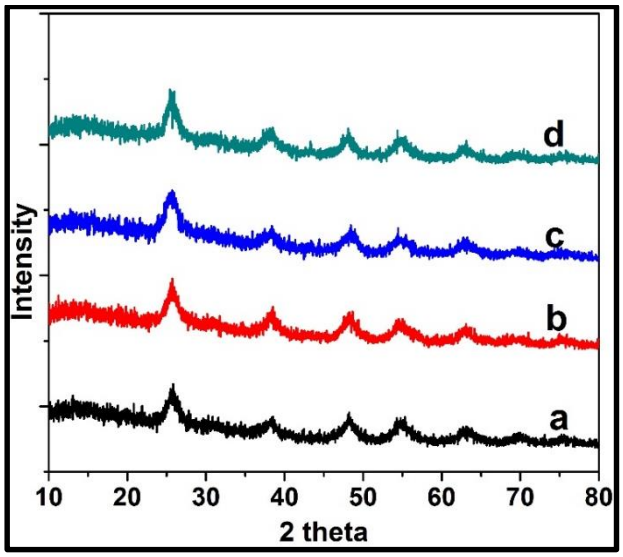

Figure 4.3. XRD patterns of (a) N-TiO_2; (b) TMS0.7; (c): TMS1.5and (d): TMS2.2.

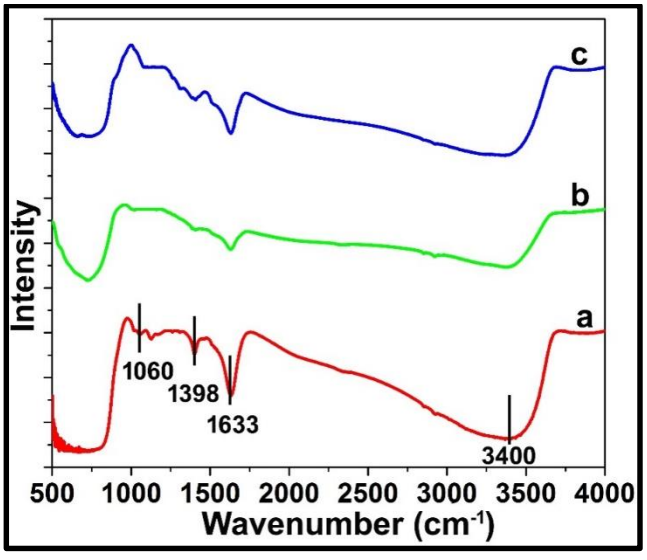

Figure 4.4. FTIR spectra of (a) N-TiO_2; (b) aN-TiO_2 and (c): TMS0.7

The Raman spectral features of N-TiO_2 and TMS0.7 are shown in Figure 4.5. Anatase phase of TiO_2 has six active Raman modes at 144 (E_g), 197 (E_g), 399 (B_{1g}), 513 (A_{1g}), 519 (B_{1g}) and 639 (E_g) cm^{-1} (Kamisaka, Adachi, & Yamashita, 2005; G. Yang et al., 2010). Commercial P25 has E_g peak at 146 cm^{-1}. The slight blue shift in E_g of N-TiO_2 and TMS0.7 may be possibly ascribed to the surface pressure and phonon confinement effect due to the ultra-small size of TiO_2 (Ong, Tan, Chai, Yong, & Mohamed, 2014). The peaks in the range of 250 to 350 cm^{-1} might have arose from the first-order traverse acoustic mode of Ti-N bond (Du, Xie, Xia, Wang, & Tian, 2014) in N-TiO_2. Thus the Raman spectra, confirmed the anatase nature of N-TiO_2 and suggest the N-doping in TiO_2.

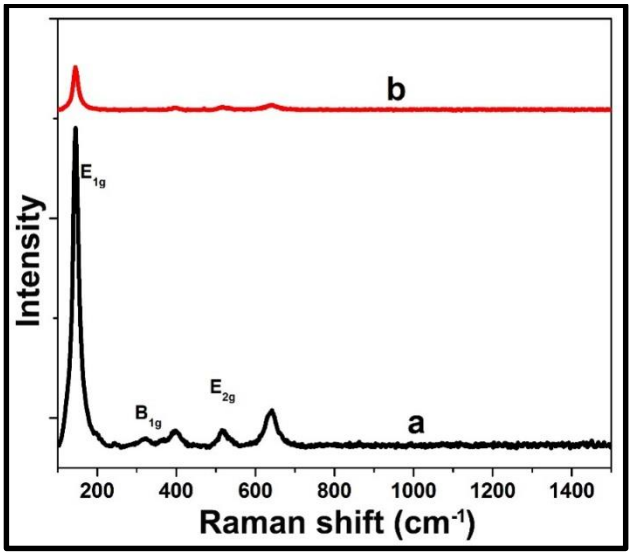

Figure 4.5. Raman spectra of (a): N-TiO_2 and (b): TMS0.7

The HRTEM images of N-TiO_2 and aN-TiO_2 are given in Figure 4.6. The lattice spacing values of 0.34 nm in the images (Figure 4.6B) confirmed the anatase form of TiO_2. The size of the particles were in the range of 4-8 nm for N-TiO_2 while it was 12-15 nm for aN-TiO_2 (Figure 4.6C). The increase in the crystalline size was explained by annealing. The HRTEM images (Figure 4.7 A&B) portrayed a homogenous structure for the composite with TiO_2 particle sizes ranging from 4-8 nm which agrees crystallite size calculated from XRD. The further magnified image

(Figure 4.7C) clearly showed that the MoS_2 were of less than 5 layer thickness. The TEM images suggested that the MoS_2 layers were uniformly distributed in the composite. The lattice spacing of the layered structure was 0.62 nm corresponding to the (002) planes of hexagonally packed MoS_2 layers. The presence of MoS_2 was further confirmed by the EDAX spectrum (Figure 4.7D) which has the peaks of Ti, O, Mo and S in the composite. Thus, the characterization results confirm the formation of TMS.

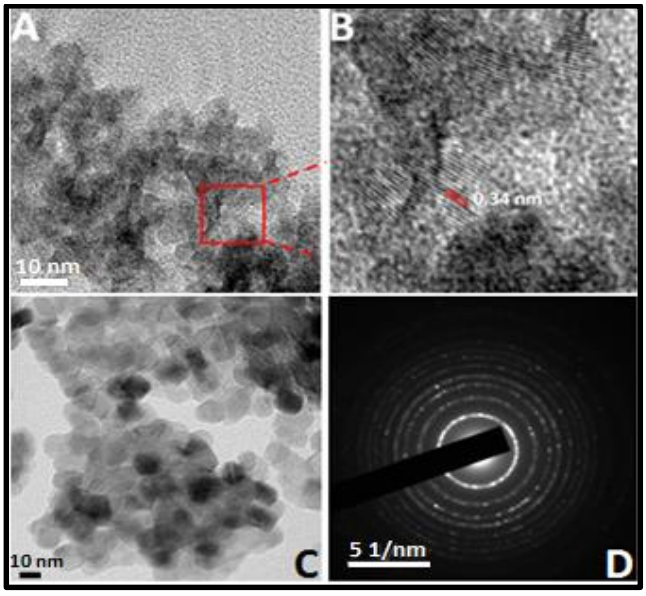

Figure 4.6. (A& B): HRTEM image of N-TiO_2 composed of ultra-fine nanoparticles and the magnified image of the portion in square box, respectively; (C & D): HRTEM image and SAED pattern of aN-TiO_2 respectively, the TEM image clearly showed the increased particle size in aN-TiO_2 and SAED pattern shows the anatase nature of aN-TiO_2. The 0.34 nm shown in the figure spacing corresponds to (101) facet of anatase TiO_2.

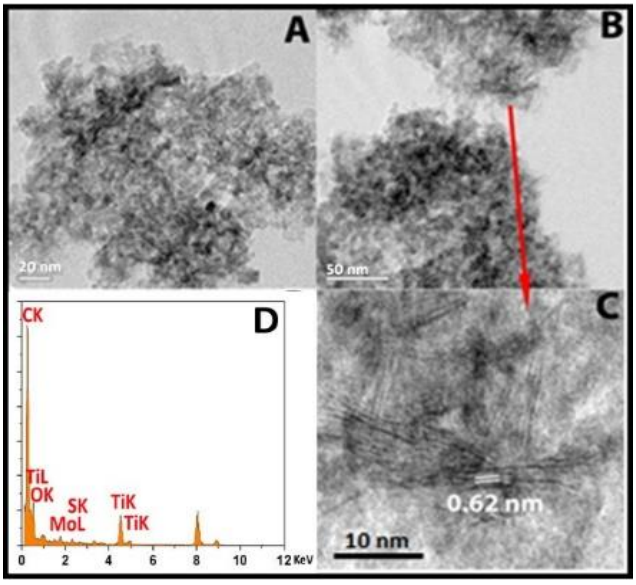

Figure 4.7. (A, B & C): HRTEM images of TMS0.7 of different magnifications and (D): EDAX spectrum of TMS0.7 showing the presence of Ti, O, Mo, S and C)

Additional HRTEM images are given in Figure 4.8, and evidently showed that the MoS_2 was more or less of 2-5 layer thickness, and were significant because the 2-5 layered structure of MoS_2 has the right energy levels to form heterostructure and thus can act as a sensitizer to TiO_2 and has VL absorption capability due to its direct band gap nature. Thus, the synthetic procedure which utilizes only organic solvents and the new precursor, $((NH_4)_2\ Mo_3S_{13}.2H_2O)$ with good solubility in the solvents creates a crystalline homogeneous and high SA TiO_2-MoS_2 composite.

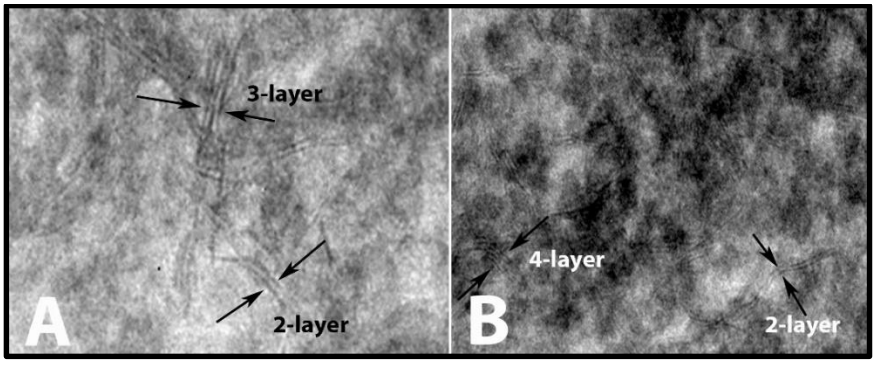

Figure 4.8. HRTEM images of TMS0.7 at higher magnifications showing MoS_2 layers.

Figure 4.9 shows the XPS data of N-TiO_2 and aN-TiO_2. Wide spectrum clearly shows the presence of Ti, O, N and C elements in N-TiO_2 and aN-TiO_2. N-

doping was evidenced by the presence of N1s binding energy levels (398-406 eV). The reduced intensity of N1s peak in the wide scan of aN-TiO_2 was due to the partial removal of surface adsorbed NO_3^- molecules. Apart from surface adsorbed N-groups, interstitial and substitutional doped N can be identified from deconvoluted spectra of XPS. Deconvolution of N1s spectra of N-TiO_2 (Figure 4.9) showed three peaks at 399.6, 400.3 and 404 eV while that of the aN-TiO_2 shows two peaks at 399 and 400.3 eV. The absence of peak at 404 eV in aN-TiO_2 was complementing the results obtained from the FTIR. The quantification of weight % of N-doping was reduced from 0.94% in N-TiO_2 to 0.52% in aN-TiO_2. At the same time N-doping weight% in N-TiO_2 (140-20), N-TiO_2 (200-20) and N-TiO_2 (180-30) are 0.64, 0.98 and 0.97% respectively. Incorporation of N can lead to an increase in the electron density on Ti atom due to the comparatively lower electronegativity of N to that of O_2, thus influencing the binding energies of nearby Ti and O atoms. Asymmetrical nature of the O1s peaks of N-TiO_2 and aN-TiO_2 as compared to that of the P25 (Figure 4.10) suggested the influence of N atom in the O1s environment other than the Ti atom (Cong, Zhang, Chen, & Anpo, 2007; Joung, Amemiya, Murabayashi, & Itoh, 2006). As expected, the binding energies of Ti2p has been shifted to 458.9 ($Ti2p_{3/2}$) and 464.6 eV ($Ti2p_{1/2}$) as compared to that of the Ti2p peaks [459.5 ($Ti2p_{3/2}$) and 465.2 eV ($Ti2p_{1/2}$)] of P25 (Figure4.10) (Junwei et al., 2007).

Reduced binding energies of Ti2p peaks of N-TiO_2 as compared to P25 (Figure 4.10) indicated the N incorporation and assist the formation of Ti^{3+} defect states. Moreover the peak at 462.7 eV corresponds to the $Ti2p_{1/2}$ peak of Ti^{3+} defect state in N-TiO_2 (M. M. Khan et al., 2014) while that peak was diminished in aN-TiO_2. This can be due to lower detection limit of XPS since the extent of N functional groups has been reduced during annealing. The presence of Ti^{3+} defect states in aN-TiO_2 can still be identified from the asymmetrical Ti2p peaks.

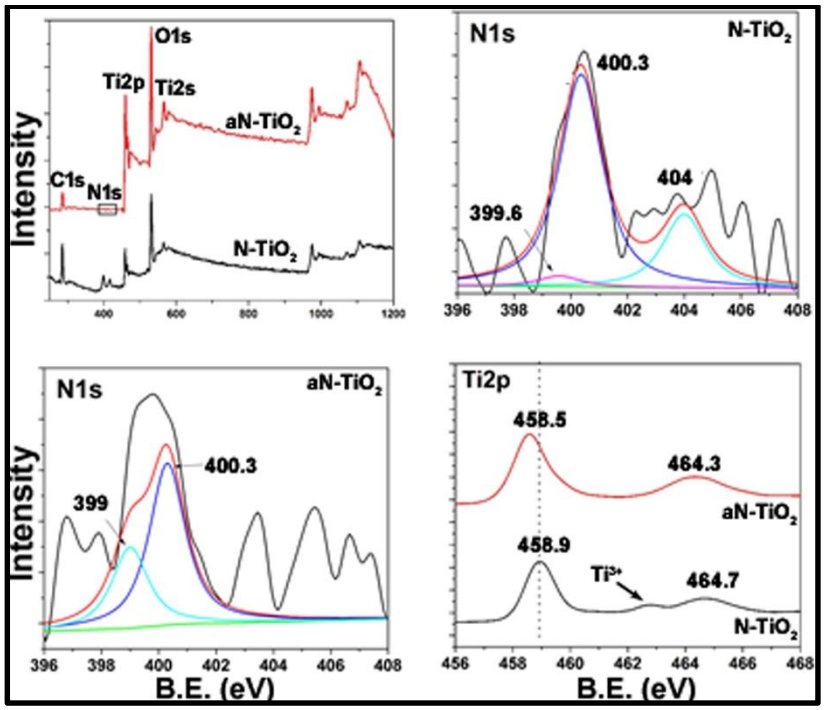

Figure 4.9. XPS data of N-TiO_2 and aN-TiO_2 corresponding to wide, deconvoluted N1s peaks and Ti2p peaks. The reduced intensity of N1s peak in aN-TiO_2 suggest the partial removal of N-doping.

It was well reported (Ryoji Asahi et al., 2014; Di Valentin et al., 2007; Livraghi et al., 2006) that N doping can induce the formation of Ti^{3+} defect states and V_o below the conduction band of TiO_2. Livraghi et al (Livraghi et al., 2006) reported the enhancement in the VL absorbance of N-doped TiO_2 due to the formation of Ti^{3+} defect states and V_o. Nitrogen doping (Kaewgun et al., 2008; Rumaiz et al., 2009) can induce the formation of V_o and therefore Ti^{3+} defect states both are known to improve the conductivity as well as the reducing the band gap.

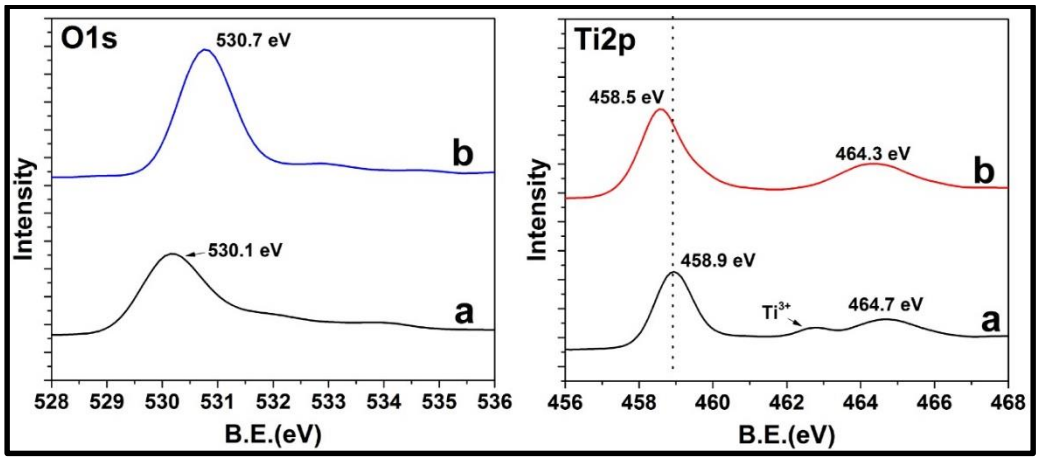

Figure 4.10. XPS data of N-TiO_2 and aN-TiO_2 corresponding to the O1s and Ti2p peaks, respectively.

The N-doping of TiO_2 was further supported by zeta potential (ZP) measurement. Table 4.1 shows the ZP and particle size values. The increase in the hydrodynamic volume of aN-TiO_2 (1704 nm) as compared to that of N-TiO_2 (803 nm) was attributed to the annealing process which increases the particle size. The ZP values of the samples showed that the ZP for N-TiO_2 (-12.9 mV) has the highest negative value compared to that of aN-TiO_2 (0.7 mV) and P25 (14 mV) which agrees with previous reports that have shown negative ZP values on N-doping. The comparatively more negative ZP of N-doped TiO_2 is attributed to the acidic properties of N-doped surface hydroxyls and due to the lower electronegativity of N compared to that of O in N-TiO_2 (Miyauchi, Ikezawa, Tobimatsu, Irie, & Hashimoto, 2004). The relatively lower ZP of aN-TiO_2 was attributed to the lesser surface groups due to the increased particle size and to the removal of surface adsorbed N-groups during annealing. Thus, the characterization techniques confirmed the doping of N in TiO_2 in a single step method using NMP solvent.

Table 4.1. ZP values and particle size of P25, N-TiO_2 and aN-TiO_2 photocatalysts.

Photocatalysts	ZP values (mV)	Particle size (nm)
N-TiO_2	-12.9	803
aN-TiO_2	0.7	1704
P25	14	1876

The XPS survey spectrum of TMS composite was given in Figure 4.11. The presence of Ti2p, Mo3d, S2p and O1s peaks suggested the formation of TMS heterostrucuture. The interaction between TiO_2 and MoS_2 is confirmed from XPS analysis. The deconvolution spectra of Ti2p show two peaks at 459 and 464.5 eV and were attributed to the Ti^{4+} oxidation state of TiO_2. The characteristic peaks of Mo were observed at 233.2 and 229.4 eV, which are ascribed to the binding energy of $Mo3d_{3/2}$ and $Mo3d_{5/2}$ orbitals with +4 oxidation state (C. M, 2012) respectively. Moreover this was further assigned to 2H-MoS_2 (Bai, Wang, Chen, Du, & Xiong, 2014; C. M, 2012). 2H type MoS_2 is semiconducting in nature as compared to 1T type MoS_2. MoS_2 formed from the molybdenum-sulphur cluster precursors are 2H-MoS_2 and semiporous in nature (Finckh, Lu, Leist, Stauf, & Lo, 1998). Absence of peaks around 236 eV suggested the absence of the oxidation product of MoS_2. The characteristic S2p peaks were observed in a broad range around 168 eV. The deconvolution of S2p peaks gave rise to 164.3, 167.9 and 171.6 eV. The lower energy peak (164.3 eV) corresponded to S2p of MoS_2. The presence of MoS_2 was further confirmed by the elemental mapping distribution by EDAX mapping of SEM image (Figure 4.12) which showed the presence of Mo, S, Ti and O. The uniform distribution of MoS_2 can be confirmed from the EDAX spectra. The N-TiO_2 showed N-doping (Mukthar Ali & Sandhya, 2016c) due to the solvents IPA and NMP, respectively, whereas N-doping was absent in TMS indicating that the MoS_2 precursor interferes with the N-doping of TiO_2 in the composite.

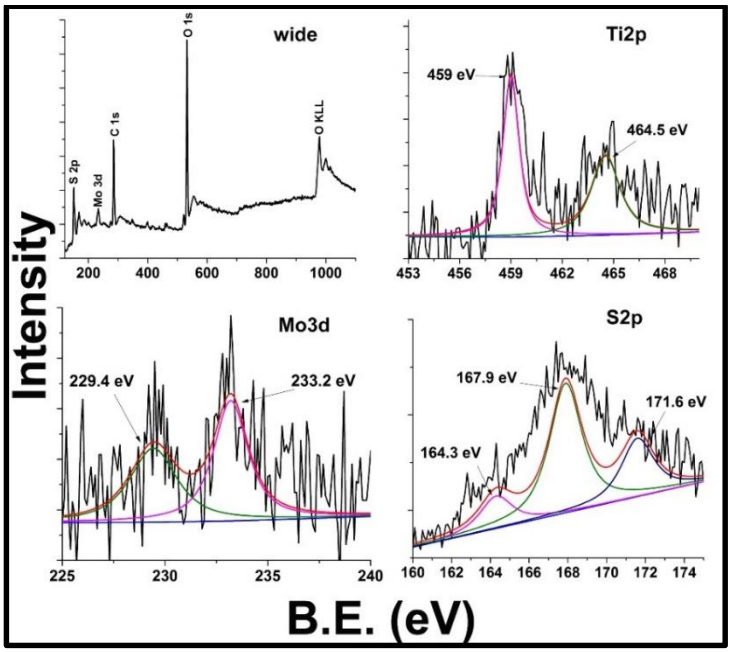

Fig. 4.11. XPS analysis of TMS0.7 (L to R) Survey spectrum and the deconvolution peaks of Ti2p, Mo3d and S2p peaks.

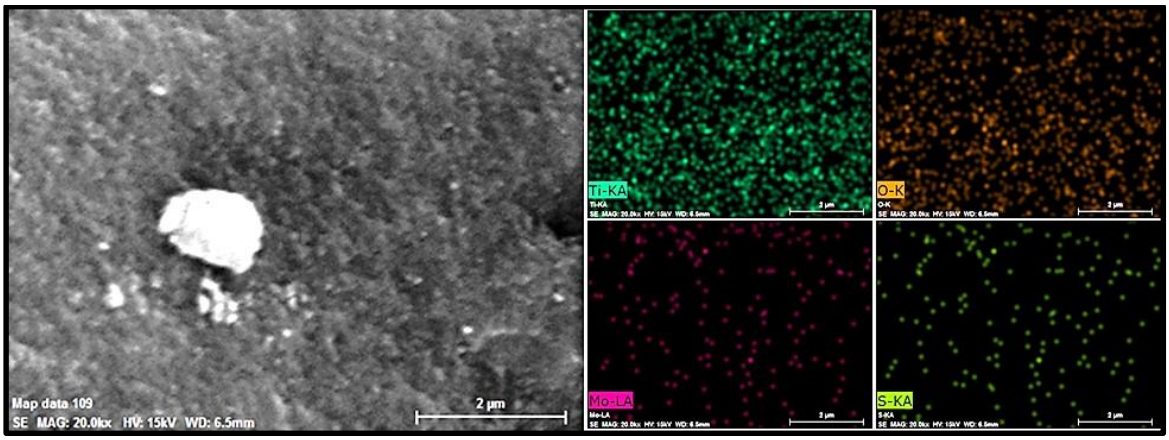

Figure 4.12. EDAX elemental mapping of the composite TMS0.7 shows the presence of Ti, O, S and Mo.

DRS spectra and Tauc Plots of P25, N-TiO_2, aN-TiO_2 and TMS0.7 (Figure 4.13) evidently showed the improved VL absorption of N-TiO_2, aN-TiO_2 and TMS0.7. Furthermore, it is clear that the TMS0.7 showed improved VL absorption than that of N-TiO_2 and aN-TiO_2 which was attributed to the presence of few layered MoS_2. The band gaps (Figure 4.13A) of N-TiO_2 and aN-TiO_2 were 3.15 and 3.1eV, respectively which were lower compared to that of the P25 (~3.3 eV). The

band gap reduction in N-TiO_2 and aN-TiO_2 were attributed to the introduction of intra-band states in the band gap of TiO_2. Annealing process bring changes in terms of N-doping, such as removal of surface adsorbed NO_3^- groups and then, partial conversion of interstitial N doping into substitutional N doping as supported by FTIR and XPS analyses. Both interstitial N and substitutional N, can cause the reduction in band gap (Di Valentin et al., 2007). The improvement in the VL absorptivity observed for aN-TiO_2 as compared to that of N-TiO_2, was attributed to the formation of additional Ti^{3+} defects and V_o during annealing procedure and was supported by XPS and previous reports (Di Valentin et al., 2007; Livraghi et al., 2006).

The N_2 adsorption-desorption isotherm and the BET SA values of P25, N-TiO_2, aN-TiO_2 and TMS composites are given in Figure 4.14 and Table 4.2, respectively. The higher SA of N-TiO_2 (4 times that of the P25) was attributed to the preparation method which utilizes organic solvent alone, resulting in ultra-fine sized particles (~5 nm) of TiO_2. The SA of aN-TiO_2 is slightly lower, (still the SA is 1.6 times higher than that of the P25) and can be assigned to the annealing process which increases the particle size. The SA of TMS composites were even higher than that of N-TiO_2. The SA increased even with very low amount (0.7%) of MoS_2 loading and reached a maximum value at 1.5% and then decreased. The decrease at higher level of MoS_2 was ascribed to the aggregation of MoS_2 layers.

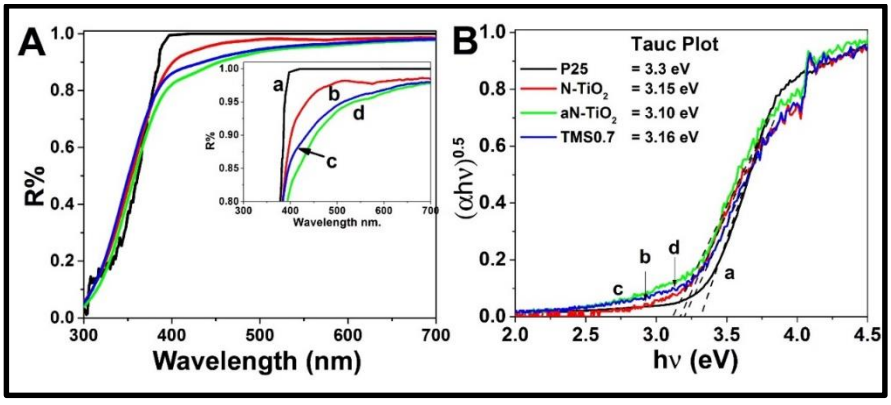

Figure 4.13. (A) DRS spectra and (B) Tauc plots of (a): P25; (b): N-TiO_2; (c): aN-TiO_2 and (d): TMS0.7.

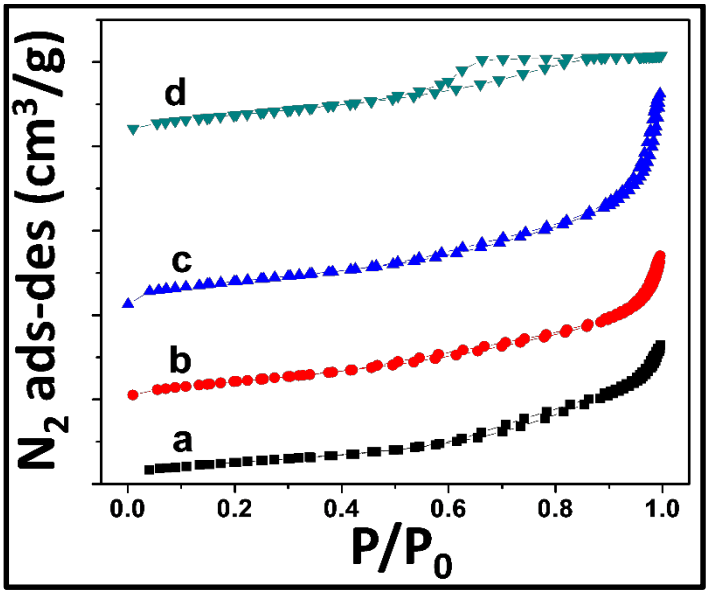

Figure 4.14. N_2 adsorption-desorption isotherms of (a): N-TiO_2; (b): TMS0.7; (c): TMS1.5 and (d): TMS2.2 at 77K using liquid N_2.

Table 4.2. BET SA of P25, N-TiO_2, aN-TiO_2 and TMS photocatalysts

Photocatalysts	BET SA (m^2/g)
N-TiO_2	191
aN-TiO_2	78
TMS0.7	274
TMS1.5	290
TMS2.2	261
P25	49

4.3.2. Photodegradation studies of N-TiO_2 and TMS

The VL PC properties VL of N-TiO_2, aN-TiO_2 and TMS composites, were analyzed using the VL PD of RhB. The result of the VL PD of RhB of N-TiO_2 prepared at different conditions were given in Figure 4.15 and shows that N-TiO_2

formed at 180°C and 20 hr showed comparatively better PD. All the N-TiO_2 prepared at > 140°C ha similar amount of N-doping as supported by XPS analysis. Therefore, we chose N-TiO_2 prepared at 180°C and 20 hr for further studies.

The result of the VL PDs of RhB in the presence of N-TiO_2, aN-TiO_2 and P25 provided in Figure 4.16. The aN-TiO_2 showed greatly improved performance as compared to N-TiO_2 and P25. The order of PD activity was as follows aN-TiO_2 > N-TiO_2 > P25 and their PD% are 80, 72 and 50%, respectively. The higher VL PC activity of N-TiO_2 and aN-TiO_2 compared to that of P25 was assigned to their better VL absorption and higher activity of aN-TiO_2 to that of N-TiO_2 was assigned to the improved VL absorption (Figure 4.13) due to the additional defects (Strunk, Vining, & Bell, 2010) formed during annealing.

In order to further ascertain the VL activity of the photocatalysts, we conducted the PD reactions under UV light and the results (Figure 4.16) showed that the order of activity of the photocatalysts has been changed from that of the VL: the order being P25 > aN-TiO_2 ≥ N-TiO_2 with 84, 65 and 57% PD, respectively. The reversal in the activities under UV light confirmed that the improved activity of aN-TiO_2 and N-TiO_2 in the VL was due to their improved VL absorption. The relatively higher activity of P25 under UV light was assigned to its better charge separation due to the rutile and anatase phase interface alignment (Scanlon et al., 2013).

The VL PD of RhB can be expected to follow mainly any of the two pathways: decolouration pathway of RhB i.e. leading primarily via the de-ethylation pathway or the mineralization pathway. It can be seen from Figure 4.17, that VL PD of RhB in the presence of aN-TiO_2 follows mainly the decolouration pathway. This was explained as follows: under VL PD, the electrons are excited from the N2p intra-band states to the CB of TiO_2. The N2p intra-band state has lower oxidation potential (E° = 2.00 eV) (Mrowetz et al., 2004) as compared to the VB of TiO_2 (E° = 2.8 eV). Since it has lower oxidation potential (E° = 2.00 eV), the holes cannot oxidize the water to form •OH intermediates. Hence the dominant $O_2^{\bullet-}$ ROS lead to the decolouration pathway.

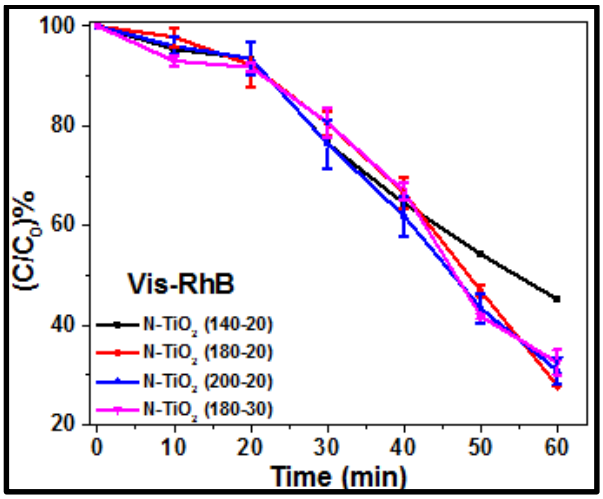

Figure 4.15. Effect of various N-TiO_2 on the VL PD of RhB.

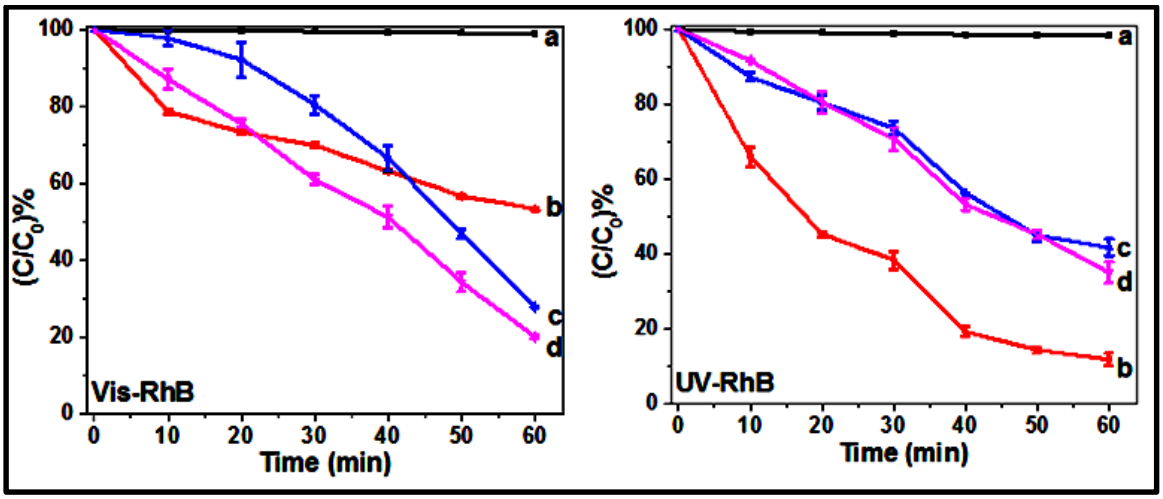

Figure 4.16. Visible and UV light PD of RhB a by (a): no catalyst; (b): P25; (c): N-TiO_2 and (d): aN-TiO_2

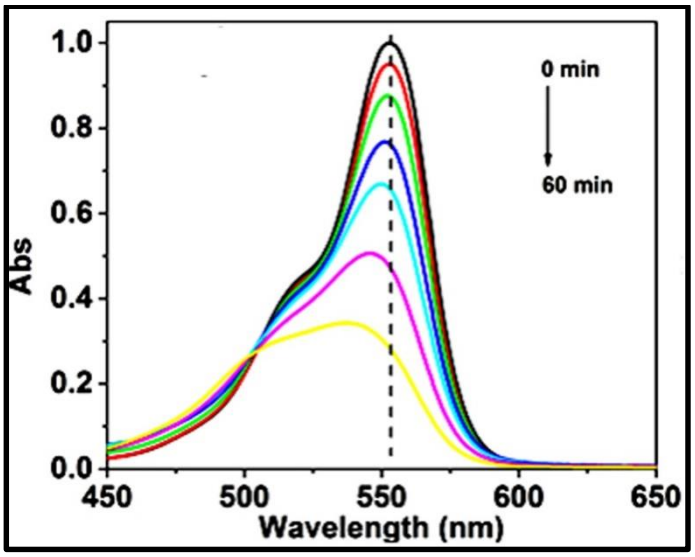

Figure 4.17. Absorption spectra of RhB during VL PD monitoring by N-TiO_2.

Further, the VL PD of RhB by the TMS composites with different wt% of MoS_2 and controls were compared in Figure 4.18. The PD activities were in the following order: TMS0.7 > TMS1.5 > TMS0.24 > N-TiO_2 > P25. In the presence of TMS0.7, 95% of RhB was degraded at 60 minutes whereas for N-TiO_2, it was 73%. The PD activity increased from 0 to 0.7% of the loading of MoS_2 and then decreased. The higher PD of the TiO_2-MoS_2 was ascribed to its improved VL response (Figure 4.13). The decrease in the PC activity above 0.7 % of MoS_2 suggested that the optimum amount of MoS_2 for PC activity based on its structure was 0.7%. The TEM images show that the MoS_2 sheets were single or few layered at this lower loading percentage and an increase in MoS_2 loading lead to stacked MoS_2 layer. Hence the reduced PC activity. The rate constant for the VL PD of RhB for P25, N-TiO_2, aN-TiO_2 and TMS photo catalysts are given in Table 4.3.

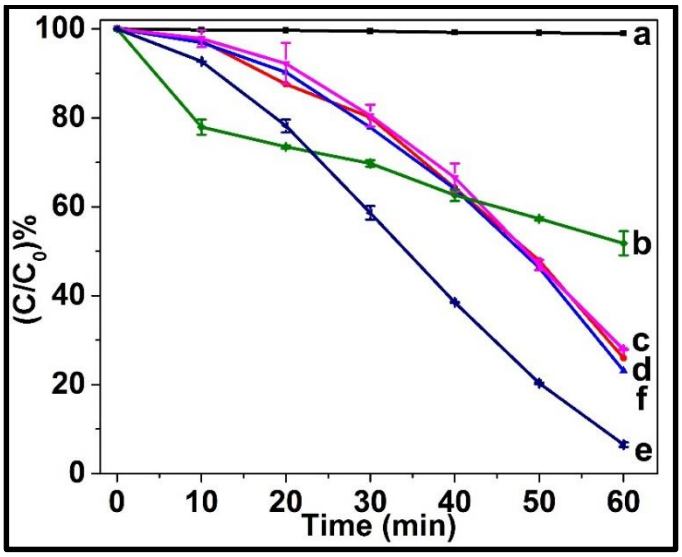

Figure 4.18. Plots of VL PD of RhB in the presence of (a): No catalyst; (b): P25; (c): N-TiO_2; (d): TMS0.24; (e): TMS0.7 and (f): TMS1.5.

Table 4.3. Rate constant values in the VL PD of RhB for N-TiO_2, aN-TiO_2 and TMS based photocatalysts.

Photocatalysts	Rate constant (min^{-1})
N-TiO_2	0.015
aN-TiO_2	0.022
TMS0.24	0.016
TMS0.7	0.035
TMS1.5	0.017
P25	0.011

Since the SA of both N-TiO_2 as well as TMS composites were high (191 and 274 cm^2 g^{-1} respectively), the interference of adsorption during the PD can be expected. To verify this, adsorption of RhB in dark for 2 hrs was done and the results were given in Figure 4.19. Adsorption has reached the equilibrium within

first one hour and no adsorption was observed after 20 minutes. Contribution of adsorption (Table 4.4) was found to be ~5% for both N-TiO_2 and aN-TiO_2 while for TMS0.7 it was ~ 22%.

Table 4.4. Adsorption % of RhB during the with P25, N-TiO_2 and TMS composites.

Photocatalysts	Adsorption %
N-TiO_2	5
aN-TiO_2	4.5
TMS0.7	22
TMS1.5	22
TMS2.2	18
P25	5.5

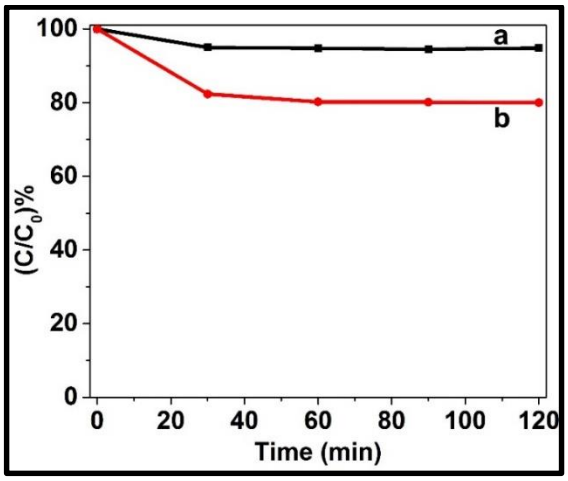

Figure 4.19. Equilibrium adsorption of RhB with N-TiO_2 and TMS0.7 composites up to 2 hr.

Electrochemical kinetics can be used to explain the charge transfer resistance across the interfaces. Nyquist plots of EIS analysis offer the idea of charge transfer resistance. Lower the charge transfer resistance smaller will be the radius of semicircle in the plot. Nyquist plots (Figure 4.20) showed that the

semicircle radius was smaller for TMS0.7 than that of both N-TiO_2 and P25 which suggested that MoS_2 nanosheets facilitates the electron transfer across the interface. Similarly, a smaller semicircle for N-TiO_2 than P25 indicated the reduced charge transfer resistance in N-TiO_2 and was attributed to the defect states introduced by N-doping.

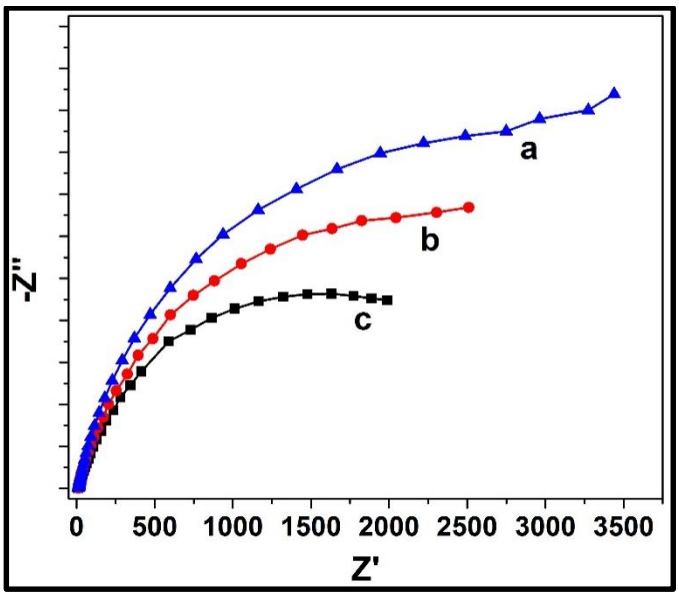

Figure 4.20. Nyquist Plots of (a): P25; (b) N-TiO_2 and (c): TMS0.7

4.3.3. Recycling studies of aN-TiO_2

To prove the photostability of aN-TiO_2, recycling studies were conducted. Recycling studies using RhB (Figure 4.21) shows that there was an initial decrease from (100 to 76%) in the PD and after that the decrease in PD efficiency observed was minimal (~1-2 %). The PD after 6 cycles was 68%. The initial decrease was attributed to the blocking of surface active sites by products/reactants which reduced the number of active sites.

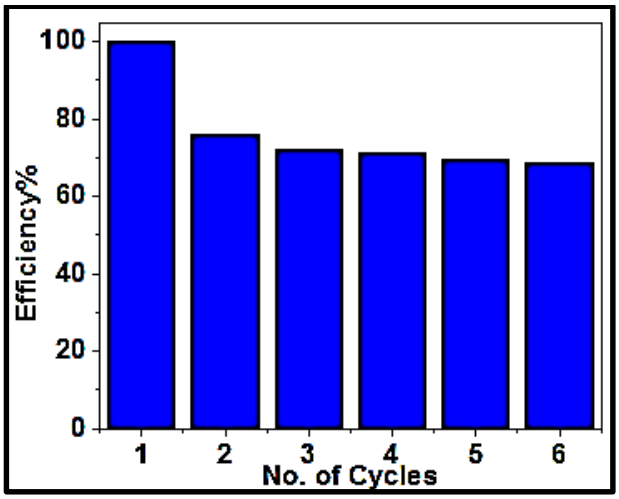

Figure 4.21. Recycling studies of aN-TiO_2 in the PD of RhB.

4.3.4. Estimation of ROS in the photodegradation of RhB by aN-TiO_2

The result of scavenging studies for the PD of RhB in the presence of aN-TiO_2 was given in Figure 4.22. The actual PD% at 60 min with no scavenger was 73% which was considered 100% for calculation purpose. Therefore, PD% at 60 min with t-BuOH, NaN_3 and BQ were 100, 23 and 79%, respectively, with respect to the 'no scavenger' experiment. The result indicated that the contribution from •OH is nil, while with NaN_3 and BQ, decrease in PD was observed, accounting to 77 and 21% contribution from $^1O_2$ and $O_2^{\bullet-}$, respectively. Based on the results, an illustrative mechanism was proposed (Figure 4.22) which demonstrates the formation of ROS based on the energy levels of the aN-TiO_2. When the aN-TiO_2 composite was excited with VL, the electrons were excited from the intra-band states of N-doped states. In addition to this, RhB can sensitize TiO_2. The hole produced in the intra-band states has lower oxidation potential (Ryoji Asahi et al., 2014; Mrowetz et al., 2004) (E° = 2.06 eV) and hence cannot oxidize the water to •OH ($E^\circ_{H2O/\bullet OH}$= 2.33 V), which explains the absence of •OH. In the meantime, the photogenerated electrons reduces the O_2 molecules to form $O_2^{\bullet-}$ which can lead to the reductive degradation of RhB or these $O_2^{\bullet-}$ further react with the holes ($E^\circ_{O2^{\bullet-}/1O2}$= 0.65 V) generated at the N2p levels to form $^1O_2$ as they are highly

reactive. The formed $^1O_2$, which is highly unstable oxidizes RhB, which explains the higher contribution of $^1O_2$ in the PD.

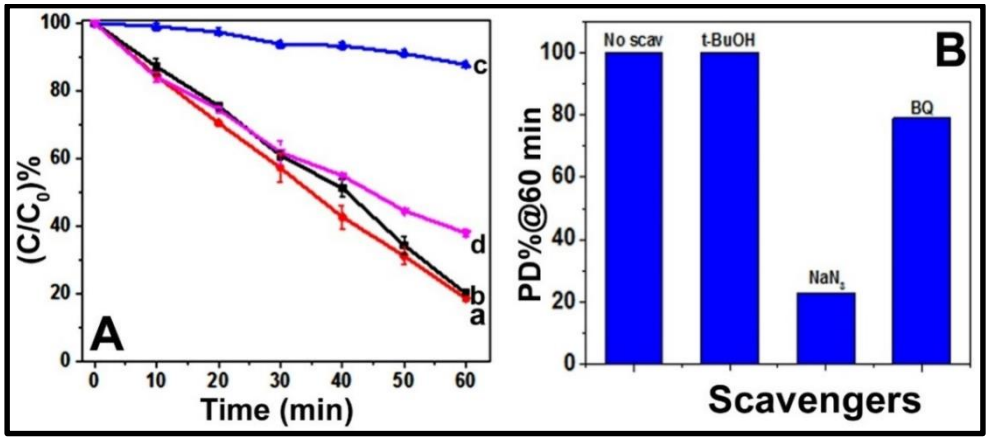

Figure 4.22. (A) VL PD of RhB by aN-TiO_2 in the presence of (a): no scavengers; (b): t-BuOH; (c): NaN_3 and (d): BQ. (B): Bar graph representation for the PD% @ 60 min in the presence of scavengers (PD% is normalized to 100% for no scavenger studies).

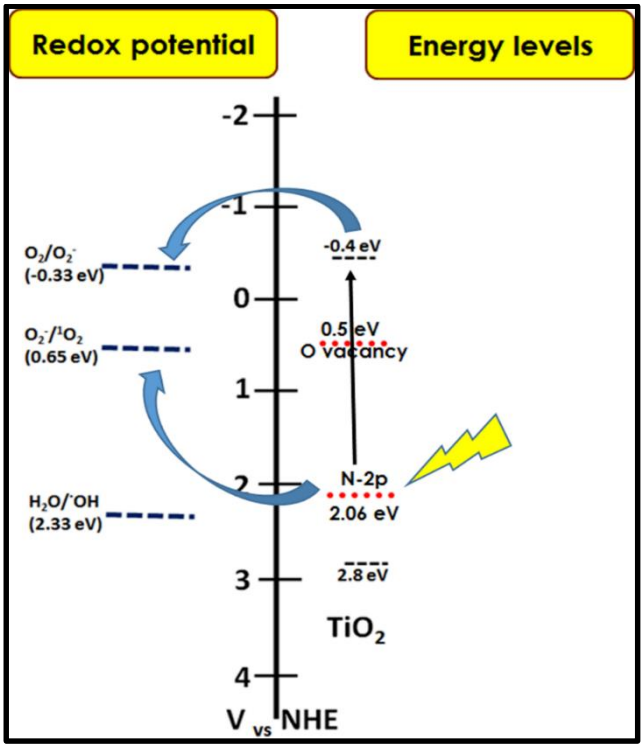

Figure 4.23. Schematics of the possible electronic transitions and the mechanism of ROS formation by aN-TiO_2 during the PD of RhB.

4.3.5. Estimation of ROS in the photodegradation of RhB by TMS

The result of scavenging studies in the presence of TMS0.7 is given in Figure 4.24. The actual PD% at 60 min with no scavenger was 94% which was considered 100% for calculation purpose. According to that PD% at 60 min with t-BuOH, NaN_3 and BQ are 100, 71 and 66% respectively. The non-suppression of PD by t-BuOH suggests nil contribution from •OH, while with NaN_3 and BQ there is ~29 and 34% suppression, corresponding to the contributions of $^1O_2$ and $O_2^{\bullet-}$, respectively. Based on the results and structure of TMS, the following mechanism was proposed (Figure 4.24). When the composite was irradiated with VL, the single/ few layered MoS_2 absorbs light and electrons get excited from its VB to CB. In addition to this transition, RhB can also sensitize TiO_2 in the composite. The CB energy level of single/few-layered MoS_2 is located above the CB of TiO_2 while in case of MoS_2 with higher number of layers, the CB level is located lower than the CB level of TiO_2. The excited electrons on the TiO_2 or MoS_2 surface on reaction with surface adsorbed O_2 yields $O_2^{\bullet-}$ (Mukthar Ali & Sandhya, 2014). Similarly, holes formed in VB of MoS_2 can either directly react with the dye and oxidize it or can oxidize the $O_2^{\bullet-}$ to $^1O_2$ ($E°_{O2\bullet-/1O2} = 0.65$ V) thus leading to the formation $^1O_2$. The VB of MoS_2 was lower (1.39 eV vs NHE) and hence cannot directly oxidize the water to $^{\bullet}OH$ since the redox potential required for the reaction $H_2O/^{\bullet}OH$ is 2.33 eV. Thus the formation of $O_2^{\bullet-}$ and $^1O_2$ and absence of $^{\bullet}OH$ during the PD process was justified.

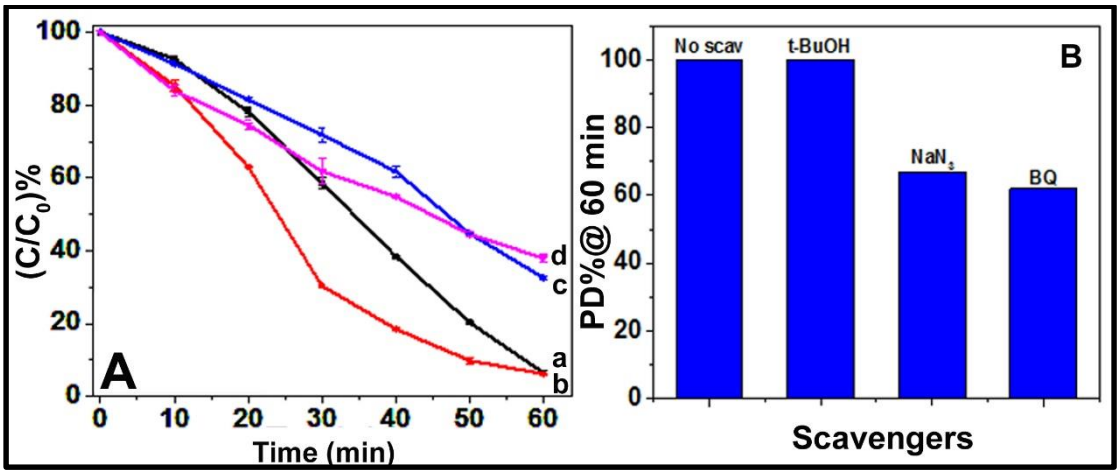

Figure 4.24. (A) VL PD of RhB by TMS0.7 in the presence of (a): no scavengers; (b): t-BuOH; (c): NaN_3 and (d): BQ. (B): Bar graph representation for the PD% @ 60 min in the presence of scavengers (PD% is normalized to 100% for no scavenger studies).

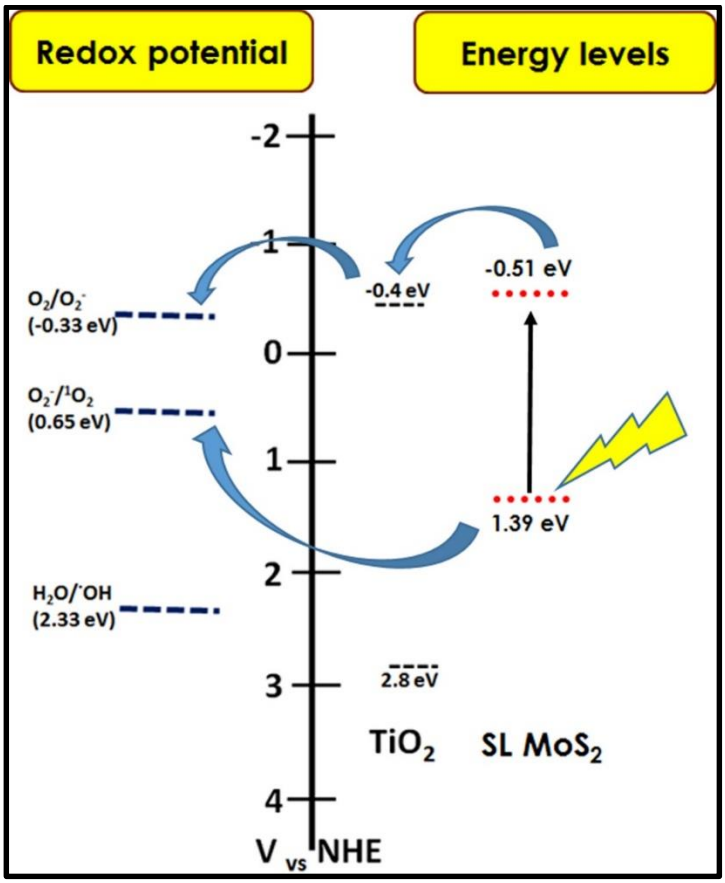

Figure 4.25. Schematics of the proposed mechanism for the ROS formation in the VL PD of RhB in the presence of TMS0.7.

4.4. Conclusions

N-doping of TiO_2 was achieved by a one-step solvothermal synthesis using NMP solvent as dopant. TMS composites were prepared in one step using a novel molybdenum-sulphur cluster compound [$(NH_4)_2$ $Mo_3S_{13}.2H_2O$]. In the case of TMS, N-doping was absent or negligible and lead to a C-doped composite TiO_2 and few layered MoS_2 distributed more or less uniformly in the composite and with a very high SA due to the nano dimensions of TiO_2 and MoS_2. Both N-TiO_2 and aN-TiO_2 were crystalline, composed of ultra-fine particle size ranging from 4-8 nm with high SA and showed improved VL absorption and slightly reduced band gap due to the intra-band states of N-doping with aN-TiO_2 being better in VL responsiveness and was assigned to the increased formation of V_o and Ti^{3+} states during annealing. Enhanced VL PC activity is exhibited by N-TiO_2 and aN-TiO_2 to that of P25. aN-TiO_2 exhibited stability as suggested by the recycling studies. Improved VL absorbance and reduced charge transfer resistance were contributed to the enhanced PC activity of both N-TiO_2 and aN-TiO_2. Lower interfacial charge resistance across the interface of the TMS composite is attributed to the built-in potential formed across MoS_2 and TiO_2 semiconductors. The dominant ROS species in the VL PD of RhB in the presence of both aN-TiO_2 and TMS0.7 are $O_2^{\bullet-}$ and $^1O_2$ and $^{\bullet}OH$ is absent in all the cases.

CHAPTER 5

P25–UNDOPED CARBON DOT COMPOSITE FOR VISIBLE LIGHT PHOTODEGRADATION

This chapter discusses about the preparation and characterization of P25/C-dot composites and their applications. A new method was adopted to synthesize carbon dot (C-dot) and was utilized to make the composite. C-dot exhibited up-conversion PL with a high PLQY (~25 %) and hence was thought to benefit in enhancing the VL PD of the composite. The PC performance of the composite was tested using the VLPD of RhB and MO and the results obtained are discussed. In addition to this, the role of ROS in the PD of RhB has been studied using the scavenger studies and a mechanism was elucidated to explain the formation of ROS.

5.1. Introduction

Carbon dots (C-dot), a new class of carbon nanomaterial, which opens up lots of interests in energy related field due to their unique properties such as high aqueous solubility, chemical inertness, electronic, optical, PL and up-conversion properties (H. Li, Kang, Liu, & Lee, 2012; S. T. Yang et al., 2009; Zhao et al., 2008). Up-conversion property of C-dot has attracted the attention of researchers in PC applications, in combination with rutile TiO_2, as its absorbance matches with the up-converted PL of C-dot (M. Shao & Zhuo, 2012). The PL properties of C-dot depends on their sizes, extent of functionalization, surface passivation and doping which in-turn and thus tailored to some extent by the synthetic methods (H. Li et al., 2012; Youfu Wang & Hu, 2014) and the precursors used. C-dot with higher PL quantum yield (PLQY) are desirable for the applications in bio imaging (Y. P. Sun et al., 2006), PC (J. Q. Pan et al., 2014), light emitting devices (Luk et al., 2012) and photovoltaics (Yan, Cui, Li, & Li, 2010) etc. There have been many methods employed to prepare C-dot such as arc discharge (Xu, Xiaoyou; Ray, Robert; Gu, Yunlong; Ploehn, HarryJ.; Gearheart, Latha; Raker, Kyle; Scrivens, 2004),

chemical and electrochemical oxidation (Yan Li et al., 2011; Xu, Xiaoyou; Ray, Robert; Gu, Yunlong; Ploehn, HarryJ.; Gearheart, Latha; Raker, Kyle; Scrivens, 2004), pyrolysis (Bourlinos, Stassinopoulos, Anglos, Zboril, Georgakilas, et al., 2008) and hydrothermal (D. Pan et al., 2012) methods. Despite those many methods, most of the undoped/ bare C-dot exhibited lower PLQY ≤10% (X. T. Zheng, Ananthanarayanan, Luo, & Chen, 2015).

It was found that smaller the size distribution of C-dot, larger the PLQY (Bourlinos, Stassinopoulos, Anglos, Zboril, Karakassides, et al., 2008). Due to the high carbon content and hydroxyl groups, C-dot prepared from carbohydrates precursors are expected to have higher material yield and PLQY. Bare C-dot from glucose by ultrasonic method was ~5 nm in size and showed a PLQY of 7% (H. Li et al., 2011). Carbonization of sucrose (J. Zhang et al., 2010) using sulphuric acid resulted in two different sized C-dot; one with blue emission with size of ~5 nm and the other with green emission and sizes of 1-2 nm. Similarly, hydrothermal treatment of CD with HCl at 70 °C yielded C-dot of 1.7 to 3.3 nm sizes and PLQY of 9.7, 13.5 and 10.6% for α, β and γ-CD, respectively (M. Hu et al., 2014). Different preparation methods using CD yielded differently sized C-dot and with different PL and PLQY (Bhaisare, Talib, Khan, Pandey, & Wu, 2015; Sahu, Behera, Maiti, & Mohapatra, 2012). Microwave assisted synthesis of C-dot (Bhaisare et al., 2015) from citric acid yields 11 % PLQY while hydrothermal based (Sahu et al., 2012) synthesis yields 25.7 % PLQY. Recently Fang et al. (Fang et al., 2012) reported a simple synthesis for the preparation of C-dot from acetic acid using P_2O_5 method which resulted in 2.3 % of PLQY. By combining this method with a carbon-rich precursor, (which is CD), C-dot with higher PLQY (~25 %) was achieved. There are not many reports on the preparation of undoped C-dot with high PLQY (Jun Wang et al., 2014; F. Zheng, Wang, Chen, & Li, 2014).

In this paper, we report a simple synthesis of undoped C-dot with up-conversion properties and high PLQY from CD. The C-dot exhibited ~25 % PLQY which is one of the highest value reported for undoped C-dot. Due to its up-conversion and high PLQY at ~400 nm (blue), the C-dot was combined with P25 (rutile-anatase phase) by simple physical mixing method to form P25/C-dot composite and the PC properties of this composite showed enhanced VL PD

towards both RhB and MO compared to that of P25. Further, ROS involved in the PD reaction of RhB in the presence of composite were determined using scavenger studies. Higher PLQY (25 %) and up-conversion PL properties of C-dot in combination with extended VL absorption of the composite was attributed to the enhanced PD properties. Scavenger studies reveal the significance of $^{\bullet}OH$, $O_2^{\bullet-}$ and $^1O_2$ in the PD of RhB.

5.2. Experimental

5.2.1. Preparation of undoped C-dot

Solid P_2O_5 (3 g) powder was added to the solid CD (150 mg) and mixed well by stirring. Then distilled water (1 ml) was added slowly until the effervescence was subdued. The change in color from white to black was observed due to the carbonization of CD by the high exothermic heat generated during the reaction between P_2O_5 and water. The mixture was diluted to 10 ml and this solution was filtered using 0.22 µm syringe filter and was used as stock solution.

5.2.2. Preparation of P25/C-dot

To the 10 ml of C-dot stock solution, 300 mg of P25 was added in 25 ml beaker and sonicated for 15 min. After that the suspension was stirred overnight at RT. The suspension was dialyzed in 1000 MWCO membrane to remove the non-adsorbed C-dot. Finally, the precipitate was washed and centrifuged plenty of times with water. The precipitate was dried at 70°C overnight.

5.3. Results and Discussion

5.3.1. Characterization of C-dot and P25/C-dot

The HRTEM images of the prepared C-dot (Figure 5.1) revealed a near uniform sized C-dot (Figure 5.1D) with an average size of 3 to 5 nm. The SAED pattern of C-dot suggested a partial crystalline nature. It was reported from literature that C-dot prepared from CD precursor lead to the formation of uniform and smaller sized C-dot (M. Hu et al., 2014).

Detailed studies on the optical properties of C-dot were carried out (Figure 5.2). the absorption spectra of C-dot showed two peaks at 280 and 365 nm (Figure 5.2A), arising from the π-π* transition and n-π* transition, respectively, corresponding to the oxygen related surface states of –C=O bond (Habiba et al., 2013; D. Pan et al., 2015). The C-dot showed strong blue color PL (Figure 5.2B), and a detailed study of PL emission revealed nearly unchanged emission wavelength (435 nm) for the excitation wavelengths from 340 to 420 nm. Excitation dependent PL of C-dot has been widely reported (Song, Zhu, & Yang, 2014; L. Zhou, He, & Huang, 2013) whereas only a few reports of excitation independent PL by C-dot (J. Zhang et al., 2010) are available. The excitation dependent PL reflects the inhomogeneity in the C-dot size and the surface states of the sample (Esteves da Silva & Goncalves, 2011) and the excitation independent PL of C-dot is an indication of uniform and homogeneity in size and surface states, respectively.

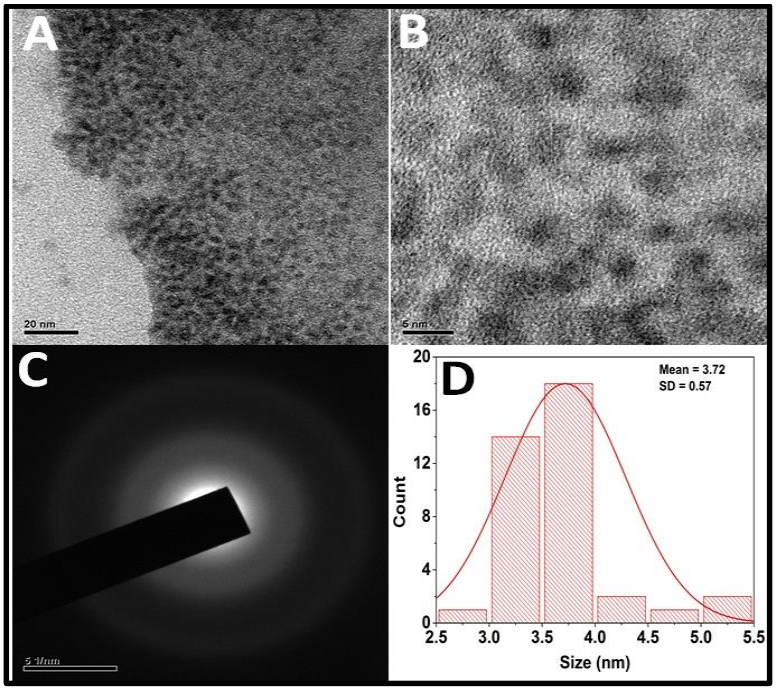

Figure 5.1. HRTEM images (A & B), SAED pattern (C) and size distribution (D) of C-dot.

The PL lifetime of C-dot was determined using time-correlated single photon count at the excitation wavelength of 344 nm (Figure 5.2C). The result shows that the PL lifetime is ~2.77 ns with a bi-exponential decay fitting. The PLQY of C-dot was calculated to be 25% and the obtained PLQY value was one of the highest value reported for the undoped C-dot. C-dot prepared from CD using hydrothermal treatment (M. Hu et al., 2014) reported a PLQY of 13.5 %, which is half the value and C-dot prepared using acetic acid as the precursor using the P_2O_5 method yielded only 2.3 % PLQY, reveals the superiority of the approach, demonstrated here.

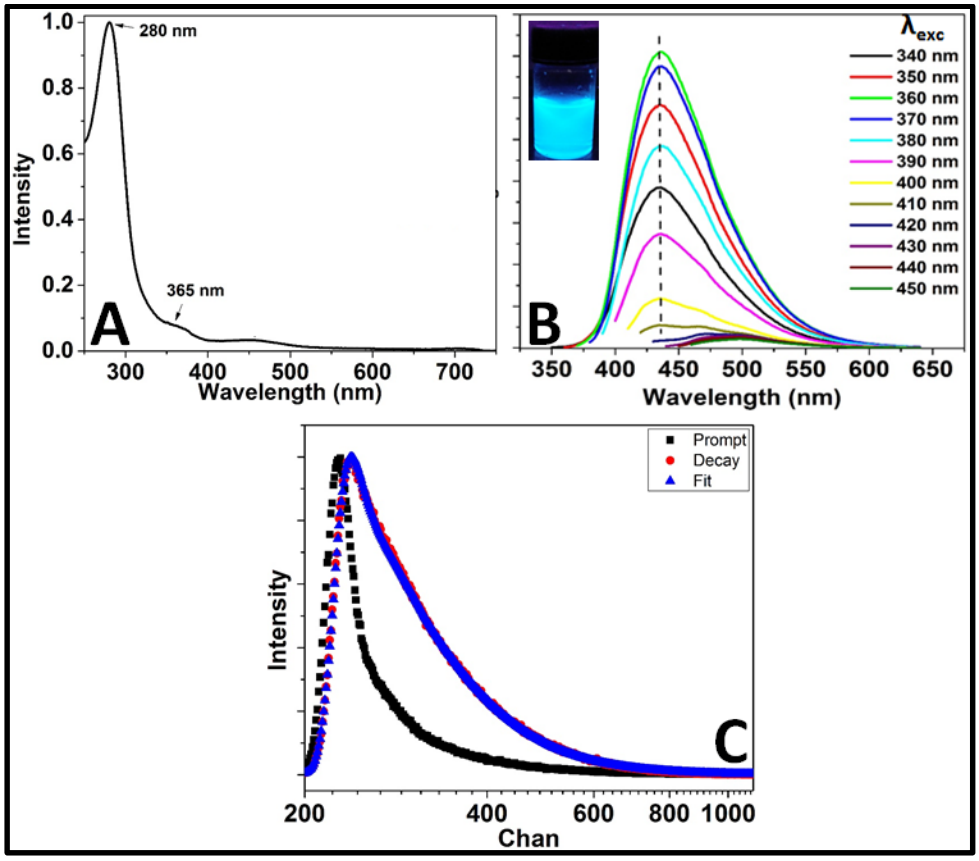

Figure 5.2 (A): UV-Vis absorption spectra; (B): PL with excitation from 340 to 450 nm (inset: photoimage of C-dot under UV irradiation) and (C): PL Lifetime decay of C-dot.

To understand the interaction between C-dot and P25 in the composite, XPS analyses were carried out and the results are given in Figure 5.3. The wide spectra

of P25/C-dot contain the peaks of C, Ti and O, confirming the presence of C-dot. In the deconvolution spectrum of C1s (Figure 5.3), three different environments of C were observed. The peaks at 284.8, 286 and 288.9 eV were assigned to the C1s of -C=C-, -C-O and –C=O bonds, respectively. The absence of Ti–C bond peak indicated that there was no C-doping in the composite and was not expected. The peaks at 529.6, 530.1 and 531.7 eV were ascribed to the O1s deconvolution of Ti-O, C=O and C–OH respectively. The Ti2p deconvoluted peaks at 458.7 and 464.4 eV corresponded to the $Ti2p_{3/2}$ and $Ti2p_{1/2}$ of P25, respectively, which indicates Ti^{4+} oxidation state in P25.

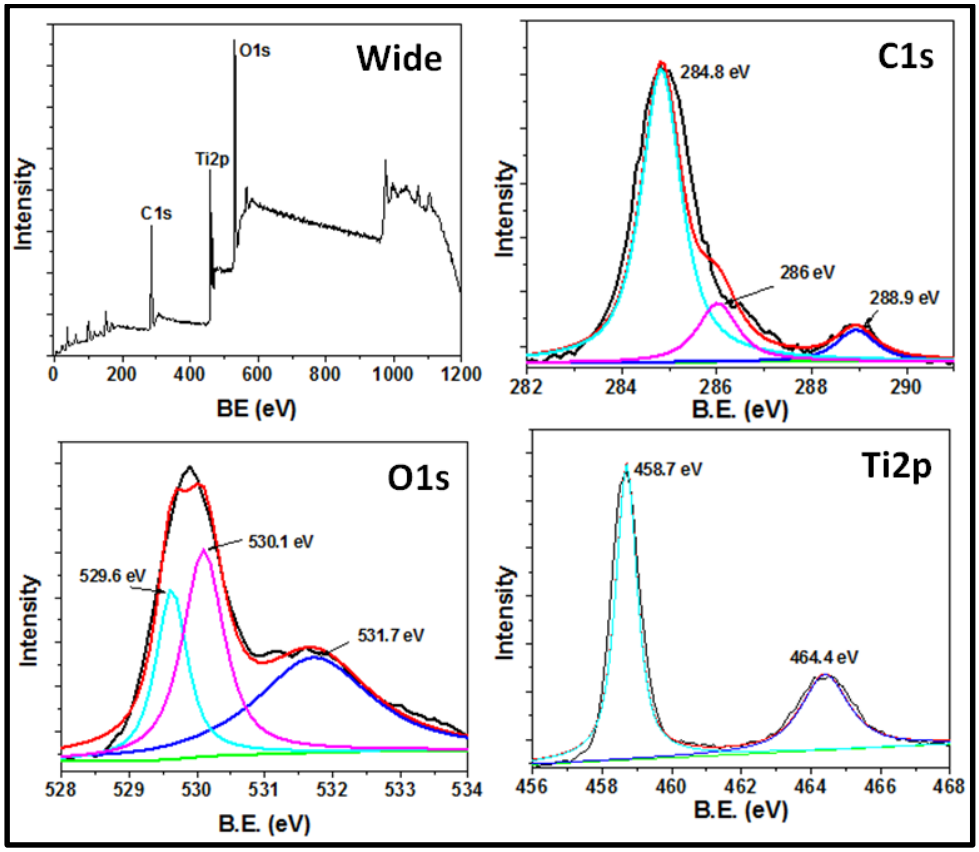

Figure 5.3. The wide, C1s, O1s and Ti2p XPS spectra of P25/C-dot.

The morphology of the composite was analyzed using the HRTEM and the C-dot (red arrows in Figure 5.4A) were found adsorbed on the edges of P25. The FTIR spectra of CD, C-dot, P25 and P25/C-dot are given in Fig. 4B. The peaks at

3350 and 1645 cm^{-1} in both P25 and P25/C-dot were attributed to the stretching and bending vibrations surface –OH groups. The inset Figure 5.4B clearly showed the presence of surface –OH groups of TiO_2 and –C-O-C stretching of C-dot, respectively (M. Hu et al., 2014; J. Tian et al., 2015). The amount of C-dot loading in P25/C-dot as calculated from the TGA (Figure 5.4D) done in air atmosphere. The weight loss from RT to 200°C was assigned to the removal of surface adsorbed water molecules and –OH groups. The weight loss above 200°C is mainly attributed to the removal of C and its functional groups from P25/C-dot and thus the difference in weight loss in this region between the P25 and P25/C-dot was considered as the C-dot loading and was determined to be 1.4%.

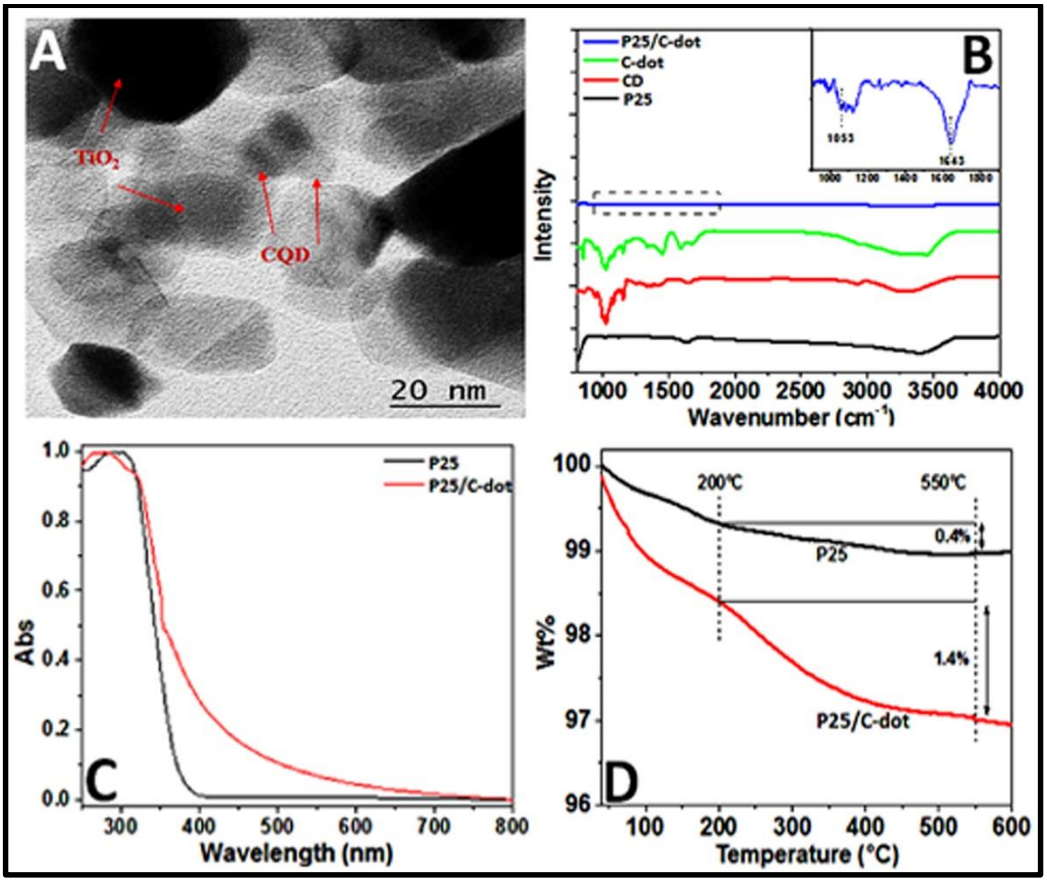

Figure 5.4. (A): HRTEM images; (B): FTIR spectra, (C): TGA done in air atmosphere with 10°C/min heating rate and (D): UV-Vis absorption spectra of P25 and P25/C-dot.

5.3.2. Photodegradation studies of P25/C-dot

The PC activity of P25 and P25/C-dot are evaluated from the VL PD studies of RhB and MO as probe molecules (Figure 5.5). The VL PD of RhB by P25/C-dot was 80% while for P25 it was only 49% (Figure 5.5A). MO was a highly stable dye molecule and was hence very difficult to degrade, its λ_{max} (460 nm) was blue-shifted compared to that of RhB. Hence the PD of MO may give better judgment in determining the VL PD ability of the composite. The results of the VL PD of MO were given in Figure 5.5B. Seldom PD observed in the case of MO in the absence of catalyst. The reaction is done till 120 min and ~40 % PD was observed in the presence of P25/C-dot while it is only 33% for P25. The improved PC activity of P25/C-dot than that of P25 was a clear indication of the contribution of C-dot towards the VL PD and was ascribed to its up-conversion PL and high PLQY. Though there is improvement observed in the VL PD of RhB, the limited improvement in the VL PD of MO, might be due to the lower C-dot loading or may be due to less % (25 %) of rutile phase (~3.0 eV) which can absorb in the near regions of 400 nm.

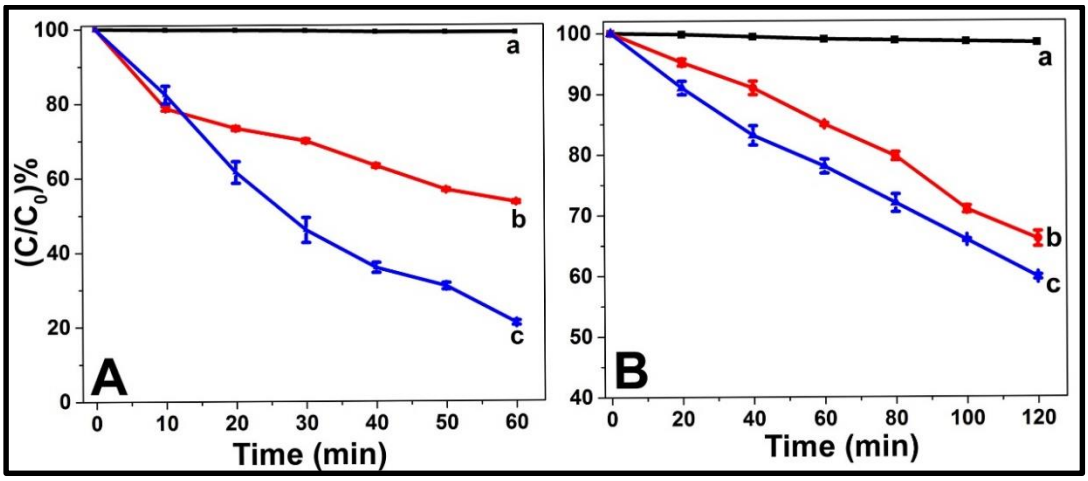

Figure 5.5. VL PD of (A) RhB and (B) MO by (a): no catalyst; (b): P25 and (c): P25/C-dot.

5.3.3. Estimation of ROS in the photodegradation of RhB by P25/C-dot

The result of scavenging studies using the PD of RhB by P25/C-dot is given in Figure 5.6. The results show that PD has been reduced to 52.5, 37 and 62.2% in the presence scavengers t-BuOH, NaN_3 and BQ, respectively from 80% of the control reaction. Considering the actual PD% in the absence of scavenger (80%) as 100% for calculation purpose and the ROS contributions were calculated as follows 34% due to •OH while 20 and 22% from $^1O_2$ and O_2•− (Figure 5.6B), respectively. For comparison scavenging study results of P25 in the VL PD of RhB were done (Figure 5.7) and showed that O_2•− plays dominant role with (28%) while •OH is only 6% and $^1O_2$ (1%). The 6 % •OH may be due to the rutile phase in P25.

In all the PD studies, except that of involving HRTiO_2-Gr (chapter 3), we observed that the UV-Vis spectra of RhB during PD showed considerable shift (~ 50 nm) in its λ_{max} value. Therefore, in order to understand the change, we further analyzed the UV-Vis absorption spectra of RhB during PD reactions by P25/C-dot in the absence and presence of the scavengers and are shown in Figure 5.8. It can be observed that the shift in the λ_{max} during PD was different for each, this indicates the effect of ROS on the PD pathway. Generally, the PD of RhB is initiated by the stepwise removal of ethyl groups from the molecule i.e. dethylation of the four ethyl groups (Figure 5.9), followed by the cleavage of chromophores which lead to the mineralization (Chang et al., 2012; Rahman, Ahmad, Misra, & Lohani, 2013; Wilhelm & Stephan, 2007). If the oxidation power of ROS involved in the PD is low, it may not lead to the mineralization straightaway, instead will stop at the dethylation process which is referred to as the decolouration pathway.

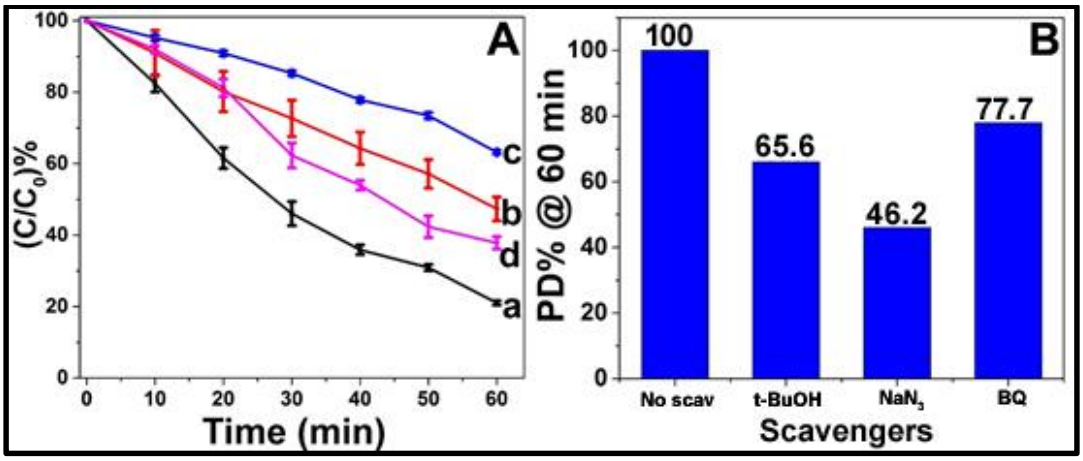

Figure 5.6. (A) VL PD of RhB by P25/C-dot in the presence of (a): no scavengers; (b): t-BuOH; (c): NaN_3 and (d): BQ. (B): Bar graph representation for the PD% @ 60 min in the presence of scavengers (PD% is normalized to 100% for no scavenger studies).

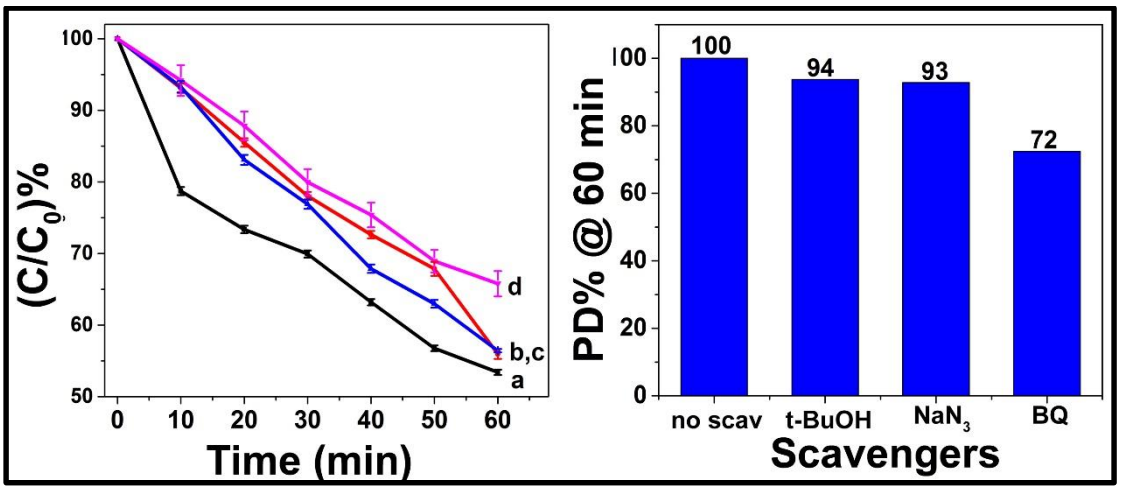

Figure 5.7. (A) VL PD of RhB by P25 in the presence of (a): no scavengers; (b): t-BuOH; (c): NaN_3 and (d): BQ. (B): Bar graph representation for the PD% @ 60 min in the presence of scavengers (PD% is normalized to 100% for no scavenger studies).

The UV-Vis spectrum of RhB in the absence of scavenger (Figure 5.8A) showed that the λ_{max} (554 nm) underwent minimal changes throughout PD, which was an indication that the PD was majorly ending up in the mineralization of RhB i.e. as the PD kinetics were faster and hence lead to mineralization. However, the λ_{max} of RhB in the presence of t-BuOH, which is a scavenger of •OH, (Figure 5.8B), underwent a blue shift (~5-8 nm), which suggests that •OH might be the ROS responsible for mineralization of RhB, which is justifiable considering the higher oxidation potential of •OH ($E° = 2.8$ eV). With NaN_3, which suppressed the activity

of both $^1O_2$ and •OH (Figure 5.8C), a greater blue shift (~10-15 nm) in the λ_{max} was observed, whereas in the presence of BQ (Figure 5.8D), which is a scavenger of O_2•−, no shift was observed in the λ_{max} of RhB. This depicts the importance of $^1O_2$ and •OH in the mineralization of RhB (Chang et al., 2012; Rahman et al., 2013; Wilhelm & Stephan, 2007; G. Zhang et al., 2014). We further recalled the absorption spectra of RhB during PD in the presence of HRTiO$_2$-Gr (Figure 3.22), the only other instance where •OH contribution was dominant and in the presence of N-TiO$_2$ (Figure 4.17) where no •OH was observed, but $^1O_2$ contribution was present. Interestingly, the spectra of RhB showed shift with N-TiO$_2$; while no shift was observed in the case of HRTiO$_2$-Gr. This led to the conclusion that •OH might be the ROS which is contributing majorly towards the mineralization of RhB. Based on the observations, we conclude that •OH is crucial and play a major role in the mineralization and faster PD of RhB and this may be true to other dyes as well due to its higher oxidation potential (E° = 2.80 eV). Our observations suggest that the synergistic effect of $^1O_2$ and •OH might be the reason behind the mineralization of RhB.

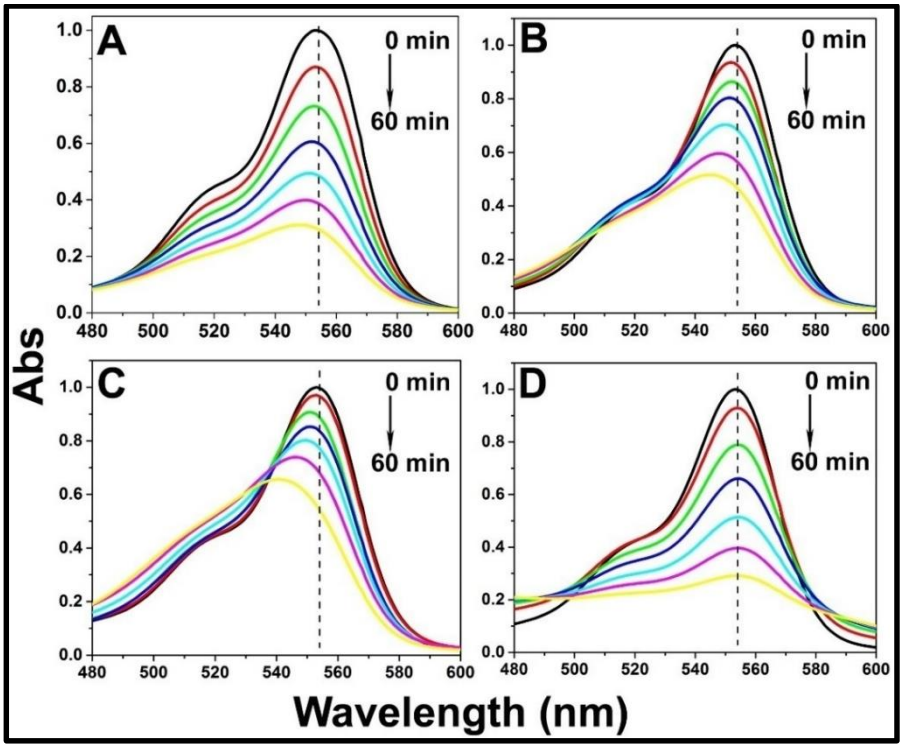

Figure 5.8. UV-Vis absorption spectra of RhB during VL PD in the presence of P25/C-dot with (A) no scavenger; (B) t-BuOH; (C): NaN$_3$ and (D): BQ

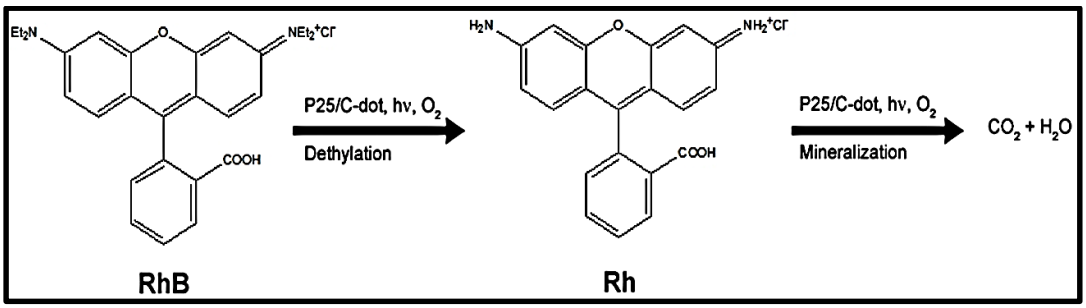

Figure 5.9. Scheme for the VL PD of RhB via dethylated mechanism.

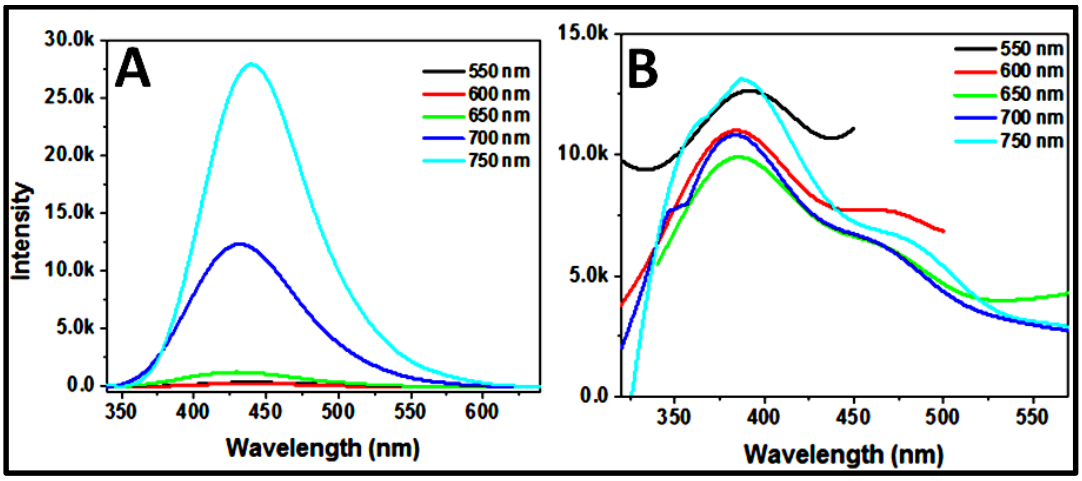

Figure 5.10. Up-converted PL of (A): C-dot and (B): P25/C-dot with low energy excitations.

Thus, the enhancement in the PC property of the composite and the mineralization of RhB was attributed to the C-dot and its up-converted PL property. The PL up-conversion property of C-dot and P25/C-dot (H. Li et al., 2012; S. T. Yang et al., 2009; Zhao et al., 2008) were studied and are given in Figure 5.10. The PL data clearly shows the up-conversion PL of the C-dot and P25/C-dot for excitation $\lambda \geq 550$ nm, which produced emission at lower wavelength regions (350 nm to 550 nm).

Based on the VL PD and scavenger studies, a mechanism was proposed (Figure 5.11). The presence of •OH suggested that holes were produced in the VB of P25 in the composite, and this can be explained by the up-conversion PL of C-dot which emits high energy (350 nm $\geq \lambda$) radiation which in turn excites P25 and generates electrons and holes. When P25/-dot composite was excited with VL, apart

from down-conversion PL, C-dot causes up-converted PL i.e. excited by λ = 550 nm to 750 nm and produces PL in the range of 350 nm to 550 nm. This up-converted PL energy was absorbed by P25 and e-h were produced. The holes in the VB of P25 oxidizes water to form •OH, which in turn oxidizes RhB, while electrons in the CB forms O_2•−, which partially goes on to form $^1O_2$ by secondary reactions and certain amount reacts with RhB. The formed $^1O_2$ further reacts with RhB, thus the presence of all the ROS in the PD of RhB by P25/C-dot can be explained. The possibility of direct excitation of P25 is minimal as VL (> 400 nm) was utilized for the PD reactions. Some contribution may be observed due to the presence of rutile phase in P25.

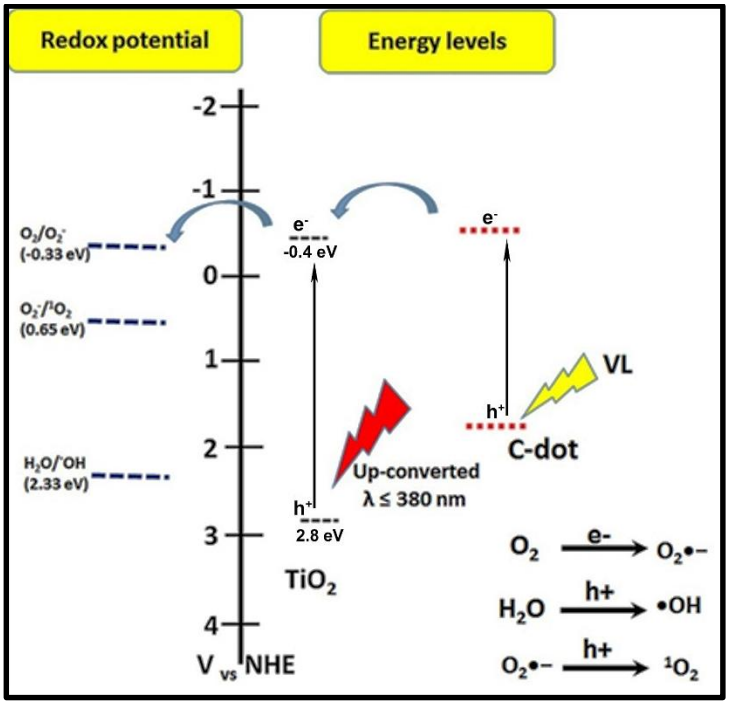

Figure 5.11. Mechanism for the formation of ROS by P25/C-dot under VL PD.

5.4. Conclusions:

Undoped C-dot with high PLQY (25%) was prepared from CD using P_2O_5-water method and was proven to be better than hydrothermal synthesis of C-dot considering the PLQY. P25/C-dot composite, exhibited excellent VL PD towards RhB (≥80%) and MO (~40%) which is higher than that of P25. The improved PD property of the composite was attributed to the up-converted PL and high PLQY of

C-dot and the extended VL absorption of the composite. All the major ROS such as •OH, O_2•− and $^1O_2$ contributed to the PD of RhB by P25/C-dot. It was found that the in the presence of P25/C-dot, RhB tend to mineralize and is attributed to the higher oxidation power if •OH and the synergistic effect of $^1O_2$ and •OH.

CHAPTER 6

GREEN METHOD FOR THE PREPARATION OF TiO_2-FULLERENE/ GRAPHENE COMPOSITES USING CD AS LINKER FOR VISIBLE LIGHT PHOTODEGRADATION OF POLLUTANTS

In this chapter, two different TiO_2 based composites, TiO_2-fullerene (TiO_2-CD-C_{60}) and TiO_2-reduced graphene oxide (TiO_2-rGO-CD), were prepared by a green photo irradiation method. In the composites TiO_2 was combined either with C_{60} or rGO using CD as linker molecule. Electron transfer properties, VL absorption and VL PC activity had been observed to be synergistically enhanced by LMCT process in TiO_2-CD-C_{60} and the electron accepting properties of C_{60} and rGO in both the composites.

6.1. Introduction

Surface adsorption of polyhydroxyl (X. Zhang et al., 2010), phenolic (Anik Sen , Bishwajit Ganguly , and Hirendra N . Ghosh , 2012; Wang, Hang, Anderson, & Lian, 2003), carboxylic (Xagas et al., 2000), peroxide (Xiangzhong Li et al., 2001; Rao & Chu, 2009), cyanide (Vrachnou et al., 1989; Weng et al., 1999), isocyanate (F. Chen et al., 2009; D. Jiang et al., 2009) or polyaromatic adsorbents (Seo et al., 2005), either chemically or physically, on TiO_2 can form LMCT complexes. It was proposed that a direct electron transfer from the surface-complexed phenol to the TiO_2 CB can be initiated through LMCT upon absorption of VL (Yan Liu, Dadap, Zimdars, & Eisenthal, 1999) and such surface complexes with extended VL absorption had been reported in phenol-TiO_2 system (Agrios, Gray, & Weitz, 2004), catechol-TiO_2 (Yan Liu et al., 1999) and TiO_2-CD system. As mentioned, these complexes can extend the absorption spectra of TiO_2 to VL region due to the transfer of electrons from the highest occupied molecular orbital (HOMO) of adsorbed substrate to the CB of TiO_2. Of these various adsorbents,

CD based LMCT complexes are attractive due to their photo stability, redox ability and moreover they can be synthesized by green method (P. Lu et al., 2004; Mukthar Ali & Sandhya, 2014; G. Wang et al., 2006; X. Zhang et al., 2010, 2011).

In LMCT based complexes, the PC properties can be further enhanced by coupling TiO_2 with either C_{60} or rGO, as these nanocarbon materials are known to enhance the electron accepting and transfer properties (Katsumata et al., 2012; Park, Singh, et al., 2009; Stengl, Popelkova, & Vlacil, 2011; Lei Sun et al., 2012; Woan et al., 2009) of the formed composite. Another advantage is that the processing of C_{60} or rGO in water can be well assisted by CD (Guo et al., 2010; Guo, Guo, Li, Wang, & Dong, 2011; Konkena & Vasudevan, 2012; Murthy & Geckeler, 2001).

Preparation of TiO_2-C_{60} composite using pure C_{60} will result in a non-uniform composite due to the tendency of C_{60} molecules to aggregate because of its strong π-π interaction and the resulting composite will therefore have relatively lower surface area and poor performance. Thus, Park et al. reported sensitization of TiO_2 by fullerol (C_{60}-OH) in TiO_2/C_{60}-OH (Park, Singh, et al., 2009). However, this method calls for the oxidation of fullerene which alters the optical and electronic properties of C_{60} and brings in complexity to the preparation of TiO_2-C_{60} composite. Therefore, we performed the preparation using CD as a linking molecule and a green method. First, inclusion complex of C_{60} in CD (Murthy & Geckeler, 2001; Nagase, 1998) was prepared which render solubility to C_{60} in water and thus keeps the C_{60} molecules intact. Further the aqueous solution of CD-C_{60} was mixed with an aqueous dispersion of TiO_2 and the resulting suspension was irradiated with UV or sunlight to produce TiO_2-CD-C_{60}.

Similarly coupling rGO with CD (rGO-CD) complex can facilitate the dispersion and processing of rGO in aqueous systems as well as retain the electronic properties of rGO (Guo et al., 2010, 2011; Konkena & Vasudevan, 2012, 2013). Gris more beneficial (Geim & Novoselov, 2007; Nair et al., 2008) in its reduced form, rGO, rather than in an oxidized form, GO, considering the electronic transport. Most of the literature reports utilized GO as the starting material for making TiO_2-Gr composites, because of the inability of Gr to disperse in water and the lack of compatibility of Gr with TiO_2, which prevents the formation of a uniform

composite. Peining et al (Peining and Nair et al, 2012) reported a TiO_2-Gr composite preparation from rGO, by a tedious and energy consuming electrospinning technique.

Therefore using these inclusion complexes of CD-C_{60} and CD-rGO, TiO_2-CD-C_{60} and TiO_2-CD-rGO were prepared respectively by a green photo irradiation method. CD on photoirradiation, can form self-assembled structures of TiO_2 such as wires or networks (J. Kim & Nichols, 2012; Miedaner, Ahrenkiel, Himmel, Curtis, & Ginley, 2005) which exhibited improved PC activity thanks to the LMCT process. The mechanism of the CD bonding to TiO_2 by photochemical method is described elsewhere (Miedaner et al., 2005). The method is of green in nature as it uses the solar light energy for the bonding of the CD to TiO_2 and the bond formation ensures the proximity between TiO_2 and C_{60} or rGO. It is well known that CD can sensitize TiO_2 to VL region (X. Zhang et al., 2011) of the solar spectrum. The combined strategies of LMCT complexes with CD and heterostructure formation with either C_{60} or rGO may lead to synergistic effect in the improvement of the PC properties of composite. Further the role of C_{60} or rGO in the ROS formation and their contribution towards VL PD of RhB were studied and mechanisms were proposed for the ROS formation.

6.2. Experimental

6.2.1. Preparation of CD-C_{60}

The preparation of CD-C_{60} composite was done by grinding C_{60} and CD in presence of 2 ml of water/ethanol (1:1). Typically, 1:4 weight ratio of C_{60} and CD were kneading using small amount of water/ethanol for 1 hr. Then the products were kept for drying overnight at 70°C followed by dialysis with 1000 MWCO membrane for one day. After drying, the product (brown powder) formed was soluble in water and yielded a yellow solution.

6.2.2. Preparation of TiO_2-CD-C_{60}

The CD-C_{60} (35 mg) was taken in 70 ml of water (0.5 mg/ml) and from this stock solution 5 ml (equivalent to 0.5 mg of C_{60}) was taken and added to a

suspension of 99.5 mg of TiO_2 anatase in 90 ml of distilled water. This suspension was sonicated for 10 min and irradiated with sunlight for 24 hr in a quartz beaker. After the irradiation, the settled product was washed, centrifuged and dried at 70°C in a static vacuum for overnight. This product was referred to as TiO_2-CD-C_{60}0.5. Composite with varying concentrations of C_{60} were prepared and named accordingly.

6.2.3. Preparation of CD-rGO

Commercial graphite powder was oxidized with H_2SO_4 and $KMnO_4$ followed by the addition of H_2O_2 to form GO (Hummers Jr & Offeman, 1958; Venugopal et al., 2012). The solid brown product of GO was filtered and washed repeatedly with 1 M HCl followed by distilled water and dried under vacuum at room temperature. In a typical rGO preparation procedure, GO (200 mg) was taken in water (200 ml) and sonicated to yield a homogeneous yellow brown dispersion. Hydrazine hydrate 2 ml (32.1 mmol) was added to the solution and was refluxed at 100ºC using water cooled condenser for 24 hr. The precipitated rGO was filtered off using glass funnel and washed copiously with water and methanol and dried at 60°C under vacuum for overnight. The CD-rGO was made by mixing rGO and CD using a mortar and pestle by a method described elsewhere (K. Liu et al., 2008). To the 100 mg of rGO, 1 g of CD was added and mixed well in a mortar using the pestle with the addition of small amount of distilled water. Totally 3 ml of water was added during the process over a period of 3 hrs. After that the product was dried at 70°C for overnight. The product was sonicated in water to form a dispersion of rGO. Now the product was purified using 1000 MWCO dialysis membrane for 24 hr to remove excess CD. After drying overnight at 70°C for 24 hr, the product CD-rGO was dispersible in water.

6.2.4. Preparation of TiO_2-CD-rGO

In a typical procedure, the proportionate amounts of CD-rGO (homogenous suspension) and TiO_2 (99.5 mg for making TiO_2-CD-rGO0.5) were taken together in 100 ml of water and sonicated to yield a suspension. The sonicated mixture was transferred to a quartz beaker and irradiated with sunlight for ~15 hr. After

irradiation, the suspension was washed with plenty of water and centrifuged to separate the grey product and dried overnight at 65°C under vacuum. TiO_2-CD-rGO with different weight percentage of rGO (0.1, 0.5, 2 and 5%) were prepared. TiO_2-CD-rGO0.1 refers to composite with 0.1% of rGO.

6.3. Results and Discussions

6.3.1. Characterization of TiO_2-CD-C_{60}

The FT-IR spectra of TiO_2, CD-C_{60} and TiO_2-CD-C_{60} are given in Figure 6.1. The spectra of TiO_2 and TiO_2-CD-C_{60} exhibited peaks at 3300 and 1640 cm^{-1} corresponding to the -OH stretching and bending frequency respectively, the intensity of the peaks were lower in the TiO_2-CD-C_{60} composite and a broadening of the peak below 1000 cm^{-1} was observed and these might be to the bond between TiO_2 and CD (J. Kim & Nichols, 2012). This is an indication of the formation of bonds between –OH groups of CD molecules with the surface –OH groups in TiO_2. The peak at 2932 cm^{-1} is attributed to $–CH_2$ group in the composite from CD. Thus, the IR spectra suggests the formation of bonds between TiO_2 and CD molecules.

TGA curves of TiO_2, CD and TiO_2-CD-C_{60} are provided in Figure 6.2. While the thermogram of TiO_2 did not show any significant weight loss till 700°C, composite showed weight loss at 300-400°C which corresponded to the decomposition of CD and the decomposition temperature of CD in the composite was comparatively higher to that of pure CD which indicated the interaction or bond formation between TiO_2 and CD. Thus, the TGA results confirmed the presence CD in the composite. The percentage of C_{60} was too low to be observed clearly in TGA.

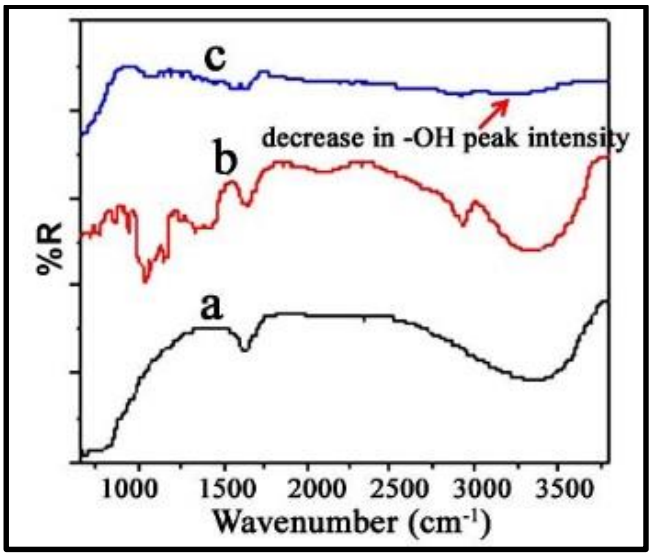

Figure 6.1. FTIR spectra of (a): TiO_2 (b): CD-C_{60} and (c): TiO_2-CD-C_{60}. The decrease in the intensity of –OH peak indicates the bond formation between the –OH peaks of CD molecules and TiO_2.

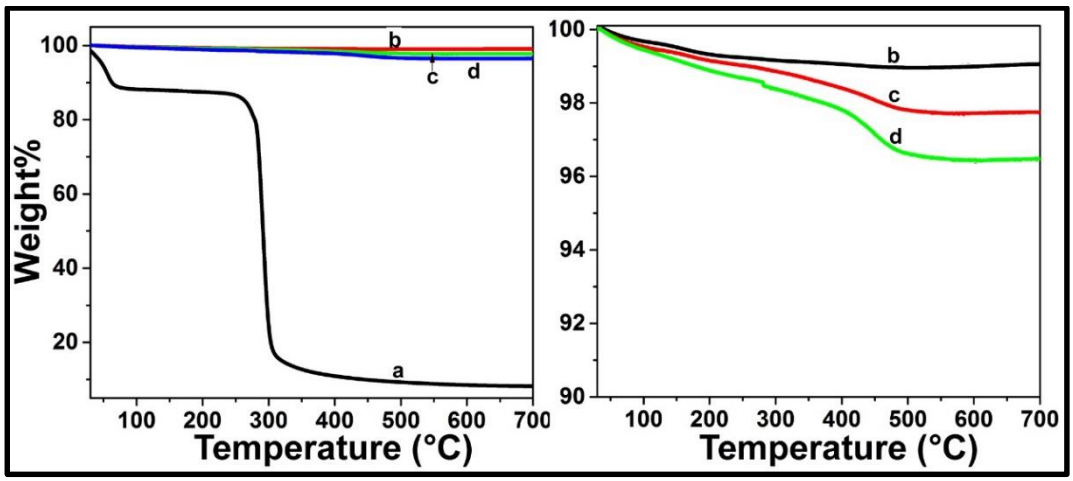

Figure 6.2. Thermograms of (A): (a) CD and expanded view of (B): (b) TiO_2 and c) TiO_2-CD-C_{60}0.5 and d) TiO_2-CD-C_{60}1.5 done under N_2 atmosphere at a heating rate of 10^0C/min

To investigate the presence of C_{60} in the composite, UV-Vis spectra of the TiO_2, CD-C_{60} and TiO_2-CD-C_{60} aqueous suspensions were done and given in Figure 6.3A. It was observed from the spectra that the absorption of TiO_2-CD-C_{60} extends further to the visible (650 nm) region compared to that of the TiO_2 (400 nm) and to CD-C_{60} (540 nm). It is well understood that typically in wide band-gap semiconductors subtle modification in the surface will impact greatly on the

surface photosensitization (Boschloo, 1997; Copidas & Kamat, 1989). These surface modifications can bring about adsorbate-adsorbent surface complexes which possess entirely different electronic properties than their parent molecules. Figure 6.3A showed the difference spectra between TiO_2-CD-C_{60} and TiO_2 and have absorption which is considerably red shifted from TiO_2 and CD-C_{60} spectra. There are reports suggesting the LMCT complexes even from the solid state TiO_2 surface (Seo et al., 2005). Therefore we assume that the peaks in the difference spectra (Figure 6.3A) are due to the LMCT bands from CD to TiO_2. CD molecules induce VL sensitization through chelation of surface Ti (IV) ions with the ene-diol groups, generally giving rise to very strong LMCT bands (Tachikawa, Tojo, Fujitsuka, & Majima, 2006; X. Zhang et al., 2011). UV-Vis DRS spectra of TiO_2 and the composites are given in Figure 6.3B. The spectra clearly suggest that both TiO_2-CD and TiO_2-CD-C_{60} have extended absorption to VL range than that of bare TiO_2. VL absorption was higher for TiO_2-CD-C_{60} than that of TiO_2-CD. Band gap energies calculated from the DRS spectra for TiO_2, TiO_2-CD and TiO_2-CD-C60 were 3.2, 3.1 and 2.98 eV respectively.

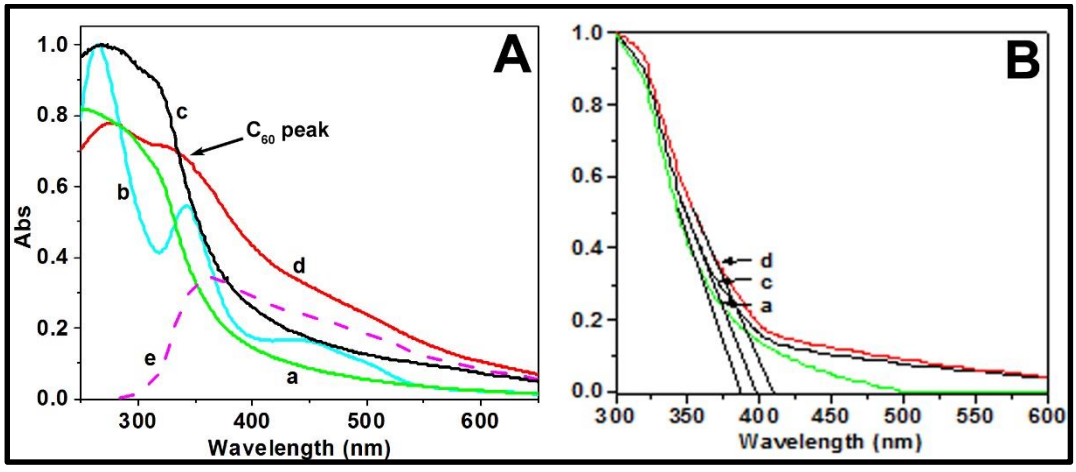

Figure 6.3.UV-Visible spectra (A) in aqueous solution: (a): TiO_2; (b): CD-C_{60}; (c): TiO_2-CD1.5; (d): TiO_2-CD-C_{60}1.5 and (d): difference of TiO_2-CD-C_{60} and TiO_2 spectra (c-a). (B) UV-Vis solid state spectra (a); TiO_2; (c): TiO_2-CD0.5 and (d) TiO_2-CD-C_{60}1.5; the spectra shows lowering of band gap in the composite. The characteristic peak of C_{60} (~340 nm) in the UV-Vis spectra of the composite confirms the presence of C_{60}. The difference spectrum is assigned to LMCT peaks.

The XRD pattern of the CD-C_{60} and the composite are shown in Figure 6.4. It can be seen that the diffraction peaks were well defined and can be assigned to the anatase TiO_2 (Reyes-Coronado et al., 2008). Peaks in the TiO_2-CD-C_{60} composite have peaks corresponding to anatase phase. In this composite, we can also observe the peaks of CD at 24.6° which is almost merging with (101) plane peak (25.6°) of TiO_2 anatase. As there was no temperature involved in the preparation, no change in the phase of TiO_2 was expected. The XRD pattern suggested that the TiO_2 nanoparticles in the composite are highly crystalline in nature.

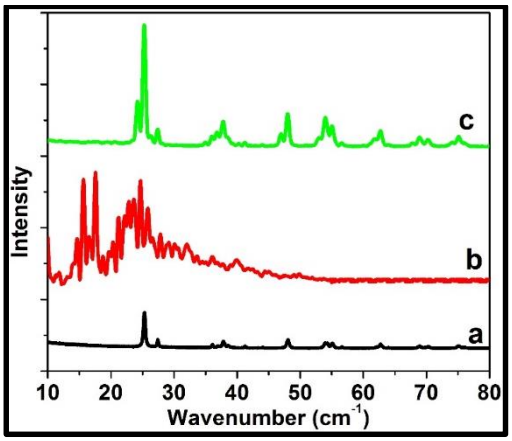

Figure 6.4. XRD patterns of (a): TiO_2; (b): CD-C_{60} and (v): TiO_2-CD-C_{60}

Electron microscopy and EDAX are important tools to study the morphology and composition, respectively. Figure 6.5 provides the SEM images (Figure 6.5A-C) and back scattered electron images (Figure 6.5D-F) of CD-C_{60} and the TiO_2-CD-C_{60} composite. SEM images suggested an almost uniform distribution of TiO_2 nanoparticles in the composite and revealed that the composite has a uniform porous structure. The back scattered electron images of CD-C_{60} (Figure 6.5D) was uniformly dark, while the composite has bright and dark contrast suggesting the presence of TiO_2 nanoparticles and carbon support. The uniform porous structure of the composite is desirable for solar cell application purposes.

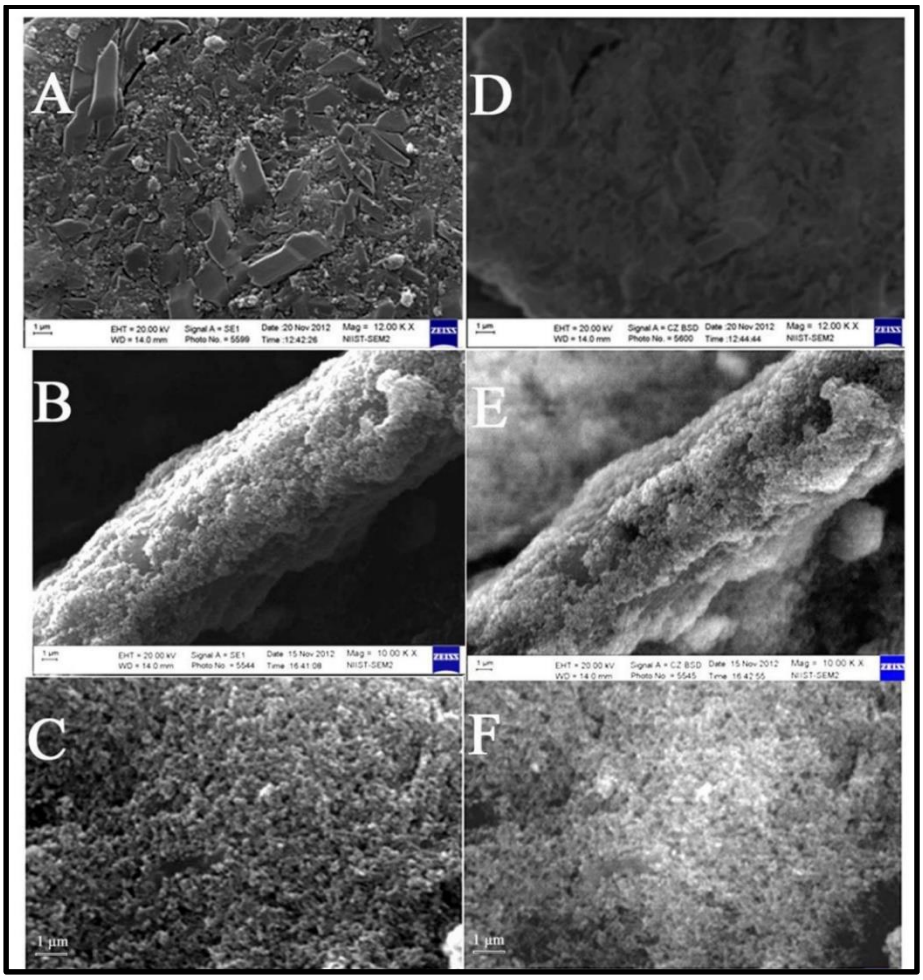

Figure 6.5. SEM images: Secondary electron images of (A) CD-C_{60} and (B, C) TiO_2-CD-C_{60}. Back scattered electron images of (D) CD-C_{60} and (E, F) TiO_2-CD-C_{60}.

The TiO_2-CD-C_{60} was characterized with HRTEM and EDAX and the results were provided in Figure 6.6. TEM images (Figure 6.6A-C) showed that the TiO_2 particles are connected together by CD thus forming a network of TiO_2, and C_{60} are found without aggregation in the composite. The structure suggested proximity between TiO_2 and C_{60} which can increase the probability of the electron transfer between them. Finally, the EDAX spectra of the composite (Figure 6.6D) confirmed the presence of C, Ti and O in the composite.

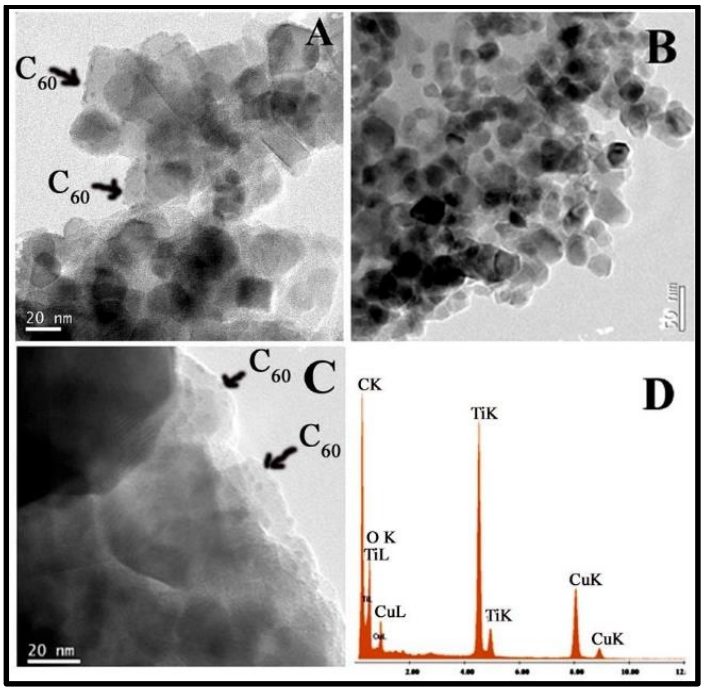

Figure 6.6. (A, B &C) HRTEM images and (D) EDAX spectrum of TiO_2-CD-C_{60}, confirms the presence of carbon, oxygen and titanium.

Solid PL spectra of pure TiO_2 and the composites were recorded at an excitation wavelength of 290 nm and are given in Figure 6.7. Compared to that of control TiO_2, the PL intensity was decreased in both TiO_2-CD and TiO_2-CD-C_{60} and the decrease was prominent in TiO_2-CD-C_{60} composites in comparison to that of TiO_2-CD. The PLQY for TiO_2-CD is 2.04% while for TiO_2-CD-C_{60}1.5, it is 1.59%. The decrease in PLQY suggests that the photogenerated e-h recombination is lower and therefore, it is clear that charge recombination is less in the composite compared to that of pure TiO_2 and TiO_2-CD. The reduced charge recombination in TiO_2-CD has been reported due to electron-donating and hole capturing nature (X. Zhang et al., 2011) of hydroxyl groups in CD moiety as well as the electron accepting properties of C60 which lead to reduced recombination. C_{60} is as an excellent electron acceptor, which is capable of accepting as many as six electrons (Koeppe & Sariciftci, 2006) due to its good delocalization of electrons and low lying triply degenerate LUMO level. There are evidences that excited fullerenes (C_{60}*) are even better electron acceptors than the ground state. Therefore, we believe that the substantial reduction in the charge recombination in the composite

is due to the synergistic effect of hole scavenging by CD and electron accepting by C_{60} in the composite.

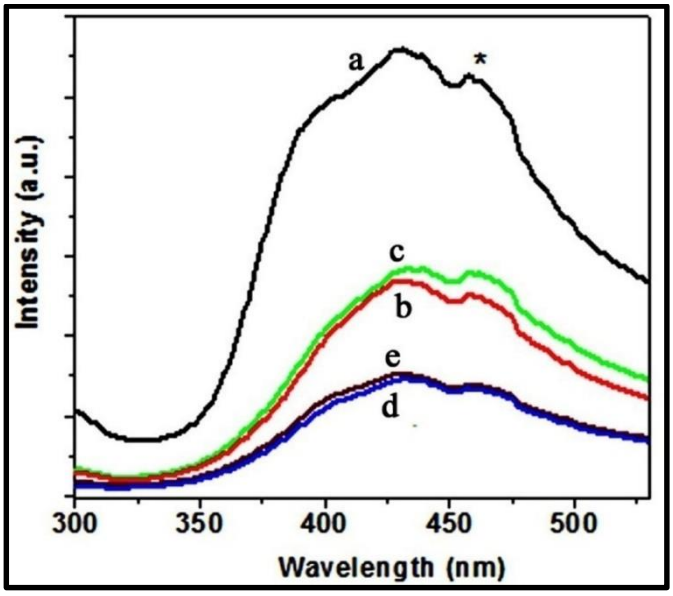

Figure 6.7. Solid state PL spectra recorded at excitation wavelength 290 nm (a) pure TiO_2 (b) TiO_2-CD1.5, (c) TiO_2-CD0.5, (d) TiO_2-CD-C_{60}1.5 and (e) TiO_2-CD-C_{60}0.5 (*-due to the xenon lamp interference)

6.3.2. Photodegradation studies of TiO_2-CD-C_{60}

PC activity of TiO_2 and the composites were conducted using the VL PD of MB and 4CP. Figure 6.8 provides the summarized results of the PC studies of MB. In the PD of MB, the remaining MB in the PD reactions using TiO_2-CD-C_{60}0.5% and bare TiO_2 at 40 min were 53 and 72%, respectively. Around 28% degradation was observed with bare TiO_2 in VL which is typically UV light active, and reports (Yuanzhi Li, Kunitake, & Fujikawa, 2006) suggested that photosensitization process of dye molecules is responsible for this degradation under VL. The rate constant values given in Table 6.1 showed that the optimum composite showed ~2 and 5 times higher PC activity than bare TiO_2. The control CD-C_{60} and CD did not show PC activity (Figure 6.9) and TiO_2-CD (Figure 6.8) did not show significant increase in PC activity from that of bare TiO_2. The improvement in the PD of MB with the composites was attributed to its VL absorption and the reduced charge

recombination properties. The effect of % loading of C_{60} on the VL PD of MB is shown in Figure 6.10.

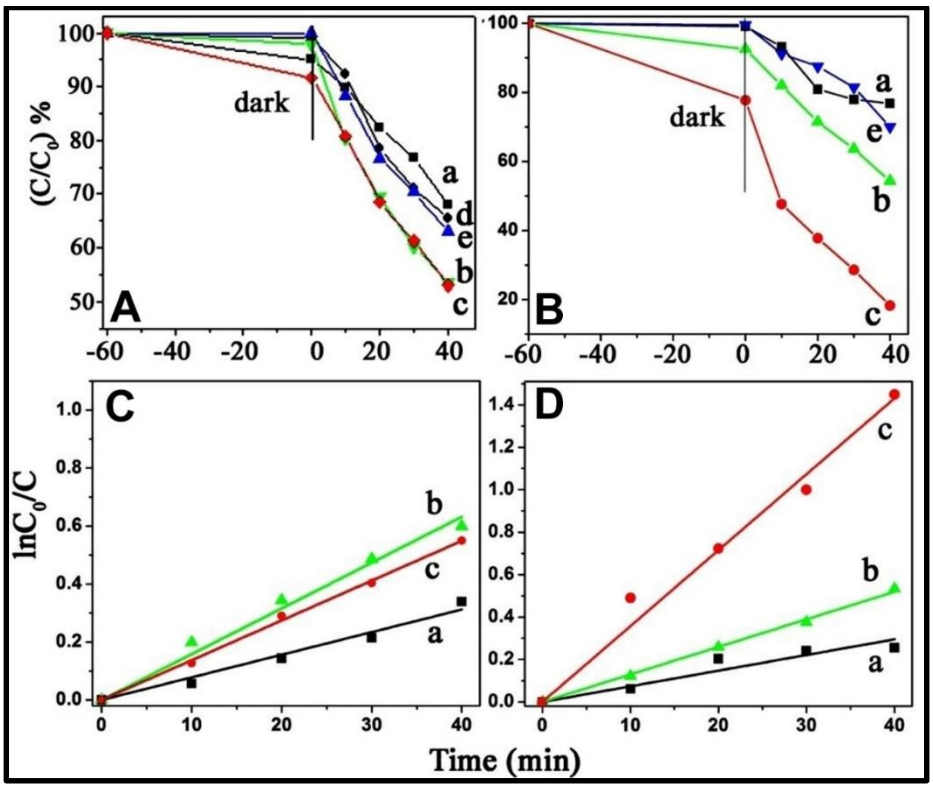

Figure 6.8. (A & C) PD of MB and its rate constant plots; (B & D) PD of 4CP and its rate constant plots under VL irradiation with (a) TiO_2; (b) TiO_2-CD-C_{60}0.5; (c) TiO_2-CD-C_{60}1.5; (d) TiO_2-CD0.5 and (e) TiO_2-CD1.5.

Table 6.1. Rate constants for the VL PD of MB and 4CP in the presence of TiO_2 or TiO_2-CD-C_{60} composites.

Photocatalysts	**Rate constant (min^{-1}) for MB**	**Rate constant (min^{-1}) for 4CP**
TiO_2	0.0078± 0.0004	0.0074± 0.0006
TiO_2-CD-C_{60}0.5	0.0158 ± 0.0005	0.013 ± 0.0002
TiO_2-CD-C_{60}1.5	0.0137 ± 0.0002	0.0357± 0.0014

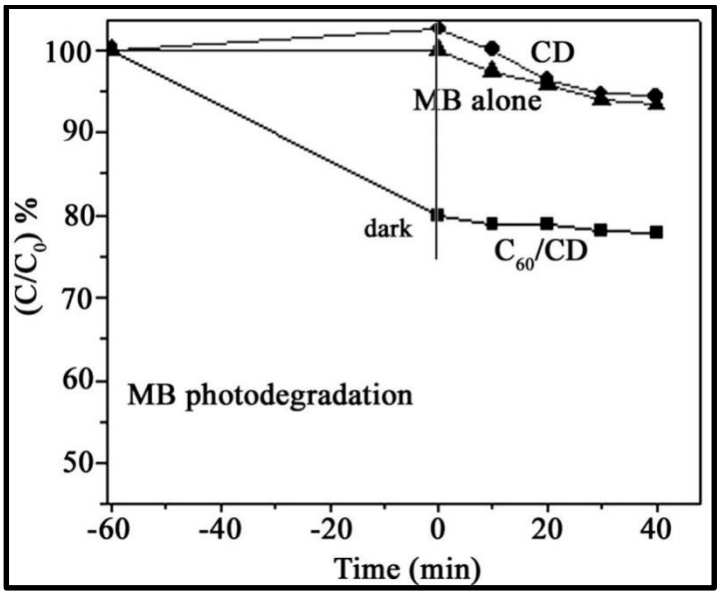

Figure 6.9. VL PD of MB in the presence of CD, CD-C_{60} and MB alone.

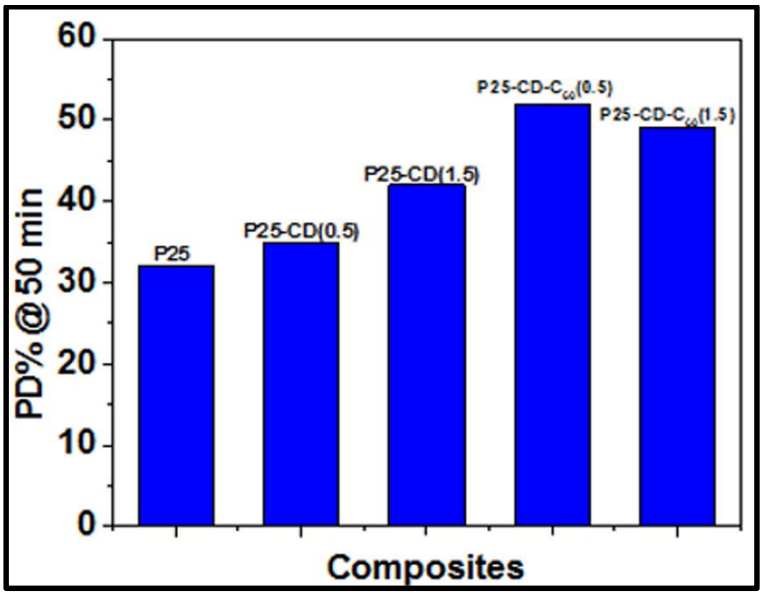

Figure 6.10. Effect of C_{60} loading on the VL PD of MB by TiO_2-CD-C_{60} composites.

6.3.3. Estimation of ROS in the photodegradation of RhB by TiO_2-CD-C_{60}

Investigations on the mechanism of ROS in the VL PD of RhB was studied using the scavengers. Scavenger studies using the VL PD of RhB in the presence of TiO_2-CD-C_{60}1.5 were conducted and the results are given in Figure 6.11. The actual PD at 60 min with no scavenger is 61.5% which is considered 100% for calculation purpose. The PD at 60 min with t-BuOH, NaN_3 and BQ were 100, 92 and 65% respectively. Therefore, the contribution from •OH is nil, whereas ~10% and 35% contribution from $^1O_2$ and O_2•− were observed, respectively.

Based on the findings, the following mechanism was proposed for the formation of ROS. When the composite was excited with VL, possible excitations apart from dye sensitization mechanism are: due to LMCT excitation from HOMO of CD in the complex to the CB of TiO_2 and second was from the HOMO of C_{60} to its LUMO. The excited electrons in the CB of TiO_2 can reduce the O_2 to O_2•− since $E°_{O2/\,O2•-}$ = -0.33 V. At the same time the excited electrons in the LUMO of C_{60} can undergo $^1O_2$ formation since C_{60} has near unity QY for triplet state formation. This process explains the formation of ROS in the VL PD of RhB.

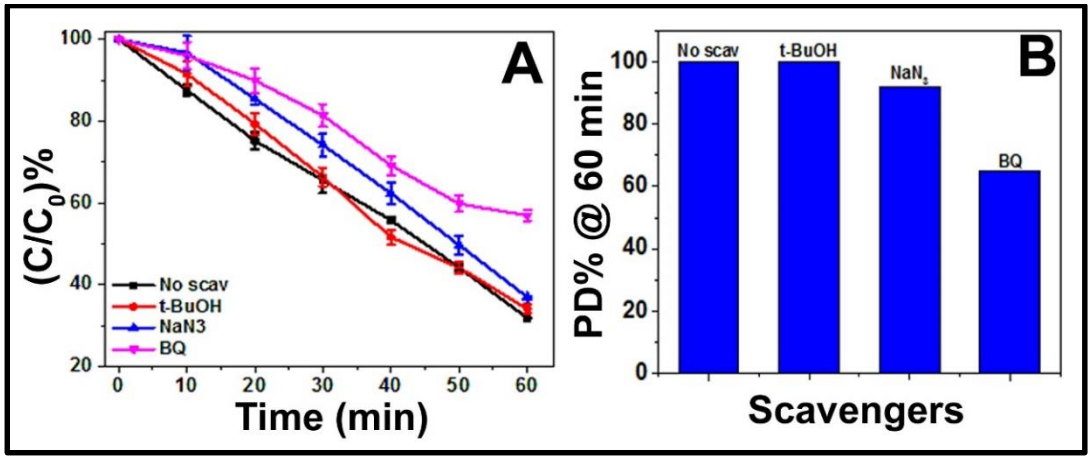

Figure 6.11. (A) VL PD of RhB by TiO_2-CD-C_{60} in the presence of (a): no scavengers; (b): t-BuOH; (c): NaN_3 and (d): BQ. (B): Bar graph representation for the PD% @ 60 min in the presence of scavengers (PD% is normalized to 100% for no scavenger studies).

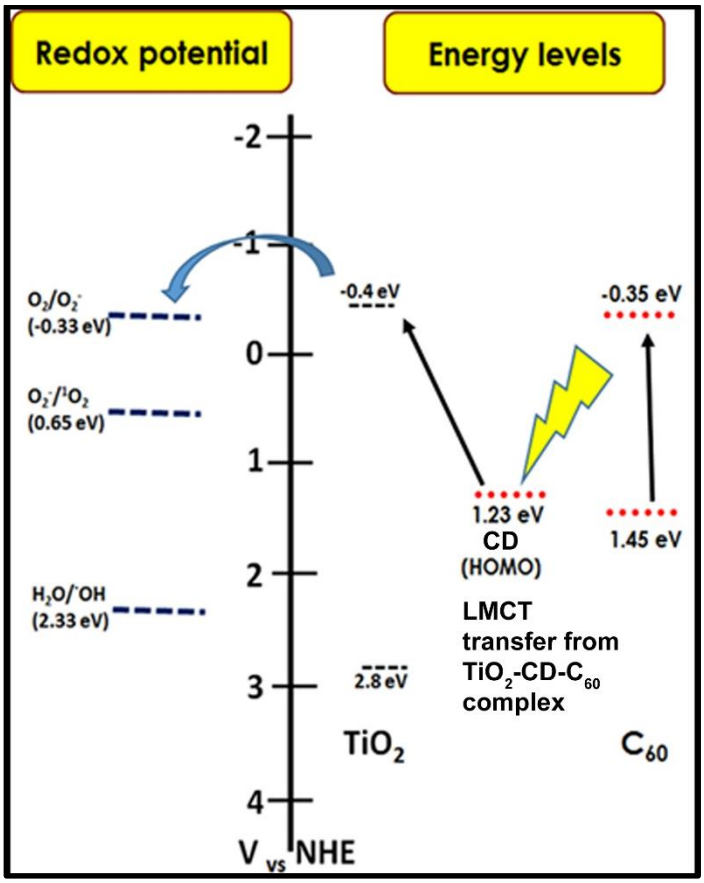

Figure 6.12. Scheme for the mechanism of ROS formation in the VL PD of RhB by TiO_2-CD-C_{60}1.5

6.3.4. Characterization of TiO_2-CD-rGO

FTIR spectra of TiO_2, CD-rGO and TiO_2-CD-rGO are shown in Figure 6.13A. In the FTIR spectrum of TiO_2, the broad peaks at 3500 cm^{-1} and 1640 cm^{-1} corresponding to the surface -OH groups stretching and the bending. The IR spectrum of CD-rGO was dominated by the CD molecule. Peaks at around 3500 and 2940 cm^{-1} in the IR of CD-rGO correspond to the stretching frequencies of -OH and $-CH_2$ groups respectively. The peak near 2940 cm^{-1} in the IR spectrum of TiO_2-CD-rGO was assigned to $-CH_2$ groups of CD. However, the peak intensity of -OH group was decreased in the spectrum of TiO_2-CD-rGO when it should have been the opposite, as both CD and TiO_2 has –OH groups. The reduction in the intensity of -OH stretching peak indicated that the -OH groups of TiO_2 and CD react photochemically to form Ti-O-C bonds (J. Kim & Nichols, 2012). Broadening of peak below 1000 cm^{-1} arose from the stretching of Ti-O-C between

TiO_2 and CD. TGA curves of CD-rGO, TiO_2 and TiO_2-CD-rGO composite are shown in Figure 6.13B. TiO_2 did not show any significant weight loss till 700°C. TiO_2-CD-rGO showed weight losses at temperatures of 300°C and from 500 to 700°C corresponding to the decomposition of CD and rGO respectively. The weight loss of rGO was attributed to the edge oxygen functional carboxylic acid group and the loss was mainly as oxides of carbon. The composite showed a decomposition percentage in between to that of TiO_2 and rGO corresponding to the weight% (1 and 5%) of CD-rGO in the composite. The lower percentages (0.1 and 0.5%) of rGO loading cannot be distinguished by TGA.

The SEM image of the TiO_2-CD-rGO and the XRD patterns of TiO_2, CD-rGO and TiO_2-CD-rGO are given in Figure 6.14. The SEM image (Figure 6.14A) showed that TiO_2 nanoparticles are closely packed onto the CD-rGO. The extent of aggregation of Gr sheets was less in the composite and the dispersion of CD-rGO was higher as a result of CD stabilized rGO. The XRD pattern (Figure 6.14B) of the TiO_2-CD-rGO revealing a highly crystalline pattern, CD-rGO the peaks at 25.6°, 37.9°, 48.1° and 54° are assigned to the (101), (004), (200) and (105) facets of anatase TiO_2. The absence of the broad rGO peak around 23° (Figure 6.14B(b)) indicates that there was no stacking of Gr sheets in the composite.

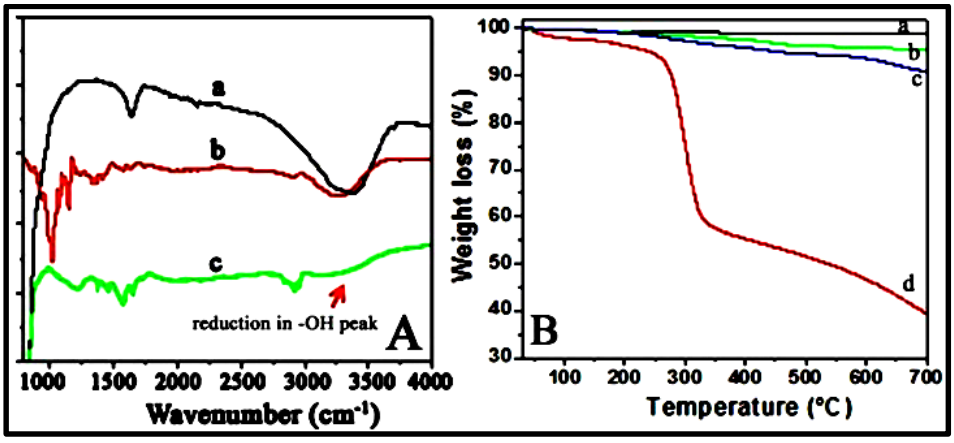

Figure 6.13. (A): FTIR of (a): TiO_2; (b): CD-rGO and (c) TiO_2-CD-rGO; (B): TGA curves of (a): TiO_2; (b): TiO_2-CD-rGO1; (c): TiO_2-CD-rGO5 and (d): CD-rGO under N_2 atmosphere.

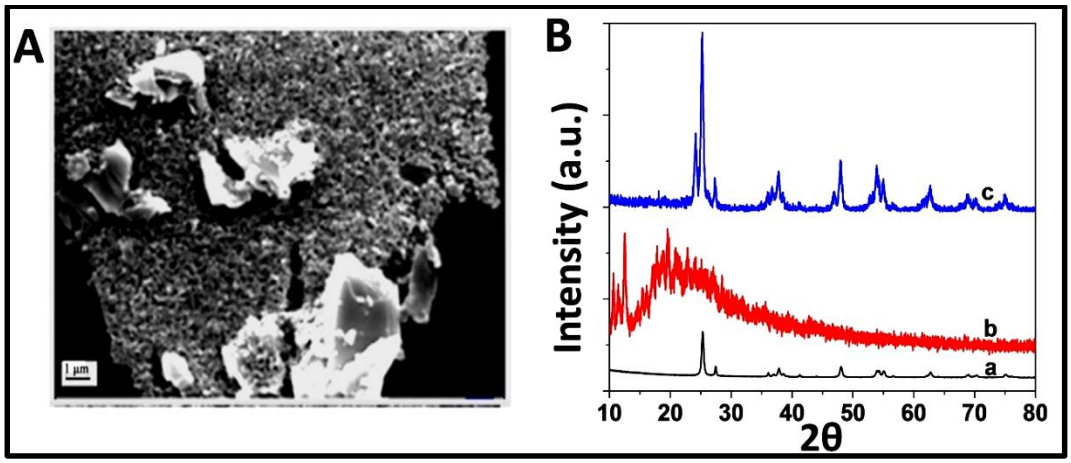

Figure 6.14. (A): SEM image of TiO_2-CD-rGO composite (B): XRD pattern of (a): TiO_2; (b): CD-rGO and (c):TiO_2-CD-rGO.

TEM images of the TiO_2-CD-rGO are shown in Figure 6.15 which showed thin Gr sheets with TiO_2 nanoparticles (Figure 6.15) on it, thus confirming that the TiO_2 nanoparticles are attached onto individual CD-rGO. Thus the characterization results confirm the formation of TiO_2-CD-rGO and show that the structure is of TiO_2 nanoparticles anchored onto CD stabilized CD-rGO due to the photochemical reaction of TiO_2 and CD. Based on the results, the mechanism of interaction between rGO, CD and TiO_2 is explained as follows. The residual oxygen functional groups of rGO especially in the edges interact with either the primary or secondary hydroxyl groups of CD molecules (K. Liu et al., 2008) by hydrogen bonding. Apart from hydrogen bonding, van der Waals force between the main skeleton of rGO and the hydrophobic part of the CD synergistically enhance the interaction between rGO and CD (Guo et al., 2010). Liu et al. (K. Liu et al., 2008) suggested a similar type of interaction between carbon nanotubes and CD self-assembly.

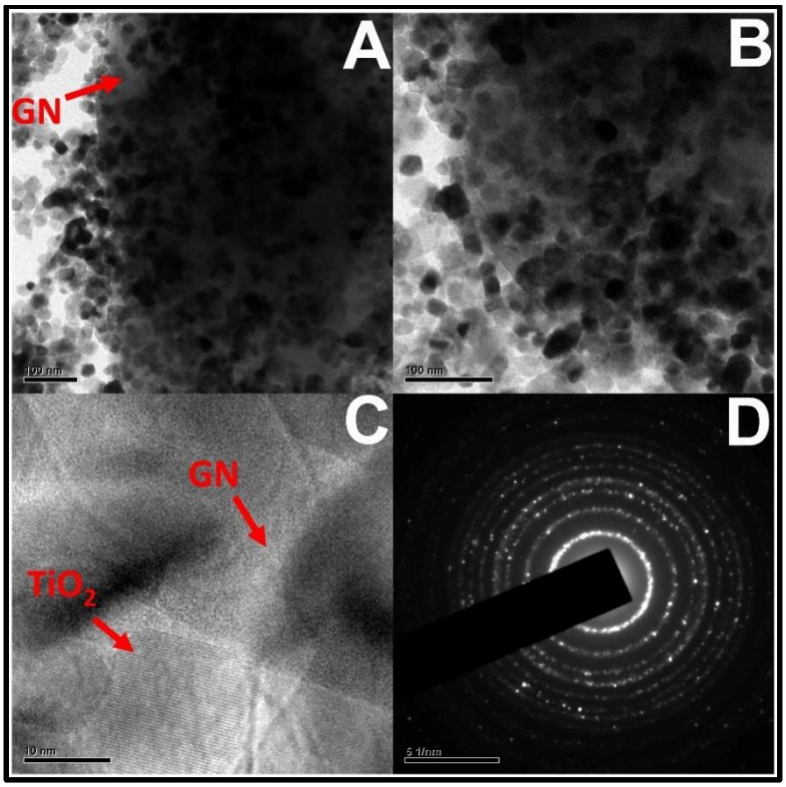

Figure 6.15**.** TEM images of different magnifications of TiO_2-CD-rGO. The images show TiO_2 nanoparticles anchored on CD-rGO. Images A, B &C shows densely packed TiO_2 on to CD-rGO.

On irradiation TiO_2 and CD-rGO with sunlight, photogenerated e-h pairs are produced on the surface of TiO_2, which are scavenged by the polyhydroxyl CD (Miedaner et al., 2005; X. Zhang et al., 2011) leading to the formation of Ti-O-C bond which is evident in the FTIR spectra and the interaction between CD-rGO and TiO_2 is evident from the SEM and TEM images, also. An illustrative mechanism of the formation of TiO_2-CD-rGO is given in Figure 6.16.

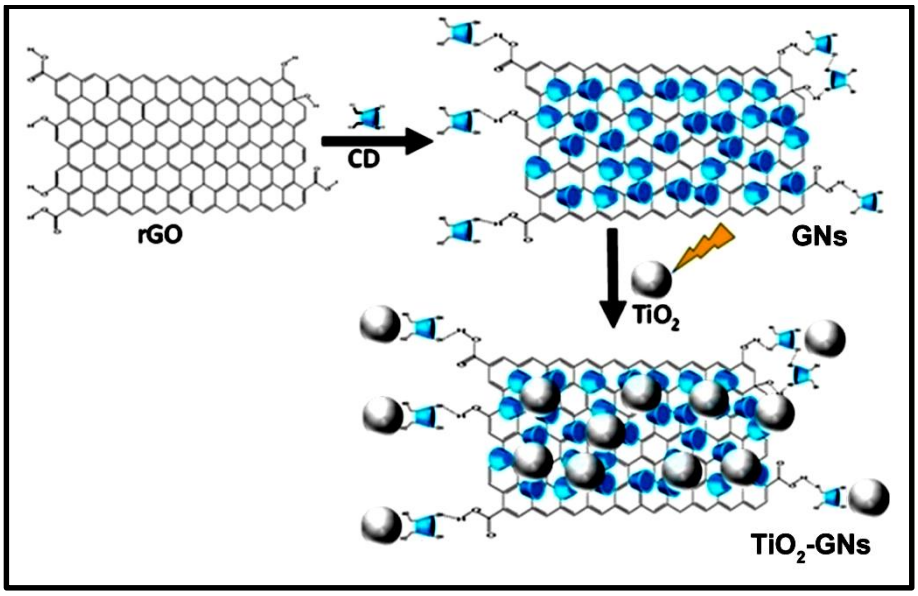

Figure 6.16. Schematic of the mechanism for the formation of TiO_2-CD-rGO composite.

Solid state PL spectra of bare TiO_2, TiO_2-CD0.5, TiO_2-CD-rGO0.1 and TiO_2-CD-rGO0.5 excited at 290 nm are provided in Figure 6.17A. TiO_2 showed PL emission with a peak around 430 nm, due to photogenerated e-h recombination. The PL intensity of TiO_2-CD-rGO was quenched compared to that of the bare TiO_2 indicating reduced charge recombination in the composite. In other words, PLQY of TiO_2-CD-rGO0.5 is 1.74% while for TiO_2-CD it was 2.04. The reduction in PLQY clearly supports the benefits of rGO (Fan et al., 2012; S. Liu et al., 2012; H. Zhang et al., 2010). It is known that efficient charge transfer between TiO_2 and CD-rGO is due to the surface conjugation (d-π conjugate) of Gr with the coordinately unsaturated Ti atoms. It is evident from the PL spectra that the emission intensity of TiO_2-CD0.5 is lower than that of bare TiO_2.

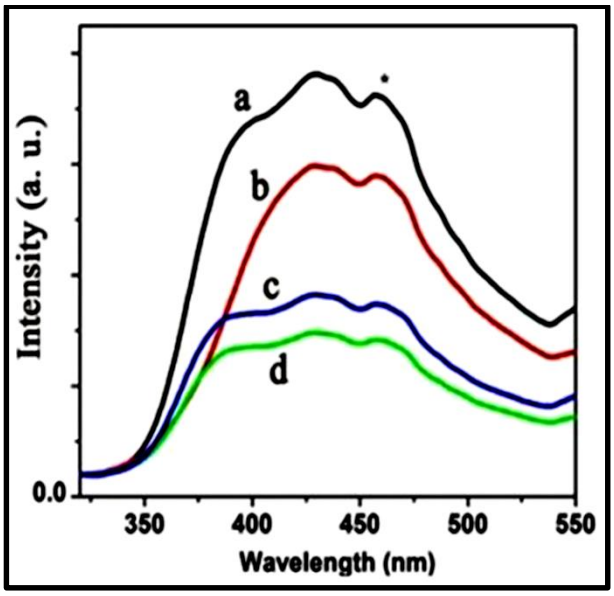

Figure 6.17. Solid state PL spectra of (a) TiO_2; (b) TiO_2-CD-rGO0s.1; (c) TiO_2-CD0.5 and (d) TiO_2-CD-rGO0.5 excited at 290 nm.

6.3.5. Photodegradation studies of TiO_2-CD-rGO

The PC efficiency was investigated using the VL PD of the MB dye. The PC efficiency follows the order of TiO_2-CD-rGO0.5 > TiO_2-CD-rGO2.5 ≈ TiO_2-CD-rGO1 > physical mixture (PM) TiO_2+rGO0.5 > TiO_2-CD-rGO0.1 > TiO_2-CD-rGO5 ≈ TiO_2 (Figure 6.18). At 60 min, the residual MB with the bare TiO_2 and TiO_2-CD-rGO0.5 were ~81.5 and 52%, respectively. The results of the PD reactions are given in Figure 6.18A & B. The rate constant (Table 6.2) of TiO_2-CD-rGO0.5 (~0.01 min^{-1}) is 3.3 and 1.5 times higher compared to that of the bare TiO_2 (0.003 min^{-1}) and the PM of TiO_2 & rGO0.5% (0.0066 min^{-1}), respectively. The higher activity of the composite from that of the PM indicated the presence of better interaction between TiO_2 and rGO through CD and may be due to the covalent bond formation between TiO_2 and CD (X. Zhang et al., 2011) in the composite.

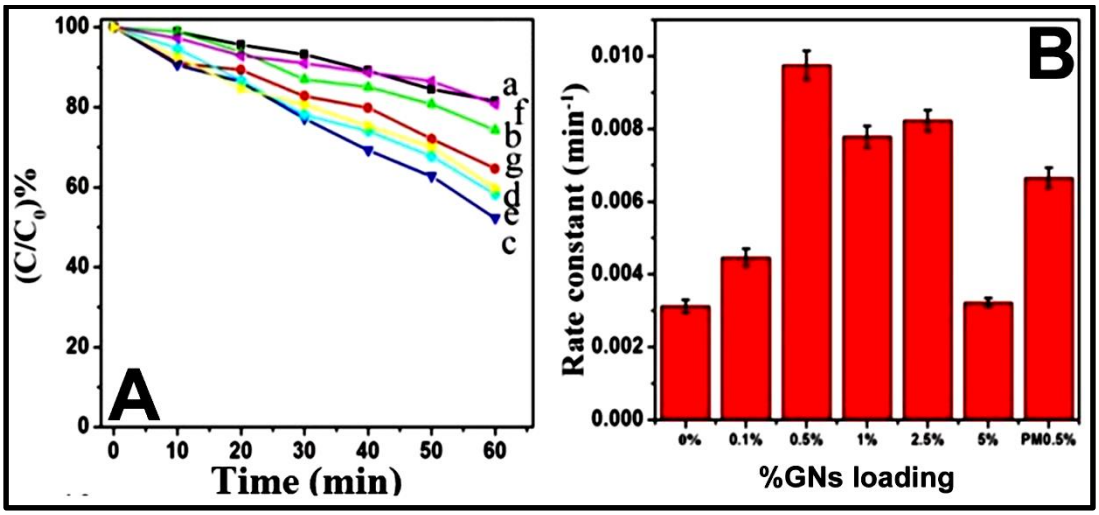

Figure 6.18. (A): VL PD of MB in presence of (a) TiO_2; (b) TiO_2-CD-rGO0.1; (c) TiO_2-CD-rGO0.5; (d) TiO_2-CD-rGO1; (e) TiO_2-CD-rGO2.5; (f) TiO_2-CD-rGO5 and (g) PM TiO_2-rGO0.5 (B): Rate constant values of TiO_2 and TiO_2-CD-rGO.

Table 6.2. Rate constants for the VL PD of MB in the presence of TiO_2 or TiO_2-CD-rGO composites.

Photocatalysts	**Rate constant (min^{-1})**
TiO_2	0.0031± 0.00017
TiO_2-CD-rGO0.1	0.0044 ± 0.00023
TiO_2-CD-rGO0.5	0.0097 ± 0.0004
PM TiO_2-CD-rGO0.5	0.0066 ± 0.00028
TiO_2-CD-rGO2.5	0.0082± 0.0003
TiO_2-CD-rGO5	0.0032±0.00012

The composites, TiO_2-CD-rGO0.5 and TiO_2-CD-rGO2.5, display 10 and 52% adsorption of MB respectively, while the adsorption by bare TiO_2 was 4%. There were no significant changes in the BET specific surface area (51.5 and 56.34 $m^2 g^{-1}$ for TiO_2 and TiO_2-CD-rGO0.5 respectively, Table 6.3). The control CD-rGO of 0.5% rGO exhibited 9% adsorption. Therefore, the improved adsorption exhibited by the composite is assigned to the selective adsorption of MB by rGO due to the π-π interaction (H. Zhang et al., 2010). However, it should be noted that the PMTiO_2+rGO0.5 showed lower adsorption (~3.5%) compared to that of the TiO_2-CD-rGO0.5. The result suggested that the CD molecules prevent the

aggregation of rGO in the composite thus enhancing the adsorption. PD efficiency of MB as a function of CD-rGO% at 60 min is given Figure 6.19.

Table 6.3. BET SA of TiO_2 and TiO_2-CD-rGO with varying amount of CD-rGO

Sample	BET SA (m^2/g)	Pore volume (cm^3/g)	Pore size (nm)
TiO_2	55.1	0.268	19.46
TiO_2-CD-rGO0.5	56.2	0.286	19.55

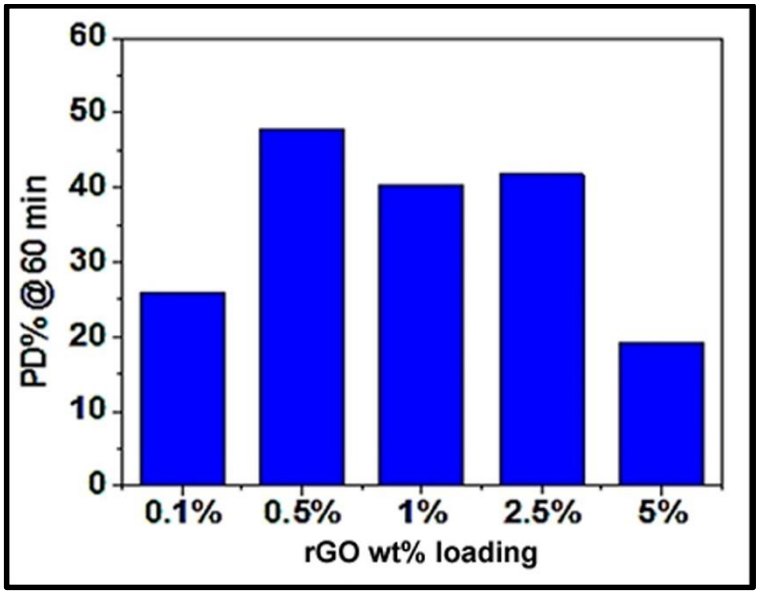

Figure 6.19. PD efficiency of MB as a function of rGO weight% at 60 min.

In order to explore the PC activity, VL PD of 4CP was conducted and the order of PC activity (Figure 6.20A & B) was as follows: TiO_2-CD-rGO1 > TiO_2-CD-rGO0.5 > TiO_2 > TiO_2-CD-rGO2.5. TiO_2-CD-rGO1 shows 43.5% of PD while it was 33% for the control TiO_2. Removal of 4CP was due to the combined effect of adsorption and PD was ~ 47 and 36% for TiO_2-CD-rGO1 and TiO_2 respectively. The degradation of 4CP (Mukthar Ali & Sandhya, 2014) 4CP was greatly enhanced in the presence of O_2 (mainly due to $^1O_2$ and to some extent by $O_2^{\bullet-}$). Formation of $^1O_2$ and $O_2^{\bullet-}$ was remarkably enhanced by the presence of C_{60} in the TiO_2-CD-C_{60} composite (Mukthar Ali & Sandhya, 2014).

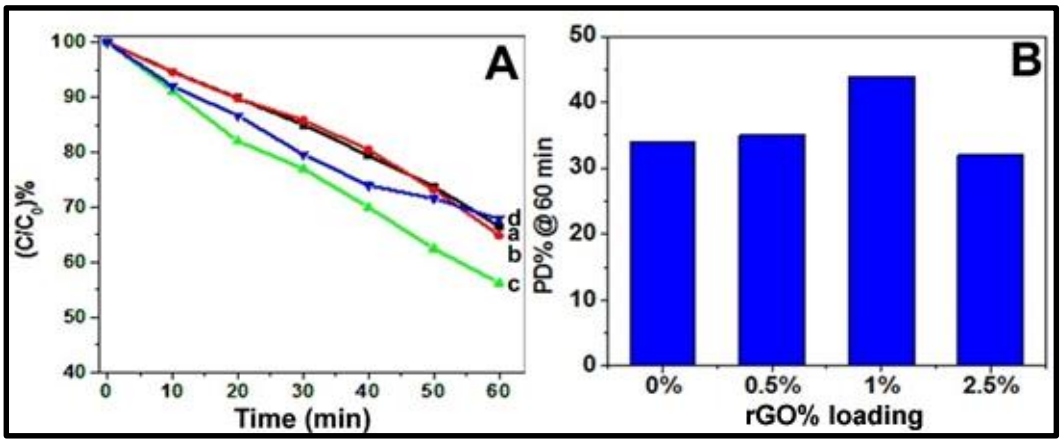

Figure 6.20. (A) VL PD of 4CP by (a): TiO_2; (b): TiO_2-CD-rGO0.5; (c): TiO_2-CD-rGO1 and (d): TiO_2-CD-rGO2.5. (B) Effect of CD-rGO% loading in the VL PD of 4CP at 60 min.

To understand the charge transfer resistance between the interfaces, EIS measurements are performed and the obtained Nqyuist plots are given in Figure 6.21. The smaller semicircle for TiO_2-CD-rGO0.5 indicated the effective charge transfer across the interfaces whereas the charge transfer resistance was higher for bare TiO_2. Arc radius of the semicircle indicates charge transfer resistance at the electrode interface, smaller the semicricle, smaller is the charge transfer resistance. The lower charge transfer resistance shall be attributed to the presence of rGO in TiO_2-CD-rGO0.5. Size of the semicircle of TiO_2-CD-rGO0.5 suggested that improved charge transfer and lower charge transfer resistance at the interfaces CD-rGO.

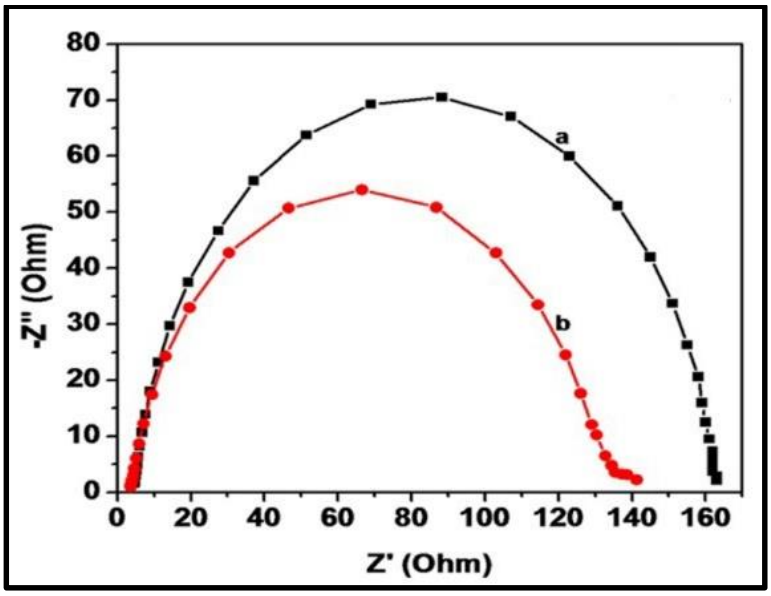

Figure 6.21. Nqyuist plots for (a) TiO_2 and (b) TiO_2-CD-rGO0.5.

6.3.6. Estimation of ROS in the photodegradation of RhB by TiO_2-CD-rGO

Scavenger studies in the VL PD of RhB for the photocatalyst TiO_2-CD-rGO0.5 was conducted and the results of scavenger studies are given in Figure 6.22. The actual PD at 60 min with no scavenger is 51.5% which was considered 100% for calculation purpose. The PD at 60 min in the presence of scavengers t-BuOH, NaN_3 and BQ were 100, 61 and 100%, respectively. Non-suppression of PD was observed with t-BuOH or with BQ suggesting nil contribution from •OH and O_2•− respectively, while with NaN_3 showed that there was ~39% contribution corresponding to $^1O_2$.

Based on the formation of ROS in VL PD of RhB, a mechanism was proposed (Figure 6.23) for the formation of the ROS. When the composite was excited with VL, apart from dye sensitization mechanism, there can be a possible excitations due to LMCT excitation from HOMO of CD in the complex to the CB of TiO_2. The excited electrons in the CB of TiO_2 was transferred to the highly electron accepting rGO nanosheet (work function of Gr is 4.7 eV). Since the rGO sheet is covered with TiO_2 particles, photoexcited electrons from LMCT process can immediately transfer the electrons to Gr sheets.

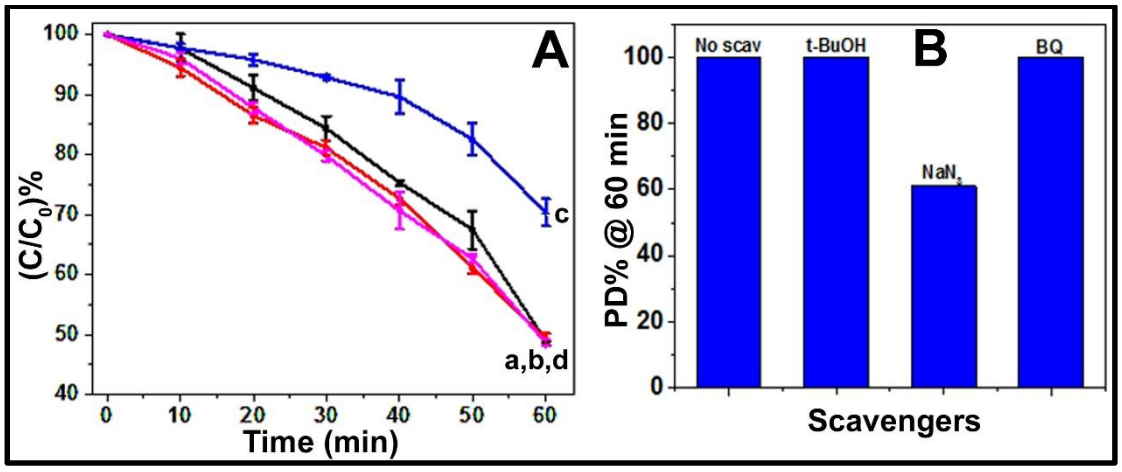

Figure 6.22. (A) VL PD of RhB by TiO_2-CD-rGO in the presence of (a): no scavengers; (b): t-BuOH; (c): NaN_3 and (d): BQ. (B): Bar graph representation for the PD% @ 60 min in the presence of scavengers (PD% is normalized to 100% for no scavenger studies).

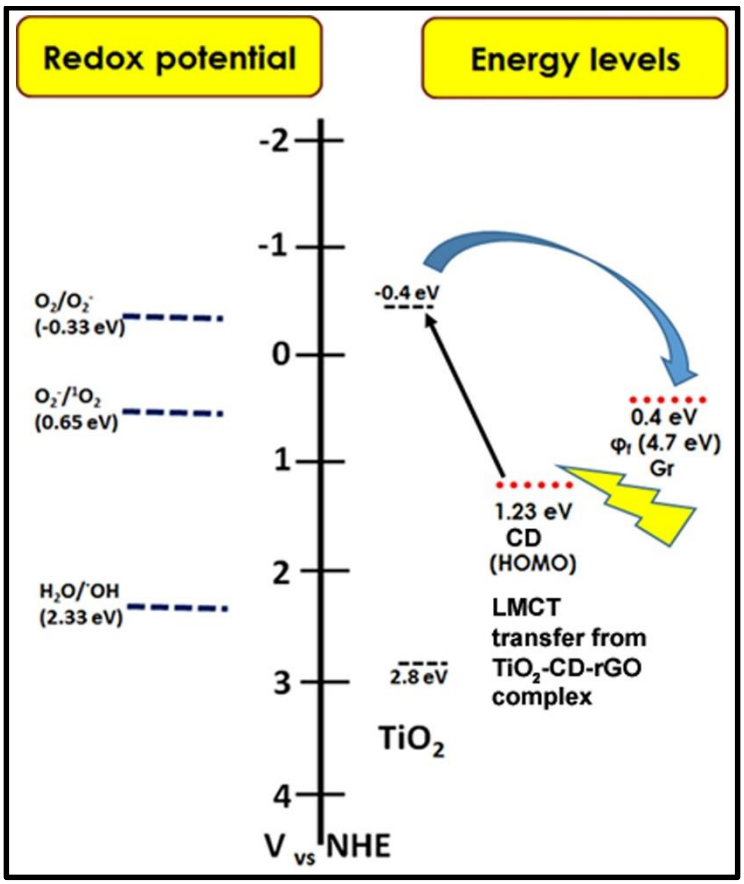

Figure 6.23. Scheme for the mechanism of ROS formation in the VL PD of RhB by TiO_2-CD-rGO.

Incorporation of Gr can enhance the formation of $^1O_2$ as proven by Khan and Wojtoniszak. (A. U. Khan, 1970; Wojtoniszak et al., 2013). Then the electrons in the rGO sheet may produce $^1O_2$, since Gr sheets facilitate the triplet state formation due to faster ISC process. As a result it could not form $O_2^{\bullet-}$.

6.4. Conclusions

TiO_2-CD-C_{60} and TiO_2-CD-rGO composites were successfully prepared using CD as linker molecule by a green photoirradiation method. Both these composites showed reduced charge recombination compared to that of control TiO_2 and TiO_2-CD. With TiO_2-CD-C_{60}1.5 composite, the PD of MB and 4CP significantly increased (~2 and 5 times respectively) compared to that of control TiO_2. The VL PD of RhB was mainly due to $O_2^{\bullet-}$ and $^1O_2$ ROS. The enhanced PC activity of the composite was attributed to its LMCT VL absorption, reduced photogenerated e-h recombination and the resultant increased charge separation due to electron transfer from TiO_2 to C_{60} and hole scavenging by CD. In TiO_2-CD-rGO composites, PC efficiency of TiO_2-CD-rGO0.5 increased to 3 times higher than that of the control TiO_2 for the PD of MB while in the PD of 4CP, TiO_2-CD-rGO1 showed best PC activity. The ROS involved in the VL PD of RhB by TiO_2-CD-rGO was $^1O_2$. Higher PC activity of the composite was attributed to the synergistic effect of reduced charge recombination, enhanced photoexcited electron transfer, effective charge separation and better electron transport.

CHAPTER 7
SUMMARY AND HIGHLIGHTS

7.1. Summary

SMPD is one of the fitting solution to the environmental issues, especially, to the waste-water treatment and pollution in water bodies. To harvest the VL energy, which is ~45% of the total from the solar irradiation, it is essential to develop photocatalysts which are VL active, photostable and with good charge-carrier transport properties. TiO_2 is a highly photostable semiconductor photocatalyst, with good charge carrier transport and hence it has been chosen for our studies. The major draw-back of TiO_2 is its lack of ability to absorb the VL or light beyond 400 nm. In our work, N-doped TiO_2, TiO_2 composites with Gr, MoS_2, C_{60} or C-dot were synthesized to achieve the VL absorption and to improve the charge carrier transport and separation in an attempt to improve its VL PC properties. Each modified TiO_2 or TiO_2 composite was characterized thoroughly for its structure, composition, morphology etc. The PC property were studied using the VL PD of various dyes/ pollutants and the involvement of ROS in the VL PD of RhB. Based on the results obtained for the all the TiO_2 based photocatalyst few conclusions were drawn. Here in this chapter we are listing out the highlights, summary and conclusions of the work.

7.2. Highlights

The major outcomes of the thesis are

- Novel or green methods were used to successfully prepare various hybrid-TiO_2 photocatalysts with materials like graphene & fullerene, MoS_2 or C-dot and N-doped TiO_2. All the composites demonstrated improved VL PC activities than their respective controls.

- Selectivity in photodegradation was observed for TiO_2 (001)-graphene composites and is attributed to the high quality graphene formed in-situ by the photoirradiation method.
- In-situ nitrogen doping of TiO_2 was achieved by solvent NMP using a single step method.
- Few layered MoS_2 was integrated into the TiO_2-MoS_2 composites using a novel molybdenum-sulfur cluster, $(NH_4)_2\ Mo_3S_{13}.2H_2O$, as MoS_2 precursor and in a single step procedure.
- C-dots with high PLQY (25%).was synthesized from β-cyclodextrin using P2O5 method.
- A green method of preparing P25-CD-GN and P25-CD-C_{60} was demonstrated.
- Among all composites prepared, TiO_2-MoS_2 composites showed highest PD (94%) of RhB followed by aN-TiO_2 & P25/C-dot (80% each) and HRTiO_2-Gr (74%).
- It was found that •OH radical (formed from TiO_2) leads to mineralization of RhB while other ROSs lead the PD via decolouration pathway and this was attributed to its higher oxidation potential.
- Mineralization of RhB was achieved by only two of composites such as HRTiO_2-Gr and P25/C-dot, interestingly both composites formed •OH (Table 7.1) during the PD of RhB while others did not. Therefore, we assume •OH with its high oxidation potential plays a major role in the PD of RhB mineralization.
- P25-CD-C_{60} degraded 4-CP, a colorless pollutant, very efficiently (~77%) which was attributed to the presence of fullerene.

Table 7.1. Comparison of VL PD of RhB by various photocatalysts and their ROS contribution.

Photocatalyst	**PD%**	**•OH% contribution**	**O_2•−% contribution**	**$^1O_2$% contribution**
P25	47 ±2	3	13	0.5
TiO_2-CD-C_{60}1.5	68	-	24	5
TiO_2-CD-rGO0.5	51 ±2	-	-	20
P25/C-dot	80 ±1	27	18	16
HRTiO_2-Gr10	74 ±3	24	-	24
aN-TiO_2	80 ±1	-	17	62
TMS0.7	94 ±1	-	32	27

7.3. Future work

To fully understand the reaction mechanism of the VL PD irrespective of the pollutant used, formation of charge carriers, e-h, can be studied using advanced electron paramagnetic resonance (EPR) technique. These techniques are important to study the versatility of the composites in other SMPC applications like H_2 generation and solar cells.

REFERENCES

1. Afanasiev, P., Xia, G.-F., Berhault, G., Jouguet, B., & Lacroix, M. (1999). Surfactant-Assisted Synthesis of Highly Dispersed Molybdenum Sulfide. *Chemistry of Materials*, *11*(11): 3216–3219.

2. Agrios, A. G., Gray, K. A., & Weitz, E. (2004). Narrow-band irradiation of a homologous series of chlorophenols on TiO_2: Charge-transfer complex formation and reactivity. *Langmuir*, *20*(14): 5911–5917.

3. Akpan, U. G., & Hameed, B. H. (2010). The advancements in sol-gel method of doped-TiO_2 photocatalysts. *Applied Catalysis A: General*, *375*(1): 1–11.

4. Allen, M. (2009). Honeycomb carbon -- A study of graphene. Journal of the *American Chemical Society*, 110(1): 184.

5. Alothman, Z. A. (2012). A review: Fundamental aspects of silicate mesoporous materials. *Materials*, *5*(12): 2874–2902.

6. Alvaro, M., Carbonell, E., Fornés, V., & García, H. (2006). Enhanced photocatalytic activity of zeolite-encapsulated TiO_2 clusters by complexation with organic additives and N-doping. *ChemPhysChem*, *7*(1): 200–205.

7. Anandan, S., Ikuma, Y., & Murugesan, V. (2012). Highly active rare-earth-metal La-doped photocatalysts: Fabrication, characterization, and their photocatalytic activity. *International Journal of Photoenergy*, *2012*, Article ID 921412.

8. Anpo, M., & Takeuchi, M. (2003). The design and development of highly reactive titanium oxide photocatalysts operating under visible light irradiation. *Journal of Catalysis*, *216*(1-2): 505–516.

9. Arbogast, J. W., Foote, C. S., & Kao, M. (1992). Electron transfer to triplet fullerene $_{C60}$. *Journal of the American Chemical Society*, *114*(6): 2277–2279.

10. Asahi, R., Morikawa, T., Irie, H., & Ohwaki, T. (2014). Nitrogen-doped titanium dioxide as visible-light-sensitive photocatalyst: Designs, developments, and prospects. *Chemical Reviews*, *114*(19): 9824–9852.

11. Asahi, R., Morikawa, T., Ohwaki, T., Aoki, K., & Taga, Y. (2001). Visible-light photocatalysis in nitrogen doped titanium oxides. *Science*, *293*(5528): 269–271.

12. Bai, S., Wang, L., Chen, X., Du, J., & Xiong, Y. (2014). Chemically exfoliated metallic MoS_2 nanosheets: A promising supporting co-catalyst for enhancing the photocatalytic performance of TiO_2 nanocrystals. *Nano Research*, *8*(1): 175–183.

13. Balcerski, W., Ryu, S. Y., & Hoffmann, M. R. (2007). Visible-light photoactivity of nitrogen-doped TiO_2: Photo-oxidation of HCO_2H to CO_2 and H_2O. *The Journal of physical chemistry C*, *111*(42): 15357–15362.

14. Banerjee, S., Pillai, S. C., Falaras, P., O'Shea, K. E., Byrne, J. A., & Dionysiou, D. D. (2014). New Insights into the Mechanism of Visible Light Photocatalysis. *The Journal of Physical Chemistry Letters*, *5*(15): 2543–54.

15. Barolo, G., Livraghi, S., Chiesa, M., Paganini, M. C., Barolo, G., Livraghi, S., Giamello, E. (2012). This is an author version of the contribution published on : Questa è la versione dell ' autore dell ' opera : The definitive version is available at : La versione definitiva è disponibile alla URL : Mechanism of the photoactivity under visible light of N, *19*(3): 1–24.

16. Bell, N. J., Ng, Y. H., Du, A., Coster, H., Smith, S. C., & Amal, R. (2011). Understanding the Enhancement in Photoelectrochemical Properties of Photocatalytically Prepared TiO_2 -Reduced Graphene Oxide Composite. *The Journal of physical chemistry C, 115*(13): 6004–6009.

17. Bhaisare, M. L., Talib, A., Khan, M. S., Pandey, S., & Wu, H. F. (2015). Synthesis of fluorescent carbon dots via microwave carbonization of citric acid in presence of tetraoctylammonium ion, and their application to cellular bioimaging. *Microchimica Acta*, *182*(13-14): 2173–2181.

18. Blake, D. M., Maness, P.-C., Huang, Z., Wolfrum, E. J., Huang, J., & Jacoby, W. a. (1999). Application of the Photocatalytic Chemistry of Titanium Dioxide to Disinfection and the Killing of Cancer Cells. *Separation & Purification Reviews*, *28*(1): 1–50.

19. Borgarello, E., Kiwi, J., Graetzel, M., Pelizzetti, E., & Visca, M. (1982). Visible light induced water cleavage in colloidal solutions of chromium-doped titanium dioxide particles. *Journal of the American Chemical Society*, *104*(11): 2996–3002.

20. Boschloo, G. K. (1997). Photoelectrochemical Study of Thin Anatase TiO_2 Films Prepared by Metallorganic Chemical Vapor Deposition. *Journal of The Electrochemical Society, 144*(4): 1311-7.

21. Bourlinos, A. B., Stassinopoulos, A., Anglos, D., Zboril, R., Georgakilas, V., & Giannelis, E. P. (2008). Photoluminescent carbogenic dots. *Chemistry of Materials*, *20*(14): 4539–4541.

22. Bourlinos, A. B., Stassinopoulos, A., Anglos, D., Zboril, R., Karakassides, M., & Giannelis, E. P. (2008). Surface functionalized carbogenic quantum dots. *Small*, *4*(4): 455–458.

23. Chang, X., Gondal, M. A., Al-Saadi, A. A., Ali, M. A., Shen, H., Zhou, Q., Ji, G. (2012). Photodegradation of Rhodamine B over unexcited semiconductor compounds of BiOCl and BiOBr. *Journal of Colloid and Interface Science*, *377*(1): 291–298.

24. Chao, C., Weimin, C., Mingce, L., Baoxue, Z., Yahui, W., Deyong, W., & Yujie, F. (2010). Synthesis of Visible-Light Responsive Graphene Oxide/TiO_2 Composites with p/n Heterojunction, *4*(11): 6425–6432.

25. Chen, C., Ma, W., & Zhao, J. (2010). Semiconductor-mediated photodegradation of pollutants under visible-light irradiation. *Chemical Society Reviews*, *39*(11): 4206–19.

26. Chen, F., Zou, W., Qu, W., & Zhang, J. (2009). Photocatalytic performance of a visible light TiO_2 photocatalyst prepared by a surface chemical modification process. *Catalysis Communications*, *10*(11): 1510–1513.

27. Chen, J. S., Tan, Y. L., Li, C. M., Cheah, Y. L., Luan, D., Madhavi, S., Lou, X. W. (2010). Constructing hierarchical spheres from large ultrathin anatase TiO_2 nanosheets with nearly 100% exposed (001) facets for fast reversible lithium storage. *Journal of the American Chemical Society*, *132*(17): 6124–6130.

28. Chen, X., Liu, L., Yu, P. Y., & Mao, S. S. (2011). Increasing solar absorption for photocatalysis with black hydrogenated titanium dioxide nanocrystals. *Science (New York, N.Y.)*, *331*(6018): 746–50.

29. Choi, W., Termin, A., & Hoffmann, M. R. (1994). The Role of Metal Ion Dopants in Quantum-Sized TiO_2: Correlation between Photoreactivity and Charge Carrier Recombination Dynamics. *The Journal of physical chemistry*, *98*(51): 13669–13679.

30. Chowdhury, P., Moreira, J., Gomaa, H., & Ray, A. K. (2012). Visible-solar-light-driven photocatalytic degradation of phenol with dye-sensitized TiO_2: Parametric and kinetic study. *Industrial and Engineering Chemistry Research*, *51*(12): 4523–4532.

31. Cong, Y., Zhang, J., Chen, F., & Anpo, M. (2007). Synthesis and characterization of nitrogen-doped TiO_2 nanophotocatalyst with high visible light activity. *The Journal of physical chemistry C*, *111*(19): 6976–6982.

32. Gopidas, K. R., & Kamat, P. V. (1989). Photochemistry on Surfaces. 4. Influence of Support Material on the Photochemistry of an Adsorbed Dye. *The Journal of physical chemistry*, *93*(14): 6428–6433.

33. Dai, G., Liu, S., Liang, Y., Liu, H., & Zhong, Z. (2013). A simple preparation of carbon and nitrogen co-doped nanoscaled TiO_2 with exposed {0 0 1} facets for enhanced visible-light photocatalytic activity. *Journal of Molecular Catalysis A: Chemical*, *368*(369): 38–42.

34. Daimon, T., & Nosaka, Y. (2007). Formation and behavior of singlet molecular oxygen in TiO_2 photocatalysis studied by detection of near-infrared phosphorescence. *The Journal of physical chemistry C*, *111*(11): 4420–4424.

35. Devi, L. G., & Kavitha, R. (2014). Enhanced photocatalytic activity of sulfur doped TiO_2 for the decomposition of phenol: A new insight into the bulk and surface modification. *Materials Chemistry and Physics*, *143*(3): 1300–1308.

36. Di Valentin, C., Finazzi, E., Pacchioni, G., Selloni, A., Livraghi, S., Paganini, M. C., & Giamello, E. (2007). N-doped TiO_2: Theory and experiment. *Chemical Physics*, *339*(1-3): 44–56.

37. Di Valentin, C., Pacchioni, G., Selloni, A., Livraghi, S., & Giamello, E. (2005). Characterization of paramagnetic species in N-doped TiO_2 powders by EPR spectroscopy and DFT calculations. *The Journal of physical chemistry B*, *109*(23): 11414–11419.

38. Diwald, O., Thompson, T. L., Goralski, E. G., Walck, S. D., & Yates, J. T. (2004). The Effect of Nitrogen Ion Implantation on the Photoactivity of TiO_2 Rutile Single Crystals. *The Journal of Physical Chemistry B*, *108*(1): 52–57.

39. Dozzi, M., & Selli, E. (2013). Specific Facets-Dominated Anatase TiO_2:

Fluorine-Mediated Synthesis and Photoactivity. *Catalysts*, *3*(2): 455–485.

40. Dozzi, M. V., D'Andrea, C., Ohtani, B., Valentini, G., & Selli, E. (2013). Fluorine-Doped TiO_2 Materials: Photocatalytic Activity vs Time-Resolved Photoluminescence. *The Journal of Physical Chemistry C*, *117*(48): 25586–25595.

41. Draper, R. B., & Fox, M. A. (1990). Titanium dioxide photosensitized reactions studied by diffuse reflectance flash photolysis in aqueous suspensions of TiO_2 powder. *Langmuir*, *6*(32): 1396–1402.

42. Du, H., Xie, Y., Xia, C., Wang, W., & Tian, F. (2014). Electrochemical capacitance of polypyrrole–titanium nitride and polypyrrole–titania nanotube hybrids. *New Journal of Chemistry*, *38*(3): 1284.

43. Emeline, A. V., Kuznetsov, V. N., Rybchuk, V. K., & Serpone, N. (2008). Visible-Light-Active Titania Photocatalysts: The Case of N-Doped TiO_2s—Properties and Some Fundamental Issues. *International Journal of Photoenergy*, *2008*: Article ID 258394.

44. Esteves da Silva, J. C. G., & Goncalves, H. M. R. (2011). Analytical and bioanalytical applications of carbon dots. *TrAC - Trends in Analytical Chemistry*, *30*(8): 1327–1336.

45. Etacheri, V., Di Valentin, C., Schneider, J., Bahnemann, D., & Pillai, S. C. (2015). Visible-light activation of TiO_2 photocatalysts: Advances in theory and experiments. *Journal of Photochemistry and Photobiology C: Photochemistry Reviews*, *25*(2015): 1–29.

46. Etacheri, V., Seery, M. K., Hinder, S. J., & Pillai, S. C. (2011). Oxygen rich titania: A dopant free, high temperature stable, and visible-light active anatase photocatalyst. *Advanced Functional Materials*, *21*(19): 3744–3752.

47. Etacheri, V., Seery, M., & Michlits, G. (2013). A Highly Efficient TiO_2-XCx Nano- Heterojunction Photocatalyst for Visible-Light Induced Antibacterial Applications, *ACS Applied Materials & Interfaces*, *5*(5): 1663-1672.

48. Fan, J., Liu, S., & Yu, J. (2012). Enhanced photovoltaic performance of dye-sensitized solar cells based on TiO_2 nanosheets/graphene composite films. *Journal of Materials Chemistry*, *22*(33): 17027.

49. Fang, Y. X., Guo, S. J., Li, D., Zhu, C. Z., Ren, W., Dong, S. J., & Wang,

E. K. (2012). Easy Synthesis and Imaging Applications of Cross-Linked Green Fluorescent Hollow Carbon Nanoparticles. *ACS Nano*, *6*(1): 400–409.

50. Finckh, E. W., Lu, S., Leist, A., Stauf, S., & Lo, S. (1998). Semiporous MoS_2 obtained by the decomposition of thiomolybdate precursors. *Journal of Materials Chemistry, 8*(1): 241–244.

51. Fu, H., Yu, K., Li, H., Li, J., Guo, B., Tan, Y., Zhu, Z. (2015). Enhanced field emission and photocatalytic performance of MoS_2 titania nanoheterojunctions via two synthetic approaches. *Dalton Trans.*, *44*(4): 1664–1672.

52. Fu, H., Zhang, L., Zhang, S., Zhu, Y., & Zhao, J. (2006). Electron spin resonance spin-trapping detection of radical intermediates in N-doped TiO_2-assisted photodegradation of 4-chlorophenol. *The Journal of physical chemistry B*, *110*(7): 3061–3065.

53. Fujishima, a, & Honda, K. (1972). Electrochemical photolysis of water at a semiconductor electrode. *Nature*, *238*(5358): 37–38.

54. Gaya, U. I. (2014). *Heterogeneous Photocatalysis Using Inorganic Semiconductor Solids*. *Springer* (Vol. 1).

55. Geim, A. K., & Novoselov, K. S. (2007). The rise of Graphene, *Nature Materials,* 6: 183–191.

56. Gerrity, D., Ryu, H., Crittenden, J., & Abbaszadegan, M. (2008). Photocatalytic inactivation of viruses using titanium dioxide nanoparticles and low-pressure UV light. *Journal of Environmental Science and Health. Part A, Toxic/hazardous Substances & Environmental Engineering*, *43*(11): 1261–1270.

57. Ghicov, A., Macak, J. M., Tsuchiya, H., & Kunze, J. (2006). Ion Implantation and Annealing for an Efficient N-Doping of TiO_2 Nanotubes, *Nano Letters,* 6(5): 1080-1082.

58. Ghosh, S. K., Srivastava, C., Nath, S., & Celis, J. P. (2013). Simple Formation of Nanostructured Molybdenum Disulfide Thin Films by Electrodeposition. *International Journal of Electrochemistry, 2013,* Article ID 138419, 1–7.

59. Gole, J. L., Stout, J. D., Burda, C., Lou, Y., & Chen, X. (2004). Highly

Efficient Formation of Visible Light Tunable TiO_2 - x N x Photocatalysts and Their Transformation at the Nanoscale. *The Journal of Physical Chemistry B*, *108*(4): 1230–1240.

60. Gong, X.-Q., & Selloni, A. (2005). Reactivity of anatase TiO_2 nanoparticles: the role of the minority (001) surface. *The Journal of Physical Chemistry. B*, *109*(42): 19560–2.

61. Goodeve, C. F., & Kitchener, J. A. (1938). Photosensitisation by titanium dioxide. *Transactions of the Faraday Society*, *34*(570): 570.

62. Gu, L., Wang, J., Cheng, H., Zhao, Y., Liu, L., & Han, X. (2013). One-step preparation of graphene-supported anatase TiO_2 with exposed {001} facets and mechanism of enhanced photocatalytic properties. *ACS Applied Materials & Interfaces*, *5*(8): 3085–93.

63. Guo, Y., Guo, S., Li, J., Wang, E., & Dong, S. (2011). Cyclodextrin-graphene hybrid nanosheets as enhanced sensing platform for ultrasensitive determination of carbendazim. *Talanta*, *84*(1): 60–64.

64. Guo, Y., Guo, S., Ren, J., Zhai, Y., Dong, S., & Wang, E. (2010). Cyclodextrin functionalized graphene nanosheets with high supramolecular recognition capability: Synthesis and host - Guest inclusion for enhanced electrochemical performance. *ACS Nano*, *4*(7): 4001–4010.

65. Habiba, K., Makarov, V. I., Avalos, J., Guinel, M. J. F., Weiner, B. R., & Morell, G. (2013). Luminescent graphene quantum dots fabricated by pulsed laser synthesis. *Carbon*, *64*: 341–350.

66. Han, Z., Wei, L., Pan, H., Li, C., & Chen, J. (2015). Variant effect of graphene sheets and ribbons on photocatalytic activity of TiO_2 sheets/graphene composite. *Journal of Molecular Catalysis A: Chemical*, *398*: 399–406.

67. He, Z., Que, W., Chen, J., Yin, X., He, Y., & Ren, J. (2012). Photocatalytic degradation of methyl orange over nitrogen-fluorine codoped TiO_2 nanobelts prepared by solvothermal synthesis. *ACS Applied Materials and Interfaces*, *4*(12): 6816–6826.

68. Hibble, S. J., & Feaviour, M. R. (2001). An in situ structural study of the thermal decomposition reactions of the ammonium thiomolybdates, $(NH_4)_2Mo_2S_{12}\cdot 2H_2O$ and $(NH_4)_2Mo_3S_{13}\cdot 2H_2O$. *Journal of Materials Chemistry*, *11*(10): 2607–2614.

69. How, G. T. S., Pandikumar, A., Ming, H. N., & Ngee, L. H. (2014). Highly exposed {001} facets of titanium dioxide modified with reduced graphene oxide for dopamine sensing. *Scientific Reports*, *4*: 5044.

70. Hsu, Y. Y., Hsiung, T. L., Paul Wang, H., Fukushima, Y., Wei, Y. L., & Chang, J. E. (2008). Photocatalytic degradation of spill oils on TiO_2 nanotube thin films. *Marine Pollution Bulletin*, *57*(6-12): 873–876.

71. Hu, C., Chen, F., Lu, T., Lian, C., Zheng, S., Hu, Q., Zhang, R. (2014). Water-phase strategy for synthesis of TiO_2-graphene composites with tunable structure for high performance photocatalysts. *Applied Surface Science*, *317*: 648–656.

72. Hu, M., Yang, Y., Gu, X., Hu, Y., Huang, J., & Wang, C. (2014). One-pot synthesis of photoluminescent carbon nanodots by carbonization of cyclodextrin and their application in Ag^+ detection. *RSC Advances*, *4*: 62446–62452.

73. Huang, D., Liao, S., Quan, S., Liu, L., He, Z., Wan, J., & Zhou, W. (2007). Preparation of anatase F doped TiO_2 sol and its performance for photodegradation of formaldehyde. *Journal of Materials Science*, *42*(19): 8193–8202.

74. Hummers Jr, W. S., & Offeman, R. E. (1958). Preparation of Graphitic Oxide. *Journal of the American Chemical Society*, *80*(6): 1339.

75. Ihara, T., Miyoshi, M., Iriyama, Y., Matsumoto, O., & Sugihara, S. (2003). Visible-light-active titanium oxide photocatalyst realized by an oxygen-deficient structure and by nitrogen doping. *Applied Catalysis B: Environmental*, *42*(4): 403–409.

76. Iijima, S. (1991). Helical microtubules of graphitic carbon. *Nature*, *354*(6348): 56–58.

77. Imahori, H., & Sakata, Y. (1997). Donor-Linked Fullerenes: Photoinduced electron transfer and its potential application. *Advanced Materials*, *9*(7): 537–546.

78. Irie, H., Watanabe, Y., & Hashimoto, K. (2003). Nitrogen-Concentration Dependence on Photocatalytic Activity of TiO_2 - x N x Powders. *The Journal of Physical Chemistry B*, *107*(23): 5483–5486.

79. Jańczyk, A., Krakowska, E., Stochel, G., & Macyk, W. (2006). Singlet

oxygen photogeneration at surface modified titanium dioxide. *Journal of the American Chemical Society*, *128*(49): 15574–15575.

80. Jiang, B., Tian, C., Pan, Q., Jiang, Z., Wang, J., Yan, W., & Fu, H. (2011). Enhanced Photocatalytic Activity and Electron Transfer Mechanisms of Graphene / TiO_2 with Exposed { 001 } Facets, *The Journal of Physical Chemistry C,* 115(48): 23718–23725.

81. Jiang, D., Xu, Y., Wu, D., & Sun, Y. (2009). Isocyanate-modified TiO_2 visible-light-activated photocatalyst. *Applied Catalysis B: Environmental*, *88*(1-2): 165–172.

82. Jiang, Z., Liu, D., Jiang, D., Wei, W., Qian, K., Chen, M., & Xie, J. (2014). Bamboo leaf-assisted formation of carbon/nitrogen co-doped anatase TiO_2 modified with silver and graphitic carbon nitride: novel and green synthesis and cooperative photocatalytic activity. *Dalton Transactions*, *43*(36): 13792–802.

83. Joensen, P., Frindt, R. F., & Morrison, S. R. (1986). Single-layer MoS_2. *Materials Research Bulletin*, *21*(4): 457–461.

84. Jong Hyeok, P., Sungwook, K., & Allen, J. B. (2006). Novel Carbon-Doped TiO_2 Nanotube Arrays with High Aspect Ratios for Efficient Solar Water Splitting. *Nano Letters, 6*(1): 24-28.

85. Joung, S. K., Amemiya, T., Murabayashi, M., & Itoh, K. (2006). Relation between photocatalytic activity and preparation conditions for nitrogen-doped visible light-driven TiO_2 photocatalysts. *Applied Catalysis A: General*, *312*(1-2): 20–26.

86. Junwei, W., Wei, Z., Yinqing, Z., & Shuangxi, L. (2007). An efficient two-step technique for nitrogen-doped titanium dioxide synthesizing: Visible-light-induced photodecomposition of methylene blue. *Journal of Physical Chemistry C*, *111*(2): 1010–1014.

87. Kaewgun, S., Mckinney, D., White, J., Smith, A., Tinker, M., Ziska, J., & Lee, B. I. (2009). Study of visible light photocatalytic activity achieved by NMP solvent treatment of polymorphic titania. *Journal of Photochemistry and Photobiology A: Chemistry*, *202*(2-3): 154–158.

88. Kaewgun, S., Nolph, C. A., & Lee, B. I. (2008). Enhancing photocatalytic activity of polymorphic titania nanoparticles by NMP solvent-based ambient condition process. *Catalysis Letters*, *123*(3-4): 173–180.

89. Kalathil, S., Khan, M. M., Ansari, S. A., Lee, J., & Cho, M. H. (2013). Band gap narrowing of titanium dioxide (TiO_2) nanocrystals by electrochemically active biofilms and their visible light activity. *Nanoscale*, *5*(14): 6323–6.

90. Kamat, P. V. (2007). Meeting the clean energy demand: Nanoestructure Architectures for Solar Energy Conversion. *The Journal of Physical Chemistry C, 111*(7): 2834–2860.

91. Kamisaka, H., Adachi, T., & Yamashita, K. (2005). Theoretical study of the structure and optical properties of carbon-doped rutile and anatase titanium oxides. *The Journal of Chemical Physics*, *123*(8): 084704.

92. Kaniyankandy, S., Rawalekar, S., Sen, A., Ganguly, B., & Ghosh, H. N. (2012). Does Bridging Geometry Influence Interfacial Electron Transfer Dynamics? Case of the Enediol-TiO_2 System. *The Journal of Physical Chemistry C, 116*(1): 98-103.

93. Katsumata, K., Matsushita, N., & Okada, K. (2012). Preparation of TiO_2-Fullerene Composites and Their Photocatalytic Activity under Visible Light. *International Journal of Photoenergy*, *2012*: Article ID 256096.

94. Khan, A. U. (1970). Singlet molecular oxygen from superoxide anion and sensitized fluorescence of organic molecules. *Science*, *168*(3930): 476–477.

95. Khan, M. (1988). Catalytic Fixation of Nitrogen by the Photocatalytic CdS/Pt/RuO_2 Particulate System in the Presence of Aqueous $[Ru(Hedta)N_2]^{\ominus}$ Complex. *Angewandte Chemie (International Ed. in English)*, *27*(7): 923–925.

96. Khan, M. M., Ansari, S. a., Pradhan, D., Ansari, M. O., Han, D. H., Lee, J., & Cho, M. H. (2014). Band gap engineered TiO_2 nanoparticles for visible light induced photoelectrochemical and photocatalytic studies. *Journal of Materials Chemistry A*, *2*(3): 637.

97. Kim, J., & Nichols, W. T. (2012). Hierarchically assembled titania-cyclodextrin nano-networks. *Materials Letters*, *67*(1): 11–13.

98. Kim, S., & Choi, W. (2005). Visible-light-induced photocatalytic degradation of 4-chlorophenol and phenolic compounds in aqueous suspension of pure titania: Demonstrating the existence of a surface-complex-mediated path. *The Journal of physical chemistry B*, *109*(11): 5143–5149.

99. Kiran, V., & Sampath, S. (2013). Facile synthesis of carbon doped TiO_2 nanowires without an external carbon source and their opto-electronic properties. *Nanoscale*, *5*(21): 10646.

100. Koeppe, R., & Sariciftci, N. S. (2006). Photoinduced charge and energy transfer involving fullerene derivatives. *Photochemical & Photobiological Sciences : Official Journal of the European Photochemistry Association and the European Society for Photobiology*, *5*(12): 1122–31.

101. Kongkanand, A., Tvrdy, K., Takechi, K., Kuno, M., & Kamat, P. V. (2008). Quantum dot solar cells. Tuning photoresponse through size and shape control of CdSe-TiO_2 architecture. *Journal of the American Chemical Society*, *130*(12): 4007–4015.

102. Konkena, B., & Vasudevan, S. (2012). Covalently linked, water-dispersible, cyclodextrin: Reduced-graphene oxide sheets. *Langmuir*, *28*(34): 12432–12437.

103. Konkena, B., & Vasudevan, S. (2013). Resonance Raman detection and estimation in the aqueous phase using water dispersible cyclodextrin: Reduced-graphene oxide sheets. *Analytical Chemistry*, *85*(10): 5114–5119.

104. Lana-Villarreal, T., Rodes, A., Perez, J. M., & Gomez, R. (2005). A spectroscopic and electrochemical approach to the study of the interactions and photoinduced electron transfer between catechol and anatase nanoparticles in aqueous solution. *Journal of the American Chemical Society, 127*(36): 12601–12611.

105. Lazzeri, M., Vittadini, A., & Selloni, A. (2001). Structure and energetics of stoichiometric TiO_2 anatase surfaces. *Physical Review B*, *63*(15): 155409.

106. Lee, H. U., Lee, Y., Chang, S., Young, S., Son, B., Won, J., Lee, J. (2014). Visible-light-responsive bicrystalline (anatase/brookite) nanoporous nitrogen-doped TiO_2 photocatalysts by plasma treatment, *Chemical Engineering Journal, 254:* 268–275.

107. Li, C. J., Xu, G. R., Zhang, B., & Gong, J. R. (2012). High selectivity in visible-light-driven partial photocatalytic oxidation of benzyl alcohol into benzaldehyde over single-crystalline rutile TiO_2 nanorods. *Applied Catalysis B: Environmental*, *115*(116): 201–208.

108. Li, D., Qin, Q., Duan, X., Yang, J., Guo, W., & Zheng, W. (2013).

General One-pot template-free hydrothermal method to metal oxide hollow spheres and their photocatalytic activities and lithium storage properties. *ACS Applied Materials and Interfaces*, *5*(18): 9095–9100.

109. Li, H., He, X., Liu, Y., Huang, H., Lian, S., Lee, S. T., & Kang, Z. (2011). One-step ultrasonic synthesis of water-soluble carbon nanoparticles with excellent photoluminescent properties. *Carbon*, *49*(2): 605–609.

110. Li, H., Kang, Z., Liu, Y., & Lee, S.-T. (2012). Carbon nanodots: synthesis, properties and applications. *Journal of Materials Chemistry*, *22*(46): 24230.

111. Li, L., Krissanasaeranee, M., Pattinson, S. W., Stefik, M., Wiesner, U., Steiner, U., & Eder, D. (2010). Enhanced photocatalytic properties in well-ordered mesoporous WO_3. *Chemical Communications*, *46*(40): 7620.

112. Li, X., Chen, C., & Zhao, J. (2001). Mechanism of Photodecomposition of H_2O_2 on TiO_2 Surfaces under Visible Light Irradiation, *Langmuir, 17*(13): 4118–4122.

113. Li, X., Wen, J., Low, J., Fang, Y., & Yu, J. (2014). Design and fabrication of semiconductor photocatalyst for photocatalytic reduction of CO_2 to solar fuel. *Science China Materials, 57,* 70-100.

114. Li, Y., Hu, Y., Zhao, Y., Shi, G., Deng, L., Hou, Y., & Qu, L. (2011). An electrochemical avenue to green-luminescent graphene quantum dots as potential electron-acceptors for photovoltaics. *Advanced Materials*, *23*(6): 776–780.

115. Li, Y., Kunitake, T., & Fujikawa, S. (2006). Efficient fabrication and enhanced photocatalytic activities of 3D-ordered films of titania hollow spheres. *The Journal of physical chemistry B*, *110*(26): 13000–13004.

116. Lin, Y., Jiang, Z., Zhu, C., Hu, X., Zhang, X., Zhu, H., Lin, S. H. (2013). C/B codoping effect on band gap narrowing and optical performance of TiO2 photocatalyst: a spin-polarized DFT study. *Journal of Materials Chemistry A*, *1*(14): 4516.

117. Linsebigler, A. L., Linsebigler, A. L., Yates Jr, J. T., Lu, G., Lu, G., & Yates, J. T. (1995). Photocatalysis on TiO_2 Surfaces: Principles, Mechanisms, and Selected Results. *Chemical Reviews*, *95*(3): 735–758.

118. Liu, B., Huang, Y., Wen, Y., Du, L., Zeng, W., Shi, Y., Wang, Y.

(2012). Highly dispersive {001} facets-exposed nanocrystalline TiO_2 on high quality graphene as a high performance photocatalyst. *Journal of Materials Chemistry*, *22*(15): 7484.

119. Liu, G., Wang, X., Wang, L., Chen, Z., Li, F., (Max) Lu, G. Q., & Cheng, H. M. (2009). Drastically enhanced photocatalytic activity in nitrogen doped mesoporous TiO_2 with abundant surface states. *Journal of Colloid and Interface Science*, *334*(2): 171–175.

120. Liu, G., Yang, H. G., Wang, X., Cheng, L., Pan, J., Qing, G., & Lu, M. (2009). Visible Light Responsive Nitrogen Doped Anatase TiO_2 Sheets with Dominant {00} facets derived from TiN. *Journal of the American Chemical Society, 131*(36): 12868–12869.

121. Liu, G., Zhang, X., Xu, Y., Niu, X., Zheng, L., & Ding, X. (2005). The preparation of Zn^{2+}-doped TiO_2 nanoparticles by sol-gel and solid phase reaction methods respectively and their photocatalytic activities. *Chemosphere*, *59*(9): 1367–1371.

122. Liu, K., Fu, H., Xie, Y., Zhang, L., Pan, K., & Zhou, W. (2008). Assembly of β-cyclodextrins acting as molecular bricks onto multiwall carbon nanotubes. *The Journal of physical chemistry C*, *112*(4): 951–957.

123. Liu, Q., Pu, Z., Asiri, A. M., Qusti, A. H., Al-Youbi, A. O., & Sun, X. (2013). One-step solvothermal synthesis of MoS_2/TiO_2 nanocomposites with enhanced photocatalytic H_2 production. *Journal of Nanoparticle Research*, *15*: 2057.

124. Liu, S., Liu, C., Wang, W., Cheng, B., & Yu, J. (2012). Unique photocatalytic oxidation reactivity and selectivity of TiO_2-graphene nanocomposites. *Nanoscale*, *4*(10): 3193–200.

125. Liu, S., Yu, J., & Jaroniec, M. (2010). Tunable Photocatalytic Selectivity of Hollow TiO_2 Microspheres Composed. *Journal of the American Chemical Society, 132*(34): 11914–11916.

126. Liu, T., & Troisi, A. (2013). What makes fullerene acceptors special as electron acceptors in organic solar cells and how to replace them. *Advanced Materials*, *25*(7): 1038–1041.

127. Liu, Y., Dadap, J. I., Zimdars, D., & Eisenthal, K. B. (1999). Study of Interfacial Charge-Transfer Complex on TiO_2 Particles in Aqueous Suspension by Second-Harmonic Generation. *The Journal of Physical Chemistry B*, *103*(13): 2480–2486.

128. Liu, Y., Yu, L., Hu, Y., Guo, C., Zhang, F., & Wen (David) Lou, X. (2012). A magnetically separable photocatalyst based on nest-like γ-Fe_2O_3/ZnO double-shelled hollow structures with enhanced photocatalytic activity. *Nanoscale*, *4*(1): 183–187.

129. Livraghi, S., Paganini, M. C., Giamello, E., Selloni, A., Valentin, C. Di, & Pacchioni, G. (2006). Origin of Photoactivity of Nitrogen-Doped Titanium Dioxide under Visible Light, *Journal of the American Chemical Society, 128*(49): 15666–15671.

130. Lu, N., Zhao, H., Li, J., Quan, X., & Chen, S. (2008). Characterization of boron-doped TiO_2 nanotube arrays prepared by electrochemical method and its visible light activity. *Separation and Purification Technology*, *62*(3): 668–673.

131. Lu, P., Wu, F., & Deng, N. (2004). Enhancement of TiO_2 photocatalytic redox ability by β-cyclodextrin in suspended solutions. *Applied Catalysis B: Environmental*, *53*(2): 87–93.

132. Lu, T., Zhang, R., Hu, C., Chen, F., Duo, S., & Hu, Q. (2013). TiO_2-graphene composites with exposed {001} facets produced by a one-pot solvothermal approach for high performance photocatalyst. *Physical Chemistry Chemical Physics, 15*(31): 12963–70.

133. Luk, C. M., Tang, L. B., Zhang, W. F., Yu, S. F., Teng, K. S., & Lau, S. P. (2012). An efficient and stable fluorescent graphene quantum dot–agar composite as a converting material in white light emitting diodes. *Journal of Materials Chemistry*, *22*(42): 22378.

134. Manish, C., Eda, G., Yamaguchi, H., Voiry, D., Fujita, T., & Chen, M., Department (2011). Photoluminescence from Chemically Exfoliated MoS_2. *Nano Letters*, *11*(12): 5111-5116.

135. Mofareh, A.S., Khan, S.U.M., & Ingler Jr, W. B. (2002). Efficient Photochemical Water Splitting by a Chemically Modified n-TiO_2. *Science, 297*: 2243–2245.

136. Martyanov, I. N., Uma, S., Rodrigues, S., & Klabunde, K. J. (2004). Structural defects cause TiO_2-based photocatalysts to be active in visible light. *Chemical Communications*, *25*(21): 2476–2477.

137. Matsubara, K., Danno, M., Inoue, M., Honda, Y., & Abe, T. (2012).

Characterization of nitrogen-doped TiO_2 powder prepared by newly developed plasma-treatment system. *Chemical Engineering Journal*, 181(182): 754–760.

138. Meng, C. H., Liu, Z. Y., Zhang, T. R., & Zhai, J. (2015). Layered MoS_2 nanoparticles on TiO_2 nanotubes by a photocatalytic strategy for use as high-performance electrocatalysts in hydrogen evolution reactions. *Green Chemistry*, *17*(5): 2764–2768.

139. Meng, Z.-D., Zhu, L., Choi, J.-G., Chen, M.-L., & Oh, W.-C. (2011). Effect of Pt treated fullerene/TiO_2 on the photocatalytic degradation of MO under visible light. *Journal of Materials Chemistry*, *21*(21): 7596.

140. Miedaner, A., Ahrenkiel, P., Himmel, M. E., Curtis, C., & Ginley, D. (2005). Self-Assembly of Photoactive TiO_2-Cyclodextrin Wires, *Journal of the American Chemical Society, 127*(43): 14968–14969.

141. Miyauchi, M., Ikezawa, A., Tobimatsu, H., Irie, H., & Hashimoto, K. (2004). Zeta potential and photocatalytic activity of nitrogen doped TiO_2 thin films. *Physical Chemistry Chemical Physics*, *6*(4): 865–870.

142. Mo, R., Lei, Z., Sun, K., & Rooney, D. (2013). Facile Synthesis of Anatase TiO_2 Quantum-Dot/Graphene-Nanosheet Composites with Enhanced Electrochemical Performance for Lithium-Ion Batteries. *Advanced Materials*, 26: 2084–2088.

143. Morales-Torres, S., Pastrana-Martinez, L. M., Figueiredo, J. L., Faria, J. L., & Silva, A. M. T. (2012). Design of graphene-based TiO_2 photocatalysts-a review. *Environmental Science and Pollution Research*, *19*(9): 3676–3687.

144. Morikawa, T., Asahi, R., Ohwaki, T., Aoki, K., & Taga, Y. (2001). Band-gap narrowing of titanium dioxide by nitrogen doping. *Japanese Journal of Applied Physics Part 2-Letters*, *40*(6A): L561–L563.

145. Morikawa, T., Ohwaki, T., Suzuki, K. ichi, Moribe, S., & Tero-Kubota, S. (2008). Visible-light-induced photocatalytic oxidation of carboxylic acids and aldehydes over N-doped TiO_2 loaded with Fe, Cu or Pt. *Applied Catalysis B: Environmental*, *83*(1-2): 56–62.

146. Morrison, S. R. (1967). Chemical Role of Holes and Electrons in ZnO Photocatalysis. *The Journal of Chemical Physics*, *47*(4): 1543.

147. Mrowetz, M., Balcerski, W., Colussi, A. J., & Hoffmann, M. R. (2004). Oxidative power of nitrogen-doped TiO_2 photocatalysts under visible illumination. *The Journal of physical chemistry B*, *108*(45): 17269–17273.

148. Mueller, M. L., Yan, X., Mcguire, J. A., & Li, L. (2010). Triplet States and Electronic Relaxation in Photoexcited Graphene Quantum Dots, *Nano Letters, 10*: 2679–2682.

149. Mukthar Ali, S. M. Y. M., & Sandhya, K. Y. (2014). Visible light responsive titanium dioxide-cyclodextrin-fullerene composite with reduced charge recombination and enhanced photocatalytic activity. *Carbon*, *70*: 249–257.

150. Mukthar Ali, S. M. Y. M., & Sandhya, K. Y. (2016a). A New Green Method for the Preparation of Titanium dioxide-Graphene Composite Using Cyclodextrin as a Linker with Enhanced Photoexcited Electron Transfer and Photocatalytic Properties. *Environmental Progress & Sustainable Energy*, *33*(2): 482–489.

151. Mukthar Ali, S. M. Y. M., & Sandhya, K. Y. (2016b). One step solvothermal synthesis of carbon doped TiO_2-MoS_2 heterostructure composites with improved visible light catalytic activity. *New Journal of Chemistry,* 40: 8123.

152. Mukthar Ali, S. M. Y. M., & Sandhya, K. Y. (2016c). One step solvothermal synthesis of ultra-fine N-doped TiO_2 with enhanced visible light catalytic properties. *RSC Advances*, *6*(65): 60522–60529.

153. Mukthar Ali, S. M. Y. M., & Sandhya, K. Y. (2016d). Selective photodegradation and enhanced photo electrochemical properties of titanium dioxide-graphene composite with exposed (001) facets made by photochemical method. *Solar Energy Materials and Solar Cells*, *144*: 748–757.

154. Murthy, C. N., & Geckeler, K. E. (2001). The water-soluble β-cyclodextrin–[60]fullerene complex. *Chemical Communications*, *60*(13): 1194–1195.

155. Nagase, H., Furushi, T., Endo, T., Ueda, H., & Nagai, T. (1998). Solubilization of C_{70} into water by Complexation with δ-Cyclodextrin. *Chemical and Pharmaceutical Bulletin, 46*(10): 1658-1659.

156. Nair, R. R., Blake, P., Grigorenko, a. N., Novoselov, K. S., Booth,

T. J., Stauber, T., Geim, a. K. (2008). Fine Structure Constant Defines Visual Transperency of Graphene. *Science*, *320*: 1308.

157. Nakamura, R., Tanaka, T., & Nakato, Y. (2004). Mechanism for visible light responses in anodic photocurrents at N-doped TiO_2 film electrodes. *The Journal of physical chemistry B*, *108*(30): 10617–10620.

158. Ng, Y. H., Lightcap, I. V., Goodwin, K., Matsumura, M., & Kamat, P. V. (2010). To What Extent Do Graphene Scaffolds Improve the Photovoltaic and Photocatalytic Response of TiO_2 Nanostructured Films? *The Journal of physical chemistry Letters*, *1*(15): 2222–2227.

159. Ni, M., Leung, M. K. H., Leung, D. Y. C., & Sumathy, K. (2007). A review and recent developments in photocatalytic water-splitting using TiO_2 for hydrogen production. *Renewable and Sustainable Energy Reviews*, *11*(3): 401–425.

160. Novoselov, K. S., Geim, A. K., Morozov, S. V, Jiang, D., Katsnelson, M. I., Grigorieva, I. V, Firsov, A. A. (2005). Two-dimensional gas of massless Dirac fermions in graphene. *Nature*, *438*(7065): 197–200.

161. Ong, W. J., Tan, L. L., Chai, S. P., Yong, S. T., & Mohamed, A. R. (2014). Self-assembly of nitrogen-doped TiO_2 with exposed {001} facets on a graphene scaffold as photo-active hybrid nanostructures for reduction of carbon dioxide to methane. *Nano Research*, *7*(10): 1528–1547.

162. Pan, D., Guo, L., Zhang, J., Xi, C., Xue, Q., Huang, H., Wu, M. (2012). Cutting sp^2 clusters in graphene sheets into colloidal graphene quantum dots with strong green fluorescence. *Journal of Materials Chemistry*, *22*(8): 3314.

163. Pan, D., Jiao, J., Li, Z., Guo, Y., Feng, C., Liu, Y., Wu, M. (2015). Efficient Separation of Electron–Hole Pairs in Graphene Quantum Dots by TiO_2 Heterojunctions for Dye Degradation. *ACS Sustainable Chemistry & Engineering*, *3*(10): 2405–2413.

164. Pan, J. Q., Sheng, Y. Z., Zhang, J. X., Wei, J. M., Huang, P., Zhang, X., & Feng, B. X. (2014). Preparation of carbon quantum dots/TiO_2 nanotubes composites and their visible light catalytic applications. *Journal of Materials Chemistry A*, *2*(42): 18082–18086.

165. Pang, Y. L., & Abdullah, A. Z. (2013). Effect of carbon and nitrogen co-doping on characteristics and sonocatalytic activity of TiO_2 nanotubes catalyst for degradation of Rhodamine B in water. *Chemical Engineering*

Journal, *214*: 129–138.

166. Park, Y., Kim, W., Park, H., Tachikawa, T., Majima, T., & Choi, W. (2009). Carbon-doped TiO_2 photocatalyst synthesized without using an external carbon precursor and the visible light activity. *Applied Catalysis B: Environmental*, *91*(1): 355–361.

167. Park, Y., Singh, N. J., Kim, K. S., Tachikawa, T., Majima, T., & Choi, W. (2009). Fullerol-titania charge-transfer-mediated photocatalysis working under visible light. *Chemistry - A European Journal*, *15*(41): 10843–10850.

168. Peining, Z., Nair, A. S., Shengjie, P., Shengyuan, Y., & Ramakrishna, S. (2012). Facile Fabrication of TiO_2−Graphene Composite with Enhanced Photovoltaic and Photocatalytic Properties by Electrospinning. *ACS Applied Materials & Interfaces*, *4*(2): 581–585.

169. M., Zhang, Y., Zhang, N., Tang, Z., & Xu, Y. (2012). Graphene Transforms Wide Band Gap ZnS to a Visible Light Photocatalyst . The New Role of Graphene as a Molecular Photosensitizer, *ACS Nano, 6*(11): 9777–9789.

170. Qin, G., Sun, Z., Wu, Q., Lin, L., Liang, M., & Xue, S. (2011). Dye-sensitized TiO_2 film with bifunctionalized zones for photocatalytic degradation of 4-cholophenol. *Journal of Hazardous Materials*, *192*(2): 599–604.

171. Quan, X., Tan, H., Zhao, Q., & Sang, X. (2007). Preparation of lanthanum-doped TiO_2 photocatalysts by coprecipitation. *Journal of Materials Science*, *42*(15): 6287–6296.

172. Rahman, Q. I., Ahmad, M., Misra, S. K., & Lohani, M. (2013). Effective photocatalytic degradation of rhodamine B dye by ZnO nanoparticles. *Materials Letters*, *91*: 170–174

173. Rao, Y. F., & Chu, W. (2009). Reaction Mechanism of Linuron Degradation in TiO_2 Suspension under Visible Light Irradiation with the Assistance of H_2O_2. *Environmental Science & Technology*, *43*(16): 6183–6189.

174. Reddy, K. R., Hassan, M., & Gomes, V. G. (2015). Hybrid nanostructures based on titanium dioxide for enhanced photocatalysis. *Applied Catalysis A: General*, *489*: 1–16.

175. Renz, C. (1921). Lichtreaktionen der Oxyde des Titans , Cers und der Erdsäuren. *Helvetica Chimica Acta*, *4*: 961–968.

176. Reyes-Coronado, D., Rodríguez-Gattorno, G., Espinosa-Pesqueira, M. E., Cab, C., de Coss, R., & Oskam, G. (2008). Phase-pure TiO_2 nanoparticles: anatase, brookite and rutile. *Nanotechnology*, *19*(14): 145605.

177. Rockafellow, E. M., Stewart, L. K., & Jenks, W. S. (2009). Is sulfur-doped TiO_2 an effective visible light photocatalyst for remediation? *Applied Catalysis B: Environmental*, *91*(1): 554–562.

178. Rumaiz, A. K., Woicik, J. C., Cockayne, E., Lin, H. Y., Jaffari, G. H., & Shah, S. I. (2009). Oxygen vacancies in N doped anatase TiO_2: Experiment and first-principles calculations. *Applied Physics Letters*, *95*(26): 2–5.

179. Sahu, S., Behera, B., Maiti, T. K., & Mohapatra, S. (2012). Simple one-step synthesis of highly luminescent carbon dots from orange juice: application as excellent bio-imaging agents. *Chemical Communications*, *48*: 8835.

180. Sakthivel, S., Shankar, M. V., Palanichamy, M., Arabindoo, B., Bahnemann, D. W., & Murugesan, V. (2004). Enhancement of photocatalytic activity by metal deposition: Characterisation and photonic efficiency of Pt, Au and Pd deposited on TiO_2 catalyst. *Water Research*, *38*(13): 3001–3008.

181. Sato, T., Aita, Y., Komatsu, M., & Yin, S. (2006). Solvothermal synthesis of visible light responsive nitrogen-doped titania nanocrystals. *Journal of Materials Science*, *41*(5): 1433–1438.

182. Sawyer, D. T., & Valentine, J. S. (1981). How super is superoxide? *Accounts of Chemical Research*, *14*(12): 393–400.

183. Scanlon, D. O., Dunnill, C. W., Buckeridge, J., Shevlin, S. A., Logsdail, A. J., Woodley, S. M., Sokol, A. A. (2013). Band alignment of rutile and anatase TiO_2. *Nature Materials*, *12*(9): 798–801.

184. Schipper, K. P. and H. M. (2012). Principles of Free Radical Biomedicine. *Principles of Free Radical Biomedicine*, *1*: 1–23.

185. Schneider, J., Matsuoka, M., Takeuchi, M., Zhang, J., Horiuchi, Y.,

Anpo, M., & Bahnemann, D. W. (2014). Understanding TiO_2 Photocatalysis : Mechanisms and Materials. *Chemical Reviews, 114*: 9919–9986.

186. Sclafani, A., & Herrmann, J.-M. (1998). Influence of metallic silver and of platinum-silver bimetallic deposits on the photocatalytic activity of titania (anatase and rutile) in organic and aqueous media. *Journal of Photochemistry and Photobiology A: Chemistry*, *113*: 181–188.

187. Segall, M. D., Lindan, P. J. D., Probert, M. J., Pickard, C. J., Hasnip, P. J., Clark, S. J., & Payne, M. C. (2002). First-principles simulation: ideas, illustrations and the CASTEP code. *Journal of Physics: Condensed Matter*, *14*(11): 2717–2744.

188. Seo, Y. S., Lee, C., Lee, K. H., & Yoon, K. B. (2005). 1:1 and 2:1 Charge-Transfer Complexes Between Aromatic Hydrocarbons and Dry Titanium Dioxide. *Angewandte Chemie - International Edition*, *44*(6): 910–913.

189. Shao, M., & Zhuo, S. (2012). Upconversion and Downconversion Fluorescent Graphene Quantum Dots: Ultrasonic Preparation and Photocatalysis. *ACS Nano*, *6*(8): 6532–6532.

190. Shao, X., Tian, J., Xue, Q., & Ma, C. (2003). Fabrication of MoO_3 nanoparticles on an MoS_2 template with $(C_4H_9Li)xMoS_2$ exfoliation. *Journal of Materials Chemistry*, *13*(3): 631–633.

191. Shen, J., Zhu, Y., Yang, X., & Li, C. (2012). Graphene quantum dots: emergent nanolights for bioimaging, sensors, catalysis and photovoltaic devices. *Chemical Communications*, *48*(31): 3686.

192. Shen, M., Yan, Z., Yang, L., Du, P., Zhang, J., & Xiang, B. (2014). MoS_2 nanosheet/TiO_2 nanowire hybrid nanostructures for enhanced visible-light photocatalytic activities. *Chem. Commun.*, *50*(97): 15447–15449.

193. Song, Y., Zhu, S., & Yang, B. (2014). Bioimaging based on fluorescent carbon dots. *RSC Advances*, *4*(52): 27184–27200.

194. Souza, J. S., Pinheiro, M. V. B., Krambrock, K., & Alves, W. A. (2016). Dye Degradation Mechanisms Using Nitrogen Doped and Copper(II) Phthalocyanine Tetracarboxylate Sensitized Titanate and TiO_2 Nanotubes. *The Journal of Physical Chemistry C*, *120*(21): 11561–11571.

195. Spadavecchia, F., Cappelletti, G., Ardizzone, S., Ceotto, M., & Falciola, L. (2011). Electronic structure of pure and N-doped TiO_2 nanocrystals by electrochemical experiments and first principles calculations. *The Journal of physical chemistry C*, *115*(14): 6381–6391.

196. Stengl, V., Popelkova, D., & Vlacil, P. (2011). TiO_2 À Graphene Nanocomposite as High Performace Photocatalysts, *The Journal of physical chemistry C, 115*(51): 25209–25218.

197. Strunk, J., Vining, W. C., & Bell, A. T. (2010). A Study of Oxygen Vacancy Formation and Annihilation in Submonolayer Coverages of TiO_2 Dispersed on MCM-48. *J. Phys. Chem. C*, *114*(40): 16937–16945.

198. Sun, L., Zhao, X., Cheng, X., Sun, H., Li, P., & Fan, W. (2012). Synergistic Effects in La / N Codoped TiO_2 Anatase (101) Surface Correlated with Enhanced Visible-Light Photocatalytic Activity, *Langmuir, 28*(13): 5882–5891.

199. Sun, L., Zhao, Z., Zhou, Y., & Liu, L. (2012). Anatase TiO_2 nanocrystals with exposed {001} facets on graphene sheets via molecular grafting for enhanced photocatalytic activity. *Nanoscale*, *4*(2): 613–20.

200. Sun, Y. P., Zhou, B., Lin, Y., Wang, W., Fernando, K. A. S., Pathak, P., Xie, S. Y. (2006). Quantum-sized carbon dots for bright and colorful photoluminescence. *Journal of the American Chemical Society*, *128*(24): 7756–7757.

201. Szatmary, L., Bakardjieva, S., Subrt, J., Bezdicka, P., Jirkovsky, J., Bastl, Z., Korenko, M. (2011). Sulphur doped nanoparticles of TiO_2. *Catalysis Today*, *161*(1): 23–28.

202. Tachikawa, T., Tojo, S., Fujitsuka, M., & Majima, T. (2006). One-electron oxidation pathways during β-cyclodextrin-modified TiO_2 photocatalytic reactions. *Chemistry - A European Journal*, *12*(29): 7585–7594.

203. Tian, F., Zhang, Y., Zhang, J., & Pan, C. (2012). Raman spectroscopy: A new approach to measure the percentage of anatase TiO_2 exposed (001) facets. *The Journal of physical chemistry C*, *116*(13): 7515–7519.

204. Tian, J., Leng, Y., Zhao, Z., Xia, Y., Sang, Y., Hao, P., Liu, H. (2015). Carbon quantum dots/hydrogenated TiO_2 nanobelt heterostructures and their broad spectrum photocatalytic properties under UV, visible, and near-infrared

irradiation. *Nano Energy*, *11*: 419–427.

205. Torres, G. R., Lindgren, T., Lu, J., Granqvist, C. G., & Lindquist, S. E. (2004). Photoelectrochemical study of nitrogen-doped titanium dioxide for water oxidation. *The Journal of physical chemistry B*, *108*(19): 5995–6003.

206. Turchi, C. S., & Ollis, D. F. (1990). Photocatalytic Degradation of Organic-Water Contaminants - Mechanisms Involving Hydroxyl Radical Attack. *Journal of Catalysis*, *122*(1): 178.

207. Varaganti, S., & Ramakrishna, G. (2010). Dynamics of Interfacial Charge Transfer Emission in Small-molecule Sensitized TiO_2 Nanoparticles : Is it Localized or Delocalized ?, *The Journal of physical chemistry, 114*(32): *13917-13925.*

208. Vayssieres, L. (2003). Growth of arrayed nanorods and nanowires of ZnO from aqueous solutions. *Advanced Materials*, *15*(5): 464–466.

209. Venugopal, G., Krishnamoorthy, K., Mohan, R., & Kim, S.-J. (2012). An investigation of the electrical transport properties of graphene-oxide thin films. *Materials Chemistry and Physics*, *132*(1): 29–33.

210. Vrachnou, E., Gratzel, M., & McEvoy, A. J. (1989). Efficient visible light photoresponse following surface complexation of titanium dioxide with transition metal cyanides. *Journal of Electroanalytical Chemistry*, *258*(1): 193–205.

211. Wang, G., Wu, F., Zhang, X., Luo, M., & Deng, N. (2006). Enhanced TiO_2 photocatalytic degradation of bisphenol E by β-cyclodextrin in suspended solutions. *Journal of Hazardous Materials*, *133*(1-3): 85–91.

212. Wang, J., Cheng, C., Huang, Y., Zheng, B., Yuan, H., Bo, L., Xiao, D. (2014). A facile large-scale microwave synthesis of highly fluorescent carbon dots from benzenediol isomers. *Journal of Materials Chemistry C*, *2*(25): 5028–5035.

213. Wang, J., Tafen, D. N., Lewis, J. P., Hong, Z., Manivannan, A., Zhi, M., Wu, N. (2009). Origin of photocatalytic activity of Nitrogen-doped TiO_2 nanobelts. *Journal of the American Chemical Society*, *131*(34): 12290–12297.

214. Wang, Y., Hang, K., Anderson, N. a, & Lian, T. (2003). Comparison of Electron Transfer Dynamics in Molecule-to-Nanoparticle and Intramolecular Charge Transfer Complexes. *The Journal of Physical Chemistry B*, *107*(35):

9434–9440.

215. Wang, Y., Hao, Y., Cheng, H., Ma, J., & Xu, B. I. N. (1999). The photoelectrochemistry of transition metal-ion-doped TiO_2 nanocrystalline electrodes and higher solar cell conversion efficiency based on Zn^2 + -doped TiO_2 electrode. *Journal of Materials Science*, *34*(12): 2773–2779.

216. Wang, Y., & Hu, A. (2014). Carbon quantum dots: synthesis, properties and applications. *Journal of Materials Chemistry C*, *2*: 6921–6939.

217. Wawrzyniak, B., Morawski, A. W., & Tryba, B. (2006). Preparation of TiO_2-nitrogen-doped photocatalyst active under visible light. *International Journal of Photoenergy*, *2006*: 1–8.

218. Wendt, S., Sprunger, P. T., Lira, E., Madsen, G. K. H., Li, Z., Hansen, J.O., Besenbacher, F. (2008). The role of interstitial sites in the Ti3d defect state in the band gap of titania. *Science*, *320*(110): 1755–1759.

219. Weng, Y.-X., Wang, Y.-Q., Asbury, J. B., Ghosh, H. N., & Lian, T. (1999). Back Electron Transfer from TiO_2 Nanoparticles to $FeIII(CN)_6^{3-}$: Origin of Non-Single-Exponential and Particle Size Independent Dynamics. *The Journal of Physical Chemistry B*, *104*(1): 93–104.

220. Wilhelm, P., & Stephan, D. (2007). Photodegradation of rhodamine B in aqueous solution via SiO_2@TiO_2 nano-spheres. *Journal of Photochemistry and Photobiology A: Chemistry*, *185*(1): 19–25.

221. Williams, G., Seger, B., & Kamat, P. V. (2008). UV-Assisted Photocatalytic Reduction of Graphene Oxide, *ACS Nano, 2*(7): 1487–1491.

222. Woan, K., Pyrgiotakis, G., & Sigmund, W. (2009). Photocatalytic Carbon-Nanotube-TiO_2 Composites. *Advanced Materials*, *21*(21): 2233–2239.

223. Wojtoniszak, M., Roginiska, D., Machalinski, B., Drozdzik, M., & Mijowskaa, E. (2013). Graphene oxide functionalized with methylene blue and its performance in singlet oxygen generation, *Materials Rsearch Bulletin, 48*: 2636–2639.

224. Xagas, a. ., Bernard, M. ., Hugot-Le Goff, a, Spyrellis, N., Loizos, Z., & Falaras, P. (2000). Surface modification and photosensitisation of TiO_2 nanocrystalline films with ascorbic acid. *Journal of Photochemistry and Photobiology A: Chemistry*, *132*(1-2): 115–120.

225. Xia, T., Zhang, W., Murowchick, J. B., Liu, G., & Chen, X. (2013). A facile method to improve the photocatalytic and lithium-ion rechargeable battery performance of TiO_2 nanocrystals. *Advanced Energy Materials*, *3*(11): 1516–1523.

226. Xiang, Q., & Yu, J. (2013). Graphene-based photocatalysts for hydrogen generation. *The Journal of physical chemistry Letters*, *4*(5): 753–759.

227. Xiang, Q., Yu, J., & Jaroniec, M. (2011). Enhanced photocatalytic H_2-production activity of graphene-modified titania nanosheets. *Nanoscale*, *3*(9): 3670–3678.

228. Xiang, Q., Yu, J., & Jaroniec, M. (2012). Graphene-based semiconductor photocatalysts. *Chemical Society Reviews*, *41*(2): 782–796.

229. Xiang, Q., Yu, J., & Jaroniec, M. (2012). Synergetic Effect of MoS_2 and Graphene as Cocatalysts for Enhanced Photocatalytic H_2 Production Activity of TiO_2 Nanoparticles. *Journal of the American Chemical Society*, *134*(15): 6575–6578.

230. Xiao, F. (2012). Construction of Highly Ordered ZnO−TiO_2 Nanotube Arrays (ZnO/TNTs) Heterostructure for Photocatalytic Application. *ACS Applied Materials & Interfaces*, *4*(12): 7055–7063.

231. Xing, M., Zhang, J., Chen, F., & Tian, B. (2011). An economic method to prepare vacuum activated photocatalysts with high photo-activities and photosensitivities. *Chemical Communications*, *47*(17), 4947–4949.

232. Xiv, V., Wold, A., & Ruff, J. K. (2007). *Inorganic Syntheses Volume XIV*.

233. Xu, Xiaoyou; Ray, Robert; Gu, Yunlong; Ploehn, HarryJ.; Gearheart, Latha; Raker, Kyle; Scrivens, W. A. (2004). Electrophoretic Analysis and Purification of Fluorescent Single-Walled Carbon Nanotube Fragments. *Journal of the American Chemical Society*, *126*(40): 12736–12737.

234. Xu, J. N., Sun, P., Zhang, X., Jiang, P., Cao, W. B., Chen, P. W., & Jin, H. B. (2014). Synthesis of N-doped TiO_2 with Different Nitrogen Concentrations by Mild Hydrothermal Method. *Materials and Manufacturing Processes*, *29*(10): 1162–1167.

235. Yamashita, H., Harada, M., Misaka, J., Takeuchi, M., Ikeue, K., & Anpo, M. (2002). Degradation of propanol diluted in water under visible light irradiation using metal ion-implanted titanium dioxide photocatalysts. *Journal of*

Photochemistry and Photobiology A: Chemistry, *148*(1-3): 257–261.

236. Yan, X., Cui, X., Li, B., & Li, L. S. (2010). Large, solution-processable graphene quantum dots as light absorbers for photovoltaics. *Nano Letters*, *10*(5): 1869–1873.

237. Yang, G., Jiang, Z., Shi, H., Xiao, T., & Yan, Z. (2010). Preparation of highly visible-light active N-doped TiO_2 photocatalyst. *Journal of Materials Chemistry*, *20*(25): 5301.

238. Yang, G., Yan, Z., & Xiao, T. (2012). Preparation and characterization of SnO_2/ZnO/TiO_2 composite semiconductor with enhanced photocatalytic activity. *Applied Surface Science*, *258*(22): 8704–8712.

239. Yang, H. G., Sun, C. H., Qiao, S. Z., Zou, J., Liu, G., Smith, S. C., Lu, G. Q. (2008). Anatase TiO_2 single crystals with a large percentage of reactive facets. *Nature*, *453*(7195): 638–41.

240. Yang, S. T., Wang, X., Wang, H., Lu, F., Luo, P. G., Cao, L., Sun, Y. P. (2009). Carbon dots as nontoxic and high-performance fluorescence imaging agents. *The Journal of physical chemistry C*, *113*(42): 18110–18114.

241. Yin, S., Zhang, Q. W., Saito, F., & Sato, T. (2003). Preparation of visible light-activated titania photocatalyst by mechanochemical method. *Chemistry Letters*, *32*(4): 358–359.

242. Yu, J., Fan, J., & Lv, K. (2010). Anatase TiO_2 nanosheets with exposed (001) facets: improved photoelectric conversion efficiency in dye-sensitized solar cells. *Nanoscale*, *2*(10): 2144–2149.

243. Yu, J., Wang, W., & Cheng, B. (2010). Synthesis and enhanced photocatalytic activity of a hierarchical porous flowerlike p-n junction NiO/TiO_2 photocatalyst. *Chemistry - An Asian Journal*, *5*(12): 2499–2506.

244. Yu, X., Liu, J., Yu, Y., Zuo, S., & Li, B. (2014). Preparation and visible light photocatalytic activity of carbon quantum dots/TiO_2 nanosheet composites. *Carbon*, *68*: 718–724.

245. Yuan, X. L., Zhang, J. L., Anpo, M., & He, D. N. (2010). Synthesis of Fe3+ doped ordered mesoporous TiO_2 with enhanced visible light photocatalytic activity and highly crystallized anatase wall. *Research on Chemical Intermediates*, *36*(1): 83–93.

246. Zhang, G., Kim, G., & Choi, W. (2014). Visible light driven photocatalysis mediated via ligand-to-metal charge transfer (LMCT): an alternative approach to solar activation of titania. *Energy Environmental. Science. 7*(3): 954–966.

247. Zhang, H., Lv, X., Li, Y., Wang, Y., & Li, J. (2010). P25-graphene composite as a high performance photocatalyst. *ACS Nano*, *4*(1): 380–6.

248. Zhang, J., Shen, W., Pan, D., Zhang, Z., Fang, Y., & Wu, M. (2010). Controlled synthesis of green and blue luminescent carbon nanoparticles with high yields by the carbonization of sucrose. *New Journal of Chemistry*, *34*(4): 591.

249. Zhang, X., Wu, F., & Deng, N. (2010). Degradation of paracetamol in self assembly β-cyclodextrin/TiO_2 suspension under visible irradiation. *Catalysis Communications*, *11*(5): 422–425.

250. Zhang, X., Wu, F., & Deng, N. (2011). Efficient photodegradation of dyes using light-induced self assembly TiO_2/ β-cyclodextrin hybrid nanoparticles under visible light irradiation. *Journal of Hazardous Materials*, *185*(1): 117–123.

251. Zhang, Z., Shao, C., Li, X., Sun, Y., Zhang, M., Mu, J., Liu, Y. (2013). Hierarchical assembly of ultrathin hexagonal SnS_2 nanosheets onto electrospun TiO_2 nanofibers: Enhanced photocatalytic activity based on photoinduced interfacial charge transfer. *Nanoscale, 5*: 606.

252. Zhao, Q.-L., Zhang, Z.-L., Huang, B.-H., Peng, J., Zhang, M., & Pang, D.-W. (2008). Facile preparation of low cytotoxicity fluorescent carbon nanocrystals by electrooxidation of graphite. *Chemical Communications, 41*: 5116.

253. Zheng, F., Wang, Z., Chen, J., & Li, S. (2014). Synthesis of carbon quantum dot-surface modified P25 nanocomposites for photocatalytic degradation of p-nitrophenol and acid violet 43. *RSC Advances*, *4*(58): 30605–30609.

254. Zheng, X. T., Ananthanarayanan, A., Luo, K. Q., & Chen, P. (2015). Glowing graphene quantum dots and carbon dots: Properties, syntheses, and biological applications. *Small*, *11*(14): 1620–1636.

255. Zhou, L., He, B., & Huang, J. (2013). Amphibious fluorescent carbon dots: one-step green synthesis and application for light-emitting polymer nanocomposites. *Chemical Communications*, *49*(73): 8078–80.

256. Zhou, W., Yin, Z., Du, Y., Huang, X., Zeng, Z., Fan, Z., Zhang, H. (2013).

Synthesis of few-layer MoS_2 nanosheet-coated TiO_2 nanobelt heterostructures for enhanced photocatalytic activities. *Small*, *9*(1): 140–147.

257. Zhou, X., Shi, T., Wu, J., & Zhou, H. (2013). (001) Facet-exposed anatase-phase TiO_2 nanotube hybrid reduced graphene oxide composite: Synthesis, characterization and application in photocatalytic degradation. *Applied Surface Science*, *287*: 359–368.

258. Zhu, J., Chen, F., Zhang, J., Chen, H., & Anpo, M. (2006). Fe^{3+}-TiO_2 photocatalysts prepared by combining sol-gel method with hydrothermal treatment and their characterization. *Journal of Photochemistry and Photobiology A: Chemistry*, *180*(1-2): 196–204.

259. Zhu, L., Jo, S. B., Ye, S., Ullah, K., & Oh, W. C. (2014). Rhodamine B degradation and reactive oxygen species generation by a ZnSe-graphene/TiO_2 sonocatalyst. *Chinese Journal of Catalysis*, *35*(11): 1825–1832.

260. Ziolli, R. L., & Jardim, W. F. (2001). Photocatalytic decomposition of seawater-soluble crude oil fractions using high surface area colloid nanoparticles of TiO_2. *Journal of Photochemistry and Photobiology A: Chemistry*, *5887*: 1–8.

261. Zong, X., Yan, H., Wu, G., Ma, G., Wen, F., Wang, L., & Li, C. (2008). Enhancement of Photocatalytic H_2 Evolution on CdS by Loading MoS_2 as Cocatalyst under Visible Light Irradiation. *Journal of the American Chemical Society*, *130*(23): 7176–7177.

262. Zuo, F., Wang, L., Wu, T., Zhang, Z., Borchardt, D., & Feng, P. (2010). Self-doped Ti^{3+} enhanced photocatalyst for hydrogen production under visible light. *Journal of the American Chemical Society*, *132*(34): 11856–11857.

LIST OF PUBLICATIONS/ PATENTS BASED ON THESIS

PUBLISHED

1. Mukthar Ali, M. and Sandhya, K.Y. (2016). One step solvothermal synthesis of carbon doped TiO_2-MoS_2 heterostructure composites with improved visible light catalytic activity. *New journal of Chemistry,* 40, 8123.

2. Mukthar Ali, M. and Sandhya, K.Y. (2016). One step solvothermal synthesis of ultra-fine N-doped TiO_2 with enhanced visible light catalytic properties. *RSC Advances,* 6, 60522-60529.

3. Mukthar Ali, M., Shukla, A. and Sandhya, K.Y. (2016). A new green method for the preparation of titanium dioxide-graphene composite using cyclodextrin as a linker with enhanced photoexcited electron transfer and photocatalytic properties. *Environmental Progress and Sustainable Energy,* DOI: 10.1002/ep.12343.

4. Mukthar Ali, M. and Sandhya, K.Y. (2016). Selective photodegradation and enhanced photoelectrochemical properties of titanium dioxide–graphene composite with exposed (001) facets made by photochemical method. *Solar Energy Materials & Solar Cells,* 144, 748–757.

5. Mukthar Ali, M. and Sandhya, K.Y. (2015). Highly Active TiO_2-MoS_2 Composite for Visible Light Photocatalytic Applications. *Materials Science Forum,* 830-831: 553-556.

6. Mukthar Ali, M. and Sandhya, K.Y. (2014). Visible light responsive titanium dioxide–cyclodextrin–fullerene composite with reduced charge recombination and enhanced photocatalytic activity. *Carbon,* 2014, 70, 249-257.

7. Mukthar Ali, M. and Sandhya, K.Y. (2014). Reduced graphene oxide as a highly efficient adsorbent for 1-naphthol and the mechanism thereof. *RSC Advances,* 2014, 04, 51624.

UNDER PREPARATION

1. Mukthar Ali, M. and Sandhya, K.Y. P25–undoped carbon dot composite for visible light photodegradation.

2. Mukthar Ali, M. and Sandhya, K.Y. A novel approach for carbon quantum dot anchored P25 composite for mineralization of rhodamine B under visible light and its mechanistic studies.

CONFERENCE PRESENTATIONS

1. Mukthar Ali, M. and Sandhya, K.Y. Selective photodegradation and enhanced photoelectrochemical properties of TiO_2-graphene with exposed (001) facets made by photochemical reduction method. *Materials Research Society of India (MRSI), Trivandrum chapter annual technical meeting, SCTIMST, Thiruvananthapuram.* 30 Jan. (2015).

2. Mukthar Ali, M. and Sandhya, K.Y. Photochemically reduced graphene oxide-high reactive facet TiO_2 composites with anti-recombination and enhanced surface area for photocatalytic applications. *International Conference on Advanced Functional Materials, ICAFM 2014, NIIST, Thiruvananthapuram.* 19-21 Feb. (2014).

3. Mukthar Ali, M. and Sandhya, K.Y. Reduced graphene oxide as high efficient adsorbent for 1-naphthol. *Research Scholar's Day, IIST, Thiruvananthapuram.* 16-17 Dec. (2013).

4. Mukthar Ali, M. and Sandhya, K.Y. Water Soluble β-Cyclodextrin-Fullerene (C_{60}) complex – An Easy and toxic solvent-free method of preparation and its Characterization Studies. *Research Scholar's Day, IIST, Thiruvananthapuram.* 17-19 Dec. (2012).

PATENTS

1. Mukthar Ali, M. and Sandhya, K.Y. A novel method for preparation of water soluble fullerenes (Indian Patent Application No. 2554/CHE/2013).